



DTU Physics
Department of Physics

Investigation of the temperature coefficient of resistance in ultra-thin metal films

Thomas Antonio Marangoni

Department of Physics
Technical University of Denmark
30-11-2021

Supervised by:
Dirch Hjorth Petersen
Benny Guralnik
Ole Hansen

Abstract

Heat and electricity are intimately connected through Joule heating and the continued downscaling of micro- and nanoscale electronic components is leading to devices with extremely high power densities. The resulting very high operating temperatures are limiting device performance, reliability and efficiency. A key design parameter is the temperature coefficient of resistance (TCR), which, when positive (e.g. in metals), compounds the negative effects of inadequate heat removal and leads to even higher power densities. The TCR can already be precisely characterized through existing methods, however they often are inflexible or involve significant sample preparation and additionally, require an independent measurement of temperature, resulting in a long measurement time.

This PhD thesis introduces a novel characterization method to extract the TCR from ultra-thin metal films. The method applies the micro four-point probe (M4PP) tool to perform a four terminal measurement at the microscale. The M4PP has been shown to accurately and very precisely measure the sheet resistance of thin conductive films. The M4PP is able to detect a rise in sheet resistance as a result of Joule heating. By modelling the induced temperature rise, the thin film TCR can be extracted from this measured increase in resistance. The method (named the M4PP-TCR method) is demonstrated on several platinum thin films of varying thickness. The increase in measured resistance was reproducible and easily detectable by the M4PP. The extracted TCR values showed near perfect correlation with independent reference measurements taken on a physical property measurement system (PPMS). The extracted values were however offset by $\sim 18\%$, attributed to omission of time dependent effects in the thermal model. This offset led to the development of an extended thermal model, currently still ongoing, that considers thermal delays and removed the dependence of the extracted TCR on the applied measurement frequency and probe size (probe pitch). The developed method does not require an independent measurement of temperature, resulting a fast, versatile and precise measurement of thin film TCR, that can be applied in high speed environments such as in-line process monitoring or

as an early diagnostic tool.

In addition, the effects of typical M4PP measurement errors on the precision of the M4PP-TCR method are evaluated. Most notably position errors, where the position of the electrodes deviates from its nominal position, are found to potentially induce sizable errors for small (probe pitch $\sim 1 \mu\text{m}$) probes. Lastly, an optimized measurement scheme is suggested, where a TCR value can be extracted from only three individual M4PP measurements. This will further reduce the measurement time and allows for an easier distinction between measurement errors and sample variability and could make the M4PP-TCR method suitable for e.g. wafer mapping.

Resumé

Varme og elektricitet er tæt forbundet via Joule-varme, og den fortsatte nedskalering af elektroniske komponenter til mikro- og nano-skala fører til enheder med ekstremt høje effekttætheder. De deraf følgende meget høje driftstemperaturer begrænser enhedens ydeevne, pålidelighed og effektivitet. En vigtig konstruktionsparameter er mostandstemperaturkoefficienten (TCR), som, når den er positiv (f.eks. i metaller), forstærker de negative virkninger af utilstrækkelig varmeafledning og fører til endnu højere effekttætheder. TCR kan allerede karakteriseres præcist ved hjælp af eksisterende metoder, men de er ofte ufleksible eller kræver en betydelig prøveforberedelse og kræver desuden en uafhængig temperaturmåling, hvilket resulterer i lange måletider.

Denne ph.d.-afhandling introducerer en ny karakteriseringsmetode til at udtrække TCR fra ultra-tynde metalfilm. Metoden anvender mikro-firepunktsprober (M4PP) til at udføre en fireterminal måling på mikroskala. M4PP har vist sig at kunne foretage en nøjagtig og meget præcis måling af flademodstanden af tynde ledende film. M4PP er i stand til at registrere en stigning i flademodstanden som følge af Joule-opvarmning. Ved at modellere den inducerede temperaturstigning kan TCR for tynde film udledes af denne målte modstandsstigning. Metoden (M4PP-TCR-metoden) er blevet demonstreret på flere tynde platin-film af forskellig tykkelse. Stigningen i den målte modstand var reproducerbar og let påviselig ved hjælp af M4PP. De ekstraherede TCR-værdier viste næsten perfekt korrelation med uafhængige referencemålinger foretaget på et system til måling af fysiske egenskaber (PPMS). De ekstraherede værdier var dog forskudt med $\sim 18\%$, hvilket skyldes at tidsafhængige effekter i den termiske model var udeladt. Denne forskydning førte til udvikling af en udvidet termisk model, som i øjeblikket stadig er under udvikling, og som tager hensyn til termiske forsinkelser og fjerner den ekstraherede TCR's afhængighed af den anvendte målefrekvens og probens størrelse (elektrodeafstand). Den udviklede metode kræver ikke en uafhængig temperaturmåling, hvilket resulterer i en hurtig, alsidig og præcis måling af tyndfilms TCR, som kan anvendes i højhastighedsmiljøer som f.eks. in-line procesovervågning eller

som et tidligt diagnostisk værktøj.

Desuden er effekten af typiske M4PP-målefejl på M4PP-TCR-metodens præcision blevet vurderet. Især positionsfejl, hvor elektrodernes position afviger fra den nominelle position, viser sig at kunne medføre betydelige fejl ved prober med små elektrodeafstande (elektrodeafstand $\sim 1 \mu\text{m}$). Endelig foreslås en optimeret målesekvens, hvor en TCR-værdi kan udtrages fra kun tre individuelle M4PP-målinger. Dette vil reducere måletiden yderligere, gøre det lettere at skelne mellem målefejl og prøvevariabilitet og kunne gøre M4PP-TCR-metoden egnet til f.eks. kortlægning af hele skiver.

Preface

This thesis has been submitted to partially fulfill the requirements of obtaining the Ph.D. degree from the Technical University of Denmark (DTU). The work, on which this thesis is based, has primarily been performed at the Department of Physics and the Department of Energy from December 2018 to November 2021. The work has been supervised by Dirch Hjorth Petersen.

I would like to thank my principle supervisor Dirch Hjorth Petersen, who has given me the opportunity to start my Ph.D. degree at DTU and has provided a stimulating work environment, with plenty of room for discussion and whose expertise in the micro four-point probe has laid the groundwork for this project. Secondly, I would like to thank my co-supervisor Benny Guralnik for his extensive assistance in both the analytical and experimental aspects of the project and furthermore constantly driving me to improve my academic skills. I would like to thank Ole Hansen whose wealth of knowledge has helped in the interpretation of the results. I would also like to thank CAPRES, who has allowed me to use their equipment and laboratory to perform the experiments and Frederik Østerberg, Kasper Borup and Thomas Pedersen for their aid in the experiments and fabrication and to Victor Rosendal, Neetu Rani, Braulio Beltrán-Pitarch, Asger Pedersen, Kristoffer Kalhauge and Maria-Louise Witthøft for their valuable input in the group meetings and making the office a pleasant place to be.

A thank you to 'Lady Luck', who ensured I obtained my crucial experimental results, one week before the corona lockdown was enforced.

I would like to thank my friends and family who have made these past three years an enjoyable experience.

Finally, a special thank you to Disha, who has put up with me through three years of struggles and triumphs. This Ph.D. would not have been possible without her endless support and encouragement.

Contents

Abstract	i
Resumé	iii
Preface	v
1 Introduction	1
1.1 Joule heating	2
1.1.1 The temperature coefficient of resistance	5
1.2 Current TCR characterisation methods	6
1.3 The proposed method	8
1.4 Thesis outline	10
2 Theory	13
2.1 Fundamentals of electrical conduction in metals	13
2.1.1 Scattering mechanisms	14
2.1.2 Mathiessen's rule	17
2.1.3 Temperature dependence of resistance	18

2.2	Thermal conduction in solids	19
2.3	Thin film effects	20
2.3.1	Thin film resistivity	20
2.3.2	The TCR in thin films	22
2.4	Four terminal sensing at the microscale	24
2.4.1	M4PP Sensitivity	29
2.4.2	The MicroRSP A300 tool	29
3	The M4PP-TCR Method	33
3.1	The M4PP on a sheet system	35
3.1.1	Current flow in a M4PP thin film measurement	36
3.2	TCR response in M4PP measurements	36
3.3	The semi-analytical model	39
3.3.1	Calculating the temperature increase	40
3.3.2	Calculating the contact resistance	46
3.3.3	Data analysis using semi-analytical model	48
3.3.4	Validation with FEM	50
3.3.5	Limitations of the Semi-analytical method	54
3.4	TCR of Pt thin films	56
3.4.1	TCR from quasi-static analysis	58
3.4.2	TCR from steady state analysis	64
4	Errors in M4PP-TCR measurements	71
4.1	Position errors	72

4.2	Electrical errors	80
5	The triplet measurement scheme	83
5.1	A single TCR measurement: a triplet	84
5.2	Triplet measurement on Pt	86
5.2.1	Results	87
6	Conclusion and Outlook	91
	Bibliography	96
A	TCR extraction from ruthenium thin films	109
B	TCR extracted from remaining configurations and subprobes on platinum thin film samples	111
B.1	B and C configurations on the 10A sub-probe	111
B.2	A, B and C configuration on the 10B sub-probe	119
B.3	A, B and C configurations on the 20 sub-probe	120
	Supplementary material	123

Chapter 1

Introduction

Science and technology has made an extraordinary jump in progress over the last century. From the invention of flight to supersonic aircraft, from the first transatlantic phone call in 1927, to live TV and from navigation using manually surveyed maps to the GPS, available on every smartphone. The extraordinary development of computers and other electronic devices have led to many of these new inventions and discoveries. Computational calculations and modelling have opened up research into more advanced climate models [1], modelling of molecular and atomic level interactions leading to advances in material science [2] and medicine [3], the development of powerful algorithms allowing the investigation of complex physical problems [4] [5] [6] [7] and countless other examples. The improvement of many electronic sensors and measuring equipment has made possible the detection of many new phenomena, such as the detection of sub-atomic particles at CERN, where the LHC experiments generate 90 petabytes of data per year [8].

From the invention of the transistor in 1947 [9] [10], one of the most essential building blocks of modern electronics, computational power has improved significant over the years. This advancement is not better illustrated by Moore's law, formulated by Gordon Moore in 1965 [11]. Moore predicted that the number of transistors on a processor chip will double every two years. Transistor count can be equated to the computational power of processors. Until recently, this assumption has held true, due to the continued advances in downscaling of electronic components and the improvement of fabrication processes of electronic devices and components. The industry is predicting a minimum physical gate length on 12nm by the end of the decade [12]. However, as the typical feature size of electronic components is reaching single-digit nanometer length scales, Moore's law is starting to stall [13]. A key contributor is the generation of heat. Excess heat

in electronic devices leads to damage, lowered performance and higher power usage. In recent years, research has intensified [14] to find ways to mitigate thermal throttling via the search of alternate materials and techniques [15] [16], optimised chip designs [17] and through software optimisation [18] [19].

The research presented in this thesis aims to contribute in the optimisation of future electronic devices by introducing an alternative method of characterisation of a key design parameter. Metrology, the science of measuring, is an essential component in science, as without a satisfactory method to measure results, progress is difficult to quantify. The method presented in this thesis has strong potential to play a role in the development of new materials and optimisation of designs of future electronic devices.

1.1 Joule heating

Excessive heat generation in electronic devices has been a common concern [20] [21]. Heat is an inherent part of any electronic system due to a process called Joule heating (also called Ohmic heating or self heating). When an electric current passes through a resistor, heat power is generated proportional to the applied current and the resistance of the resistor:

$$P = I^2 R \tag{1.1}$$

In an effort to continue to enhance device performance, electronic components have been scaled down to nanometer dimensions and alternative designs, such as 3D layer stacking [22], are being explored. This has led to improved performance of electronic devices as more transistors can fit on a chip. However, the increased device density comes at the cost of an increased power density (as a result of Joule heating). These high power densities generate a significant amounts of heat. Without adequate heat dissipation methods the resulting high temperatures will negatively impact device performance and reliability and can even irreparably damage the device, as shown in Fig. 1.1a. If the temperature reaches critical levels, software must throttle the maximum allowed current densities in the device, reducing device performance.

Interconnects have been identified as the dominant factor in the rise of micro-electronic power densities. [23] [24]. Interconnects are metallic lines acting as the connections between different chip components. Reducing interconnect line width and pitch has introduced significant thermal problems, as the reduced dimensions increase the interconnect line resistance as well as increasing the power density

[25] [26] [27]. Due to the close proximity, interconnect lines are embedded in dielectric materials to reduce inter-line capacitance. [28] However, the low thermal conductivity of these barrier layers limits effective heat removal away from the interconnect lines, exposing the metallic lines to thermal stresses. Device demands might require high and rapid temperature fluctuations which can lead to thermal fatigue. Thermal fatigue can have catastrophic consequences for interconnect reliability, where in extreme cases the lifetime can be reduced to a mere 6 months [29], seen in Fig. 1.1b. Damage due to electromigration, a process where the conductor material can be moved away from high current density areas due to momentum transfer between the material and the charge carriers, is increased with higher temperature [30] [31] [32].

The thermal conductivity of a materials is dependent of the mean free path of the dominant heat carriers.[33] As the dimensions of the microelectronic components (e.g. line width, grain size, thickness) is reduced, the thermal conductivity, and thus the effectiveness of the heat transport, will reduce as well. [34] [35] [36]. This decrease in thermal conductivity can be significant, e.g. the thermal conductivity of silicon nanowires can drop as low as $\sim 8 \text{ W m}^{-1} \text{ K}^{-1}$ at diameters of 22 nm compared to the $\sim 130 \text{ W m}^{-1} \text{ K}^{-1}$ bulk value [37]. The more tightly packed chip architectures exacerbate the issue by introducing more interfaces in the heat transport pathways, which mostly have a negative impact on the effectiveness of the heat diffusion. [36] [38]. Traditional forced convection cooling (via e.g. a fan) combined with heat sinks is unable to effectively deal with the increasing power densities [39] and liquid cooling (more effective) is often not practical. The application of thermoelectric materials to act as microscale refrigerators has shown promise [40] [41] [42] [43], but is being held back by the lack of high efficiency thermoelectric materials and effective integration into microelectronic devices (e.g. hot and cold reservoirs cannot be infinitesimally close together along with, often device specific, optimisation of the refrigerator-device interface being required before net cooling can be achieved) [44].

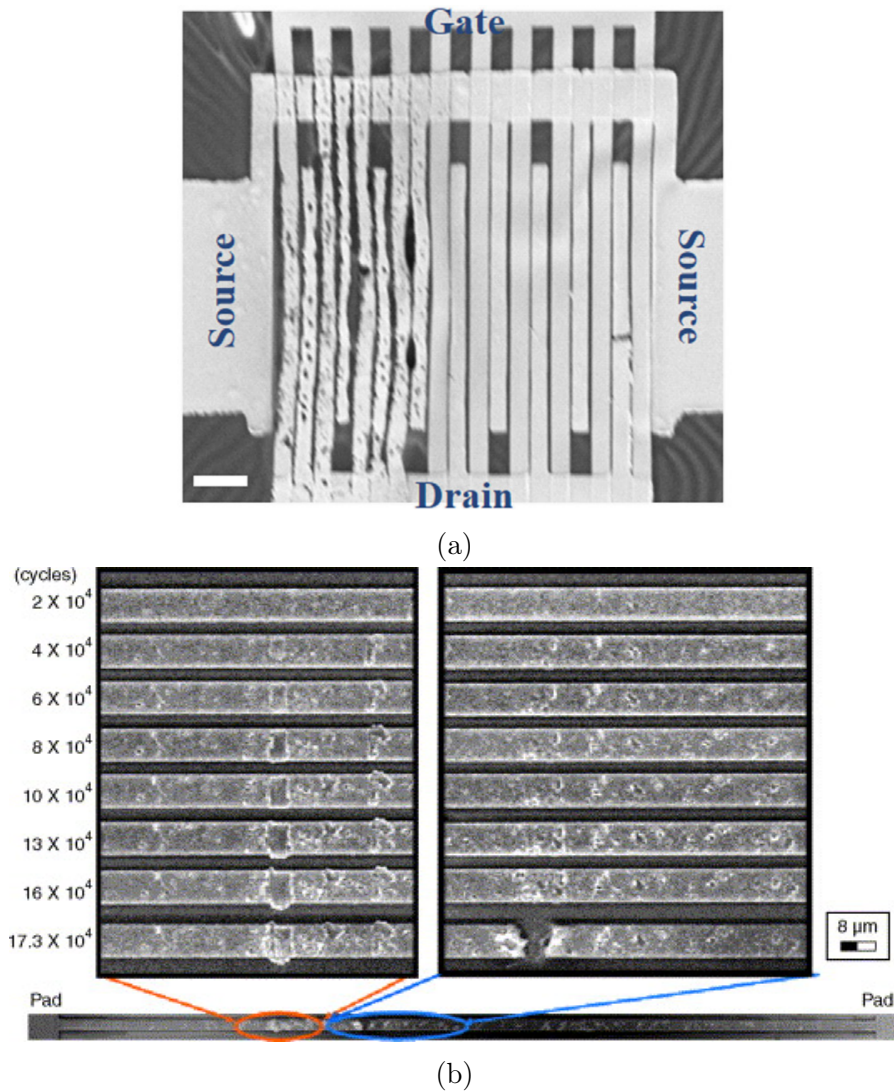


Figure 1.1: A few examples of thermal damage in microelectronic devices. (a) Thermal damage sustained in a flexible graphene field effect transistor. Figure adapted from [33] (b) Thermal fatigue in an interconnect line can result in complete failure of the interconnect. Fig adapted from [45]

1.1.1 The temperature coefficient of resistance

For most materials there exists a functional relationship between their resistivity and temperature moderated by the temperature coefficient of resistance (TCR):

$$\frac{dR}{R} = \alpha_{TCR}dT \quad (1.2)$$

The TCR (α_{TCR}) compiles the various temperature dependent processes that influence a material's resistivity [46]. In many metals, often used as interconnect material, an increase in temperature results in an increase in resistivity (i.e. they have a positive TCR) [46]. Excessive heat generation, combined with an inability to effectively remove the heat and the increased resistance caused by a positive TCR will only lead to even higher power densities. In addition, the high operating temperatures result in a lower efficiency of the electronics (due to higher resistance), meaning higher power consumption, which, while certainly detrimental to the average personal computer, can become significant for large scale operations such as server rooms or supercomputers [47].

As the TCR is the result of various processes, all with their own dependencies on temperature, conductor geometry, defects, impurities and many more material and environmental properties, the TCR is not a constant but can vary significantly across these material properties. For example, the TCR of silicon varies from positive to negative values depending on the temperature and dopant type [48] (Fig. 1.2b). An example of the geometrical dependence is the decrease in TCR when the thickness of thin films is reduced (Fig. 1.2a) [49] [50]. Models of the TCR dependence to certain isolated effects (e.g TCR w.r.t. film thickness [51] [52]) have been derived, however due to its complex origins, a complete mathematical description of the TCR is often out of reach or impractical. It is often far easier to simply obtain the TCR from a direct measurement. Due to the complex geometries and environments in modern day chip architectures, micro- and nanoscale characterisation of TCR is essential in the design and fabrication of new electronic devices. Furthermore, as the industry is looking towards replacement materials for copper interconnects [53], accurate and precise knowledge of the the micro- and nanoscale TCR of these candidate materials is essential to judge whether they are suitable as an interconnect material and how they should be incorporated [54]. The advent of low to zero TCR [55] [56] as well as tunable TCR [57] materials incorporated into electronic devices will require characterisation at the micro- and nanoscale.

In addition to aiding in the design of new electronic devices, TCR measurements are already used to characterise the cross-sectional area [58] and reliability [59] of interconnects. Due to the TCR dependence on doping density, a TCR

measurement can be used to characterise doping levels in silicon resistors [60]. Furthermore, knowledge of the TCR is essential in the fabrication and operation of thermal and flow sensors [61] [62]. Microscale TCR metrology, enabling direct characterisation methods of samples 'in situ', will remain relevant for the foreseeable future in the development and operation of various electronic devices and in the quest to limit negative impact of self heating to device operational efficiency and reliability.

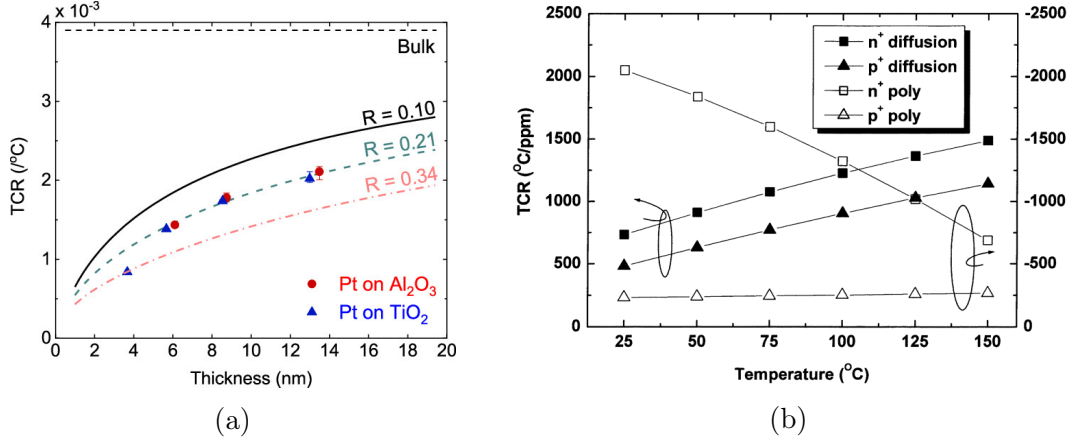


Figure 1.2: Examples of the dependence of TCR to various material and environmental parameters. (a) The dependence of TCR on the thickness of a platinum thin film. Figure adapted from [50] (b) The TCR in polysilicon, which is dependent on the dominant carrier type, as well as the temperature. Figure adapted from [48]

1.2 Current TCR characterisation methods

The straightforward method to determine the TCR is to simply measure the resistance of the sample while controlling the device temperature [63] and has been the standard way to characterise the TCR of metals for decades [64] [65] [66] [67] with the only difference being more advanced temperature control systems and more precise electrical measurement equipment. From the obtained resistance change ΔR measured over a certain temperature range ΔT , the TCR can be obtained from the slope (as visualised in Fig. 1.3), normalised with the resistance at the temperature of interest:

$$\alpha_{TCR} = \frac{1}{R} \frac{\Delta R}{\Delta T} \quad (1.3)$$

The above method only applies if the resistance change within the investigated temperature range is linear. In general, most metals show a linear response and

the above method can be applied over a wide temperature range [46]. For e.g. semiconductor materials with highly non-linear response, a sufficiently small temperature range must be chosen so the linear approximation can be made.

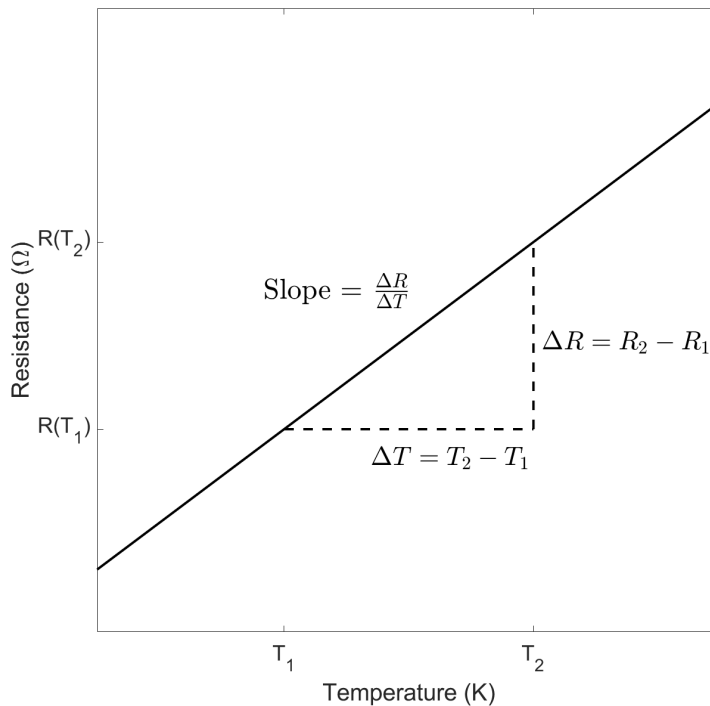


Figure 1.3: A simple schematic of a TCR measurement, where the resistance change is measured across a temperature difference. The obtained slope enables the determination of the TCR via Eq. 1.3.

As electronic devices have become scaled down, these standardised measurements are becoming more demanding. Small changes in feature sizes (i.e different widths of interconnect lines) have large implications on the device properties. As such, localised measurements are often needed. Micro- and nanoscale thermal behaviour is complicated. Many integrated circuits use a variety of semiconductor materials, metals, oxides and dielectrics, which will have different heat transport mechanisms [68]. In addition, at these small length scales ballistic heat transport might be significant [69] [70]. As a result, the easiest way to characterise micro- and nanoscale TCR is to measure the resistance locally while controlling the temperature globally, though, if one wants to go one step further, methods do exist to measure the local temperature. Local resistance measurements are straightforward and, for example by using the four terminal sensing technique, can be

easily restricted to only the structure of interest [71]. Some additional fabrication (e.g. contact pads) might be required. There are a wide range of temperature control systems to vary the sample temperature. The simplest method is to place the sample on a hotplate or heated chuck [50]. The disadvantage is that the temperature at the sample surface might differ from the indicated temperature on the hot plate or chuck, especially if one expects significant convective or radiative heat loss. More precise temperature control can be achieved by placing the sample inside a temperature controlled chamber, e.g. a physical property measurement system (PPMS). The downside is that one is limited by the size of the temperature controlled chamber (often restricted to samples with a few square millimeters of surface area), and few chambers exist that allow for variable measurement locations, so that if several locations need to be characterised, the sample must be taken out of the chamber, the contacts moved and placed back into the chamber again. Depending on what temperature ranges are used, the chamber might take many hours to reach the goal temperature. On the plus side, the TCR can be characterised over a wide range of temperatures, in principle all the way up to the melting temperature.

One of the major downsides of global temperature control is the omission of self heating and local effects. In certain devices this could lead to large inaccuracies in TCR characterisation. In this case, local micro- and nanoscale temperature measurements are an option [72] [73], though it must not interfere with the electrical measurement. For instance, micro-thermocouples can be used to measure the temperature on or near the device. However, since the thermocouple is in contact with the sample the local temperature may be modified, as heat dissipates away via the thermocouple and can lead to inaccurate measurements (cold finger effect). An alternative route are fabricated nanoscale thermocouples on the sample, which provide a local measurement of the temperature [74]. Crucially, it can be done simultaneously with the resistance measurement, and includes any self heating effects as well. It is however very inflexible, since the thermocouple obviously cannot be moved to a different location. In addition, it requires an additional characterisation step of the thermocouple and restricts the characterisation to specially designed test structures.

1.3 The proposed method

This thesis introduces a new method of TCR characterisation that aims to address the majority of disadvantages of the established methods. The method uses the four terminal sensing technique to obtain precise resistance measurements of the

investigated samples [71]. Localised measurements are achieved via the micro four-point probe (M4PP) instrument [75], a widely used electrical characterisation tool. The M4PP is able to characterise micro- and nanoscale structures using micro fabricated electrodes with (sub-) micron inter-electrode spacing. An image of a typical probe head is shown in Fig. 1.4. The M4PP tool, as well as all probe head designs used in this thesis are from CAPRES A/S - a KLA company. In Fig. 1.4, the probe has seven electrodes which contact the surface of a sample, enabling a wide choice of four terminal measurement configurations. This allows, among other things, characterisation over several lengthscales during the same measurement. The M4PP has demonstrated extremely precise measurements of resistance on a wide array of structures, e.g. conductive thin films [76][77] [78], magnetic tunnel junctions [79], ultra-shallow junctions [80] [81] [82] and fins [83] [84]. M4PP excels in its versatility (the probe head can land anywhere on the sample), allowing for accurate characterisation on samples ranging from small test pads [85] [86] to entire wafer scans [87]. Due to its high precision, it should easily detect resistance changes due to the self heating effect [88]. The method presented is able to extract the TCR of measured metallic thin films from this observed increase in resistance by calculating the Joule heating induced temperature fields. Due to the absence of an independent temperature measurement, the TCR can be characterised extremely quickly (a single TCR measurement can take under a second). The versatility of the M4PP means the probe can land anywhere on the sample and no sample preparation is required (e.g. additional fabrication of contact pads), so that the sample can be characterised in situ. With refinement of the method, it could be suitable as an in-line process monitoring method.

This thesis explores the introductory steps of a new method which has so far been tested on a number of ultra-thin platinum film samples. The results show that M4PP measurements can induce significant and reproducible response to self heating effects, which can be translated to a TCR value. The method, which has been assigned the name the M4PP-TCR method, has demonstrated great precision ($< 2\%$) and a good correlation with reference values, although the extracted TCR value is offset from independent reference values. The method has so far been tested on a rather limited range of materials and sample types. However, the promising results show potential for application to a wider range of materials and devices. Currently the method is limited by the significant assumptions that must be made on the electrical and thermal system of the sample. Very heterogeneous samples (e.g. a sample with variable grain sizes or many surface features) will pose a challenge to the electrical and thermal calculation schemes used here. Semiconductor materials may introduce non-linear behaviour (e.g. via non-ohmic contacts [89]) and thermoelectric materials require more elaborate calculation of temperature to account for the Peltier effect. The small length-scales mean that

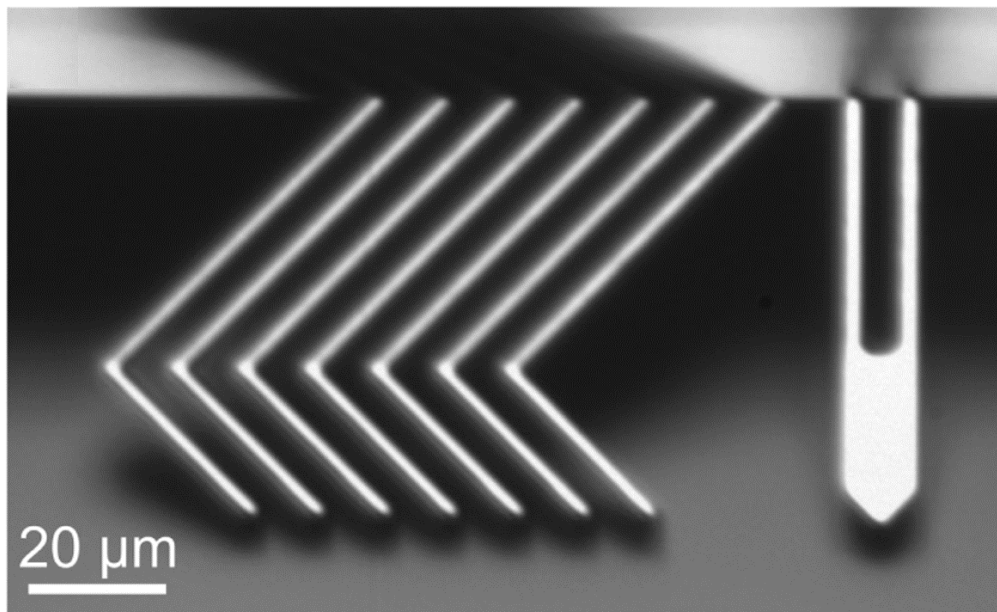


Figure 1.4: *An optical microscope image of a M₄PP probe head, carrying seven electrodes. The seven electrodes allow for the creation of several subprobes (e.g. the four leftmost electrodes), which enables four terminal measurements at different lengthscales. On the right is a strain gauge, used for surface detection. Figure adapted from [87]*

in some substrates ballistic heat transport might play a non-trivial role in the dissipation of heat. The assumed simple conductive model of heat transport does not hold in multilayer samples either. Despite these limitations, I strongly believe that with more iterations of the method, the list of suitable materials will increase and the accuracy of the extracted TCR will improve.

1.4 Thesis outline

The thesis is from here on divided into a further four chapters. **Chapter 2** provides a theoretical background to the concepts used in the M₄PP-TCR method. A brief overview of the electrical and thermal theory of metals is provided, before discussing the origin of the TCR and thin film effects. Lastly an outline of the instrument used in the method is given. **Chapter 3** describes the main result of the thesis; the developed M₄PP-TCR method. The chapter includes the derivation of the analysis processes and showcases the main results on platinum thin films.

Chapter 4 details early examinations of the effect of errors in the position of the electrodes and electrical noise on the extracted TCR values. Finally, **Chapter 5** portrays the idea of an optimised measurement scheme, potentially capable of improving the precision of the M4PP-TCR method.

Chapter 2

Theory

The M4PP-TCR method relies on a good understanding of the electrical and thermal system of the measured samples. This thesis concerns itself with measurements on metallic thin films deposited on oxides. Therefore the electrical transport in metals and the impact of the sample geometry (thin film effects) must be considered. Furthermore, the method relies on a good knowledge of four terminal sensing and its application on the micro-scale.

2.1 Fundamentals of electrical conduction in metals

A current flow consists of a stream of electrons, moving from a region of negative charge to a region of positive charge, under the influence of an applied electric field. Current is a measure of the rate of the movement of charge with SI unit Ampere. Precisely, 1A is defined as 1 Coulomb of charge passing a specific point per second. A current is induced by a disparity between regions of charge, expressed in volts. One Volt is defined as the energy consumption of 1 Joule for 1 Coulomb of charge. One can consider the ratio of the current and the voltage, that is to say, if one would apply a voltage of 1V across some material, how much current would flow? This naturally depends which material the current is passing through and its resistance, R , against the current. The higher the material's resistance, the less current would flow. We now arrive at Ohm's law [90]:

$$\frac{V}{I} = R \tag{2.1}$$

Ohm's law relates the three most important quantities in electronics with each other. Ohm's Law expressed as in equation 2.1 is dependent on the dimensions of the material. If one adds more material, more current can flow and the resistance decreases. By considering instead the quantities electric field $\mathbf{E} = -\nabla V$ (volt per meter) and current density $\mathbf{J} = I/A$ (current per unit area), a more robust version of Ohm's Law that is independent of the dimensions of the material can be developed:

$$\frac{\mathbf{E}}{\mathbf{J}} = \rho \quad (2.2)$$

where now ρ is the resistivity, a material property independent of the shape of any resistor. By substituting the electric field and current density into equation 2.1, one can deduce the relationship:

$$R = \frac{\rho l}{A} \quad (2.3)$$

In other words, the resistance of any resistor is dependent on the material it's made of (ρ) and its dimensions (l, A).

2.1.1 Scattering mechanisms

In 1900, soon after the discovery of the electron, German physicist Paul Drude published his model attempting to describe the electrical and thermal conductivity of metals [91]. Drude assumed that the electrons present on the outer shell of metallic atoms, the so called valence electrons, can become detached and wander freely through the metal, while the remaining metal ions are static. These valence electrons, also called free electrons, would then behave as a classical perfect gas, allowing the application of the kinetic theory of gasses to this so called 'free electron' gas. These assumptions suggest a picture such as in Fig. 2.1 where electrons move in straight paths between random scattering events.

Figure 2.1 intuitively underlines the results found in Eq. 2.3. If the resistor is widened (increase of the cross-sectional area A) more electrons will be able flow and therefore the resistance of the resistor is lowered. However, if the resistivity of the material is increased, either by a denser array of dots or by increasing their size (higher potential repulsion from the ions) fewer electrons are able to pass and the resistance will increase.

Paul Drude derived the conductivity of metals by considering the current density of the electron gas, which as there are n electrons per unit volume in the free electron gas, each with a charge of $-e$ and velocity \mathbf{v} , the charge crossing the area

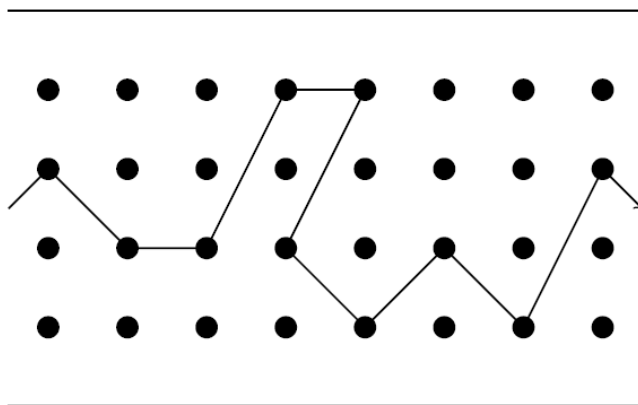


Figure 2.1: A schematic of the simplified electron transport picture inferred by Drude's model. The electron is scattered randomly by the static metal ions. With the application of an electric field the electron gains an additional drift velocity along the direction of the field, driving the transport of current.

A in time dt will be $n(-e)(\mathbf{v}dt)A$. The current density then reduces to:

$$\mathbf{J} = -nev \quad (2.4)$$

where here \mathbf{v} is the average velocity of all electrons. Drude, still unaware of the quantum mechanical effects, obtained this from the Maxwell-Boltzmann velocity distribution of the electrons in the gas. In the absence of an electric field, the electron motion can be assumed to be random and the distribution of the electron velocities will average out to zero, meaning there will be no current, as expected. However when an electric field \mathbf{E} is applied, each electron will gain an additional drift velocity in the direction of the field between the scattering events. In the assumption that each scattering event randomizes the electron velocity and the electric field is constant, the drift velocity becomes:

$$v_d = \frac{-e\mathbf{E}\tau}{m_e} \quad (2.5)$$

where m_e is the electron effective mass and τ , is the relaxation time (also known as mean scattering time); the average time between collisions. τ can also be expressed as the mean free path λ , the average distance travelled by an electron between collisions. From Eq. 2.5, the proportionality constant between the drift velocity and electric field can be defined as:

$$\mu_e = \frac{e\tau}{m_e} \quad (2.6)$$

which is known as the electron mobility, a measure of the ease of movement of an electron through the material for a given electric field. A more general carrier mobility (for e.g. holes) can be defined by replacing the carrier dependent parameters. Similarly, from Ohm's law, $\mathbf{J} = \sigma \mathbf{E}$, the expression for conductivity can be determined from Eq. 2.5:

$$\sigma = \frac{ne^2\tau}{m_e} \quad (2.7)$$

Drude's model, which also included a derivation for the metallic thermal conductivity, became popular due to the apparent explanation of Wiedemann-Franz law, which states that the ratio of the electronic and thermal conductivity is proportional to its temperature via a proportionality constant, the Lorenz number. However, Drude's model failed in the prediction of several other materials parameters, such as overestimating the electronic specific heat capacity by a factor of 100. With the emergence of quantum mechanics in the early 20th century it became clear the classical description of the electron gas was inadequate and the successful description of Wiedemann-Franz law was a result of two large errors canceling each other out. A key quantum mechanical result was Pauli's exclusion principle, which states that two identical fermions (to which electrons belong) cannot occupy the same state. At absolute zero (0 K), electrons will occupy the states with the lowest available energy first so that all the states below a certain energy are occupied and all the states above this energy are not. This cutoff energy is known as the Fermi energy E_F . At non-zero temperature T , the electrons will gain a thermal energy of the order of $k_B T$, allowing states above the Fermi energy to be occupied. The probability of a state being occupied is given by the Fermi-Dirac distribution:

$$f(E) = \frac{1}{1 + \exp\left(\frac{E - E_F}{k_B T}\right)} \quad (2.8)$$

where k_B is the Boltzmann constant and T is the temperature of the sample. At $T > 0$, the Fermi function $f(E_F) = 1/2$.

Arnold Sommerfeld applied the Fermi-Dirac statistics to Drude's free electron gas model [92]. As a consequence of Pauli's exclusion principle, electrons can only scatter into an empty state. Since low energy states are fully occupied, the scattering of these electrons is highly suppressed (as scattering event with sufficiently large energy transfers are necessary). Therefore, only the electrons near the Fermi energy are able to contribute to the electronic conduction. The resulting current (in 1D) is analogous to Eq. 2.4:

$$J = n_F e v_F \quad (2.9)$$

but here n_F is the number of conduction electrons in the Fermi window (ΔE , the energies able to contribute to conduction), and v_F is the Fermi velocity (the velocity of these conduction electrons). The number of conduction electrons in the Fermi window is determined by the density of states $g(E)$ i.e. how many states are available at energy E , so that $n_F = g(E_F)\Delta E$. ΔE can be shown to be given by $\Delta E = ev_F\tau E_x$, where E_x is the electric field [46]. The conductivity of Fermi electrons is then given by:

$$\sigma = \frac{1}{3}e^2v_F^2\tau g(E_F) \quad (2.10)$$

where the $1/3$ fraction arising from the switch to three dimensional conduction. Equation 2.10 indicates that a materials conductivity is dependent on the density of states at the Fermi energy. This is opposed to Drude's classical approach, which suggests all electrons contribute to conduction. The quantum mechanical expression is able to explain why e.g. copper has a higher conductivity than magnesium, despite magnesium having two valence electrons to copper's one.

2.1.2 Mathiessen's rule

The mean scattering time τ (average time between scattering events) is almost always a result of several different scattering mechanisms. Not only can an electron be scattered by the lattice ions such as depicted in Fig. 2.1, but also by lattice vibrations (phonons), lattice impurities, crystal grain boundaries and material surfaces among others. All these scattering mechanisms contribute to a materials resistivity by reducing the time between scattering events. Provided each scattering event is independent of each other the chance of an electron to scatter within a small time interval is the sum of all probabilities of each scattering mechanism:

$$\frac{1}{\tau} = \sum_i \frac{1}{\tau_i} \quad (2.11)$$

As resistivity is inversely proportional to the drift mobility, which itself is proportional to mean scattering time ($\rho \propto \mu^{-1}$, $\mu \propto \tau$), this result can be extended to resistivity:

$$\rho = \sum_i \rho_i \quad (2.12)$$

Equation 2.12 is known as Matthiessens's rule and states that the resistivity of a material is the sum of the contributions from independent scattering mechanisms.

2.1.3 Temperature dependence of resistance

One can conclude from Matthiessen's rule (Eq. 2.12) that the resistivity of a metal is the result of temperature independent scattering mechanisms such as impurity or grain boundary scattering and temperature dependent scattering mechanisms such as e.g. electron-phonon scattering (scattering due to lattice vibrations, where at higher temperatures the metal ions will vibrate more and therefore present themselves as larger targets for the electrons to hit). The dependence of the resistance on temperature is moderated by the temperature coefficient of resistance (TCR or α_{TCR}) as discussed in Chapter 1 and is obtained empirically through a direct resistance measurement of a sample across a temperature range (Fig. 1.3 and Eq. 1.3).

Metal	$\rho(\text{n}\Omega \text{ m})$	TCR (10^{-3} K)
Aluminium	26.7	4.5
Cobalt	63	6.6
Copper	16.94	4.3
Gold	22	4
Iron	101	6.5
Lead	206	4.2
Magnesium	42	4.25
Nickel	69	6.8
Platinum	105.8	3.92
Ruthenium	77	4.1
Silver	16.3	4.1
Titanium	540	3.8

Table 2.1: *Typical values of the resistivity (at 20°C) and TCR (in the range 0°C to 100°C) of a few selected metals. Data taken from [93].*

The temperature dependence of resistance of metals can often be approximated by linear relationship ($\rho \propto T$). The scattering in these metals is dominated by lattice vibrations, which scale linearly with temperature. The values of a few selected metals are shown in table 2.1. Consider the resistivity of a typical metal, e.g. copper in Fig. 2.2. Three distinct regions can be identified. The low temperature region, independent of temperature, is the result of the temperature independent scattering mechanisms, known as the residual resistivity (ρ_R). Several metals additionally exhibit superconductivity (where $\rho = 0$) at very low temperatures. Above a certain temperature (in this case around 100 K) the resistance increase with temperature can be approximated as a linear function of temperature. Therefore, the resistance at a given temperature T_1 can be obtained from the resistance at a

reference temperature and the TCR:

$$R_1 = R_{ref} (1 + \alpha_{TCR} \Delta T) \quad (2.13)$$

where $\Delta T = T_1 - T_{ref}$; the temperature difference between the given temperature and the reference temperature. Equation 2.13 is known as the linear approximation and holds for most non-magnetic metals in the room temperature range, provided α_{TCR} is temperature independent over this range. In addition, for sufficiently small temperature ranges Eq. 2.13 can be applied to all materials.

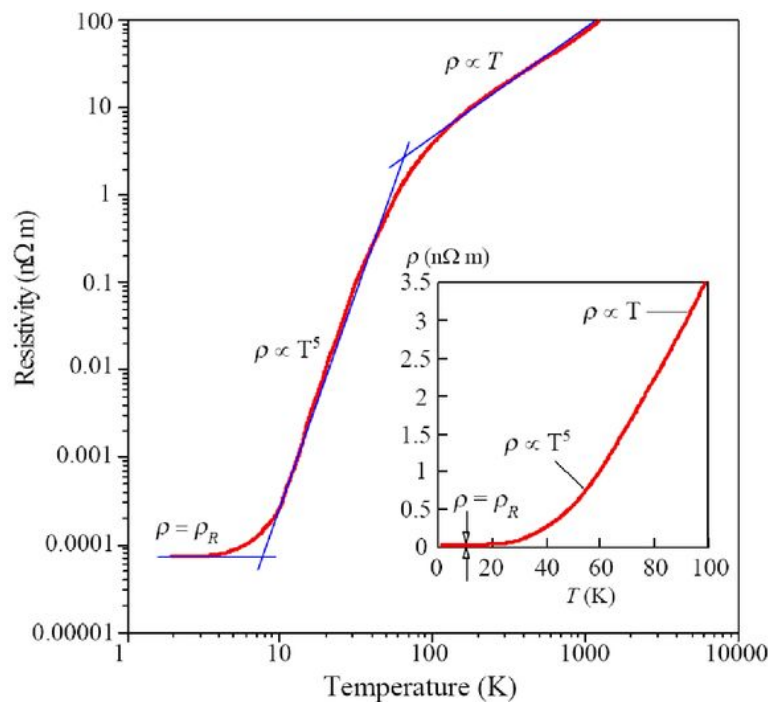


Figure 2.2: *The resistivity of copper across a wide temperature range. Three distinct regions can be identified, where the temperature dependence of the resistivity at $>\sim 100$ K can be approximated by the linear approximation (Eq. 2.13). Figure adapted from [46]*

2.2 Thermal conduction in solids

Consider a material that is heated on one end. Increase in the thermal energy on this side will result in increasing vibrational energy in the case of phonon heat transport or an increase in the kinetic energy of electrons in the case of electronic

heat transport. Through the coupling of these vibrations or the increasing random walk the thermal energy will transfer to the cold side. The amount of heat energy per second $\dot{Q} = \delta Q / \delta t$ flowing through a cross sectional area A as a result of a thermal gradient [46]:

$$\frac{\dot{Q}}{A} = -\kappa \frac{\delta T}{\delta x} \quad (2.14)$$

where κ is the thermal conductivity, a measure of the ease of heat flow through a material. Equation 2.14 is known as Fourier's law of thermal conduction and is analogous to Ohm's law (Eq. 2.2). The negative sign is a result of heat flowing in the opposite direction of a thermal gradient. Heat flow has many similarities to current flow and much of the same reasoning can be used, such as the definition of a thermal resistance Θ :

$$\dot{Q} = \frac{\Delta T}{\Theta} \quad (2.15)$$

where, analogously, the thermal resistance can be expressed in terms of the resistor geometry and thermal conductivity:

$$\Theta = \frac{L}{\kappa A} \quad (2.16)$$

Equation 2.14 can be used to describe the temperature from a point source with a constant heating power $\dot{Q} = P = I^2 R$, position at location \mathbf{r}' on a semi-infinite medium from which follows:

$$\Delta T(\mathbf{r}) = \frac{I^2 R}{2\pi\kappa} \frac{1}{|\mathbf{r} - \mathbf{r}'|} \quad (2.17)$$

2.3 Thin film effects

As materials are scaled down to comparable dimensions as the electron mean free path, the resistivity increases [94]. In contrast to bulk, where the resistivity in metals is dominated by phonon scattering, in thin metal films the scattering of electrons to the external surfaces as well as grain boundaries start to dominate [94].

2.3.1 Thin film resistivity

From Matthiesen's rule (Eq. 2.12) the external surface and grain boundary scattering mechanisms add to the total resistivity of the material. If the grain sizes are

comparable to the mean free path of electrons, the typical movement through the film will involve mostly ballistic transport inside the grains with the majority of the scattering occurring at the boundaries. The grain boundary scattering mean free path (equal to the grain size d_G) can therefore be added to the single crystal mean free path λ :

$$\frac{1}{l} = \frac{1}{\lambda} + \frac{1}{d_G} \quad (2.18)$$

The distance between the grain boundaries (grain size d_G) is often equivalent to the thickness of the film. The ratio of the thin film resistivity compared to the bulk (single crystal) resistivity can then be given by:

$$\frac{\rho}{\rho_{bulk}} = 1 + \frac{\lambda}{d_G} \quad (2.19)$$

As the grain size decreases (i.e. the film thickness), the thin film resistivity will increase. A scattering event at a grain boundary could result in the electron being bounced back into to the same grain. Mayadas and Schatzkes developed a model that considers the reflection coefficient R and reach a thin film resistivity expression [95]:

$$\frac{\rho}{\rho_{bulk}} \approx 1 + 1.33 \frac{\lambda}{d} \left(\frac{R}{1-R} \right) \quad (2.20)$$

Surface scattering (scattering from external surfaces or interfaces) is scattering where the electron is reflected back from the surface or interface, which if inelastic, will increase the resistivity through the film. Similarly to Eq. 2.18, Matthiessen's rule can be used to obtain the total mean free path in the film from the 'bulk' and surface contributions:

$$\frac{1}{l} = \frac{1}{\lambda} + \frac{\cos \theta}{2d} \quad (2.21)$$

where d is the thickness of the film. As the reflected electron cannot leave the film, the angle of reflection θ must be within $-\frac{\pi}{2}$ and $\frac{\pi}{2}$. The ratio of the thin film resistivity ρ to the bulk resistivity is then found to be:

$$\frac{\rho}{\rho_{bulk}} = 1 + \frac{1}{\pi} \frac{\lambda}{d} \quad (2.22)$$

Surface scattering often is both an elastic or inelastic scattering event. Fuchs and Sondheimer [96] developed a model considering the specular coefficient p (how much of the scattering is elastic) finding a thin film resistivity:

$$\frac{\rho}{\rho_{bulk}} \approx 1 + \frac{3}{8d} (1-p) \quad (2.23)$$

The reflection and specular coefficients R and p are generally obtained by fitting the above models to the measurement.

2.3.2 The TCR in thin films

C.R. Tellier and A.J. Tossier developed analytical expressions based on the M-S and F-S models for thin film resistivity to describe the observed decrease in TCR with decreasing thin film thickness [49] [51]. They obtained an expression for the thin film TCR of polycrystalline films:

$$\alpha_{TCR, film} = \alpha_{TCR, bulk} \left(1 + \frac{G(a)}{F(a)} \right) \quad (2.24)$$

where

$$\begin{aligned} G(a) &= -\frac{3}{2}a + 6a^2 + \frac{3a^3}{1+a} - 9a^3 \ln \left(1 + \frac{1}{a} \right) \\ f(a) &= 1 - \frac{3}{2}a + 3a^2 - 3a^3 \ln \left(1 + \frac{1}{a} \right) \\ a &= \frac{\lambda}{d_G} \left(\frac{R}{1-R} \right) \end{aligned}$$

An extensive derivation can be found in [49] and [51]. In the derivation of the above expression, the thermal expansion coefficients of the grains and film thickness was ignored considering their value near 10^{-5} K^{-1} . However, it is possible a mismatch in thermal expansion coefficients between a film and the substrate causes significant stress (or strain) in the film, influencing the thin film TCR [97].

F. Warkuzs developed a model for the TCR of metal films considering the surface scattering and grain boundary scattering. [52] [98] [99] The result is a rather lengthy expression:

$$\alpha_{TCR, film} = \frac{1}{\rho_0} \frac{d\rho_0}{dT} \left(1 - \frac{K}{F(K, p, q, a)} \frac{\partial F(K, p, q, a)}{\partial K} + \frac{a}{F(K, p, q, a)} \frac{\partial F(K, p, q, a)}{\partial a} \right) - \frac{1}{T} \quad (2.25)$$

where

$$a = \frac{\lambda}{d_G} \left(\frac{R}{1-R} \right)$$

$$K = \frac{d}{\lambda}$$

$$F(K, p, q, a) = f(a) - \frac{3}{\pi K} \int_0^{\pi/2} d\phi \int_0^1 \frac{\cos^2(\phi)}{H} (t - t^3) \frac{1 - \exp(-KH/t)}{1 - pq \exp(-2KH/t)} dt$$

$$(2 - (p + q) + (p - 2pq) \exp(-KH/t))$$

$$f(a) = 1 - \frac{3}{2}a + 3a^2 - 3a^3 \ln \left(1 + \frac{1}{a} \right)$$

$$H = 1 + \frac{a}{\sqrt{(1-t^2)} \cos(\phi)}$$

and p and q are the specularity coefficient of the two film surfaces (top and bottom), $t = \cos \theta$, ϕ and θ are scattering angles of the film surfaces and ρ_0 is the bulk resistivity.

Both models predict a decrease in TCR with decreasing film thickness, as shown in Fig. 2.3. The complexity of both models underline the fact that a direct measurement of TCR is preferred over the use of the presented analytical expressions. Especially since the expressions require measured or fitted parameters themselves (e.g. p and R), also implying that the TCR will depend on the conduction mechanism in the thin film [100].

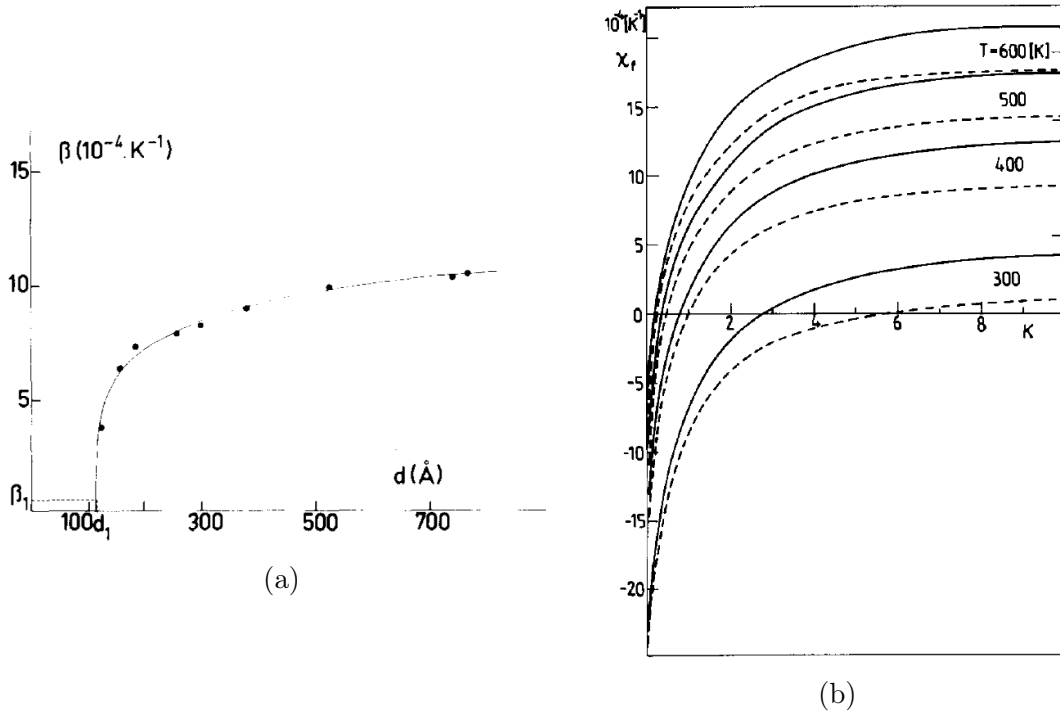


Figure 2.3: The predicted TCR behaviour when the film thickness is reduced. (a) The Tellier and Tosser model (Eq. 2.24, solid line) described the observed TCR of aluminium thin films (dots) of varying thickness. Figure adapted from [49] (b) The Warkusz model (Eq. 2.25) showing the drop in TCR for decreasing thickness. The absolute value of TCR depends on the scattering coefficients, shown by the solid line ($a = 0$) and the dashed line ($a = 1/15$) as well as the temperature. Figure adapted from [52].

2.4 Four terminal sensing at the microscale

Four terminal sensing is well established technique to characterize the resistivity of samples. By using highly resistive voltage electrodes, one can characterise the resistivity while ignoring the contact resistances at the current electrodes. The method was first demonstrated by Frank Wenner while attempting the measure the Earth's resistivity [101]. In 1954 Leopoldo Valdes applied the method to semiconductor wafers and has since become a staple in the microelectronics industry [102]. Besides the wide range of applicable length scales (from microelectronic devices to planet Earth) the method is simple to use and provides accurate results with high precision.

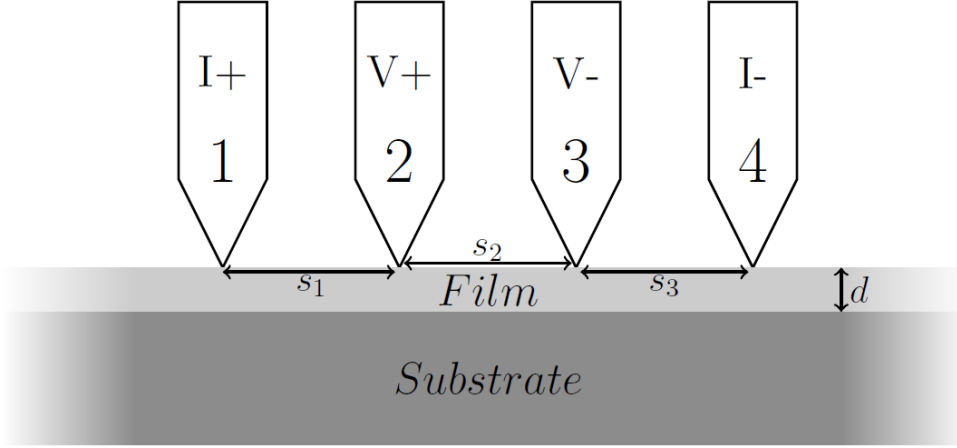


Figure 2.4: The setup of a four terminal resistance measurement on a thin film of thickness d . The current is sourced between the carrying electrodes are denoted by I_+ and I_- . The induced voltage is measured by the two remaining electrodes.

The typical four probe geometry is shown in Fig. 2.4, with two current electrodes (denoted I_+ and I_- representing the source and drain respectively) and two voltage electrodes (denoted V_+ and V_-) in contact with the sample surface. The electrodes are separated by the respective distances s_1 , s_2 and s_3 . This thesis concerns itself with ultra thin films, i.e. 2D conductive films (or sheets), where the film thickness d is much smaller than the electrode spacing (s_1 , s_2 , s_3). Here, the current flow can be modelled as a cylindrical current expanding from the current electrode contact. The current density, for a semi-infinite sample, is then given by:

$$J = \frac{I}{2\pi r d} \quad (2.26)$$

from which the potential drop can be determined:

$$\frac{-dV}{dr} = E(r) = \rho J = \frac{I\rho}{2\pi r d} \quad (2.27)$$

The voltage at a distance r_1 from the current electrode on the sheet is then obtained:

$$V(r_1) = \frac{I\rho}{2\pi d} \ln(r_1) \quad (2.28)$$

Applying above to a collinear four point probe as pictured in Fig. 2.4, the voltage measured at voltage electrode V_+ is the sum of the voltages emerging from both current electrodes. The measured four-point probe voltage across the two voltage

probes is then:

$$\begin{aligned}
 V_{4PP} &= V_{v+} - V_{v-} = \frac{I\rho}{2\pi d} \left[\ln\left(\frac{s_2 + s_3}{s_1}\right) - \ln\left(\frac{s_3}{s_1 + s_2}\right) \right] \\
 V_{4PP} &= \frac{I\rho}{2\pi d} \ln\left(\frac{(s_1 + s_2)(s_2 + s_3)}{s_1 s_3}\right)
 \end{aligned} \tag{2.29}$$

In the case of an equidistant probe where $s_1 = s_2 = s_3 = s$ the resistivity of the thin film can then be obtained from the measured voltage $V = V_{4PP}$ and applied current I :

$$\begin{aligned}
 \rho &= \frac{2\pi d}{\ln(4)} \frac{V}{I} \\
 \rho &= \frac{\pi d}{\ln(2)} \frac{V}{I}
 \end{aligned} \tag{2.30}$$

A commonly used quantity is the sheet resistance $R_S = \frac{\rho}{d}$. Sheet resistance has units of Ohms (Ω) however it is frequently denoted as Ωsq^{-1} (Ohms per square). This is because a square of material will have the same sheet resistance regardless of the size of the square. Consider a slab with cross-sectional area of width times thickness (wd), equation 2.3 reduces to the sheet resistance when the length equals the width $l = w$: $R = \frac{\rho w}{wd}$. It is valuable when evaluating different area of the same thickness. For example, an interconnect line with side w and $3w$ will have three times the resistance as a square contact pad with sides $12w \times 12w$.

Equation 2.30 expressed as sheet resistance is then:

$$R_S = \frac{\pi}{\ln(2)} \frac{V}{I} = F \frac{V}{I} \tag{2.31}$$

The quantity F is known as the geometrical correction factor and is dependent on the location of the probe electrodes as well as the dimensionality of the current transport in the measured sample as demonstrated. The setups used throughout this thesis are of in-line, equidistant probes on 2D materials.

The electrode roles can be freely interchanged to obtain several probe configurations as visualised if Fig. 2.5. The three main configurations (A, B and C) have their reciprocal counterparts where the current and voltage electrodes are swapped, denoted as prime (A', B' and C'). In addition the polarities of the current and voltage electrodes can be swapped to create additional configurations. A standard notation is denoting the electrode roles in the following order: I_+ , V_+ , V_- , I_- . The A configuration would then be denoted as 1,2,3,4.

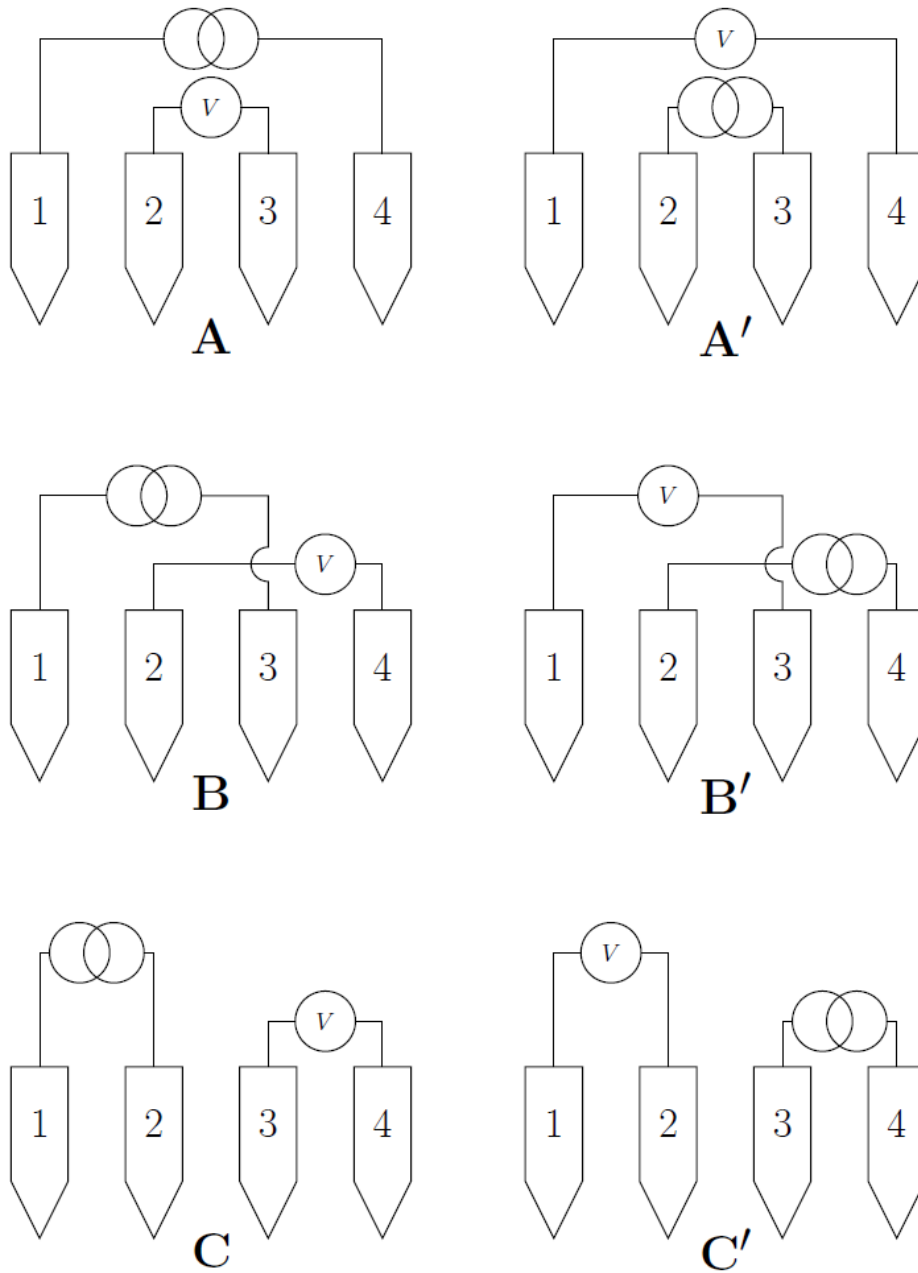


Figure 2.5: The six configurations available on a M_4PP . Additional varieties can be created by swapping the polarities of the current and voltage electrodes.

A valuable theorem in thin film resistivity measurements is the Van der Pauw theorem [78] which enables measurements on thin films of arbitrary shape, provided the electrodes are placed on the perimeter of the sample. On the micro-scale however, placing a probe near the perimeter is often impractical and can be further complicated by a curved or ill-defined sample edge. Placing a collinear probe on the mirror plane of a sample however has the same effect as if placing it on an insulating boundary (since the current density normal to the mirror plane vanishes $\mathbf{J} \cdot \hat{\mathbf{n}} = 0$), and therefore Van der Pauw's theorem is applicable. It has fortunately been demonstrated that this is applicable in a wide region near the mirror plane, meaning the der Pauw's equation is easily used to obtain the sheet resistance for thin films [85]. The (modified) van der Pauw equations are:

$$\begin{aligned} \exp\left(\frac{2\pi R_A}{R_S}\right) - \exp\left(\frac{2\pi R_B}{R_S}\right) &= 1 \\ \exp\left(\frac{-2\pi R_A}{R_S}\right) + \exp\left(\frac{-2\pi R_C}{R_S}\right) &= 1 \\ \exp\left(\frac{2\pi R_C}{R_S}\right) - \exp\left(\frac{-2\pi R_B}{R_S}\right) &= 1 \end{aligned} \quad (2.32)$$

Where the subscripts A , B and C refer to the configuration used to measure the four point probe resistance $R = V/I$. By inserting the measured values of R_A , R_B and R_C into the one of the above equations the sheet resistance can be easily found. The M4PP has been able by using the van der Pauw approach to measure the sheet resistance to a precision of 0.1%.

Scaling down the four terminal measurements to the micro scale introduces a number of challenges. Most notably is the stability of the electrodes (cantilevers). Mechanical vibrations from the environment, as well as thermally induced vibrations from Joule heating in the cantilevers, might shift the position of the electrodes from their nominal positions. As equation 2.31 shows, this will impact the accuracy of the sheet resistance measurement. Recent investigations [103] [104] [105] have shown L-shaped cantilevers to be extremely tolerant to external vibrations. In addition these cantilevers put less stress onto the sample and will therefore limit damage. Furthermore, at very small probe pitches, one must be mindful for electrical or thermal interference due to proximity of electrodes as well as high current densities resulting in electromigration damage when using very small electrodes. The scaling issues and the size limits of M4PPs has been evaluated in [106].

The measurements performed throughout this thesis were all done with probes using L-shaped cantilevers, such as shown in Fig. 1.4. The probes are always referred to by their name, for example L7PP, where the 'L' refers to the L-shaped

cantilever design and the number '7' refers to the number of electrodes present on the probe.

2.4.1 M4PP Sensitivity

From equation 2.31 the measured four point probe resistance is dependent on the sheet resistance via the geometrical correction factor: $R = \frac{R_S}{F}$. However, this assumes a homogeneous sample with constant sheet resistance R_S over the entire measured area. In reality, defects, thickness fluctuations, variations in grain sizes and modified resistance due to TCR will induce variations in the local sheet resistance $R_{S,L}$. The sheet resistance in the measured area Ω is dependent on the local sheet resistance [107] [108]:

$$R_S = \int_{\Omega} \hat{S}(\mathbf{r}) R_{S,L}(\mathbf{r}) d\Omega \quad (2.33)$$

where \hat{S} is known as the sensitivity function. The sensitivity function acts as a weighing function, relating the location of sheet resistance inhomogeneities to the final measured resistance. They will affect the M4PP measurement differently depending on where on the sheet the variation occurred and which configuration is being measured in. It can be shown that the thin film sensitivity function is given by the dot product of the current densities in the standard (e.g. A configuration) and the reciprocal (e.g. A' configuration) configurations [107]:

$$\hat{S}(\mathbf{r}) = \frac{\mathbf{J}_S \cdot \tilde{\mathbf{J}}_S}{\int_{\Omega} [\mathbf{J}_S \cdot \tilde{\mathbf{J}}_S] d\Omega} \quad (2.34)$$

where the 'tilde' signifies the reciprocal configuration. The sensitivity function can become negative, meaning that in certain locations, an increase in local sheet resistance can cause a decrease in measured four-point probe resistance. The sensitivity function calculated for a collinear M4PP in the A, B and C configurations is shown in Fig. 2.6.

2.4.2 The MicroRSP A300 tool

All experiments in this thesis were performed using the MicroRSP A300 tool from CAPRES A/S [109]. The tool is capable of fully automated sheet resistance measurements on up to 12-inch wafers. The configuration sequence and the measurement currents can be fully customised to allow for specially designed measurements

of sample properties on a wide variety of different probe types. The landing is done fully automatic via a strain gauge included in most probe designs that is used to detect the sample surface. The 'engage depth', i.e. how hard the probe is pushed into the sample, and a 'punch-through' current (initial current application before the measurements starts) can be set up to ensure good sample contact has been achieved.

The tool sources an AC current of up to 5 mA and the induced voltage is measured via a lock-in amplifier and is outputted as a resistance value:

$$R_{n\omega} = \frac{V_{n\omega}}{\sqrt{2}I_{RMS}} \quad (2.35)$$

where n denotes the desired harmonic. The output data files include phase measurements, as well as resistance and phase data of the 2-point resistance (source to drain) to allow for comprehensive data analysis and filtering.

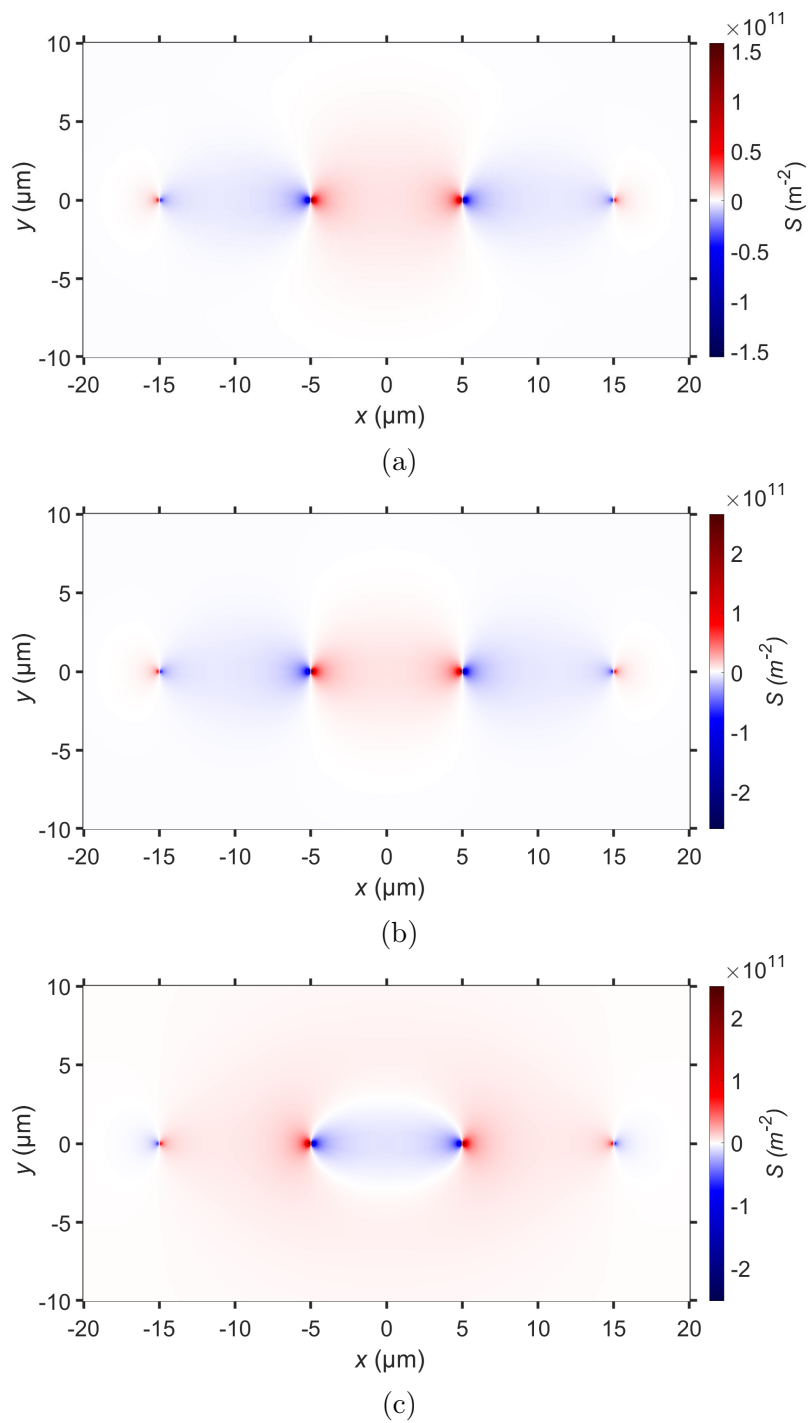
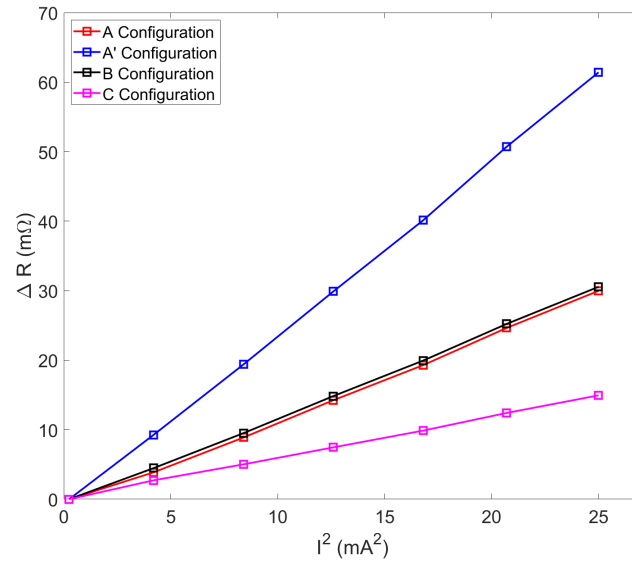


Figure 2.6: *The sensitivities of the (a) A, (b) B and (c) C configurations for an equidistant, co-linear $10\ \mu\text{m}$ pitch M_4PP . The electrodes are positioned on the $y = 0$ line between $\pm 15\ \mu\text{m}$*

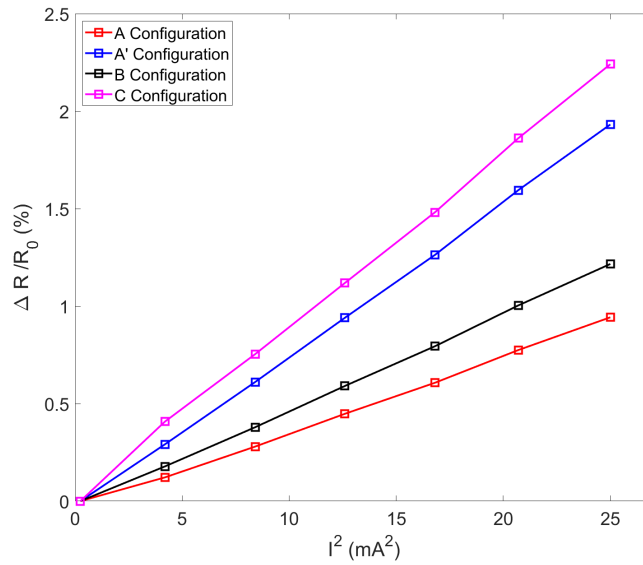
Chapter 3

The M4PP-TCR Method

Joule heating during a M4PP measurement will raise the sample temperature which, in turn, will result in a change in measured resistance, dependent on the materials' TCR value. This behaviour is commonly seen in M4PP measurements, as is shown in Fig. 3.1 which presents the results of a measurement on a metallic thin film. Unlike traditional measurement setups where the entire sample is heated, the M4PP will only locally heat the sample, dependent on the magnitude and path of current during the measurement. As a result, the inputted Joule heating power ($P = I^2R$) can not be easily equated to a temperature difference ΔT , as the M4PP sensitivity (section 2.4.1) makes the TCR response non-trivial. This is evidenced by the different responses arising from the varying configurations in Fig. 3.1a, despite near equal power being deposited into the sample. It must be noted that while it seems the TCR response in the C configuration is the weakest, when normalised with the 'zero current' resistance R_0 (i.e. when no Joule heating power is deposited), the C configurations appear the strongest (together with the A') (Fig. 3.1b). Therefore, to extract the TCR from the observed increase in resistance, the induced temperature field and its interaction on the local sheet resistance and M4PP sensitivity will need to be determined. One option is to scale the observed ΔR with inputted power, rather than temperature, and obtain the power coefficient of temperature (PCR). The PCR is used in the estimation of the self heating effect in electronics [110] [111] [112]. While this circumvents the complications associated with the modeling of the thermal system, the TCR is a more fundamental metric, applicable in not only the characterisation of the self heating effect, but also in the design and operation of various electronic devices, sensors and characterisation techniques. Therefore, the method is chosen to be labelled as the micro four-point probe temperature coefficient of resistance method (M4PP-TCR method).



(a)



(b)

Figure 3.1: The data is taken from a M_4PP measurement on an ultra-thin platinum film. (a) The increase in measured resistance with increasing measurement current per unique configuration. As the B and C configuration are symmetric in both the full electrical-thermal system, the reciprocal configurations would elicit the same response. (b) The increase in resistance normalised with the 'zero current' resistance (fractional increase).

3.1 The M4PP on a sheet system

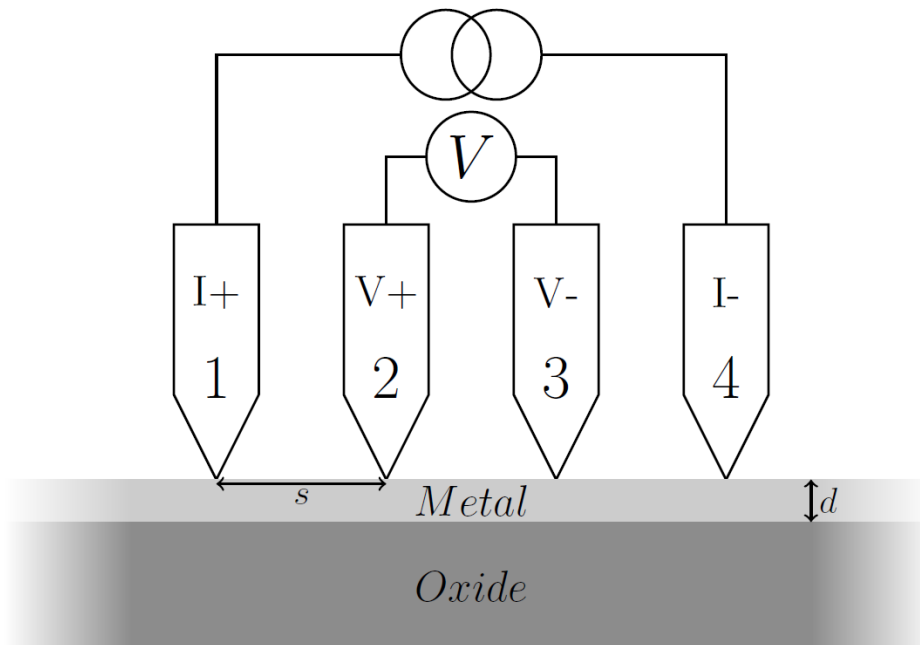


Figure 3.2: A schematic of a M4PP-TCR measurement. Four (or more) electrodes contact the surface of a thin metal film of thickness d , deposited on a thick insulating substrate. The electrodes are equidistantly placed and separated by distance s (pitch). Depicted is the A configuration, but the electrode roles can be freely interchanged.

The method has been initially developed for the characterisation of TCR on ultra thin metal films, where we have the following geometry as visualised in Fig. 3.2: The MicroRsP A300 probe head lands on the surface of an ultra thin metal sheet of thickness d and sheet resistance $R_S = \rho/d$, deposited on a thick insulating substrate. The four electrodes are equidistantly spaced by a distance s (probe pitch). The four contact points are denoted \mathbf{r}_+ and \mathbf{r}_- for the current inlet and outlet respectively and \mathbf{r}_{V+} and \mathbf{r}_{V-} indicating the voltage electrodes and their polarity. The electrode roles can be freely interchanged while the M4PP is engaged with the surface. The film thickness is of the order of a few nanometers (negligible compared to all other distances involved), allowing the film to be approximated as an infinitely thin conducting sheet, as the insulating substrate restricts the current to the metal film only. The measurement is assumed to take place far enough from the edges of the sample so that the substrate can be assumed to be semi-infinite.

3.1.1 Current flow in a M4PP thin film measurement

During a M4PP measurement a current flows from the current inlet at \mathbf{r}_+ to the current outlet positioned at \mathbf{r}_- . The sheet current density in the film can be written as a superposition of the radial sheet current densities from two point sources:

$$\mathbf{J}_s = \frac{I(\mathbf{r} - \mathbf{r}_+)}{2\pi|\mathbf{r} - \mathbf{r}_+|^2} + \frac{-I(\mathbf{r} - \mathbf{r}_-)}{2\pi|\mathbf{r} - \mathbf{r}_-|^2} \quad (3.1)$$

The Joule heating power density generated at a location \mathbf{r} on the film is given by the sheet resistance and current density at that location:

$$p_S(\mathbf{r}) = R_S(\mathbf{r})|\mathbf{J}_s(\mathbf{r})|^2 \quad (3.2)$$

Which, by considering the dot product of the current densities:

$$\mathbf{J}_s \cdot \mathbf{J}_s = \left(\frac{I}{2\pi}\right)^2 \left(\frac{\mathbf{r} - \mathbf{r}_+}{|\mathbf{r} - \mathbf{r}_+|^2} - \frac{\mathbf{r} - \mathbf{r}_-}{|\mathbf{r} - \mathbf{r}_-|^2}\right) \cdot \left(\frac{\mathbf{r} - \mathbf{r}_+}{|\mathbf{r} - \mathbf{r}_+|^2} - \frac{\mathbf{r} - \mathbf{r}_-}{|\mathbf{r} - \mathbf{r}_-|^2}\right) \quad (3.3)$$

reduces to:

$$p_S(\mathbf{r}) = R_S \left(\frac{I}{2\pi}\right)^2 \frac{|\mathbf{r}_+ - \mathbf{r}_-|^2}{|\mathbf{r} - \mathbf{r}_+|^2|\mathbf{r} - \mathbf{r}_-|^2} \quad (3.4)$$

However, the sheet resistance R_S itself is temperature dependent. The sheet resistance is locally modified by the local temperature and the TCR:

$$R_S(\mathbf{r}) = R_{S,0}[1 + \alpha_{TCR}\Delta T(\mathbf{r})] \quad (3.5)$$

Here, $R_{S,0}$ is the sheet resistance at the reference temperature T_0 (i.e. when no Joule heating is taking place). For a homogeneous film, $R_{S,0}$ is constant across the sheet. Equation 3.5 can be substituted into Eq. 3.4 to reach:

$$p_S(\mathbf{r}) = R_{S,0}[1 + \alpha_{TCR}\Delta T(\mathbf{r})] \left(\frac{I}{2\pi}\right)^2 \frac{|\mathbf{r}_+ - \mathbf{r}_-|^2}{|\mathbf{r} - \mathbf{r}_+|^2|\mathbf{r} - \mathbf{r}_-|^2} \quad (3.6)$$

Equation 3.6 returns the location dependent Joule heating power deposited into the sample. Note that power density is dependent on temperature (which itself is dependent on the sheet power density) and so to obtain the true sheet power density, Eq. 3.6 will have to be iterated.

3.2 TCR response in M4PP measurements

The measured transfer resistance (M4PP resistance) can be expressed as a function of the local sheet resistance (which itself is modified by the temperature R_S (Eq.

3.5) and the sensitivity [107]:

$$R = \frac{1}{F} \int_{\Omega} R_{s,0} [1 + \alpha_{TCR} \Delta T(\mathbf{r})] \hat{S}(\mathbf{r}) d\Omega \quad (3.7)$$

where Ω is the measured area and F is geometrical correction factor defined in section 2.4. Since $\frac{1}{F} \int_{\Omega} R_{s,0}(\mathbf{r}) \hat{S}(\mathbf{r}) d\Omega = R_0$, the transfer resistance at the reference temperature T_0 , the fractional change in transfer resistance due to the induced temperature change becomes:

$$\frac{R - R_0}{R_0} = \alpha_{TCR} \int_{\Omega} \Delta T(\mathbf{r}) \hat{S}(\mathbf{r}) d\Omega \quad (3.8)$$

By evaluating the integral, the TCR can be easily determined from the measured values R and R_0 . Note that R_0 is the resistance of the sample at zero current (the reference temperature T_0 is the temperature of the sample with no current flow). In practice this idealised 'zero current' resistance will be a measurement at either very low current or the 3-omega corrected resistance value [88].

It is useful to dive a bit deeper into how the TCR from Eq. 3.8 is obtained in practice. The MicroRsP A300 tool applies an AC current of frequency f and measures the induced voltage via a lock-in amplifier. It expresses the results as root mean square (RMS) values as explained in section 2.4.2. Equation 3.7 can be alternatively expressed as a time dependent voltage:

$$V(t) = \frac{I_0 \sin(\omega t)}{F} \int_{\Omega} R_{s,0} [1 + \alpha_{TCR} \Delta T(\mathbf{r}, t)] \hat{S}(\mathbf{r}) d\Omega \quad (3.9)$$

where $\omega = 2\pi f$. Note the temperature increase is also time dependent, as it is dependent on the current via Joule heating. Applying the same substitutions as before to obtain R_0 , Eq. 3.9 becomes:

$$V(t) = I_0 \sin(\omega t) R_0 \left[1 + \alpha_{TCR} \int_{\Omega} \Delta T(\mathbf{r}, t) \hat{S}(\mathbf{r}) d\Omega \right] \quad (3.10)$$

Equation 3.10 is essentially the linearised resistivity model (Eq. 2.13) with an effective temperature $\int_{\Omega} \Delta T(\mathbf{r}, t) \hat{S}(\mathbf{r}) d\Omega = \Delta T_{\text{eff}}$. Since the temperature is proportional to I^2 , $\Delta T_{\text{eff}} = \Theta R_{\text{eff}} I^2$ where Θ is the thermal resistance of the system, R_{eff} is the effective electrical resistance of the system. This enables the voltage to be written as:

$$V(t) = R_0 \left(I_0 \sin(\omega t) + \alpha_{TCR} \Theta R_{\text{eff}} (I_0 \sin(\omega t))^3 \right) \quad (3.11)$$

$$V(t) = R_0 \left(I_0 \sin(\omega t) + \alpha_{TCR} \Theta R_{\text{eff}} \left[\frac{3}{4} I_0^3 \sin(\omega t) + \frac{1}{4} I_0^3 \sin(3\omega t) \right] \right) \quad (3.12)$$

where the trigonometric identity $\sin^3(x) = \frac{1}{4} [3 \sin(x) - \sin(3x)]$ was used to obtain Eq. 3.12. Equation 3.12 shows that the TCR response is present in both the first harmonic and the third harmonic, which can be isolated using the lock-in amplifier. The obtained RMS harmonic voltages are then:

$$V_{RMS,1\omega} = R_0 I_{RMS} + \frac{3}{2} I_{RMS}^3 R_0 \alpha_{TCR} \Theta R_{eff} \quad (3.13)$$

$$V_{RMS,3\omega} = \frac{1}{2} I_{RMS}^3 R_0 \alpha_{TCR} \Theta R_{eff} \quad (3.14)$$

where the current amplitude has been substituted for the RMS values $I_0 = \sqrt{2} I_{RMS}$. Equations 3.13 and 3.14 show that the TCR response in the first harmonic is three times the size of that observed in the third harmonic. This can be confirmed by M4PP resistance measurements as seen in Fig. 3.3. Additionally, no TCR response is observed in the second harmonic, as expected. The insert in Fig. 3.3 shows that the relationship in a measurement might not be exactly 3 : 1, likely due to additional harmonic contributions.

Equating the first harmonic voltage from Eq. 3.13 to the fraction of the measured resistance increase in Eq. 3.8 shows:

$$\frac{\left(\frac{V_{RMS,1\omega}}{I_{RMS}} \right) - R_0}{R_0} = \frac{3}{2} I_{RMS}^2 \alpha_{TCR} \Theta R_{eff} = \frac{3}{2} \alpha_{TCR} \int_{\Omega} \Delta T(\mathbf{r}, t) \hat{S}(\mathbf{r}) d\Omega \quad (3.15)$$

In other words, when measuring with AC currents, equation 3.8 needs to be corrected by a factor of $\frac{3}{2}$. A pre-factor can therefore be added:

$$\frac{R - R_0}{R_0} = c \alpha_{TCR} \int_{\Omega} \Delta T(\mathbf{r}) \hat{S}(\mathbf{r}) d\Omega \quad (3.16)$$

where $c = \frac{3}{2}$ for AC measurements, and $c = 1$ for DC measurements.

The third harmonic is also shown to be a more advantageous signal as the TCR response can be deduced from just the magnitude of the third harmonic and does not need to be extracted from a difference. Similarly, the third harmonic can also be used to remove Joule heating contributions from M4PP resistance measurements. This correction is known as the 3ω ('three omega') correction, discussed in detail in [88] (Paper II).

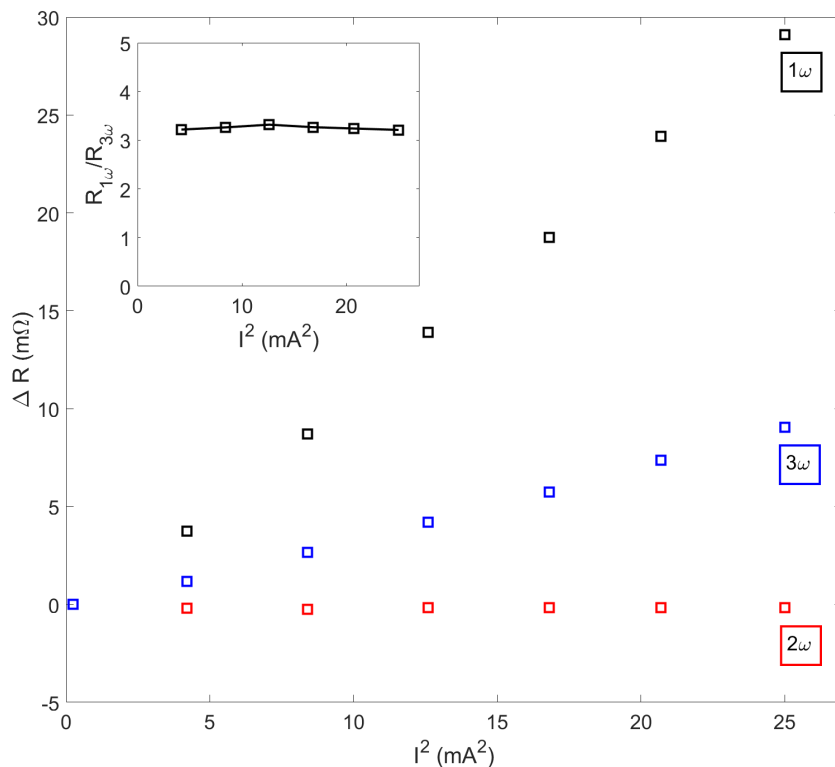


Figure 3.3: *The measured increase in resistance in the different harmonics from a M4PP measurement on a thin platinum film. The insert shows the ratio between the first and third harmonics, whereas the second harmonic does not give a TCR response.*

3.3 The semi-analytical model

In order to evaluate the integral in Eq. 3.16, a semi-analytical approach was adopted, where an analytical expression of the temperature for a point heat source was derived and then evaluated over a meshed surface of the measured area Ω . The surface was meshed via a custom mesh. The mesh approximated the contact regions (More on the contacts in section 3.3.2) by a 18-sided polygon (comparable to a curvature factor of ≈ 0.35). Concentric polygons are drawn up from each contact at increasing radii, with a growth rate of 1.08. The outer extent of the mesh was set to a perimeter radius to 3 times the probe footprint (the distance between the two outer electrodes) from the probe center. Any irregularities remaining (e.g. at the meeting points of two concentric polygons belonging to different contacts)

are patched with triangular mesh elements. The obtained mesh typically has between four to five thousand elements and takes only a couple of seconds to generate.

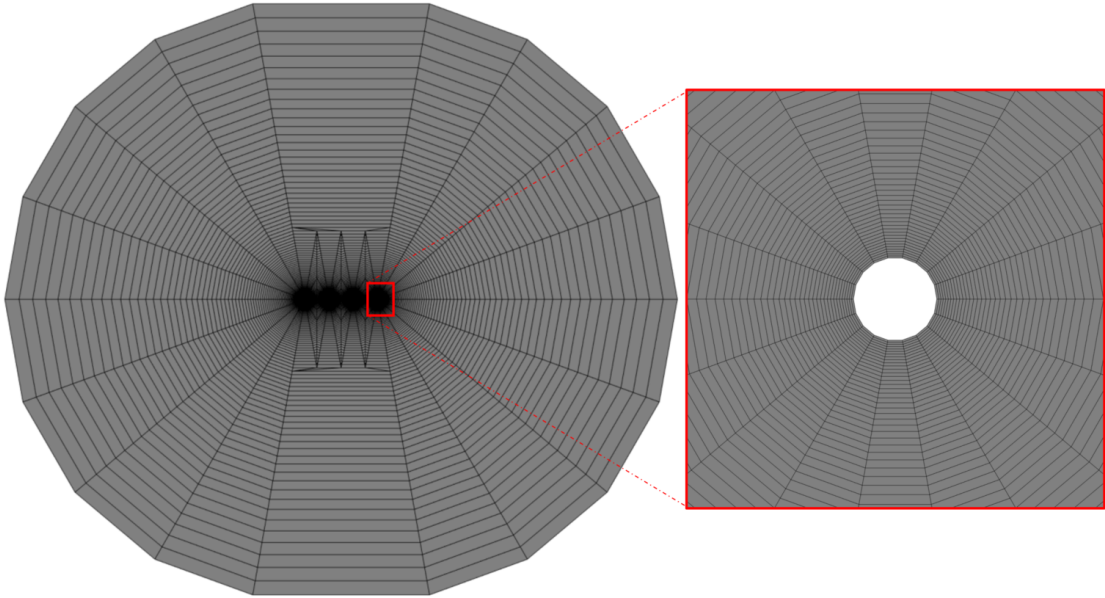


Figure 3.4: *An overview of the generated mesh used to evaluate M4PP-TCR measurements. A zoom-in at the contacts shows the 18-sided polygon used to approximate the circular contacts.*

3.3.1 Calculating the temperature increase

The induced temperature fields were obtained using two approaches. Initially, a quasi-static model was derived, where no thermal delays were considered. The model assumes a constant (DC) current, where the use of AC currents in the measurements are corrected for via the pre-factor in Eq. 3.16 and the use of RMS current values. The hope was that the frequency used in the initial measurements ($f \approx 12.55$ Hz) was low enough to make thermal delays insignificant. This was not the case and therefore a fully time dependent model was derived. The model is named the steady state model as, while it does consider the temperature change over time, it ignores transient effects. This model includes thermal delays by accounting for the thermal diffusivity of the heat governing material. It was further assumed in both models that the heat dissipation is solely driven by classical heat conduction (governed by Fourier's law) through the substrate. Any heat transport through the metal films or the electrodes is assumed to be negligible.

The neglect of any heat transport through the metal film can be investigated by equating the thermal conductance from both components. The thermal conductance is, analogous to the relationship between resistivity and resistance, given by $K = \frac{\kappa A}{l}$. Equalling the thermal conductance through the film and the substrate:

$$\frac{\kappa_f 2\pi r d}{r} = \frac{\kappa_s 2\pi r^2}{r} \quad (3.17)$$

where the subscripts f and s refer to the film and substrate respectively. Rearranging for r and inputting typical values gives:

$$r = \frac{\kappa_f d}{\kappa_s} \approx \frac{30 \times 10^{-9}}{1.4} \approx 215 \text{nm} \quad (3.18)$$

where the thin film thermal conductivity was chosen to be that typical of a platinum thin film [113]. In other words, at distances greater than $\approx 200 \text{nm}$ the thermal resistance of the film is lower, and heat transport though the film is unfavourable. While the effect of the metal thin film is minimal, ignoring the effect might result in a slightly lower temperature than calculated, meaning the extracted TCR might be slightly underestimated. Similarly, the effect of the electrode heat transport (cold finger effect) may be investigated by equating the thermal resistance of the cantilevers and the thermal spreading resistance into the substrate. One finds that for substrates with low thermal conductivity the effect might be significant and will result in lower temperatures than calculated, meaning the TCR will be underestimated.

The quasi-static model

Consider point heat source i with power P_i placed at \mathbf{r}_i on the surface of a semi-infinite medium. The temperature rise experienced at \mathbf{r} due to the power dissipated by the point heat source due to conduction is given by (Section 2.2):

$$\Delta T_i(\mathbf{r}) = \frac{P_i}{2\pi\kappa|\mathbf{r} - \mathbf{r}_i|} \quad (3.19)$$

Contributions from additional point heat sources can added together:

$$\Delta T_{i+j}(\mathbf{r}) = \frac{P_i}{2\pi\kappa|\mathbf{r} - \mathbf{r}_i|} + \frac{P_j}{2\pi\kappa|\mathbf{r} - \mathbf{r}_j|} \quad (3.20)$$

Using this methodology, a surface can be divided into a distribution of point heat sources to calculate the temperature at \mathbf{r}' on a heated sheet.

$$\Delta T_{\text{Sheet}}(\mathbf{r}) = \int_{\mathbf{r}' \in \Omega} \frac{p_S(\mathbf{r}')}{2\pi\kappa} \frac{d\Omega}{|\mathbf{r}' - \mathbf{r}|} \quad (3.21)$$

where $p_S(\mathbf{r})$ is the sheet power density, determining the power of each point heat source on the sheet and Ω is the total area. Applying this to the M4PP measurements, where the sheet power density is given by Eq. 3.6:

$$\Delta T_{\text{Sheet}}(\mathbf{r}) = \frac{I^2 R_{S,0} |\mathbf{r}_+ - \mathbf{r}_-|^2}{8\pi^3 \kappa} \int_{\mathbf{r}' \in \Omega} \frac{1 + \alpha_{TCR} \Delta T(\mathbf{r}')}{|\mathbf{r}' - \mathbf{r}_+|^2 |\mathbf{r}' - \mathbf{r}_-|^2 |\mathbf{r}' - \mathbf{r}|} d\Omega \quad (3.22)$$

Additional heat is dissipated at the contacts due to the contact resistance. Two point heat sources, each placed at the current carrying contact positions can be added to Eq. 3.22 to obtain the final temperature field resulting from a M4PP measurement:

$$\Delta T(\mathbf{r}) = \frac{I^2}{2\pi\kappa} \left(\frac{R_+}{|\mathbf{r} - \mathbf{r}_+|} + \frac{R_-}{|\mathbf{r} - \mathbf{r}_-|} + \frac{R_{S,0} |\mathbf{r}_+ - \mathbf{r}_-|^2}{4\pi^2} \int_{\mathbf{r}' \in \Omega} \frac{1 + \alpha_{TCR} \Delta T(\mathbf{r}')}{|\mathbf{r}' - \mathbf{r}_+|^2 |\mathbf{r}' - \mathbf{r}_-|^2 |\mathbf{r}' - \mathbf{r}|} d\Omega \right) \quad (3.23)$$

The determination of the contact resistances is given in Section 3.3.2. The induced temperature fields are shown in Fig. 3.5, which presents the result of a finite element simulation with the same assumptions as Eq. 3.23. The temperature is a result of a M4PP measurement with a DC current of 5 mA on a metal thin film with $R_S = 14.4 \Omega$ and $\alpha_{TCR} = 0.002 \text{ K}^{-1}$ and no contact resistance (but with a contact radius $r_0 = 100 \text{ nm}$) deposited on a fused silica substrate with $\kappa = 1.4 \text{ W m}^{-1} \text{ K}^{-1}$. The two configurations shown are the A and the A' configurations. Paired with the sensitivity in the A configuration (Fig. 2.6a), the difference in the observed resistance increase (Fig. 3.1) can be understood, as a larger fraction of the high temperature regions is located in areas of positive sensitivity.

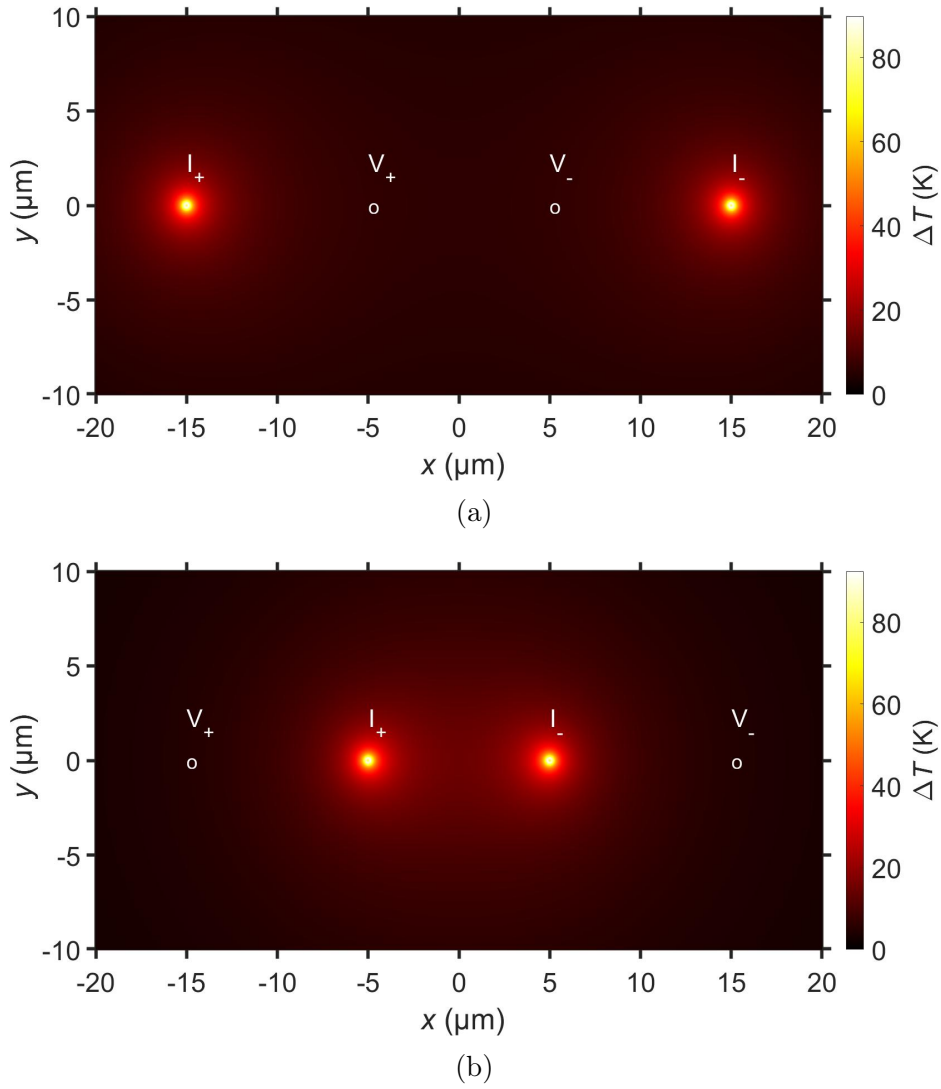


Figure 3.5: *The temperature fields induced by a M4PP measurement with a DC current of 5 mA obtained from finite element simulations (equivalent to the temperature fields obtained from the quasi-static model). The simulated experiment was performed on a metallic thin film with $R_S = 14.4 \Omega$ and $\alpha_{TCR} = 0.002 \text{ K}^{-1}$ deposited on a substrate with $\kappa = 1.4 \text{ W m}^{-1} \text{ K}^{-1}$ and zero contact resistances.*

Steady state model

Consider a harmonic point power source on the surface of a semi-infinite sample at $\mathbf{r} = 0$ with a sinusoidal (with frequency f) power:

$$P(t) = \text{Re} \sum_{n=0} P_n \exp(in\omega_0 t) \quad (3.24)$$

where $\omega_0 = 2\pi f$, P_n is the amplitude and n is the harmonic. The temperature resulting from this point power source is governed by the heat equation:

$$\frac{\partial T}{\partial t} = D \nabla^2 T \quad (3.25)$$

where D is the thermal diffusivity of the material $D = \frac{\kappa}{c_p \rho}$ where κ is the thermal conductivity, c_p is the specific heat capacity and ρ is the material density. Note, that since the ultra-thin film is considered 'infinitely' thin, i.e any heat transport through the thin film is ignored, the thermal diffusivity in Eq. 3.25 refers to the substrate.

The (complex) temperature induced by Eq. 3.24 is likewise harmonic and can therefore be defined as:

$$\tilde{T}_n(\mathbf{r}, t) = T_{n,0}(\mathbf{r}) \exp(in\omega_0 t) \quad (3.26)$$

where $T_{n,0}(\mathbf{r})$ is the temperature amplitude at distance \mathbf{r} from the point source. The derivative with respect to time is then given by:

$$\frac{\partial \tilde{T}_n(\mathbf{r}, t)}{\partial t} = in\omega_0 T_{n,0}(\mathbf{r}) \exp(in\omega_0 t) \quad (3.27)$$

And since:

$$\nabla f = \frac{\partial f}{\partial r} \hat{\mathbf{r}} \rightarrow \nabla^2 f = \frac{1}{r^2} \frac{\partial}{\partial r} \left(r^2 \frac{\partial f}{\partial r} \right) \quad (3.28)$$

solving for $T_{n,0}(\mathbf{r})$:

$$\frac{in\omega_0}{D} T_{n,0}(\mathbf{r}) = \frac{1}{r^2} \frac{\partial}{\partial r} \left(r^2 \frac{\partial}{\partial r} T_{n,0}(\mathbf{r}) \right) \quad (3.29)$$

The solution to this second order differential equation is:

$$T_{n,0}(\mathbf{r}) = \frac{A}{r} \exp\left(-\frac{1+i}{\sqrt{2}} \sqrt{\frac{n\omega}{D}} r\right) + \frac{B}{r} \frac{-(1-i)}{\sqrt{2}} \sqrt{\frac{D}{n\omega}} \exp\left(\frac{1+i}{\sqrt{2}} \sqrt{\frac{n\omega}{D}} r\right) \quad (3.30)$$

As $T_{n,0}(\mathbf{r}) \rightarrow 0$ when $r \rightarrow \infty$, $B = 0$ and $T_{n,0}(\mathbf{r})$ becomes:

$$T_{n,0}(\mathbf{r}) = \frac{A}{r} \exp(-(1+i) k_n r) \quad (3.31)$$

where $k_n = \sqrt{\frac{n\omega}{2D}}$. The second boundary condition requires that at $r \rightarrow 0$, the heat flux must be equal to the input power:

$$P_n = \lim_{r \rightarrow 0} \left(-2\pi r^2 \kappa \frac{\partial T_{n,0}(\mathbf{r})}{\partial r} \right) \quad (3.32)$$

$$P_n = \lim_{r \rightarrow 0} \left(-2\pi r^2 \kappa A \exp(-(1+i)k_n r) \left[\frac{-1}{r^2} - \frac{(1+i)k_n}{r} \right] \right) \quad (3.33)$$

$$P_n = 2\pi \kappa A \quad (3.34)$$

The spacial temperature can then be written:

$$T_{n,0}(\mathbf{r}) = \frac{P_n}{2\pi \kappa r} \exp(-(1+i)k_n r) \quad (3.35)$$

The time component can be added to obtain the time dependent complex temperature arising from the point heat source:

$$\tilde{T}_n(\mathbf{r}, t) = \frac{P_n}{2\pi \kappa r} \exp(-(1+i)k_n r) \exp(in\omega_0 t) \quad (3.36)$$

So that the full temperature field induced by the harmonic point power source (Eq. 3.24) becomes:

$$\Delta T(\mathbf{r}, t) = \text{Re} \sum_{n=0} \frac{P_n}{2\pi \kappa r} \exp(-(1+i)k_n r) \exp(in\omega_0 t) \quad (3.37)$$

Carslaw and Jaeger have provided a similar solution for the temperature increase resulting from a periodic power source embedded in a full 3D material [114]. In the case of Joule heating, power contributions exist in the zeroth and second harmonic ($n = 0, 2$). Therefore, including the use of sinusoidal time dependence as $\Delta T(\mathbf{r}, 0) = 0$, the temperature arising at time t at location \mathbf{r} from a (Joule heating) point source (at $\mathbf{r}' = 0$):

$$\Delta \tilde{T}(\mathbf{r}, t) = \frac{P_0}{2\pi \kappa \mathbf{r}} \left[\frac{1}{2} (1 - \exp(-(1+i)k_2 \mathbf{r}) \exp(i2\omega t)) \right] \quad (3.38)$$

where $k_2 = \sqrt{\frac{\omega}{D}}$ and P_0 is the power amplitude of the point source. Applying this to our thermal system, with the power density in the sheet given by Eq. 3.6 and additional power from the the contacts, the time dependent temperature can be

written as:

$$\begin{aligned} \Delta\tilde{T}(\mathbf{r}, t) = & \frac{I_0^2}{2\pi\kappa} \left[\frac{R_+}{|\mathbf{r} - \mathbf{r}_+|} \left(\frac{1}{2} (1 - \exp -(1+i)k_2|\mathbf{r} - \mathbf{r}_+|) \exp(i2\omega t) \right) + \right. \\ & \frac{R_-}{|\mathbf{r} - \mathbf{r}_-|} \left(\frac{1}{2} (1 - \exp -(1+i)k_2|\mathbf{r} - \mathbf{r}_-|) \exp(i2\omega t) \right) + \\ & \left. \frac{R_{S,0}|\mathbf{r}_+ - \mathbf{r}_-|^2}{4\pi^2} \int_{\mathbf{r}' \in \Omega} \frac{1 + \alpha_{TCR}\Delta T(\mathbf{r}')}{|\mathbf{r}' - \mathbf{r}_+|^2 |\mathbf{r}' - \mathbf{r}_-|^2 |\mathbf{r}' - \mathbf{r}|} \right. \\ & \left. \left(\frac{1}{2} (1 - \exp -(1+i)k_2|\mathbf{r}' - \mathbf{r}|) \exp(i2\omega t) \right) d\Omega \right] \quad (3.39) \end{aligned}$$

From which the real temperature, to be used in Eq. 3.8, can be obtained via $\Delta T(\mathbf{r}, t) = \text{Re}(\Delta\tilde{T}(\mathbf{r}, t))$.

3.3.2 Calculating the contact resistance

The sheet power density obtained in Eq. 3.6 has two singularities at the electrode contacts at \mathbf{r}_+ and \mathbf{r}_- . To address this, and at the same time be able to include the any additional power deposited at the contacts (due to e.g. spreading resistance), a contact region is defined. A circular area of radius r_0 around the contact point is assigned to be the contact area. All power deposited inside this area is assigned to a point heat source position at \mathbf{r}_\pm . The contact resistances will likely vary between engages and even change during an engage, due to e.g. position changes, re-punch through at high currents, abrasion of the electrode tips and material mixing. As a result pre-calculating or using nominal values is not possible in our measurements and the contact resistance have to be determined at each engage.

The electrode specific contact resistances can be calculated during a M4PP measurement via the use of the load resistance R_{load} . The load resistance is the two-point resistance measurement between the source and drain, i.e. the series resistance of the sample resistance, the contact resistances and the resistance in the lead electronics up to the electrode contact. The load resistance of a M4PP measurement with electrode i and j as the current carrying electrodes is:

$$R_{load,i,j} = R_{lead,i} + R_{contact,i} + R_{sample} + R_{contact,j} + R_{lead,j} \quad (3.40)$$

The lead resistance can be obtained from a preceding measurement on a bulk metal slab or any highly conductive substrate with good contact, where the sample and contact resistance are negligible compared to the lead resistances, so that $R_{load,i,j} \approx R_{lead,i} + R_{lead,j}$. The contacts can be modelled as two cylinders with

equipotential edges separated by distance $D_{i,j}$, as in section 2.4. The sample resistance is then [106]:

$$R_{\text{sample}} = \frac{R_{s,0}}{\pi} \arccos\left(\frac{D_{i,j}}{2r_0}\right) \quad (3.41)$$

The calculated sample resistance and the measured lead resistances can then be subtracted from the load resistance to obtain:

$$\tilde{R}_{i,j} = R_{\text{contact},i} + R_{\text{contact},j} \quad (3.42)$$

By switching probe configurations three measurements can be obtained:

$$\begin{aligned} \tilde{R}_{1,2} &= R_{\text{contact},1} + R_{\text{contact},2} \\ \tilde{R}_{2,3} &= R_{\text{contact},2} + R_{\text{contact},3} \\ \tilde{R}_{1,3} &= R_{\text{contact},1} + R_{\text{contact},3} \end{aligned} \quad (3.43)$$

where the numbered subscripts refer to current carrying electrode. The three equations then can be linearly combined to obtain the electrode specific contact resistance of electrode 1 (and analogously for electrode 2 and 3):

$$R_{\text{contact},1} = \frac{\tilde{R}_{1,2} + \tilde{R}_{1,3} - \tilde{R}_{2,3}}{2} \quad (3.44)$$

In a more general case of m measurements with n electrodes, Eq. 3.40 can be rewritten in matrix form:

$$R_{\text{load}} = MR_{\text{lead}} + MR_{\text{contacts}} + R_{\text{sample}} \quad (3.45)$$

where R_{load} , R_{lead} and R_{sample} are $1 \times m$ vectors containing the measured and calculated values and M is a $n \times m$ matrix marking the current carrying electrodes with a 1 and the rest with 0. Solving for R_{contacts} we get:

$$R_{\text{contacts}} = (M^T M)^{-1} M^T (R_{\text{load}} - MR_{\text{lead}} - R_{\text{sample}}) \quad (3.46)$$

which will return a $n \times 1$ matrix with the contact resistances, provided the number of unique measurements is equal or larger than n .

Use of the above technique maintains the total amount of power deposited into the sample, regardless of chosen contact radius. In order to verify that extracted TCR is independent of chosen contact radius, the TCR can be extracted from a M4PP measurement using various contact radii. The extracted TCR is negligibly affected by chosen contact radii within the range of $30 \text{ nm} < r_0 < 1000 \text{ nm}$. At very low

contact radii, the extracted TCR deviates as the designed mesh is likely not fine enough near the contact regions, as the deviation reduces when the growth rate is halved. At the very large contact radii the resulting thermal system approximated by the mesh deviates too much from the reality. From experience with M4PP measurements on metals, the typical contact radius is around 100 nm, which is the value used in the subsequent data analysis.

3.3.3 Data analysis using semi-analytical model

Using the quasi-static model to evaluate the temperature increase, Eq. 3.16 is evaluated over the meshed surface to calculate the fractional resistance increase for a given TCR value:

$$\frac{R - R_0}{R_0} = c \alpha_{TCR} \sum_{n=1}^N \Delta T(\mathbf{r}_n) \hat{S}(\mathbf{r}_n) d\Omega_n \quad (3.47)$$

where N is the number mesh elements, \mathbf{r}_n is the location of the centroid of mesh element n and $d\Omega_n$ is the corresponding area of mesh element n . The TCR is extracted using the non-linear least square fit method, where the model (Right hand side in above equation) is fit to the measured data ($\frac{R-R_0}{R_0}$, left hand side), using α_{TCR} as the fitting parameter [115]. MatLab [116] is used to perform the fit using the in-built non-linear least square fit function ('lsqnonlin' in MatLab). Most default settings were maintained with the function utilising the trust region-reflective fitting algorithm and a step tolerance of 10^{-8} . The function 'nlparci' is used to obtain the 95% confidence interval and the standard error from the fit. A diagram of the data analysis process is shown in Fig.3.6a (as the sharing of the scripts is prohibited).

Application of the time dependent temperature model is a little more involved. To capture the time dependent effects, the induced voltage is evaluated over time across the meshed surface:

$$V(t) = \frac{I(t)}{F} \sum_{n=1}^N R_{s,0} [1 + \alpha_{TCR} \Delta T(\mathbf{r}_n, t)] \hat{S}(\mathbf{r}_n) d\Omega_n \quad (3.48)$$

where N is the number mesh elements, \mathbf{r}_n is the location of the centroid of mesh element n , $d\Omega_n$ is the corresponding area of mesh element n and $\Delta T(\mathbf{r}_n, t)$ is the real component of the temperature in Eq. 3.39. The obtained voltage trace is entered into a digital lock-in amplifier, which emulates an analog device [117]. It

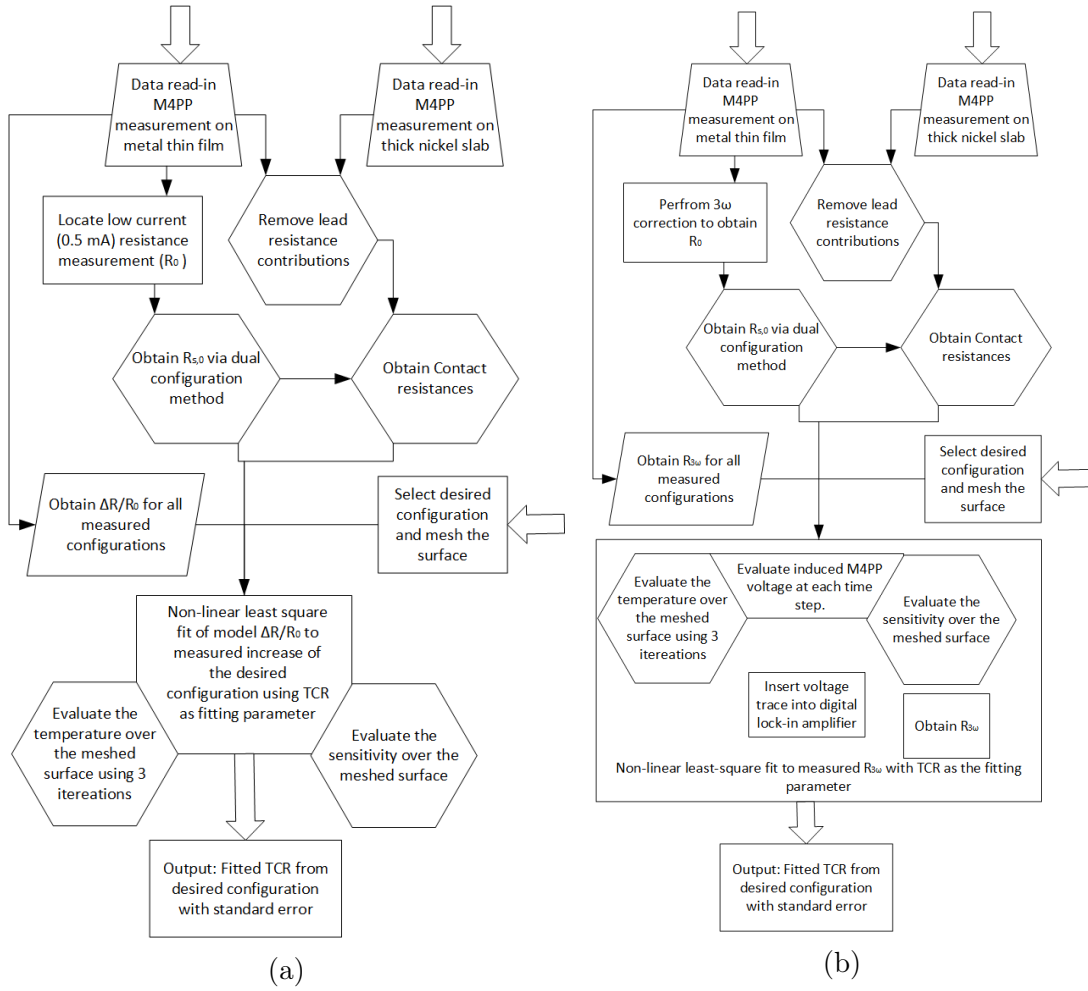


Figure 3.6: Schematics of the analysis code procedures. (a) The Quasi-static analysis procedure (b) The steady state analysis procedure

returns the first, second and third harmonic voltages, which are converted to RMS values and a resistance, as to match the tool output:

$$R_{n\omega} = \frac{V_{n\omega}}{\sqrt{2}I_{RMS}} \quad (3.49)$$

where $n = [1, 2, 3]$, denoting the harmonics. Again, a non-linear least square fit of the obtained harmonic resistance value is performed against the measured values using α_{TCR} as the fitting parameter. A diagram of the analysis process is shown in Fig.3.6b.

3.3.4 Validation with FEM

The semi-analytical approach has been validated against finite element simulations via the use of two finite element models developed in COMSOL multiphysics [118]. The first FEM model was developed to verify the quasi-static semianalytical model (in the DC limit). The second model was used to compare against the steady state model and was an evolution of the first, with some additional adjustments to correctly implement the time dependent effects. Both models make use of the 'multiphysics' capability of COMSOL to link two modules 'electric currents in shells' and 'heat transport in solids' together to simulate the Joule heating effect in the metallic thin film.

The quasi-static finite element model was made up of a rectangular domain $800 \times 800 \times 400 \mu\text{m}$ in size assigned as the fused silica substrate. The top boundary, via use of the 'electric currents in shells' module, was designated as the platinum thin film. At the bottom boundary the reference temperature was maintained. The contacts are simulated by adding circular domains of radius r_0 in the work plane of the 'electric currents in shells' module, which will mimic the cylindrical contacts assumed in the analytical model when the film thickness is applied in the module. The contacts are positioned so that the probe center is located at the center of the top boundary. The current is injected and extracted at the perimeter of the contacts. The inside of the current carrying contacts is excluded from the electrical domain. Additionally, the simulated film is not included in the 'heat transport in solids' module, as the fused silica substrate is assumed to be wholly responsible for the heat diffusion away from the film. The voltage is measured at the voltage electrode contacts by averaging over the voltage across the entire contact area (πr_0^2) of each contact. This does mean that unlike with the current electrode contacts, the voltage electrode contact area is included in the electrical domain. The mesh is generated by COMSOL Multiphysics using the physics based mesh settings, with a minimum element size of 10 nm and a maximum element size of $100 \mu\text{m}$. These settings were paired with a curvature factor of 0.2 and a maximum element growth rate of 1.3. The result is a mesh of ≈ 90000 elements. The curvature factor and minimum element size result in a good element density around the contacts, where the sensitivity and temperatures gradients are high.

The FEM and the quasi-static models are compared by considering a 16 nm thin platinum film, with a room temperature sheet resistance of $R_{s,0} = 14.5 \Omega$ and obeying the linearised resistivity model with a TCR of $\alpha_{TCR} = 0.002 \text{K}^{-1}$. The film is deposited on top of a fused silica substrate with thermal conductivity $\kappa = 1.4 \text{W m}^{-1} \text{K}^{-1}$. The fractional resistance increase is obtained from both models considering a $10 \mu\text{m}$ pitch probe and $r_0 = 100 \text{nm}$ contact radii with zero

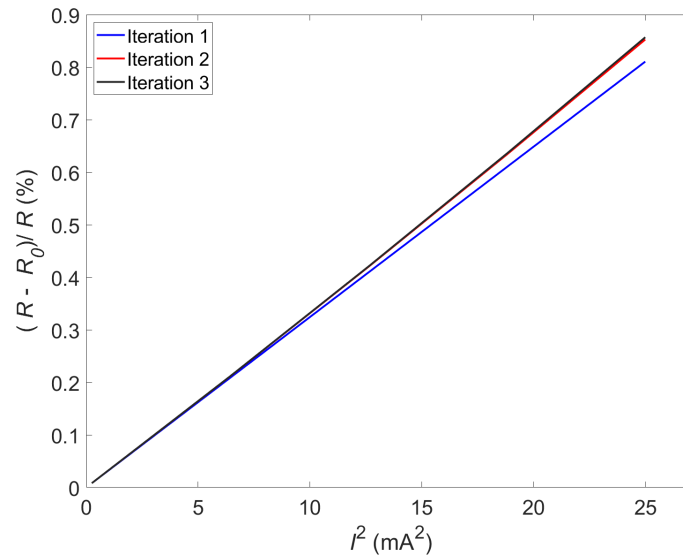
contact resistance over a range of 0.5 – 5 mA DC currents. As the semi-analytical model is implicit, the increase in resistance is calculated over several iterations. The model converged after three iterations as shown in Fig. 3.7a.

The result of the comparison is shown in Fig. 3.7b for both the A and A' configurations. The semi-analytical model matches the finite element simulations to an acceptable degree, with about $< 2\%$ difference at the higher currents. This validates the use of the DC semi-analytical model in the TCR extraction.

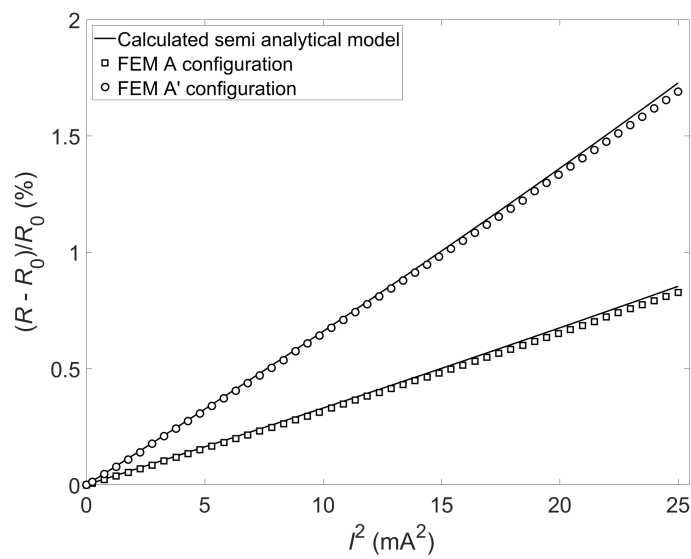
The time dependent finite element model was set up slightly differently. The domain is now a hemisphere, for a more efficient heat transport domain, with the top boundary assigned as the 'electric shell' acting as the conductive film as before. The radius of the hemisphere was set to 50 times the probe footprint, i.e. $150s$, at which point the solutions converged. The outer shell of the hemisphere is fixed at the reference temperature. The current injection is identical to the previous model, but the voltage is now measured at the perimeter of the electrode contacts with the contact area excluded from the electrical domain, mimicking the semi-analytical mesh. The injected current is now time dependent: $I(t) = \sqrt{2}I_{RMS} \sin(2\pi ft)$. The output is divided in 64 time steps per period, where at each time step the induced voltage as measurement by the M4PP is recorded. The mesh settings were optimised to the following settings: a maximum element size of $200 \mu\text{m}$, a maximum element growth rate of 2 and a curvature factor of 1. To ensure a good element density regardless of chosen contact size, the minimum element size is dependent on the contact radius: $\frac{r_0}{2}$. The model takes around 5 minutes to simulate a full current period.

The FEM was compared to the steady state semi-analytical model, with $I_{RMS} = 5 \text{ mA}$. Two current periods were simulated in the FEM with only the voltage induced over the second period being used for the analysis to minimise transient effects, which are not included by the semi-analytical model. The fused silica properties of $\rho = 2200 \text{ kg m}^{-3}$, $C_p = 730 \text{ J kg}^{-1} \text{ K}^{-1}$ and $\kappa = 1.4 \text{ W m}^{-1} \text{ K}^{-1}$ were set in both models. The platinum thin film was again assigned the typical room temperature sheet resistance $R_{S,0} = 14.5 \Omega$ and the linearised resistivity model with a TCR value of $\alpha_{TCR} = 1.75 \times 10^{-3} \text{ K}^{-1}$.

As with the time dependent semi-analytical model we expect to capture size and frequency dependent effects, the two models were compared over a frequency range of 10^{-2} to 385.75 Hz , where the lowest frequency should be identical to the DC limit (the quasi-static model). The higher frequency steps were determined by $f = 3.0137 \times 2^n$ with $n \in [0, 1, 2, \dots]$, mirroring the selectable frequencies on the MicroRsP A300. The result of a comparison with the A and A' configurations

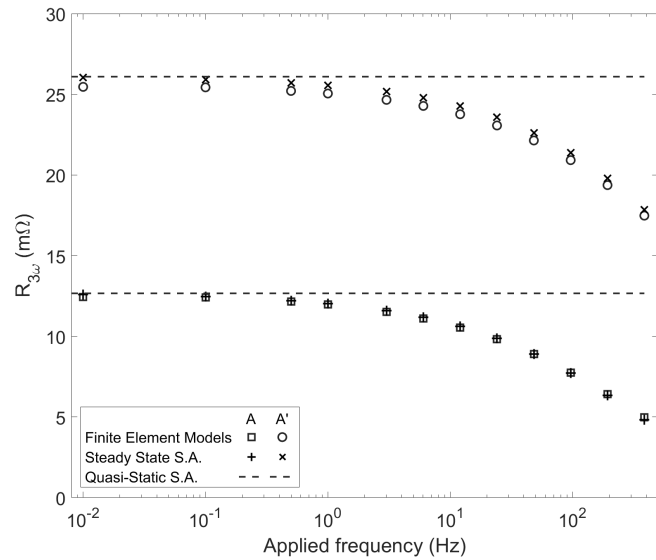


(a)

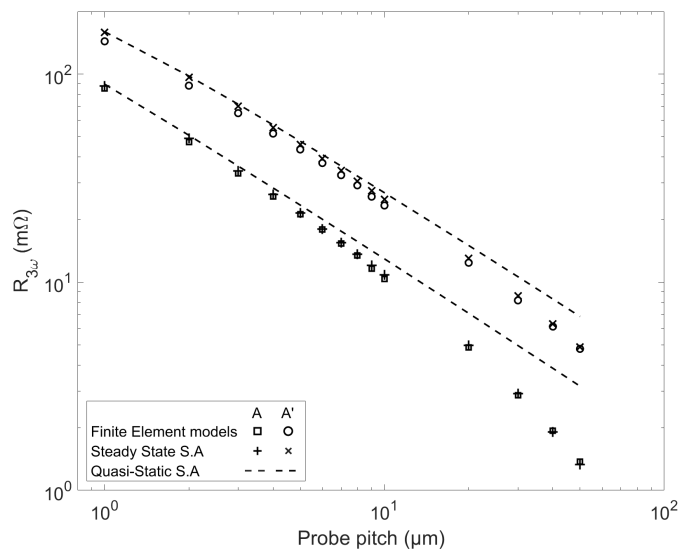


(b)

Figure 3.7: (a) The convergence of the quasi-static semi-analytical model after three iterations of the temperature calculation (Eq. 3.23). (b) A comparison between the quasi-static semi-analytical model and finite element simulations (FEM) of a M4PP measurement on an identical thin film. The quasi-static model and the FEM both agree on the increase in M4PP resistance to approximately 2%.



(a)



(b)

Figure 3.8: (a) The $R_{3\omega}$ obtained from the quasi-static and steady state semi-analytical model compared to finite element simulations of an identical platinum thin film system. The probe pitch is set to $s = 10 \mu\text{m}$ and the applied frequency is varied. (b) The $R_{3\omega}$ obtained from the two semi-analytical models compared to finite element simulations while varying the pitch of an equidistant probe with a current frequency of $f = 12.055 \text{ Hz}$.

is shown in Fig. 3.8a. In addition the quasi-static model is plotted as well. At the lowest frequencies (in the DC limit), the FEM, the steady state model and the quasi-static model all agree fairly well ($< 2\%$). With increasing frequency the FEM and steady state models begin to diverge from the quasi-static solution as a result of the thermal delays in the system. Figure 3.8a validates that the extended time dependent model captures the frequency dependence of $R_{3\omega}$ well and can be used for TCR extraction at varying current frequencies. A similar comparison was performed at the fixed frequency of $f = 12.055\text{Hz}$ with probe pitches ranging from $1 - 50\ \mu\text{m}$. Again a fairly good ($< 3\%$) match was found between the finite element model and the extended semi-analytical model as is shown in Fig. 3.8b. Both results validate the use of the extended time dependent semi-analytical model to extract TCR from M4PP measurements performed at variable frequency and pitch.

3.3.5 Limitations of the Semi-analytical method

The quasi-static model is able to provide a fast analysis and return a TCR value (roughly 30 seconds per configuration) within the limits of the assumed system. However, to obtain the TCR from more complex samples, the semi-analytical approach might need to be expanded. The steady state model is already showing the limitations of the semi-analytical modeling, with a drastically increased analysis time (about forty-fold). An argument can be made for an FEM-based approach in favor of the semi-analytical models, especially when considering the possible future corrections to the steady state model, such as the inclusion of transient effects, multi-layer heat contributions and temperature dependent contact resistance and current densities.

As the MicroRsP A300 sources an AC current, transient effects will influence the obtained harmonics, especially at higher frequencies. Figure 3.9 shows FEM simulations at $f \approx 385.75\ \text{Hz}$ of M4PP measurements on platinum thin films with the obtained first and third harmonics resistance presenting the effect of transients. A $\sim 1.5\%$ deviation is seen in the third harmonic, and deviation the first harmonic persists for many periods of the applied current. It is possible to circumvent the effects by establishing a waiting period in the measurements, where a current is applied over multiple periods before initiating the measurement. While this does mostly alleviate any issues arising from transient behaviour (Fig. 3.9), it is at the cost of significantly increasing the measurement time.

The temperature dependence of the sheet resistance $R_s = f(T)$ is included in

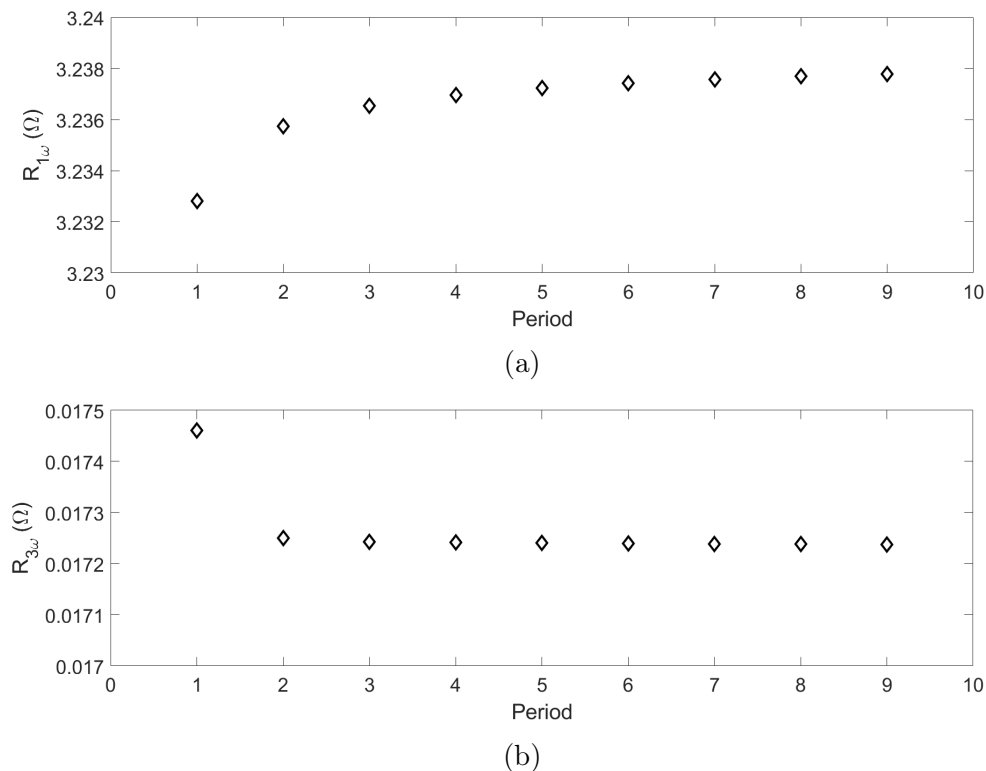


Figure 3.9: *The extracted first (a) and third (b) harmonic resistances obtained from a digital lock-in amplifier of a FEM simulation of a M4PP measurement with an AC current with frequency 385.75 Hz on a platinum thin film. The resistances are extracted over a single period for 9 periods to illustrate transient effect, which will influence the obtained resistances of early periods. It is therefore wise to institute a waiting period, where the voltage measurement is delayed by a number of periods.*

the two models and implemented via iterative procedures. In the platinum thin film measurements (where the sheet heating dominates: $P_S \gg P_{\pm}$) this proved to be sufficient to describe the observed increase in resistance. However, the (effective) contact resistances also carry a temperature dependence ($R_{\pm} = f(T)$), currently not included in the model, since R_{sample} (Eq. 3.41) is obtained from $R_{S,0}$. At high current measurements, the obtained contact resistance therefore are overestimated, as they compensate for the excluded increase in sample resistance. Overestimating the deposited power into the sample will lead to an underestimation in the extracted TCR values. Samples where the contact resistances have a larger contribution to the total power will likely require a more comprehensive calculation of temperature. One option is to use the sheet resistance R_S obtained from the transfer resistance measurements at each current to calculate the sam-

ple resistance, rather than $R_{S,0}$. A more comprehensive calculation involves the inclusion of the two point sensitivity ($\hat{S}_{2p}(\mathbf{r})$):

$$R_{\text{Sample}} = \frac{R_{S,0}}{F_{2p}} \left(1 + \alpha_{TCR} \int_{\Omega} \Delta T(\mathbf{r}) \hat{S}_{2p}(\mathbf{r}) d\Omega \right) \quad (3.50)$$

where F_{2p} is the two-point geometric correction factor. Note that the above equation is dependent on the TCR, which means it has to be incorporated into the iterative process, significantly lengthening the analysis time.

In addition, a change in the local sheet resistance (due to ΔT) will affect the local electric field (since the current 'wants' to avoid high resistance regions) which, in turn, will affect the local sensitivity (Eq. 2.34) [108]. This suggests additional iteration is also required here as the not-iterated sensitivity is overestimated.

Thus the induced temperature field appears implicit in four parameters (R_+ , R_- , R_S and \hat{S}) as well as influenced by transient effects. While some iterative procedures will provide negligible improvement in certain sample types (e.g. contact resistance iteration in sheet power dominated samples), expanding the semi-analytical approach to include the above mentioned effects will be required to push the M4PP-TCR method towards high accuracy TCR characterisation. Potentially, the added computational cost might become too large. Especially since more M4PP measurements on more complex samples, such as multi-layered samples or samples with surface structures or patterning [119] will also require a significant expansion of the thermal model as different heat pathways become available. A finite element model will be able to include all the above effects with relative ease, so that a FEM model combined with a digital lock-amplifier can be used to extract the TCR of an M4PP measurement.

3.4 TCR of Pt thin films

The M4PP-TCR method was used to extract the TCR of several platinum thin film samples. The choice of platinum is rooted in the slightly higher resistivity compared to most other suitable metals such as gold or copper, meaning the Joule heating effects should be enhanced. Its comparatively lower thermal conductivity will minimise any heat transport contributions from the film as assumed. In addition, platinum shows minimal oxidation at room temperature [120] resulting in stable and easy to contact films. The platinum was deposited on a double side polished 4-inch fused silica wafer. Fused silica, being an insulator, will restrict the current (and thus also the Joule heating) to the platinum thin film and its low

thermal conductivity ($1.4 \text{ W m}^{-1} \text{ K}^{-1}$) will magnify any thermal gradients in the film. A 1 nm titanium layer was deposited first to aid adhesion of the platinum layer to the substrate. The platinum (and titanium) was deposited via e-beam evaporation in a Wordentec QC800. A total of three samples were fabricated with three different platinum layer nominal thicknesses: 7 nm, 10 nm and 16 nm. Low deposition rates were chosen for the titanium layer (1.3 \AA s^{-1}) and the platinum layer (5 \AA s^{-1}). The chosen thicknesses should give distinct TCR values according to thin film TCR models (section 2.3.2) [51] [52] and previous observations [50]. Unfortunately the vacuum seal during the deposition of the 10 nm sample was broken, leading to higher inhomogeneity of the film as the Ti layer oxidised before the subsequent platinum deposition. The fabricated wafers were then cut in half using a dicer (1 mm s^{-1} feed rate, 0.25 mm lift height). One half was broken into smaller coupons, with a maximum size of $11 \times 14 \text{ mm}$. The films showed good coverage, though the 7 nm did display some discontinuities. This was reflected in the measurement yield, with 73% of engages on the 7 nm film being successful, compared to 98% on the 10 nm film and 100% on the 16 nm film.

Three coupons of each platinum thickness were selected for further measurements. To obtain an independent reference of TCR, each coupon was characterised using a physical property measurement system (PPMS from Quantum design). Four locations on the surface of the platinum thin film were contacted via the use of conductive silver paste. The contacts were placed at the edges of each coupon to allow for a four terminal measurement of the films' resistance. The coupons were then placed in a temperature controlled chamber, capable of precise ($< 0.02\%$) temperature control. The temperature was varied from 290 K to 310 K in steps of 5 K. At each temperature step, the sample was allowed to reach thermal equilibrium before continuing. During the experiment the resistance was continuously measured using an AC current with $I_{RMS} = 5 \text{ mA}$ and $f = 18.3 \text{ Hz}$. The paired resistance and temperature data was plotted as shown in Fig. 3.10. Only the data points where the temperature was stabilised was considered. From the slope ($\frac{\Delta R}{\Delta T}$) the room temperature (300 K) TCR can be obtained from:

$$\alpha_{TCR} = \frac{1}{R(T_{Room})} \frac{\Delta R}{\Delta T} \quad (3.51)$$

The M4PP measurements were performed on the MicroRsP A300 tool (section 2.4.2) in two separate experiments. The first experiment was analysed using the quasi-static model and the results were published in [121] (Paper I). Later experiments involved fine tuning of the steady state model, to eliminate the dependence of the TCR on the applied frequency and probe pitch. The manuscript is currently in preparation (Paper III).

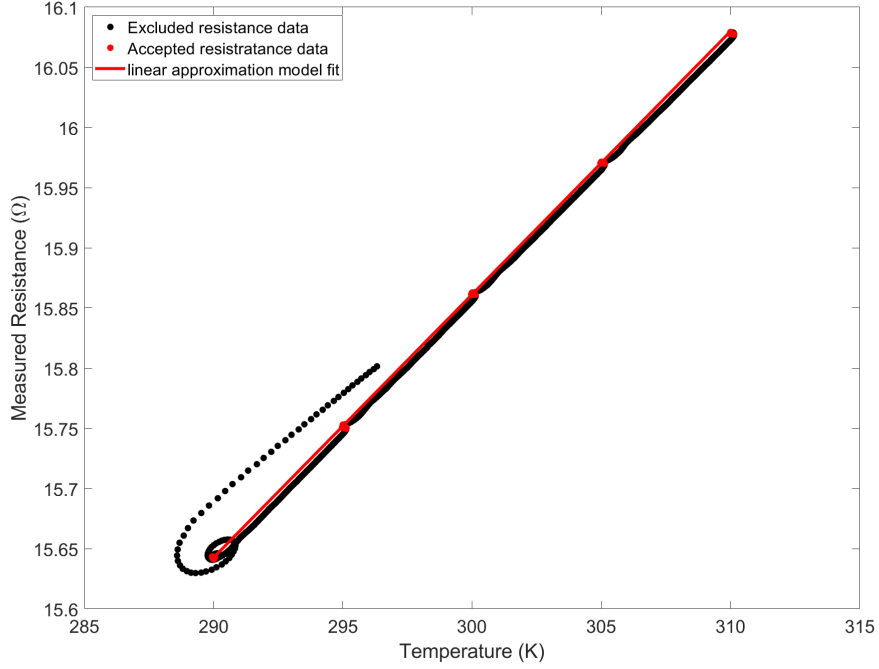


Figure 3.10: *The measured resistance in the PPMS on the 10 nm thin platinum film. The resistance was continuously measured as the temperature was increased from 290 K to 310 K. Only the resistance values measured at 5 K intervals, where the temperature was held stable to the sample to reach thermal equilibrium, are included in the fit to the linear approximation model (Eq. 2.13).*

3.4.1 TCR from quasi-static analysis

M4PP measurements were performed on each coupon using an equidistant seven-point probe (L7PP) with a probe pitch of 10 μ m using the L-shaped cantilever design. A total of twenty engages were performed on the 16nm and 10nm coupons. Thirty engages were done on the 7nm coupons due to the lower measurement yield. The measurements were performed near the centre of the coupon and laterally spaced apart by 20 μ m. At each engage, an AC current with a frequency of $f = 12.055$ Hz is forced through the sample, starting at $I_{RMS} = 5$ mA down to $I_{RMS} = 0.5$ mA in seven intermediary steps, equidistant in I^2 space. For each engage, the probe is cycled through all configurations, including the reverse polarity configurations. The resulting sequence is as follows: $[A_1, A'_1, A_2, A'_2, B_1, B'_1, \text{etc.}]$ for a total of 12 configurations per sub-probe. A_2 refers to the reverse polarity configuration, e.g. $[4, 3, 2, 1]$, instead of $[1, 2, 3, 4]$ for A_1 . The three equidistant

sub-probes on the L7PP are used, starting with the 20 μm pitch sub-probe before measuring with the two 10 μm pitch sub-probes (first 10A (The four left-most electrodes), then 10B (the four right-most electrodes)). As a result 36 configurations are measured at each current step. A contact radius of $r_0 = 100 \text{ nm}$ is chosen for the analysis. At the start and end, as well as in between every 10 engages a reference measurement is made on a thick nickel slab ($R_S = 0.48 \Omega$) to characterise the lead resistances and enable the calculation of the contact resistances (as explained in section 3.3.2)

The obtained resistance increase versus current squared plots for the A and A' configurations for the measured coupons are shown in Figs. 3.11, 3.12 and 3.13. The data points shown in the figures are the average value over all successful engages, with the error bars inside the symbols. The increase in measured resistance is incredibly reproducible across all engages, with a standard deviation in $\frac{\Delta R}{R}$ of 1 – 3%. At the maximum current (5 mA) the TCR signal in the thickest film (16 nm) is around 2% for the A' configuration and 1% for the A configuration. Considering the M4PP is capable of measuring resistance to a precision of 0.1%, the TCR response is easily detectable by the M4PP. The TCR response increases for the thinner films (up to 3% for the A' and 2% for the A configurations), despite their expected lower TCR values, due to the significantly higher sheet resistance of the thinner films. The typical effective contact resistances obtained were $\sim 1 \Omega$ for the 16 nm film, $\sim -3 \Omega$ for the 10 nm and $\sim -5 \Omega$ for the 7 nm film. Negative effective contact resistance can arise as a result of the chosen contact radius. The low contact resistances indicate that the majority of the Joule heating occurs in the sheet. Changing the radius has a negligible effect on the obtained TCR.

The semi-analytical model is independently fit to the A and A' configuration from the 10A subprobe and returns a TCR value along with 95% confidence intervals and the standard error. The TCR values from the fits in Figs. 3.11, 3.12 and 3.13 are shown in table 3.1, with additionally the reference TCR values obtained from the PPMS. The results of table 3.1 are additionally plotted in Fig. 3.14, where the M4PP-TCR shown values are the average values of the two configurations. As expected the TCR is dependent of the film thickness d , decreasing as the films get thinner. The increased inhomogeneity of the 10 nm film is clearly represented by the different sheet resistance of the two coupons and is also visible in the obtained TCR from the PPMS. The TCR obtained from the M4PP measurements detects a similar difference in TCR, indicating that the M4PP-TCR method is at least as sensitive as PPMS TCR measurements. There is a small discrepancy ($\sim 4\%$) between the M4PP-TCR obtained from the A and A' configurations. This can mostly likely be attributed to the larger heating volume in the A configurations and the associated thermal delays that are not included the quasi-static semi-analytical

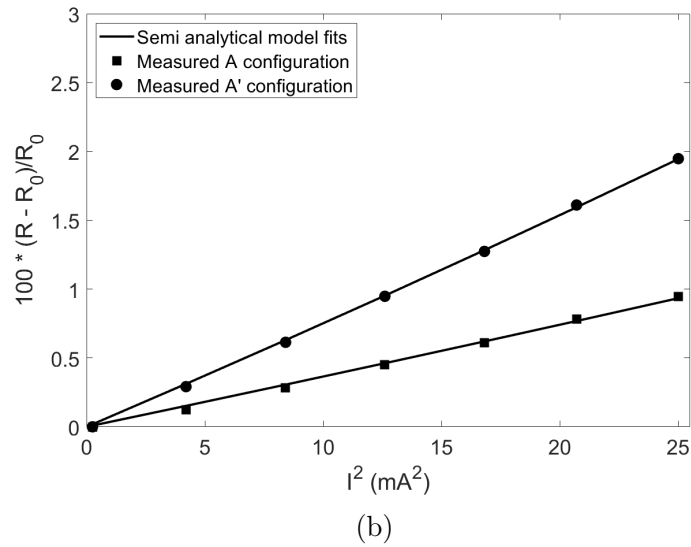
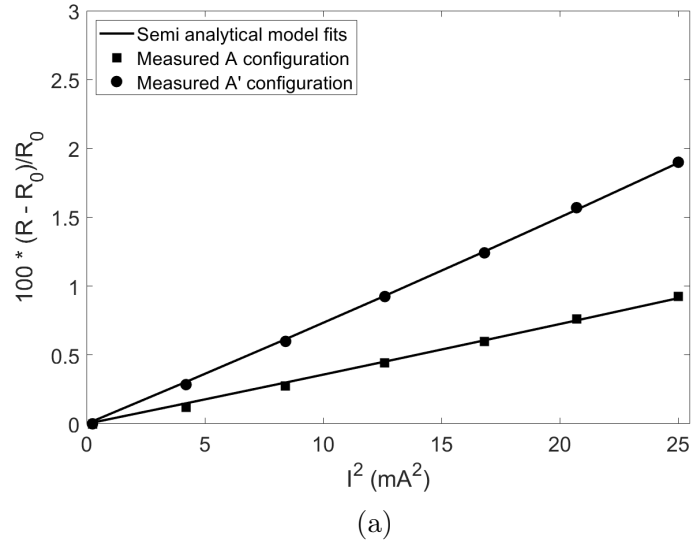


Figure 3.11: The fit of the quasi static semi analytical model to the measured resistance increase on the various platinum thin film samples. The data shown is the mean value of 20 engages, with the errorbar inside the symbols. The A and A' configuration are fit separately. The coupons shown are as follows: (a) Pt-16a, (b) Pt-16c.

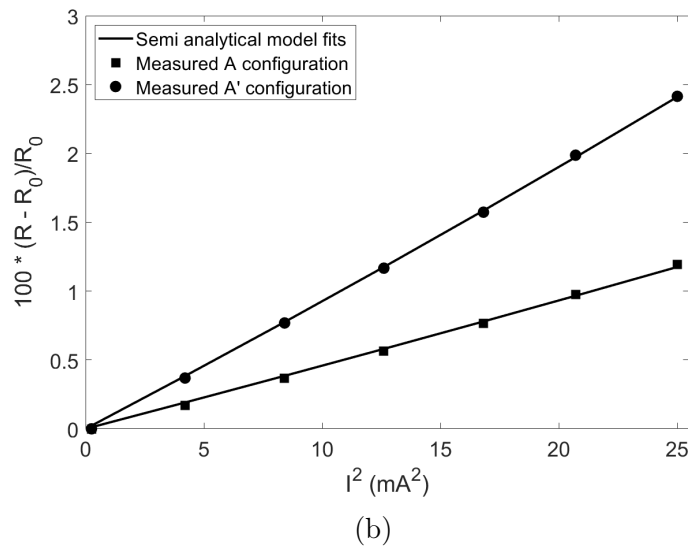
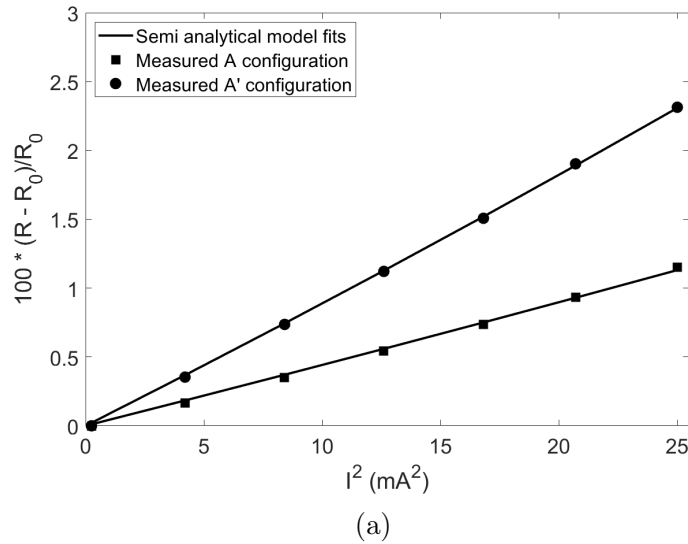


Figure 3.12: The fit of the quasi static semi analytical model to the measured resistance increase on the various platinum thin film samples. The data shown is the mean value of 20 engages, with the errorbar inside the symbols. The A and A' configuration are fit separately. The coupons shown are as follows: (a) Pt-10a, (b) Pt-10b.

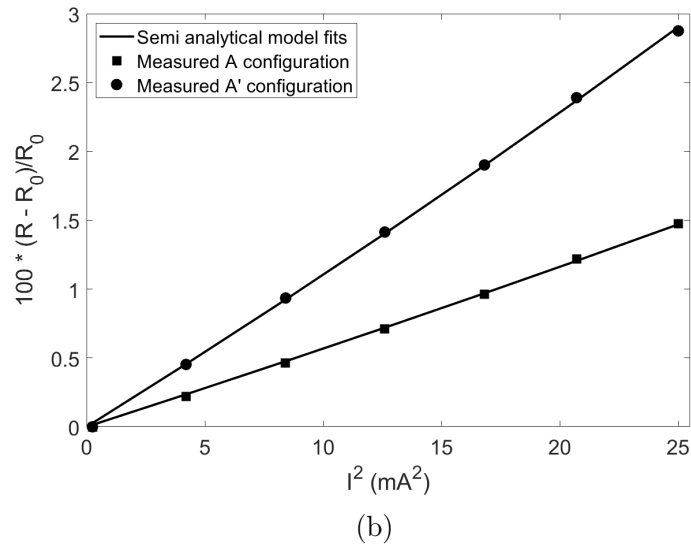
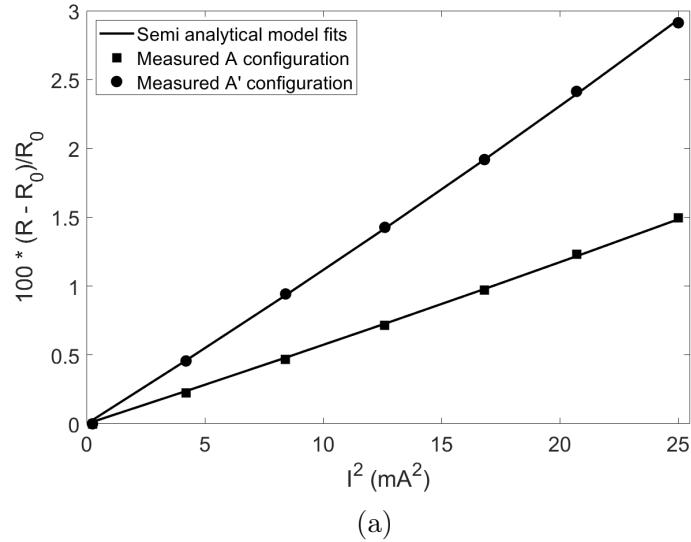


Figure 3.13: *The fit of the quasi static semi analytical model to the measured resistance increase on the various platinum thin film samples. The data shown is the mean value of 20 engages, with the errorbar inside the symbols. The A and A' configuration are fit separately. The coupons shown are as follows: (a) Pt-7b, (b) Pt-7c.*

Film thickness (nm)	coupon ID	Sheet resistance (Ω)	M4PP TCR A (10^{-3} K)	M4PP TCR A' (10^{-3} K)	TCR PPMS (10^{-3} K)
7	Pt-7nm-b	50.59	0.73 ± 0.01	0.76 ± 0.01	0.96 ± 0.05
	Pt-7nm-c	50.40	0.74 ± 0.01	0.74 ± 0.01	0.97 ± 0.05
10	Pt-10nm-a	28.05	1.13 ± 0.02	1.17 ± 0.01	1.38 ± 0.07
	Pt-10nm-b	24.05	1.34 ± 0.02	1.40 ± 0.01	1.60 ± 0.08
16	Pt-16nm-a	14.55	1.59 ± 0.03	1.63 ± 0.01	1.71 ± 0.09
	Pt-16nm-c	14.48	1.58 ± 0.02	1.63 ± 0.01	1.77 ± 0.09

Table 3.1: *The results of the A configuration fit on the 10 μm pitch 10A subprobe. The reported errors are the standard error from the fit.*

model. This has been addressed in the steady state semi-analytical model. The M4PP-TCR values as a whole underestimate the independent reference values by an average of 18%. As M4PP resistance measurements are extremely precise ($< 0.1\%$), the major contribution (since the contact resistances are very small) is likely the negligence of frequency dependent effects in the quasi-static model, where it is assumed that the temperature is affected everywhere instantly, when in reality there is a thermal delay, modifying the actual magnitude of the temperature. The result is that the quasi-static model likely overestimates the temperature, resulting in an underestimation of the TCR. Furthermore, the neglect of heat transport through the platinum film and the electrodes, while not expected to be significant, will also result in an underestimation of the TCR. Despite this underestimation, the two data sets are remarkably correlated, showcased by a Pearson's correlation coefficient of 0.99.

The precision of the M4PP-TCR method is excellent ($< 2\%$), with the method being able to clearly identify the different film thicknesses (Fig. 3.14). This high precision indicates that the method is suitable to be employed as a relative comparison method between films of different thicknesses. Other than the A configurations shown, the TCR has also been extracted from the B and C configurations as well as on the two other equidistant subprobes available on the L7PP. The results of the specific configurations are shown in detail in appendix B.

In addition to the platinum samples, the M4PP-TCR was initially tested on several ruthenium thin film samples. The samples differed in structure from the platinum samples as the ruthenium was deposited on a 90 nm thick SiO_2 barrier layer on a silicon substrate. The TCR extraction was unsuccessful, mostly

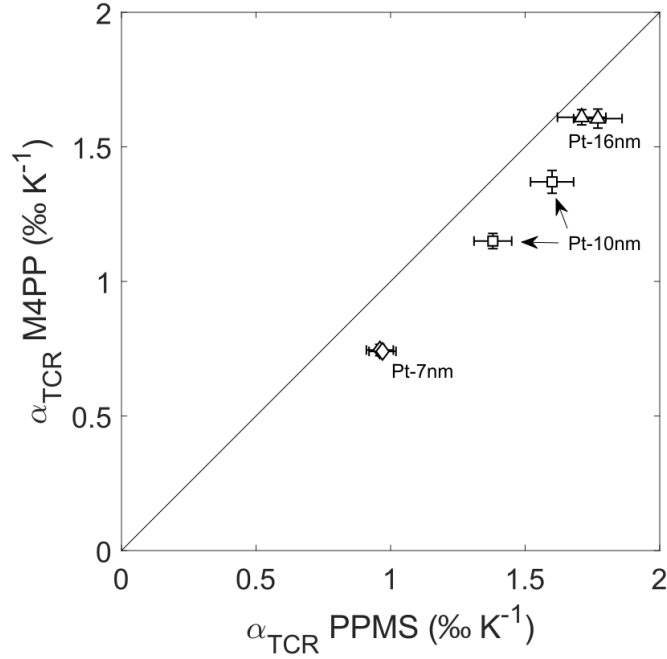


Figure 3.14: A comparison of the extracted TCR from the M4PP-TCR and the reference measurements taken on the PPMS of the six investigated coupons. The M4PP value was obtained from both the A and A' measurements.

attributed to the significant difference in the assumed thermal system (i.e. the substrate is wholly responsible for the heat conduction away from the film) and the suspected real thermal transport. An overview of the measurement results is given in Appendix A.

3.4.2 TCR from steady state analysis

In response to the observed discrepancies observed in the quasi-static analysis between the extracted TCR from the M4PP measurements and the reference TCR values obtained from the PPMS (Fig. 3.2 and table 3.1), the steady state semi-analytical model was developed to account for the effects of thermal delays in the system, which was postulated to be the main reason of the inaccuracy of the extracted TCR values in the measured platinum thin film samples. The model was not finalised within the project's time frame, with the inaccuracies remaining unsolved, however the following experiment did demonstrate the removal of the

dependence on the selected probe pitch and current frequency on the extracted TCR value.

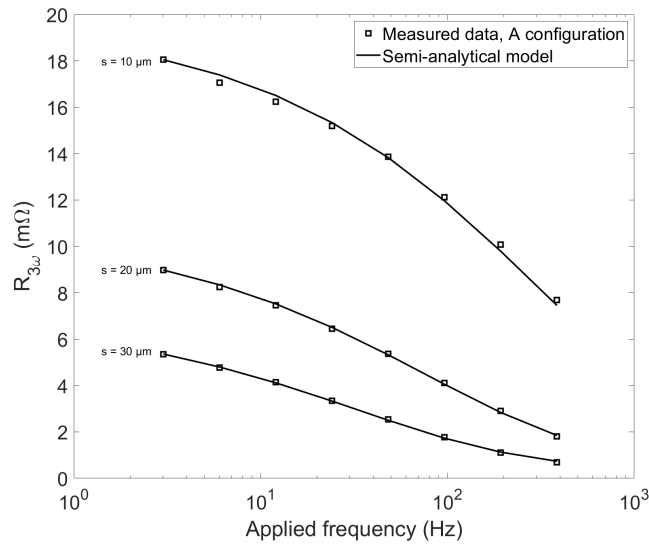
The steady state experiments were again performed on the MicroRsP A300 system from CAPRES. The probe used was the L10PP, carrying a total of 10 electrodes equidistantly spaced by $10\ \mu\text{m}$. The probe is capable of creating three equidistant sub-probes with a pitch of $10\ \mu\text{m}$, $20\ \mu\text{m}$ and $30\ \mu\text{m}$. The measurement was done on part of the same $16\ \text{nm}$ platinum thin film wafer used in the quasi-static measurements. An AC current with $I_{RMS} = 5\ \text{mA}$ is delivered to the sample. The 'zero current' resistances (e.g. R_0 and $R_{S,0}$) were obtained from the 3ω correction [88]. The frequency is varied from the lowest frequency ($f \approx 3.01\ \text{Hz}$) through all selectable frequencies ($f = 3.0137 \times 2^n$ with $n \in [0, 1, 2, \dots]$) up to $f = 3.0137 \times 2^7 \approx 385.75\ \text{Hz}$. The measurement follows an identical configuration sequence as used in the quasi-static experiment ($[A_1, A'_1, A_2, A'_2, B_1, B'_1, \text{etc.}]$) assigned to each sub-probe, starting with the $10\ \mu\text{m}$ pitch sub-probe, followed by the $20\ \mu\text{m}$ pitch and $30\ \mu\text{m}$ pitch sub-probes. This results in 36 configurations per frequency step. At the very start of each engage, one frequency step is measured but ignored in the analysis, acting as a 'burn in' measurement, since it was observed this improved the precision of the resistance measurement of the first analysed frequency step. Two measurements of 30 engages each were performed, where each engage was laterally spaced apart by $20\ \mu\text{m}$. Before and after each measurement a series of characterisation measurements on a thick nickel slab ($R_S = 0.48\ \Omega$) were performed to extract the lead resistances and calculate the contact resistance as shown in section 3.3.2. In order to reduce transient effects, a waiting period was introduced, where the current was supplied for several periods before the resistance measurement took place. The TCR is extracted using the measured third harmonic signal $R_{3\omega}$ and the calculation of the voltage trace combined with a digital lock-in amplifier (Eq. 3.48).

The measured $R_{3\omega}$ of the A configurations of an engage are plotted in Fig 3.15 as the symbols. As expected from the steady state model and finite element simulations (Fig. 3.8), $R_{3\omega}$ decreases with increasing frequency and pitch. Based on the magnitude of the $R_{3\omega}$ at the lowest applied frequency ($f = 3.0137\ \text{Hz}$) and pitch ($10\ \mu\text{m}$), the expected decline in $R_{3\omega}$ can be calculated using the steady state semi-analytical model and is represented in Fig. 3.15 as the solid lines. The measured data follows the predicted decline in magnitude extremely well, both across the frequency range as for the different pitches. Figures 3.15 and 3.8 highlight the improvement in M4PP-TCR measurements when using the steady state model, as the dependence of the TCR response to the applied frequency and used pitch is correctly mimicked. This leads to much more accurate characterisation of TCR, as well as opens up the M4PP-TCR method to more flexibility. For example, since

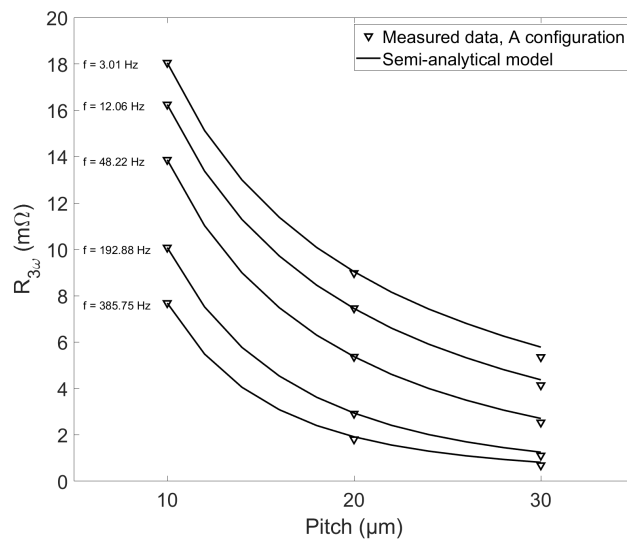
high frequency measurements are significantly faster, high resolution wafer mapping of TCR becomes a possibility, whereas removing the probe pitch dependence will enable TCR characterisation at various length scales.

Both the quasi-static and the steady state model were used to extract the TCR across a variety of applied frequencies and pitches. The result is shown in Fig.3.16, which illustrates the improvement of the steady state model well. The TCR extracted from the quasi-static model decreases sharply with increasing frequency, with values obtained at the highest applied frequency 55% to 73% lower than at the lowest frequency. Similarly, the TCR obtained from 10 μm pitch sub-probe is 16% lower than the 10 μm pitch sub-probe at $f \approx 3.01$ Hz. This difference increases to $> 50\%$ at higher frequencies ($f > 48.2$ Hz). The TCR obtained by the 10 μm pitch sub-probe at $f \approx 12.055$ Hz (identical settings to the quasi static experiment) via the quasi-static method is $\sim 10\%$ lower than the apparent value obtained using the steady state model. While it doesn't fully cover the $\sim 18\%$ offset to the reference values observed in the previous experiment, the results in Fig. 3.16 bring us one step closer to accurate TCR characterisation using M4PP measurements. At high frequencies (> 100 Hz) the extracted TCR values start to drift, initially in the larger probes. As this is not reflected in the quasi-static results this must arise from either the steady state model or the measured $R_{3\omega}$. Currently this behaviour is not fully understood.

Unfortunately the TCR value obtained from the steady state analysis, as well as from the low frequency quasi-static analysis, ($\sim 1.3 \times 10^{-3} \text{ K}^{-1}$) in this experiment is significantly lower than what was observed in the earlier experiment ($\sim 1.6 \times 10^{-3} \text{ K}^{-1}$) and even further removed from the reference values obtained from the PPMS ($\sim 1.7 \times 10^{-3} \text{ K}^{-1}$). A possible cause is a change in film properties, as the measurements were taken 18 months apart. However this appears unlikely, as not only is platinum very stable at room temperature [120], the sheet resistances measured in both experiments are very similar, indicating the films' composition has remained unchanged. It is important to be reminded that the obtained TCR value is intimately connected to the assumed thermal conductivity of the system, and any change here would affect the extracted TCR value. However there is nothing that suggests that this has changed. The main difference between the two experiments are much higher contact resistance ($\sim 15 \Omega$ compared to $\sim 1 \Omega$) which will correspond to a significantly higher power deposited into the sample. In the measurements, the contact force was not tracked (how hard the electrode is pressed against the surface). It is not inconceivable that the reason for the different contact resistances is a significantly different contact force. A much higher increase of the third harmonic load resistance (the in-series resistance of the leads, contacts and sample) is observed, which indicates significantly more power



(a)



(b)

Figure 3.15: (a) The measured $R_{3\omega}$ from a measurement on a 16 nm platinum thin film with three differently sized probe sizes. The steady state semi-analytical model is used to predict the decrease in $R_{3\omega}$ with increasing applied frequency based on the magnitude of $R_{3\omega}$ at $f = 3.01 \text{ Hz}$. (b) The measured $R_{3\omega}$ from a measurement on a 16 nm platinum thin film with three differently sized probe sizes. The steady state semi-analytical model is used to predict the decrease in $R_{3\omega}$ with increasing probe pitch based on the magnitude of $R_{3\omega}$ at $s = 10 \mu\text{m}$ at various selected frequencies.

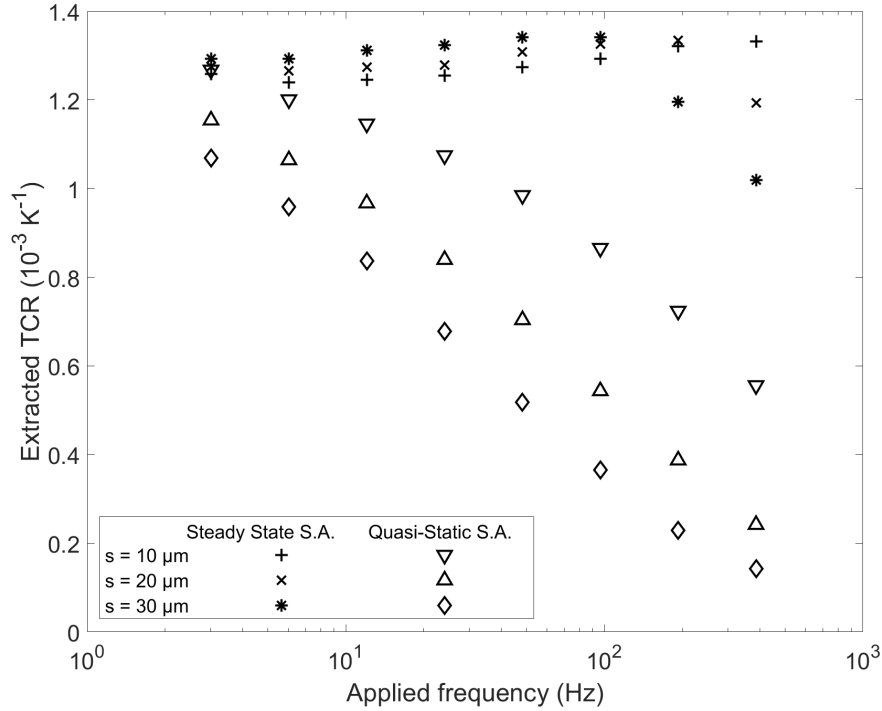


Figure 3.16: *The TCR extracted from M4PP measurements on a 16 nm platinum thin film on three differently sized subprobes. The TCR extracted using quasi-static model shows a clear dependence on the applied frequency and the probe pitch (s). The steady state model removes these dependencies and obtains a stable TCR through the applied frequencies and pitches, save for deviations at the higher frequencies.*

is indeed deposited into the sample (higher sheet and contact heating) compared to the previous measurements. It is possible that the temperature dependence of the contact resistances needs to be included, as alluded to in section 3.3.5. The current implementation possibly overestimates the contact resistances, which will lead to an overestimation of the temperature and an underestimation of the TCR. Furthermore, it is likely the cold finger effect is playing a role here as the contact resistances are significant (comparable to the sample resistance). Heat dissipating away via the electrodes results in lower contact heating than calculated, which again will lead to an underestimation of the TCR.

Despite the success of the steady state model to eliminate the dependencies on applied frequency and probe pitch, the model needs some refinement to pinpoint the reasons for the observed mismatch in extracted TCR values. A first step would

be a measurement at different contact forces, to investigate whether the extracted TCR is dependent on the varying contact resistances. If so, the thermal model must be extended to include the cold finger effect and possibly multi-layer heat transport.

This chapter has showcased the M4PP-TCR method, capable of obtaining precise ($< 2\%$) measurements of ultra thin platinum films. Two approaches were taken, with the initial model developed assuming a quasi-static regime, where thermal delays were not considered. Later, the model was extended by considering the time dependent Joule heating power deposited into the sample which removed the dependence of the extracted TCR on the applied frequency of the current and the size of the measurement probe. The very high correlation with the independent reference values from the PPMS shows great promise, showing the method is at least as sensitive as PPMS. The offset in absolute TCR values compared to the PPMS is an obstacle however, especially since the steady state model has not been able to address it. It underlines the main limitation of the method, i.e. the need for quite significant assumptions on the electrical and thermal transport through the film and substrate.

The M4PP-TCR method has however shown its strengths through an incredibly fast measurement time; a single engage takes less than a minute, which can be shortened through optimisation of the measurement scheme. The versatility of the M4PP instrument means that large areas on the platinum thin films can be characterised with no sample preparation requirements. While the method will likely not be able to compete with the very high precision obtainable from measurements in high quality temperature controlled chambers, the M4PP-TCR method has the potential to become a standard in areas where speed and versatility are valuable, such as in a process monitoring role or as a primary diagnostic tool.

Chapter 4

Errors in M4PP-TCR measurements

Due to application at the micro scale M4PP measurements are sensitive to any positional errors of the electrodes. These errors can be caused by e.g. external vibrations, landing on samples with a rough or slanted surface or movement induced by the thermal expansion of the electrodes. As an example, the measured transfer resistance (four-point resistance) is dependent on the locations of the four electrodes as discussed in section 2.4. For convenience, the relevant result is shown again:

$$R = \frac{R_S}{F}, \quad F = \frac{2\pi}{\ln\left(\frac{|\mathbf{r}_+ - \mathbf{r}_{V-}| |\mathbf{r}_- - \mathbf{r}_{V+}|}{|\mathbf{r}_+ - \mathbf{r}_{V+}| |\mathbf{r}_- - \mathbf{r}_{V-}|}\right)}$$

where F is known as the geometrical correction factor. If the electrodes deviate from their nominal positions (\mathbf{r}_+ , \mathbf{r}_- , \mathbf{r}_{V+} and \mathbf{r}_{V-}), the sheet resistance measurement R_S will be imprecise. Consequently, the M4PP-TCR method will be similarly affected by position errors. Deviations from nominal positions will lead to inconsistencies in the calculated sheet power density (Eq. 3.6), M4PP sensitivity (Eq. 2.34) and the temperature (Eq. 3.23 and Eq. 3.39).

Position errors on co-linear four-point probes can typically be divided into three categories. The electrodes can deviate from their nominal positions as in-line and off-line errors. Previous work has shown that the in-line position errors dominate over off-line errors (when the size of the error is small compared to the electrode pitch) [122]. In addition, the errors can be classified as static or dynamic. Static position errors occur throughout the engage and are typically caused by e.g. landing on a rough surface, whereas dynamic position errors occur during an engage, e.g. as a result of external vibrations.

It is vital to understand the sensitivity of the M4PP-TCR method to position errors to fully maximise the method precision [122] [123]. Static position errors can be corrected by implementation of position correction schemes [124] [125]. Dynamic position errors are primarily limited by minimising the time spent measuring. In addition, electrical noise will have an impact in the ideal precision achievable. As the M4PP-TCR method benefits from measurements at the highest possible current and smallest available pitch (to maximise the TCR response), the effects of electrical noise are rarely expected to dominate over position errors on the measured platinum samples. However, measurements where a low TCR response is expected, such as low TCR materials, measurements using large probe pitches or at low currents, the electrical noise might become a limiting factor in the precision of the method. In more challenging samples, a balance might need to be considered, where increasing the probe pitch will lower the sensitivity to position errors, but increases the sensitivity to electrical noise.

4.1 Position errors

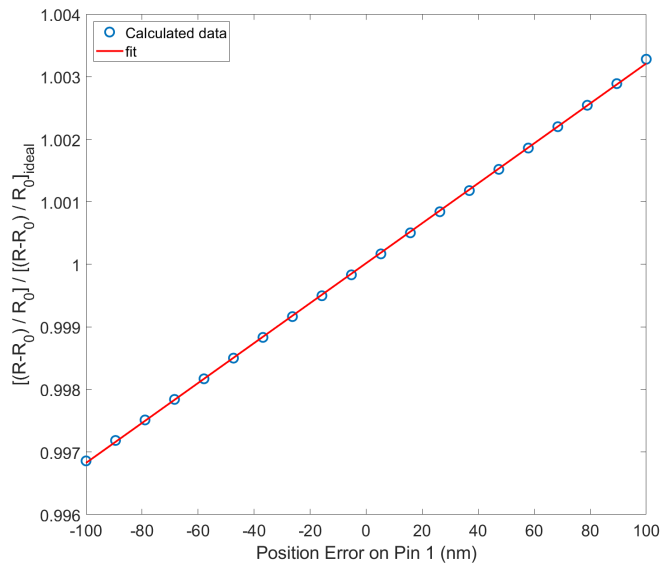
The relative standard deviation due to (in-line) position errors in M4PP-TCR measurement can be given by [126]:

$$\sigma^{rel} = \frac{1}{\left(\frac{R-R_0}{R_0}\right)_{ideal}} \sqrt{\sum_{N=1}^4 \left(\frac{\partial\left(\frac{R-R_0}{R_0}\right)}{\partial X_N}\right)^2 \sigma_{X_N}^2} \quad (4.1)$$

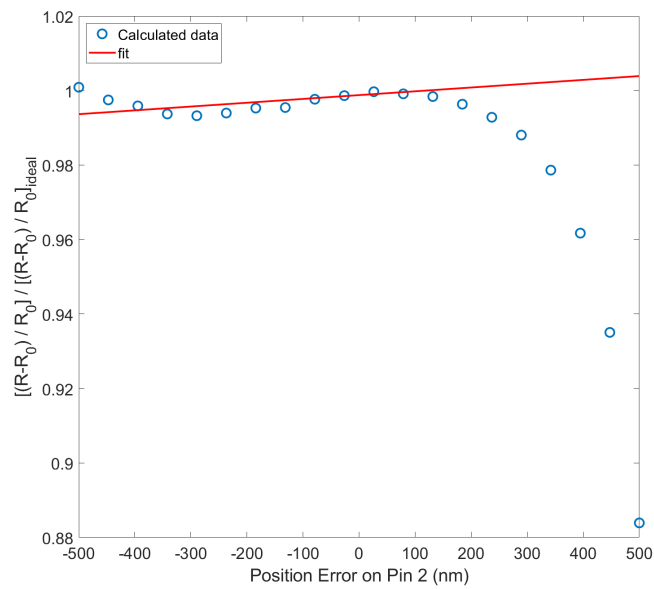
where $\left(\frac{R-R_0}{R_0}\right)_{ideal}$ is the resistance increase with the electrodes in their nominal positions, $\frac{R-R_0}{R_0}$ is the measured resistance increase and $\sigma_{X_N}^2$ is the variance in the electrode position.

The derivative $\left(\frac{\partial\left(\frac{R-R_0}{R_0}\right)}{\partial X_N}\right)$ can be evaluated using the semi-analytical approaches derived in chapter 3. The increase in resistance can be calculated for several electrode positions to obtain a fit of $\left(\frac{\partial\left(\frac{R-R_0}{R_0}\right)}{\partial X_N}\right)$, such as in Fig. 4.1. Repeated for the four electrodes, the relative standard deviation can be calculated for a given configuration and position error variance.

In some cases, the response is non-linear as shown in Fig. 4.1b. From observation, this occurred especially in non-equidistant configurations. The response in equidistant configurations was always linear within the maximum tested range



(a)



(b)

Figure 4.1: (a) The change in $\Delta R/R_0$ when the position of electrode 1 is changed from its nominal position in the A configuration on an equidistance four-point probe. (b) An example of a non-linear response. Taken from the B configuration of the L8PP probe. For small position errors the fit may still approximate well.

(± 500 nm). A good approximation can still be obtained from the non-linear response as smaller position errors as demonstrated in Fig. 4.1b. Alternatively, the relative standard deviation can be obtained from a Monte Carlo experiment, where $\left(\frac{R-R_0}{R_0}\right)$ is calculated when applying random position errors to the four electrodes over a large number of repetitions. The non-linearities will be easily incorporated but it is significantly more time consuming and as most scenarios discussed in this section consider large equidistant probes, the above presented method is deemed sufficient.

Using Eq. 4.1 and the quasi-static model (Eq. 3.16), the resulting relative standard deviation due to in-line position errors on a standard equidistant four-point probe with a pitch of $10\ \mu\text{m}$ is determined. The measurement represents the Pt/SiO₂ thin film measurements with $R_S = 14.5\ \Omega$, $\alpha_{\text{TCR}} = 0.002\ \text{K}^{-1}$, $I_{\text{RMS}} = 5\ \text{mA}$ and $\kappa = 1.4\ \text{W m}^{-1}\ \text{K}$. The contact resistances are set to zero (mimicking a measurement dominated by Joule heating in the sheet). Two scenarios are considered, one with a 5% position error deviation ($\sigma_{X_N} = 500\ \text{nm}$), and one with a 1% error ($\sigma_{X_N} = 100\ \text{nm}$). The results are shown in table 4.1. The A, A', B and C configurations are considered as unlike the A configurations, the B (C) and B' (C') are symmetric in both the electrical and thermal systems and would give in an identical result.

Position error	error / pitch	A	A'	B	C
500 nm	5%	2.4 %	4.0 %	2.0 %	3.4 %
100 nm	1%	0.5 %	0.8 %	0.4 %	0.7 %

Table 4.1: *The obtained relative standard deviations resulting from position errors on a $10\ \mu\text{m}$ pitch probe during a M4PP-TCR measurement on a metallic thin film with $R_S = 14.5\ \Omega$, $\alpha_{\text{TCR}} = 0.002\ \text{K}^{-1}$, $I_{\text{RMS}} = 5\ \text{mA}$ and $\kappa = 1.4\ \text{W m}^{-1}\ \text{K}$*

The results in table 4.1 show that the A' configuration is the most sensitive to position errors. Furthermore, the errors obtained for the 5% error case are roughly 5 times larger than if 1% errors are considered, suggesting a linear relationship of the relative standard deviation with the error to pitch ratio. As expected, the position errors will become more relevant for smaller probes, as visualised in Fig. 4.2. Here, the above experiment was repeated for $\sigma_{X_N} = 50\ \text{nm}$ with an equidistant probe in the A configuration with a probe pitches ranging from $1\ \mu\text{m}$ to $50\ \mu\text{m}$.

Figure 4.2 shows the linear relationship of the induced relative standard deviation and the ratio of the error to the probe pitch. When considering position errors with $\sigma_{X_N} = 50\ \text{nm}$ the commonly used probe sizes ($30\ \mu\text{m}$, $20\ \mu\text{m}$, $10\ \mu\text{m}$ and $8\ \mu\text{m}$) experience related errors of less than 1% (on a measurement with $R_S = 14.5\ \Omega$,

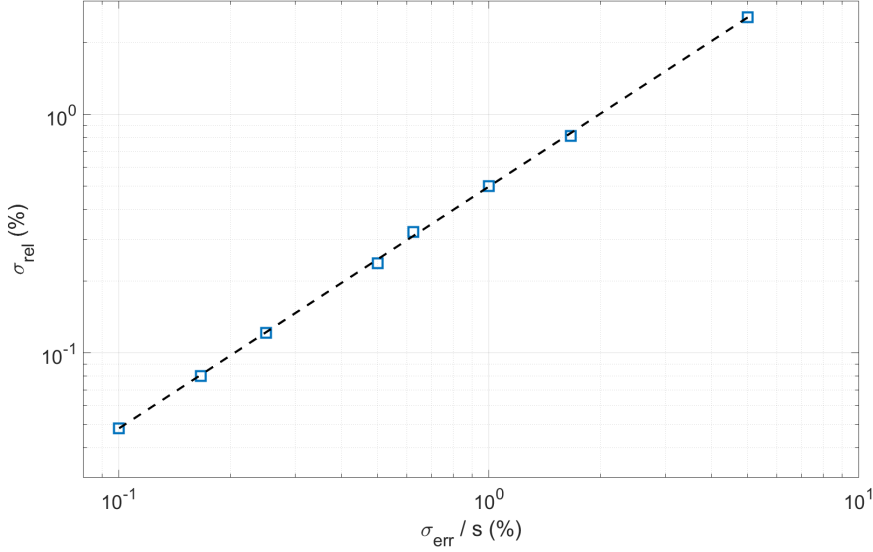


Figure 4.2: The resulting relative standard deviation (σ_{rel}) in $\Delta R/R_0$ signal used to extract the TCR as a result of position errors. As the error in position ($\sigma_{err} = 50$ nm) increases comparable to the pitch of the probe (s), σ_{rel} increases in significance. The results shown are for an equidistant probe with $s = 10$ μm in the A configuration and $I_{RMS} = 5$ mA on a sample with $R_S = 14.5$ Ω , $\alpha_{TCR} = 0.002$ K^{-1} and no contact resistances.

$\alpha_{TCR} = 0.002$ K^{-1} , $I_{RMS} = 5$ mA and $\kappa = 1.4$ $\text{W m}^{-1} \text{K}$). Common position errors on flat conductive films are the same order of magnitude [126] [127] and the observed relative standard deviations are likewise similar [128] [129]. Therefore the careful conclusion can be made that position errors are not a limiting factor in the M4PP-TCR measurements on the platinum films. Identical simulations with $\alpha_{TCR} = 0.0005$ K^{-1} returned very similar results, as did a third set of simulations with $I_{RMS} = 1$ mA, suggesting the determining factor in the effect of position errors is the probe size.

In addition to the probe size, the position error sensitivity is also appears dependent on the distribution of the Joule heating power. In samples where the contact heating dominates, an error in the electrode position will also significantly alter the temperature field and sensitivity function. The experiment in table 4.1 is repeated for different power distributions. The results are visualised in Fig. 4.3 which shows the relative error in $\left(\frac{R-R_0}{R_0}\right)$ of the different configurations as the deposition of power is shifted from the left contact (the I_+ contact) to the sheet while the total Joule heating power is kept the same. Figure 4.3 highlights that

the B configuration is very dependent on where the power is deposited however a useful observation is that if the power gets imbalanced, the position errors become more significant in all configurations.

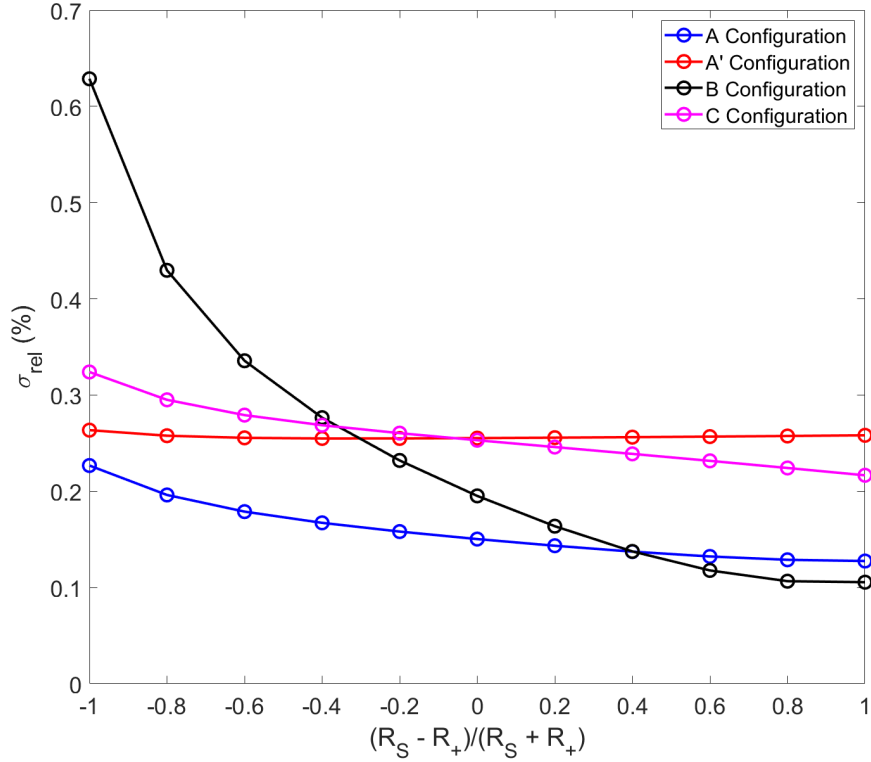


Figure 4.3: *The evolution of the relative standard deviation in the increase in resistance as the Joule heating power is distributed from the left (I_+) contact to the sheet.*

The scenarios considered above were applied to two additional probe types. Firstly, the so called L8PP is considered, which has a total of eight L-shaped electrodes. The L8PP is capable of creating several non-equidistant sub-probes, however here solely the near-equidistant subprobe is considered. Secondly a subprobe of the Y10PP, a ten-point probe, with a small electrode pitch ($1\ \mu\text{m}$) is investigated. The subprobe electrode positions are shown in Fig.4.4. The different probe types (near-equidistant and small) should give an idea of how the variable the observed position errors are. For each probe, the obtained relative standard deviation for the four configurations is given for four scenario's, each with a different power distribution in the sample. The results are shown in table 4.2, table 4.3 and table 4.4.

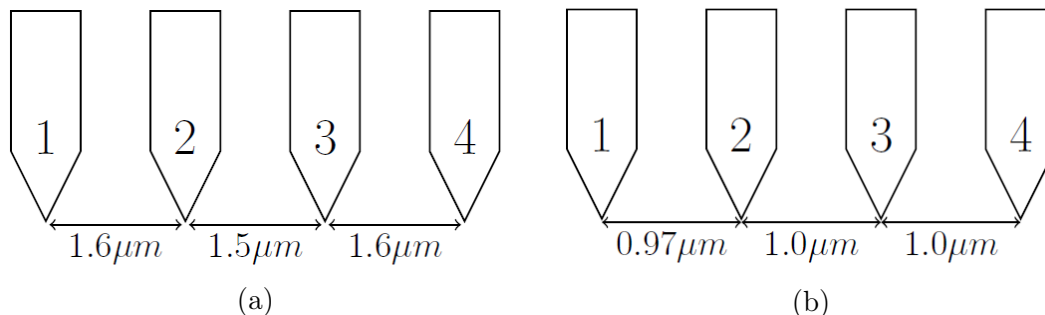


Figure 4.4: (a) The electrode spacing for the L8PP subprobe. (b) The electrode position for the Y10PP subprobe

As the same position error is used (100 nm) it is no surprise the errors are more severe for the Y10PP probe (table 4.4), as the error to pitch ratio here is 10%. The observed errors for this probe are roughly 10 times larger than the $10\mu\text{m}$ pitch L4PP probe (table 4.2), in line with Fig. 4.2 considering the simulated Y10PP subprobe is for all intents and purposes an equidistant probe. The L8PP subprobe (table 4.3) similarly returns large errors. The ever so slight deviation from equidistant positions does not appear to enhance the susceptibility to position errors in most scenarios.

These results, alongside Fig. 4.2, underline the conclusion that position errors will be able to affect the precision of M4PP-TCR measurement using small probes. To maintain acceptable precision ($< 2\%$) the ratio of the position error and probe pitch must be at most 1 – 2%. Measurements with higher ratios will need to implement a position correction scheme in the analysis process.

The M4PP-TCR method prefers measurements at the highest achievable currents, as this maximises Joule heating in the samples and subsequently maximises the TCR response. Measuring at different currents does not directly affect the relative standard deviations due to position errors. However, high currents might increase the chance and severity (magnitude of σ_{X_n}) of position errors to occur via thermally induced movement, resulting from Joule heating in the electrodes.

A more comprehensive look is required to fully understand the effect of position errors on M4PP-TCR measurements. In order to deal with the non-linear responses observed particularly for non-equidistant probes, a Monte Carlo experiment will be beneficial.

Power location	Configuration			
	A	A'	B	C
$R_s = 20 \Omega$ $R_+ = 0 \Omega$ $R_- = 0 \Omega$	0.5%	0.8%	0.4%	0.7%
$R_s = 0 \Omega$ $R_+ = 10 \Omega$ $R_- = 10 \Omega$	0.6%	1.0%	0.4%	0.9%
$R_s = 0 \Omega$ $R_+ = 20 \Omega$ $R_- = 0 \Omega$	1.0%	1.1%	2.6%	1.3%
$R_s = 0 \Omega$ $R_+ = 0 \Omega$ $R_- = 20 \Omega$	1.0%	1.1%	0.9%	0.7%

Table 4.2: *The relative standard deviation in the increase in measured resistance from $\sigma_{X_N} = 100 \text{ nm}$ on a $10 \mu\text{m}$ pitch L4PP probe*

Power location	Configuration			
	A	A'	B	C
$R_s = 20 \Omega$ $R_+ = 0 \Omega$ $R_- = 0 \Omega$	2.9%	4.4%	3.0%	3.3%
$R_s = 0 \Omega$ $R_+ = 10 \Omega$ $R_- = 10 \Omega$	3.7%	6.4%	2.9%	5.1%
$R_s = 0 \Omega$ $R_+ = 20 \Omega$ $R_- = 0 \Omega$	6.8%	6.7%	20.2%	7.8%
$R_s = 0 \Omega$ $R_+ = 0 \Omega$ $R_- = 20 \Omega$	6.9%	6.5%	5.3%	3.8%

Table 4.3: *The relative standard deviation in the increase in measured resistance from $\sigma_{X_N} = 100 \text{ nm}$ on a L8PP probe*

Power location	Configuration			
	A	A'	B	C
$R_s = 20 \Omega$ $R_+ = 0 \Omega$ $R_- = 0 \Omega$	4.6%	5.2%	5.0%	4.3%
$R_s = 0 \Omega$ $R_+ = 10 \Omega$ $R_- = 10 \Omega$	6.1%	8.9%	4.7%	7.9%
$R_s = 0 \Omega$ $R_+ = 20 \Omega$ $R_- = 0 \Omega$	11.3%	9.1%	25.1%	12.2%
$R_s = 0 \Omega$ $R_+ = 0 \Omega$ $R_- = 20 \Omega$	10.9%	9.3%	7.1%	5.6%

Table 4.4: *The relative standard deviation in the increase in measured resistance from $\sigma_{X_N} = 100 \text{ nm}$ on a Y10PP probe*

4.2 Electrical errors

Electrical noise is the sum of unwanted contributions to the electrical signal. Some contributions are unavoidable, such thermal noise (Johnson-Nyquist noise) [130] [131], which is generated by the thermal movement of the charge carriers. Other contributions are a result of the particular electronic circuit, where, for example, conductive wires placed close together could exhibit capacitive coupling. It is imperative that the signal to noise ratio is high enough to distinguish the TCR response. The M4PP-TCR measurements benefit from being measured at the highest possible current, as this maximises the TCR response. Therefore, as long as the circuit dependent noise is minimised, the electrical noise is likely not a defining factor in the precision of the M4PP-TCR method on metallic thin films. This is corroborated by the typical M4PP noise being of the order of tens of nanovolts [129]. However, if the method is to be applied on materials with e.g. a low TCR value, the TCR response may be sufficiently small to be impacted by electrical noise.

The effect of electrical noise on the obtained TCR can be investigated via a Monte Carlo simulation of the induced $\left(\frac{R-R_0}{R_0}\right)$ or $R_{3\omega}$. The induced voltage of a M4PP-TCR measurement can be calculated via Eq. 3.10, which for convenience is repeated:

$$V(t) = I_0 \sin(\omega t) R_0 \left[1 + \alpha_{\text{TCR}} \int_{\Omega} \Delta T(\mathbf{r}, t) \hat{S}(\mathbf{r}) d\Omega \right]$$

where $\omega = 2\pi f$ with f being the frequency of the applied current. A period is divided into 64 time steps where for each time step the induced voltage is calculated using the equation above. The temperature $\Delta T(\mathbf{r}, t)$ can either be calculated using the quasi-static model (Eq. 3.23) (using $I = I_0 \sin(\omega t)$) or the steady state model (Eq. 3.39). At each time step, random Gaussian noise with σ_{noise} is added to the obtained voltage. An example is shown in Fig. 4.5. The final trace can be fed into a digital lock-in amplifier to obtain, among others, the induced $R_{3\omega}$, which can be equated to the TCR response. This process can be repeated for N repetitions, to then approximate the subsequent standard deviation in $R_{3\omega}$ resulting from the electrical noise.

The relative standard deviation on the third harmonic $R_{3\omega}$ has been obtained from a Monte Carlo simulation of a M4PP measurement on a metal thin film with $R_s = 14.5 \Omega$, $\alpha_{\text{TCR}} = 0.002 \text{ K}^{-1}$, $I_{\text{RMS}} = 5 \text{ mA}$ and $f \approx 12.055 \text{ Hz}$ to mimic the M4PP-TCR measurements using a $10 \mu\text{m}$ pitch probe on the platinum thin films. The quasi-static model was used to calculate the temperature. The standard

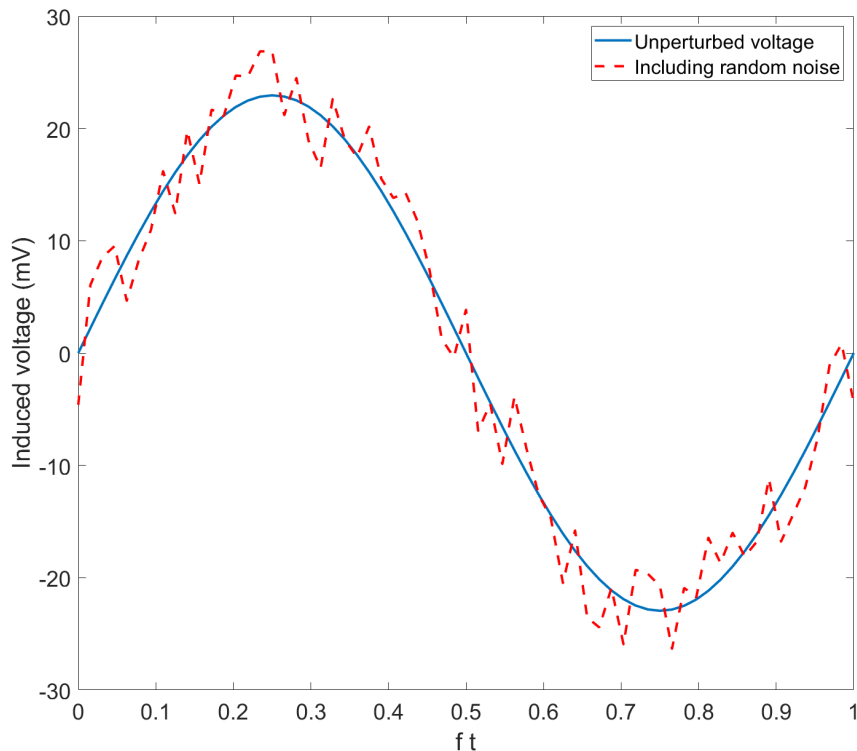


Figure 4.5: *An example of the effect of noise on the measured voltage trace of a M4PP measurement in the A configuration on a film with with a $R_s = 14.5 \Omega$, $\alpha_{TCR} = 0.002 \text{ K}^{-1}$, $I_{RMS} = 5 \text{ mA}$ and $f \approx 12.055 \text{ Hz}$. For the purpose of this figure the effect is highly exaggerated with random noise with a standard deviation of 3 mV is applied*

deviation of the electrical noise was varied from 10 nV to $10 \mu\text{V}$, where at each step 200 repetitions were performed. The results are shown in Fig. 4.6.

Figure 4.6 shows that the effect of electrical noise is negligible if below 500 nV , an order of magnitude higher than the typically reported electrical noise level in previous M4PP measurements [129]. It can therefore be confidently stated that the electrical noise is not a limiting factor in the precision of the platinum thin film measurements. Measurements on lower TCR materials or those deposited on substrates with higher thermal conductivity will exhibit a lower TCR response and therefore will be more susceptible to electrical noise. An identical experiment with $\alpha_{TCR} = 0.0005 \text{ K}^{-1}$ (4 times lower) resulted in standard deviations of roughly 4 times larger, suggesting a linear response to the ratio of the electrical noise to

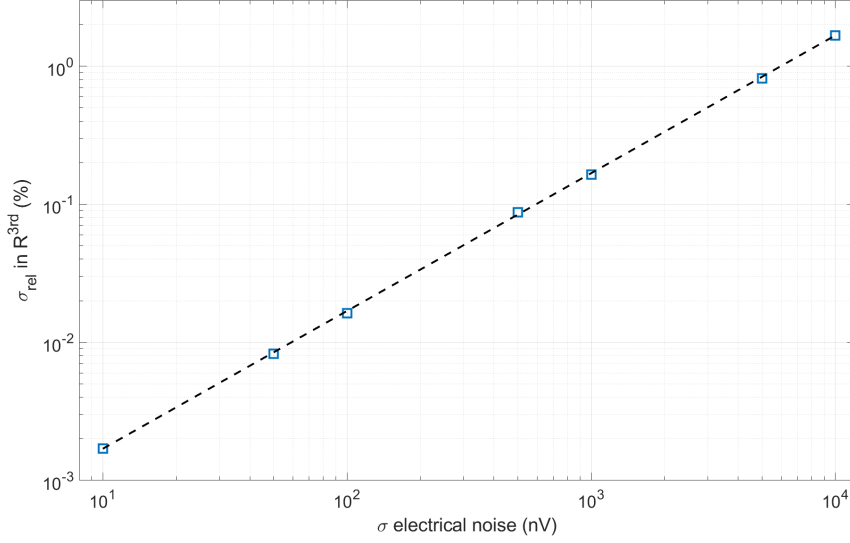


Figure 4.6: *The resulting relative standard deviation on $R_{3\omega}$ as a result of random electrical noise in the measured voltage, obtained from a Monte Carlo experiment with 200 repetitions. The experiment considered a measurement on a typical metallic thin film with $I_{RMS} = 5$ mA and $\alpha_{TCR} = 0.002$ K $^{-1}$.*

the voltage amplitude, however more experiments are required to confirm this. Similarly, an experiment with $I_{RMS} = \frac{5}{4}$ mA and $\alpha_{TCR} = 0.002$ K $^{-1}$ has significant effects on the precision of R^{3rd} with 500 nV of electrical noise inducing a $\sigma_{rel} \sim 6\%$. This result accentuates the need to measure at the highest possible current for successful M4PP-TCR measurements.

It must be noted that the errors obtained from the first harmonic results are a factor 1000 smaller. However, TCR extraction using the first harmonic requires R_0 , which is either obtained from a low current measurement (high noise) or the 3ω correction (limited by R^{3rd} noise). The magnitude of the noise experienced during an M4PP measurement will require a complete evaluation of potential noise sources in the electronic circuit of the A300 tool, such as any capacitive or inductive coupling, transient effects or harmonic distortion. However, this was not done within the project's time frame.

Chapter 5

The triplet measurement scheme

The M4PP-TCR measurements on the platinum thin film samples described in section 3.4 have so far involved at minimum 20 engages to extract a single TCR value. On the homogeneous platinum samples the variability was minimal and the observed resistance increases were very stable. However, if the method is to be applied on less homogeneous samples, averaging across many engages will lead to a lower than achievable precision and will mask any sample inhomogeneity. Furthermore, measurement variability between engages (e.g. position errors), will inflate the measurement precision. An example is shown in Fig. 5.1, displaying the extracted TCR on the 16 nm platinum thin film (using the quasi-static model) per engage. The offset in engage 18 for example could have been caused by position errors. A smarter measurement procedure could identify and minimise erroneous values caused by e.g. position errors, increasing the maximum achievable precision of the extracted TCR.

The same methodology can be extended to the measurements within an engage. In the measurement displayed in Fig. 5.1 three sub-probes were measured, each with twelve configurations at seven current steps, for a total of 252 configurations. In general, one would want to minimise the time spent measuring, as this increases the chance for variations to occur during the measurement, such as a vibration induced shift in an electrode position (dynamic position errors). This principle has already been applied in M4PP sheet resistance measurements, where precise R_S characterisation is achieved by measuring a total of 8 configurations [132]. This chapter will explore the foundation behind TCR measurements involving the fewest possible individual configuration measurements with a future aim to design an optimised configuration sequence for TCR extraction.

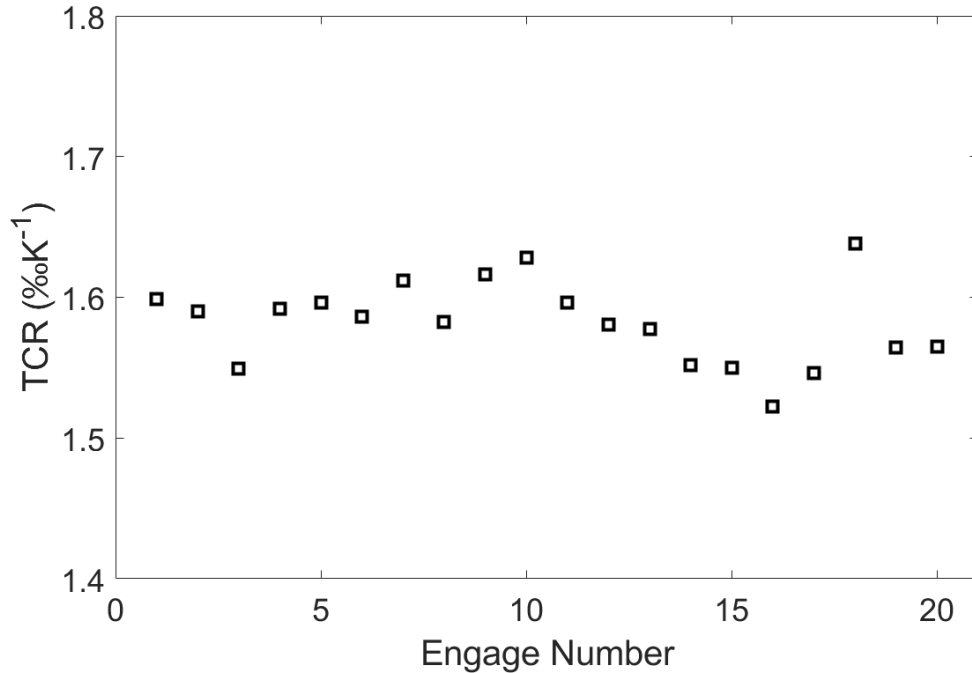


Figure 5.1: *The extracted TCR per engage for an M_4PP -TCR measurement on a 16 nm platinum thin film.*

5.1 A single TCR measurement: a triplet

The fewest configuration measurements needed for a TCR measurement is limited by the calculation of the contact resistances, where a minimum of three configurations are needed to obtain the contact resistance of a group of three electrodes (section 3.3.2). Each electrode in this group must be used as a current carrier twice. In addition, to obtain the sheet resistance (via the dual configuration), measurements are needed of opposite 'groups', e.g. an A and B configuration or a B and C configuration. These constrictions result in four main 'triplets', a group of three configuration measurements from which a TCR value can be extracted, shown in Fig. 5.2. Variations can be made by switching the polarity of individual configurations (e.g. A_2 instead of A_1) for a total of 32 'unique' triplets.

A triplet is entirely self contained and the contact and sheet resistance calculated from the three configuration measurements can be used to obtain three (interdependent) TCR values. By measuring using a sequence of triplets, an optimised measurement can be designed (similar to the R_S measurements [132]), where the measuring time is minimised. Additionally, a triplet sequence allows for

1	I_+	V_+	V_-	I_-
A'	2	1	4	3
B	1	2	4	3
C	1	3	4	2

2	I_+	V_+	V_-	I_-
A	1	2	3	4
B'	2	1	3	4
C	1	3	4	2

3	I_+	V_+	V_-	I_-
A	1	2	3	4
B	1	2	4	3
C'	3	1	2	4

4	I_+	V_+	V_-	I_-
A'	2	1	4	3
B'	2	1	3	4
C'	3	1	2	4

Figure 5.2: An overview of the four main triplets with the current and voltage roles assigned to M4PP electrodes. Each triplet consists of three configurations from which the contact resistances of the three current electrodes as well as the sheet resistance can be determined. Additional variations can be made by switching the current directions (and polarity of the voltage measurement) of the configuration.

the adoption of several filtering schemes. Since the obtained TCR values should not be configuration dependent (with the steady state model), an internal check within each triplet can be done to verify if the measurement was successful. Large variations within a triplet could be a sign of dynamic position errors or electrical noise affecting the measurement. Furthermore, as the different triplets share certain configurations (e.g. the C configuration in triplet 1 and 2 as per Fig. 5.2), a measurement sequence can utilise one configuration measurement in two or even three triplets. The TCR value extracted from the two (or three) different triplets can be compared and can give further insight into if any dynamic errors have occurred.

For the M4PP-TCR method a sequence of triplet measurements could be devised, to optimally (in as few configuration measurements as possible) provide a precise determination of the sample TCR. A wide variety of different configuration sequences can be created such the two examples in Fig. 5.3. To help judge the suitability of a given configuration sequence, two properties are examined, namely the sequence 'efficiency' and 'diversity'. Sequence efficiency denotes the number of triplets that can be formed from the configuration sequence. More triplet measurements in fewer configurations leads to more TCR measurements in a shorter

time period. Diversity denotes the number of different configurations used in the sequence. Restricting to only a few configurations can be detrimental as if a certain electrode has an issue (e.g. bad contact) all measurements will be compromised.

#	cfg	I_+	V_+	V_-	I_-
1	A'	2	1	4	3
2	B	1	2	4	3
3	C	1	3	4	2
4	B'	2	1	3	4
5	A	1	2	3	4
6	B	1	2	4	3
7	C'	3	1	2	4
8	B'	2	1	3	4
9	A'	2	1	4	3

(a)

#	cfg	I_+	V_+	V_-	I_-
1	A'	2	1	4	3
2	B'	2	1	3	4
3	C'	3	1	2	4
4	A'	2	1	4	3
5	B'	2	1	3	4
6	C'	3	1	2	4
7	A'	2	1	4	3
8	B'	2	1	3	4
9	C'	3	1	2	4

(b)

Figure 5.3: An example of possible configuration sequences. (a) The four main triplets can be obtained from 9 configuration measurements, indicated by the loops on the right. Here several configuration measurements (e.g. #3) are used in two triplets and as such will return two TCR values that can be compared. E.g. a shift in electrode position during the configuration measurement #5 will result in a difference in TCR obtained from #3. (b) The most dense configuration sequence is just one repeated triplet at the cost of a low variation in configurations.

5.2 Triplet measurement on Pt

A measurement was devised to analyse the effectiveness of the triplet measurement scheme. This measurement was performed on a 16nm platinum film with an equidistant 10 point probe, allowing for measurements at pitches of 10, 20 and 30 μ m. A total of 100 engages were measured, where at each engage the probe cycles through a custom developed configuration sequence. The sequence contains all 32 'unique' triplets and each of the 12 configurations is utilised with equally

frequency to extract a TCR value. By analysing the variability in each configuration, a measure of the position errors sensitivity can be made (i.e. are certain triplets more suited to M4PP-TCR measurements than others?). This sequence is repeated for the three probe pitches per engage, which will additionally allow for an analysis into probe pitch dependent errors. The measurement was repeated at three different frequencies ($f \approx 12.055\text{Hz}$, $f \approx 24.11\text{Hz}$, $f \approx 48.22\text{Hz}$). To alleviate any transient effects, a waiting period (settle time) is introduced, where the current is initially applied for a number of periods before the voltage measurement starts. All measurements are performed at the maximum current of $I_{\text{RMS}} = 5\text{mA}$, where the TCR can be extracted using either the measured third harmonic resistance value R^{3rd} (steady state model) or the $\Delta R/R_0$ where R_0 is obtained from the 3ω correction (quasi static mode). Measuring at only one current drastically speeds up the measurement, so that these 100 engages can be measured in a similar time frame as the 20 engages from the measurement in section 3.4. Before and after the measurement a characterisation measurement is performed on a thick nickel slab ($R_S = 0.48\ \Omega$) to obtain the lead resistances.

5.2.1 Results

The measurement was performed at a time when the steady state model was not yet fully developed. As a result, the results were analysed using the quasi-static approach, where, unfortunately, the extracted TCR is very dependent on the measurement configurations as shown in Fig. 5.4. Therefore the evaluation of the precision and the optimisation of the triplet measurement scheme was not possible, as differences in extracted TCR values were due to the different configurations rather than any position errors or electrical noise. This part of the analysis was delayed until the steady state model was ready, which unfortunately was not completed within the projects time frame. However, some interesting and unexpected observations were still made using the quasi-static model.

The lowest relative standard deviations achieved were of the order of $\sim 2.5-3\%$ achieved in all configurations at the largest pitch subprobe ($30\ \mu\text{m}$) except for the B configurations. Interestingly, the contact resistances in the B configuration measurements were fairly imbalanced (a higher resistance on one of the electrodes), which could suggest the higher standard deviation is rooted in position errors based on the results found in Fig. 4.3 in chapter 4. The achieved precision using the $10\ \mu\text{m}$ pitch subprobe is slightly higher ($3-4\%$) compared to the initial measurements in section 3.4 ($\sim 2\%$). A likely culprit is sample inhomogeneity, as the 100 engages cover significantly more sample area than the 20 engages in the initial

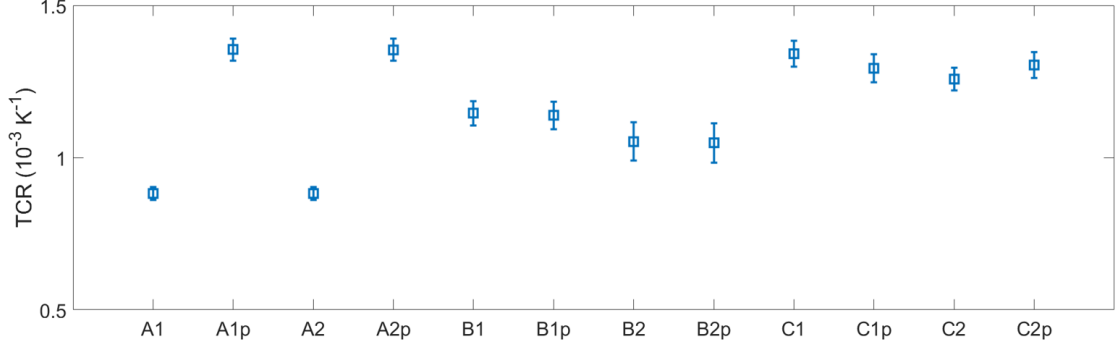


Figure 5.4: *The extracted TCR from all configurations measured across 100 engages using the subprobe with a pitch of $30 \mu\text{m}$. The errorbar is the standard deviation. The TCR extracted using quasi-static model is configuration dependent which can clearly be seen here, where the larger the distance between the current electrodes, the lower the extracted TCR is.*

measurements. 20 engage sections in the 100 engages can be found where the precision reaches a comparable $\sim 2\%$. The similar precision validates the extraction of TCR from only one current measurement, which will drastically reduce overall measurement time.

Certain configurations in the chosen measurement sequence can be part of two triplets (i.e. as shown in Fig 5.3). Figure 5.5 shows the TCR extracted from the measured resistance increase of the C_2' (C2p) configuration from both triplets it is a part of. Large differences between the extracted TCR may indicate changes during the measurement, e.g dynamic position errors. However, as can be seen in Fig. 5.5 the obtained TCR values agree well with each other across the 100 engages, as is the case for the other configurations that are part of two triplets. The relative difference between the two TCR values is in almost all cases less than 1% (with the majority $< 0.5\%$), suggesting the M4PP-TCR method precision could, using an optimised sequence, reach similar levels.

The triplet experiment has generated a multitude of data, with a total of 282 configuration measurements to be analysed per engage, for 100 engages, repeated at three different frequencies. While the measurement of each frequency step took only about half an hour, the data analysis time took far longer and as a result, only the $f \approx 12.055 \text{ Hz}$ experiment has so far been analysed with the quasi static model. Analysis with the steady state model (the initial goal) must wait until the model has been optimised. A completed analysis will indicate how stable the TCR is within the different triplets are, which in turn will facilitate the design of data filters. For example, a median based filter where if the extracted TCR

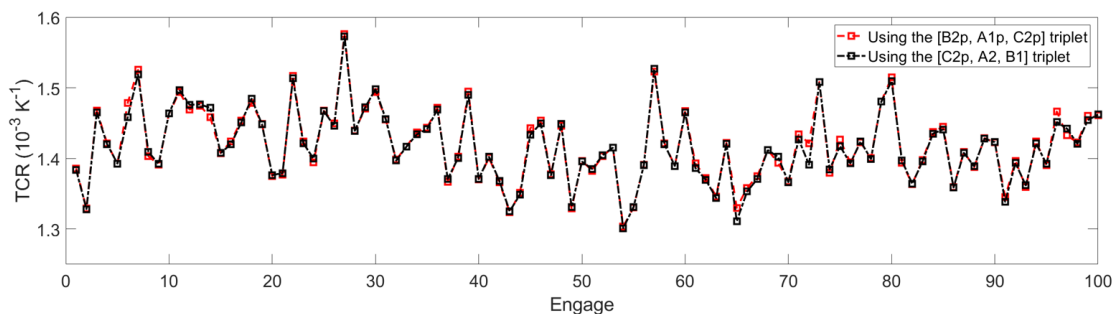


Figure 5.5: *An evaluation of the stability of the extracted TCR from the same measured configuration using the different triplets it is a part of. The TCR extracted is from the C_2 configuration of the $10\ \mu\text{m}$ pitch subprobe. This particular configuration is the 13th measured configuration in the full sequence. The red line is the TCR extracted using the first triplet, the black line the second.*

values within a triplet are too spread out (deviate too far from the median value), the triplet will be rejected. Applying appropriate filters to reject outliers will significantly improve the methods precision. Secondly, the stability of the TCR during an engage is similar interest, as it will indicate how many configuration measurements are needed to reach acceptable precision. Thirdly, the analysis can be performed with and without position correction algorithms to illustrate their effectiveness in the M4PP-TCR method.

Chapter 6

Conclusion and Outlook

During this PhD project a novel method was developed for the characterisation of the temperature coefficient of resistance (TCR) of ultra-thin metal films using a micro four-point probe (M4PP) instrument. By calculating the thermal fields induced by Joule heating, and pairing that with the observed increase in measured M4PP resistance, a value for the TCR could be extracted. As an independent measurement of temperature is no longer needed (a requirement in alternative thin film TCR characterisation methods) a TCR value can be extracted in a matter of seconds. This is significantly faster than e.g. placing samples in a temperature controlled chamber, where the entire sample must reach thermal equilibrium before the electrical measurement can take place. Measurements with a local temperature measurement via e.g. microfabricated thermocouples can compete with the M4PP-TCR method in terms of measurement speed, however it requires complex fabrication steps and is furthermore inflexible. The M4PP can land on a wide array of samples and can be precisely positioned anywhere on the sample surface. This enables the possibility for e.g. wafer maps with microscale resolution, currently out of reach of conventional methods. In addition, the method is developed to be independent of electrode configuration and position, meaning the TCR can be probed at a variety of different lengthscales, as M4PP probes with probe pitches down to 1 μm are available. The project has opened a significant understanding of the thermal system during a M4PP measurement. The derived temperature fields can be applied in the determination of other thermal related sample properties from M4PP measurements, such as the Seebeck coefficient or the thermal conductivity. However, the method is currently limited by the assumptions made on the thermal system, which need to be addressed in future iterations of the method. Furthermore, the M4PP tool used for the development is currently not able to

measure at any temperature other than room temperature.

The TCR is extracted from the M4PP resistance measurements using a semi-analytical approach. The induced temperature increase due to Joule heating was calculated from the measured sheet resistance, via the current density arising from 2D current transport throughout the film. The contact resistances were obtained from the measured 2-point resistance from which the lead resistances were subtracted with the help of an additional characterisation measurement. The temperature field is evaluated over a meshed surface, together with the M4PP sensitivity, a weighing function relating the location and magnitude of local resistance variations to a change in the measured M4PP resistance. The quasi-static semi-analytical model, initially assuming a static system with no thermal delays, is able to predict the rise in measured M4PP resistance for a given TCR value and RMS current. From a fit of this model to the measured data, using the TCR as a fitting parameter, the TCR can be extracted from the measured resistance increase. The model was compared to finite element simulations and a good match ($< 2\%$ difference) was achieved.

The method was demonstrated with a measurement on three platinum thin film samples. The three samples consisted of a deposited platinum layer on a thick fused silica substrate with the help of a 1 nm titanium adhesion layer. The platinum layers were 7 nm, 10 nm and 16 nm thin. Due to thin film effects, these three layer thicknesses give distinct TCR values. A series of M4PP measurements were performed on each sample, 20 to 30 engages with an AC current with $I_{RMS} = 0.5$ mA to 5 mA with a frequency of $f \approx 12$ Hz. The obtained TCR values were compared to independent reference measurements performed on the same samples using a physical property measurement system (PPMS). The TCR values show good correlation with the PPMS measurements, as evidenced by a Pearson's correlation coefficient of 0.99, but underestimated the reference values by $\sim 18\%$. Despite this mismatch, the results were encouraging, as the measured resistance increases were highly reproducible and easily detectable by the M4PP. The mismatch was attributed to an overestimation of the temperature field, resulting primarily from the neglect of thermal delays.

The use of the quasi-static model resulted in TCR values that were dependent on the frequency of the applied current, as well as the size of the probe. An extended model was developed, which calculated the induced temperature fields resulting from a harmonic power source, rather than a static source. This was then used to obtain the induced voltage, which is then fed into a digital lock-in amplifier, mimicking a measurement on the used M4PP instrument. It was demonstrated that the third harmonic voltage can be related to the TCR response.

The third harmonic signals obtained from the extended model were compared to finite element simulations, and again a decent match was obtained ($< 3\%$ difference), with the model now correctly accounting for the applied frequency and probe size. Further measurements were taken on the 16 nm thin platinum sample with a 10-point probe, capable of creating three differently sized subprobes. The behaviour of the measured third harmonic signals with increasing frequency and probe size showed excellent agreement with the model, though the offset between the M4PP measurements and the PPMS was not solved at the project's end date.

A brief investigation was made into the sensitivity of the M4PP-TCR method to electrode position errors and electrical noise. The probe pitch was found to be the dominant factor in the sensitivity for equidistant probes, however due the dependence of the sensitivity and temperature to the electrode positions, the distribution of the Joule heating power also played a role, with primarily the B configuration being heavily dependent on whether the Joule heating is dominated by the sheet or the contacts. Monte Carlo simulations of different probe types and power distributions will be able to provide more insight into the sensitivity of position errors of the M4PP-TCR method, especially for non-equidistant probes. Electrical noise was found to potentially become relevant for low TCR materials as well as thin films deposited on substrates with a high thermal conductivity as the TCR response will be significantly smaller. Likewise, measurements at higher probe pitches or lower currents will be more susceptible to electrical noise. More thorough Monte Carlo simulations should be able to provide minimum pitches and applied current for specific probe and sample types. In addition, evaluating the application of position correction algorithms will be essential in applying the M4PP-TCR method to a wider range of samples and smaller probes.

Lastly, an optimised measurement sequence was postulated, using a triplet; a sequence of three configuration measurements to extract a TCR value. The main goal of such a sequence would be to minimise the time spent measuring, as this increases the chance for any dynamic errors to affect the measurement precision. An experiment was devised to test the effectiveness of such a measurement sequence, however the required analysis method was not completed in time.

Several avenues can be taken to improve and expand the M4PP-TCR method. First of all, the analysis of the sensitivity to position and electrical errors can be expanded to include more measurement scenarios. Of particular interest are the non-equidistant configurations. All measurements in this thesis were performed using equidistant probes as they are the most well understood, however it is conceivable that certain non-equidistant configurations can magnify the TCR response, which will be useful in measurement systems that are limited by the electrical

noise. Completing the idea of triplet measurements will undoubtedly optimise the method with respect to time and susceptibility to position errors. However, this would first of all require the data to be analysed with the steady state model.

Additional measurements on other metallic thin films (e.g. copper, gold or ruthenium) will evaluate whether the method can be used to compare across films (i.e. whether the observed $\sim 18\%$ offset is material dependent). A fruitful analysis would be a measurement on less homogeneous materials, such as heavily oxidised metallic thin films, to assess the impact of imperfect 2D current transport. Similarly, demonstrating successful measurements on different substrates will broaden the range of applicable samples, where of particular interest are samples with a silicon substrate, as this will open up the method to far more industry relevant applications.

Further down the road, an expansion of the thermal system is a must. More complex samples will require a more careful analysis of the heat transport through the device. For example multilayer samples, where lateral heat transport through the different layers will significantly effect the temperature field in the top film. If the current is restricted to the top ultra-thin film, the sheet power density derived in this thesis can still be applied to the multilayer samples (i.e. the electrical system remains the same). The thermal transport through the various layers will however need to be solved using Green's function approach. [133] [134] [135].

A closer look into the impact of the contact resistances is needed. A measurement where the contact force is varied, which will generally result in a varying contact resistance, can be used to verify if the extracted TCR is constant. If not, the cold finger effect is likely responsible, and the thermal modeling will need to account for that.

Measurements on 1D samples (e.g. fins or interconnects) are very relevant to industry. A M4PP measurement on a fin will result in 1D current transport, where the Joule heating is restricted to the area between the current pins (with length L and width W). If the current is restricted to the surface of a fin (via e.g. doping), a similar approach can be taken as the sheet, where instead the fin power density is given by:

$$p_F(x, y) = \begin{cases} \frac{R_s(x, y)I^2}{W^2}, & \text{if } |x| \leq L/2 \text{ and } |y| \leq W/2 \\ 0, & \text{elsewhere} \end{cases} \quad (6.1)$$

where of course $R_S(x, y)$ depends on the local temperature induced by Joule heating ($\Delta T(x, y)$).

Application of the method to thermoelectric materials requires significant expansion of the theory, as the thermoelectric effect manifests itself both in the electrical system (through a Seebeck voltage) and the thermal system (through Peltier heating).

Finally, the development of a finite element model might prove beneficial in the analysis of more complex structures or thermoelectric materials. As already experienced in the relatively simple platinum thin film samples, the semi-analytical approach might become too cumbersome when accounting for the many temperature dependent parameters. Finite element modeling appears to be the most time efficient way to analyse the data. Naturally, one can speed up the analysis time by investigating the severity of each step of implicitness, and find out under what conditions they need to be included.

The measurements showcased in this project have provided a great proof of concept for TCR characterisation using M4PP measurements. The good reproducibility and precision provide a good foundation for expansion of the method to new materials and sample types. Some issues remain however, most notably finding the appropriate description of the thermal system.

Bibliography

- [1] P. N. Edwards, “History of climate modeling,” *Wiley Interdisciplinary Reviews: Climate Change*, vol. 2, no. 1, pp. 128–139, 2011.
- [2] R. O. Jones, “Density functional theory: Its origins, rise to prominence, and future,” *Reviews of modern physics*, vol. 87, no. 3, p. 897, 2015.
- [3] E. H. Shortliffe, E. H. Shortliffe, J. J. Cimino, and J. J. Cimino, *Biomedical informatics: computer applications in health care and biomedicine*. Springer, 2014.
- [4] B. J. Alder and T. E. Wainwright, “Studies in molecular dynamics. i. general method,” *The Journal of Chemical Physics*, vol. 31, no. 2, pp. 459–466, 1959.
- [5] B. J. Alder and T. E. Wainwright, “Studies in molecular dynamics. ii. behavior of a small number of elastic spheres,” *The Journal of Chemical Physics*, vol. 33, no. 5, pp. 1439–1451, 1960.
- [6] N. Metropolis, A. W. Rosenbluth, M. N. Rosenbluth, A. H. Teller, and E. Teller, “Equation of state calculations by fast computing machines,” *The journal of chemical physics*, vol. 21, no. 6, pp. 1087–1092, 1953.
- [7] J. Carlson and R. Schiavilla, “Structure and dynamics of few-nucleon systems,” *Reviews of Modern Physics*, vol. 70, no. 3, p. 743, 1998.
- [8] CERN. (2019). “Storage,” [Online]. Available: <https://home.cern/science/computing/storage> (visited on 11/12/2020).
- [9] J. Bardeen, “Surface states and rectification at a metal semi-conductor contact,” *Physical Review*, vol. 71, no. 10, p. 717, 1947.
- [10] J. Bardeen and W. H. Brattain, “The transistor, a semi-conductor triode,” *Physical Review*, vol. 74, no. 2, p. 230, 1948.
- [11] G. E. Moore *et al.*, “Cramming more components onto integrated circuits,” *Electronics*, vol. 38, no. 8, pp. 114–117, 1965.

- [12] B. Hoefflinger, “IRDS International Roadmap for Devices and Systems, Rebooting Computing, S3S,” in *NANO-CHIPS 2030*, Springer, 2020, pp. 9–17.
- [13] M. M. Waldrop, “The chips are down for moore’s law,” *Nature News*, vol. 530, no. 7589, p. 144, 2016.
- [14] S. Lohrasbi, R. Hammer, W. Essl, G. Reiss, S. Defregger, and W. Sanz, “A comprehensive review on the core thermal management improvement concepts in power electronics,” *IEEE Access*, vol. 8, pp. 166 880–166 906, 2020.
- [15] Y. Fu, J. Hansson, Y. Liu, S. Chen, A. Zehri, M. K. Samani, N. Wang, Y. Ni, Y. Zhang, Z.-B. Zhang, *et al.*, “Graphene related materials for thermal management,” *2D Materials*, vol. 7, no. 1, p. 012 001, 2019.
- [16] S. S. Murshed and C. N. De Castro, “A critical review of traditional and emerging techniques and fluids for electronics cooling,” *Renewable and Sustainable Energy Reviews*, vol. 78, pp. 821–833, 2017.
- [17] N. H. Naqiuddin, L. H. Saw, M. C. Yew, F. Yusof, T. C. Ng, and M. K. Yew, “Overview of micro-channel design for high heat flux application,” *Renewable and Sustainable Energy Reviews*, vol. 82, pp. 901–914, 2018.
- [18] A. K. Coskun, J. L. Ayala, D. Atienza, T. S. Rosing, and Y. Leblebici, “Dynamic thermal management in 3d multicore architectures,” in *2009 Design, Automation and Test in Europe Conference and Exhibition*, IEEE, 2009, pp. 1410–1415.
- [19] J. M. Cruz-Duarte, I. Amaya, J. C. Ortíz-Bayliss, and R. Correa, “Solving microelectronic thermal management problems using a generalized spiral optimization algorithm,” *Applied Intelligence*, pp. 1–22, 2021.
- [20] P. Ball, “Computer engineering: Feeling the heat,” *Nature News*, vol. 492, no. 7428, p. 174, 2012.
- [21] S. V. Garimella, A. S. Fleischer, J. Y. Murthy, A. Keshavarzi, R. Prasher, C. Patel, S. H. Bhavnani, R. Venkatasubramanian, R. Mahajan, Y. Joshi, B. Sammakia, B. A. Myers, L. Chorosinski, M. Baelmans, P. Sathyamurthy, and P. E. Raad, “Thermal challenges in next-generation electronic systems,” *IEEE Transactions on Components and Packaging Technologies*, vol. 31, no. 4, pp. 801–815, 2008.
- [22] P. G. Emma and E. Kursun, “Is 3d chip technology the next growth engine for performance improvement?” *IBM journal of research and development*, vol. 52, no. 6, pp. 541–552, 2008.

- [23] M. T. Bohr, "Interconnect scaling—the real limiter to high performance ULSI," in *Proceedings of International Electron Devices Meeting*, IEEE, 1995, pp. 241–244.
- [24] J. D. Meindl, "Beyond moore's law: The interconnect era," *Computing in Science & Engineering*, vol. 5, no. 1, pp. 20–24, 2003.
- [25] P. Kapur, J. P. McVittie, and K. C. Saraswat, "Technology and reliability constrained future copper interconnects. i. resistance modeling," *IEEE Transactions on Electron Devices*, vol. 49, no. 4, pp. 590–597, 2002.
- [26] P. Kapur, G. Chandra, J. P. McVittie, and K. C. Saraswat, "Technology and reliability constrained future copper interconnects. ii. performance implications," *IEEE Transactions on Electron Devices*, vol. 49, no. 4, pp. 598–604, 2002.
- [27] F. Chen and D. Gardner, "Influence of line dimensions on the resistance of cu interconnections," *IEEE Electron Device Letters*, vol. 19, no. 12, pp. 508–510, 1998.
- [28] T. Gupta, *Copper interconnect technology*. Springer Science & Business Media, 2010.
- [29] R. Mönig, Y.-B. Park, and C. Volkert, "Thermal fatigue in copper interconnects," in *AIP Conference Proceedings*, American Institute of Physics, vol. 817, 2006, pp. 147–156.
- [30] J. R. Black, "Electromigration—a brief survey and some recent results," *IEEE Transactions on Electron Devices*, vol. 16, no. 4, pp. 338–347, 1969.
- [31] J. R. Black, "Physics of electromigration," in *12th International Reliability Physics Symposium*, IEEE, 1974, pp. 142–149.
- [32] K.-N. Tu, "Recent advances on electromigration in very-large-scale-integration of interconnects," *Journal of applied physics*, vol. 94, no. 9, pp. 5451–5473, 2003.
- [33] A. L. Moore and L. Shi, "Emerging challenges and materials for thermal management of electronics," *Materials Today*, vol. 17, no. 4, pp. 163–174, 2014, ISSN: 1369-7021.
- [34] D. G. Cahill, K. Goodson, and A. Majumdar, "Thermometry and Thermal Transport in Micro/Nanoscale Solid-State Devices and Structures," *Journal of Heat Transfer*, vol. 124, no. 2, pp. 223–241, Dec. 2001.
- [35] K. E. Goodson and Y. S. Ju, "Heat conduction in novel electronic films," *Annual Review of Materials Science*, vol. 29, no. 1, pp. 261–293, 1999.

- [36] D. G. Cahill, “Heat transport in dielectric thin films and at solid-solid interfaces,” *Microscale Thermophysical Engineering*, vol. 1, no. 2, pp. 85–109, 1997.
- [37] D. Li, Y. Wu, P. Kim, L. Shi, P. Yang, and A. Majumdar, “Thermal conductivity of individual silicon nanowires,” *Applied Physics Letters*, vol. 83, no. 14, pp. 2934–2936, 2003.
- [38] E. T. Swartz and R. O. Pohl, “Thermal boundary resistance,” *Reviews of modern physics*, vol. 61, no. 3, p. 605, 1989.
- [39] P. Rodgers, V. Evely, and M. G. Pecht, “Extending the limits of air-cooling in microelectronic equipment,” in *EuroSimE 2005. Proceedings of the 6th International Conference on Thermal, Mechanical and Multi-Physics Simulation and Experiments in Micro-Electronics and Micro-Systems, 2005.*, IEEE, 2005, pp. 695–702.
- [40] C. Gould, N. Shamma, S. Grainger, and I. Taylor, “Thermoelectric cooling of microelectronic circuits and waste heat electrical power generation in a desktop personal computer,” *Materials Science and Engineering: B*, vol. 176, no. 4, pp. 316–325, 2011.
- [41] P. E. Phelan, V. A. Chiriach, and T.-Y. Lee, “Current and future miniature refrigeration cooling technologies for high power microelectronics,” *IEEE Transactions on Components and Packaging Technologies*, vol. 25, no. 3, pp. 356–365, 2002.
- [42] B. Yang, P. Wang, and A. Bar-Cohen, “Mini-contact enhanced thermoelectric cooling of hot spots in high power devices,” *IEEE Transactions on Components and Packaging Technologies*, vol. 30, no. 3, pp. 432–438, 2007.
- [43] A. Shakouri and J. E. Bowers, “Heterostructure integrated thermionic coolers,” *Applied Physics Letters*, vol. 71, no. 9, pp. 1234–1236, 1997.
- [44] A. Ziabari, M. Zebarjadi, D. Vashaee, and A. Shakouri, “Nanoscale solid-state cooling: A review,” *Reports on Progress in Physics*, vol. 79, no. 9, p. 095 901, 2016.
- [45] Y.-B. Park, R. Mönig, and C. A. Volkert, “Thermal fatigue as a possible failure mechanism in copper interconnects,” *Thin Solid Films*, vol. 504, no. 1-2, pp. 321–324, 2006.
- [46] S. O. Kasap, *Principles of electronic materials and devices*. McGraw-Hill New York, 2006, vol. 3.
- [47] J. Cho and Y. Kim, “Improving energy efficiency of dedicated cooling system and its contribution towards meeting an energy-optimized data center,” *Applied energy*, vol. 165, pp. 967–982, 2016.

- [48] H.-M. Chuang, K.-B. Thei, S.-F. Tsai, and W.-C. Liu, "Temperature-dependent characteristics of polysilicon and diffused resistors," *IEEE Transactions on electron devices*, vol. 50, no. 5, pp. 1413–1415, 2003.
- [49] C. Tellier and A. Tossier, "The temperature coefficient of resistivity of polycrystalline radio frequency sputtered aluminium films," *Thin Solid Films*, vol. 43, no. 3, pp. 261–266, 1977.
- [50] H. J. K. Kim, K. E. Kaplan, P. Schindler, S. Xu, M. M. Winterkorn, D. B. Heinz, T. S. English, J. Provine, F. B. Prinz, and T. W. Kenny, "Electrical properties of ultrathin platinum films by plasma-enhanced atomic layer deposition," *ACS applied materials & interfaces*, vol. 11, no. 9, pp. 9594–9599, 2019.
- [51] C. Tellier and A. Tossier, "Exact and approximate expressions for the temperature coefficient of resistivity of polycrystalline films using the mayadas-shatzkes model," *Thin Solid Films*, vol. 44, no. 2, pp. 141–147, 1977.
- [52] F. Warkusz, "Temperature effects in thin metal films," *Thin solid films*, vol. 148, no. 3, pp. 343–353, 1987.
- [53] S. Dutta, S. Kundu, A. Gupta, G. Jamieson, J. F. G. Granados, J. Bömmels, C. J. Wilson, Z. Tókei, and C. Adelman, "Highly scaled ruthenium interconnects," *IEEE Electron Device Letters*, vol. 38, no. 7, pp. 949–951, 2017.
- [54] K. Croes, C. Adelman, C. J. Wilson, H. Zahedmanesh, O. V. Pedreira, C. Wu, A. Leśniewska, H. Oprins, S. Beyne, I. Ciofi, *et al.*, "Interconnect metals beyond copper: Reliability challenges and opportunities," in *2018 IEEE International Electron Devices Meeting (IEDM)*, IEEE, 2018, pp. 5–3.
- [55] L. Ding, C. Wang, L. Chu, J. Yan, Y. Na, Q. Huang, and X. Chen, "Near zero temperature coefficient of resistivity in antiperovskite $\text{mn}_3\text{ni}_1\text{-xcuxn}$," *Applied Physics Letters*, vol. 99, no. 25, p. 251905, 2011.
- [56] E. Chi, W. Kim, and N. Hur, "Nearly zero temperature coefficient of resistivity in antiperovskite compound cunmn_3 ," *Solid State Communications*, vol. 120, no. 7-8, pp. 307–310, 2001.
- [57] S. Lin, B. Wang, J. Lin, Y. Huang, W. Lu, B. Zhao, P. Tong, W. Song, and Y. Sun, "Tunable room-temperature zero temperature coefficient of resistivity in antiperovskite compounds $\text{ga}_1\text{-xcfe}_3$ and $\text{ga}_1\text{-yalycfe}_3$," *Applied Physics Letters*, vol. 101, no. 1, p. 011908, 2012.
- [58] C. Adelman, "On the extraction of resistivity and area of nanoscale interconnect lines by temperature-dependent resistance measurements," *Solid-State Electronics*, vol. 152, pp. 72–80, 2019.

- [59] A. Von Glasow, A. Fischer, and G. Steinlesberger, "Using the temperature coefficient of the resistance (tcr) as early reliability indicator for stressvoiding risks in cu interconnects," in *2003 IEEE International Reliability Physics Symposium Proceedings, 2003. 41st Annual.*, IEEE, 2003, pp. 126–131.
- [60] M. Olszacki, C. Maj, M. Al Bahri, J. Marrot, A. Boukabache, P. Pons, and A. Napieralski, "Experimental verification of temperature coefficients of resistance for uniformly doped p-type resistors in soi," *Journal of Micromechanics and Microengineering*, vol. 20, no. 6, p. 064008, 2010.
- [61] T. Dinh, H.-P. Phan, A. Qamar, P. Woodfield, N.-T. Nguyen, and D. V. Dao, "Thermoresistive effect for advanced thermal sensors: Fundamentals, design considerations, and applications," *Journal of Microelectromechanical Systems*, vol. 26, no. 5, pp. 966–986, 2017.
- [62] S. Wu, Q. Lin, Y. Yuen, and Y.-C. Tai, "Mems flow sensors for nano-fluidic applications," *Sensors and Actuators A: Physical*, vol. 89, no. 1-2, pp. 152–158, 2001.
- [63] H. A. Schafft and J. S. Suehle, "The measurement, use and interpretation of the temperature coefficient of resistance of metallizations," *Solid-state electronics*, vol. 35, no. 3, pp. 403–410, 1992.
- [64] J. H. Dellinger, *The temperature coefficient of resistance of copper*, 147. US Government Printing Office, 1911.
- [65] R. B. Belser and W. H. Hicklin, "Temperature coefficients of resistance of metallic films in the temperature range 25 to 600 c," *Journal of Applied Physics*, vol. 30, no. 3, pp. 313–322, 1959.
- [66] J. Dewar and J. Fleming, "Xxvi. the electrical resistance of metals and alloys at temperatures approaching the absolute zero," *The London, Edinburgh, and Dublin Philosophical Magazine and Journal of Science*, vol. 36, no. 220, pp. 271–299, 1893.
- [67] J. Dewar and J. A. Fleming, "Xxv. the variation in the electrical resistance of bismuth, when cooled to the temperature of solid air," *The London, Edinburgh, and Dublin Philosophical Magazine and Journal of Science*, vol. 40, no. 244, pp. 303–311, 1895.
- [68] D. G. Cahill, P. V. Braun, G. Chen, D. R. Clarke, S. Fan, K. E. Goodson, P. Keblinski, W. P. King, G. D. Mahan, A. Majumdar, *et al.*, "Nanoscale thermal transport. ii. 2003–2012," *Applied physics reviews*, vol. 1, no. 1, p. 011305, 2014.
- [69] S. Lepri, R. Livi, and A. Politi, "Thermal conduction in classical low-dimensional lattices," *Physics reports*, vol. 377, no. 1, pp. 1–80, 2003.

- [70] G. Chen, “Ballistic-diffusive heat-conduction equations,” *Physical Review Letters*, vol. 86, no. 11, p. 2297, 2001.
- [71] I. Miccoli, F. Edler, H. Pfnür, and C. Tegenkamp, “The 100th anniversary of the four-point probe technique: The role of probe geometries in isotropic and anisotropic systems,” *Journal of Physics: Condensed Matter*, vol. 27, no. 22, p. 223 201, 2015.
- [72] J. Christofferson, K. Maize, Y. Ezzahri, J. Shabani, X. Wang, and A. Shakouri, “Microscale and Nanoscale Thermal Characterization Techniques,” *Journal of Electronic Packaging*, vol. 130, no. 4, Nov. 2008, 041101, ISSN: 1043-7398.
- [73] L. D. Carlos and F. Palacio, *Thermometry at the nanoscale: Techniques and selected applications*. Royal Society of Chemistry, 2015.
- [74] G. P. Szakmany, A. O. Orlov, G. H. Bernstein, and W. Porod, “Single-metal nanoscale thermocouples,” *IEEE Transactions on Nanotechnology*, vol. 13, no. 6, pp. 1234–1239, 2014.
- [75] C. L. Petersen, T. M. Hansen, P. Bøggild, A. Boisen, O. Hansen, T. Hassenkam, and F. Grey, “Scanning microscopic four-point conductivity probes,” *Sensors and Actuators A: Physical*, vol. 96, no. 1, pp. 53–58, 2002.
- [76] A. Uhlir Jr, “The potentials of infinite systems of sources and numerical solutions of problems in semiconductor engineering,” *Bell System Technical Journal*, vol. 34, no. 1, pp. 105–128, 1955.
- [77] F. Smits, “Measurement of sheet resistivities with the four-point probe,” *Bell System Technical Journal*, vol. 37, no. 3, pp. 711–718, 1958.
- [78] L. Van der Pauw, “A method of measuring specific resistivity and hall effect of discs of arbitrary shape,” *Philips Res. Rep*, vol. 13, no. 1, pp. 1–9, 1958.
- [79] D. Worledge and P. Trouilloud, “Magnetoresistance measurement of unpatterned magnetic tunnel junction wafers by current-in-plane tunneling,” *Applied Physics Letters*, vol. 83, no. 1, pp. 84–86, 2003.
- [80] D. H. Petersen, O. Hansen, T. M. Hansen, P. Bøggild, R. Lin, D. Kjær, P. F. Nielsen, T. Clarysse, W. Vandervorst, E. Rosseel, *et al.*, “Review of electrical characterization of ultra-shallow junctions with micro four-point probes,” *Journal of Vacuum Science & Technology B, Nanotechnology and Microelectronics: Materials, Processing, Measurement, and Phenomena*, vol. 28, no. 1, pp. C1C27–C1C33, 2010.

- [81] D. Kjaer, R. Lin, D. H. Petersen, P. M. Kopalidis, R. Eddy, D. A. Walker, W. F. Egelhoff, and L. Pickert, “Micro four-point probe with high spatial resolution for ion implantation and ultra-shallow junction characterization,” in *AIP Conference Proceedings*, American Institute of Physics, vol. 1066, 2008, pp. 167–170.
- [82] D. H. Petersen, R. Lin, T. M. Hansen, E. Rosseel, W. Vandervorst, C. Markvardsen, D. Kjær, and P. F. Nielsen, “Comparative study of size dependent four-point probe sheet resistance measurement on laser annealed ultra-shallow junctions,” *Journal of Vacuum Science & Technology B: Microelectronics and Nanometer Structures Processing, Measurement, and Phenomena*, vol. 26, no. 1, pp. 362–367, 2008.
- [83] J. Bogdanowicz, S. Folkersma, S. Sergeant, A. Schulze, A. Moussa, D. H. Petersen, O. Hansen, H. H. Henrichsen, P. F. Nielsen, and W. Vandervorst, “Width-dependent sheet resistance of nanometer-wide si fins as measured with micro four-point probe,” *physica status solidi (a)*, vol. 215, no. 6, p. 1 700 857, 2018.
- [84] S. Folkersma, J. Bogdanowicz, A. Schulze, P. Favia, D. H. Petersen, O. Hansen, H. H. Henrichsen, P. F. Nielsen, L. Shiv, and W. Vandervorst, “Electrical characterization of single nanometer-wide si fins in dense arrays,” *Beilstein journal of nanotechnology*, vol. 9, no. 1, pp. 1863–1867, 2018.
- [85] S. Thorsteinsson, F. Wang, D. H. Petersen, T. M. Hansen, D. Kjær, R. Lin, J.-Y. Kim, P. F. Nielsen, and O. Hansen, “Accurate microfour-point probe sheet resistance measurements on small samples,” *Review of Scientific Instruments*, vol. 80, no. 5, p. 053 902, 2009.
- [86] F. Osterberg, D. H. Petersen, F. Wang, E. Rosseel, W. Vandervorst, and O. Hansen, “Accurate micro hall effect measurements on scribe line pads,” in *2009 17th International Conference on Advanced Thermal Processing of Semiconductors*, IEEE, 2009, pp. 1–6.
- [87] D. M. Mackenzie, K. G. Kalhauge, P. R. Whelan, F. W. Østergaard, I. Pasternak, W. Strupinski, P. Bøggild, P. U. Jepsen, and D. H. Petersen, “Wafer-scale graphene quality assessment using micro four-point probe mapping,” *Nanotechnology*, vol. 31, no. 22, p. 225 709, 2020.
- [88] B. Guralnik, O. Hansen, H. H. Henrichsen, B. Beltrán-Pitarch, F. W. Østerberg, L. Shiv, T. A. Marangoni, A. R. Stilling-Andersen, A. Cagliani, M. F. Hansen, *et al.*, “3 w correction method for eliminating resistance measurement error due to joule heating,” *Review of Scientific Instruments*, vol. 92, no. 9, p. 094 711, 2021.

- [89] S. Folkersma, J. Bogdanowicz, D. H. Petersen, O. Hansen, H. H. Henrichsen, P. F. Nielsen, L. Shiv, and W. Vandervorst, “Electrical contact formation in micro four-point probe measurements,” *physica status solidi (a)*, vol. 217, no. 5, p. 1 900 579, 2020.
- [90] G. S. Ohm, *Bestimmung des Gesetzes, nach welchem Metalle die Contaktelektricität leiten: Nebst einem Entwurfe zur einer Theorie des Voltaischen Apparates und des Schweiggerschen Multiplimators*. Journal für Chemie und Physik, 1826.
- [91] P. Drude, “Zur elektronentheorie der metalle,” *Annalen der physik*, vol. 306, no. 3, pp. 566–613, 1900.
- [92] A. Sommerfeld, “Zur elektronentheorie der metalle auf grund der fermischen statistik,” *Zeitschrift für Physik*, vol. 47, no. 1-2, pp. 1–32, 1928.
- [93] S. Kasap, *Springer handbook of electronic and photonic materials*. Springer Science & Business Media, 2006.
- [94] C. R. Tellier and A. J. Tossier, *Size effects in thin films*. Elsevier, 2016, vol. 2.
- [95] A. Mayadas, M. Shatzkes, and J. Janak, “Electrical resistivity model for polycrystalline films: The case of specular reflection at external surfaces,” *Applied Physics Letters*, vol. 14, no. 11, pp. 345–347, 1969.
- [96] E. Sondheimer, “The mean free path of electrons in metals,” *Advances in Physics*, vol. 1, no. 1, pp. 1–42, 1952.
- [97] P. M. Hall, “The effect of expansion mismatch on temperature coefficient of resistance of thin films,” *Applied Physics Letters*, vol. 12, no. 6, pp. 212–212, 1968. DOI: 10.1063/1.1651956.
- [98] F. Warkusz, “The size effect and the temperature coefficient of resistance in thin films,” *Journal of Physics D: Applied Physics*, vol. 11, no. 5, p. 689, 1978.
- [99] F. Warkusz, “The size effect and the temperature coefficient of total resistance in thin metal films,” *Journal of Physics D: Applied Physics*, vol. 11, no. 14, p. 2035, 1978.
- [100] L. Kazmerski, D. M. Racine, and M. Ayyagari, “Temperature coefficient of resistance in ultrathin metal films,” *Journal of Applied Physics*, vol. 46, no. 6, pp. 2658–2661, 1975.
- [101] F. Wenner, *A method of measuring earth resistivity*, 258. US Government Printing Office, 1916.
- [102] L. B. Valdes, “Resistivity measurements on germanium for transistors,” *Proceedings of the IRE*, vol. 42, no. 2, pp. 420–427, 1954.

- [103] F. Wang, D. H. Petersen, H. V. Jensen, C. Hansen, D. Mortensen, L. Friis, and O. Hansen, “Three-way flexible cantilever probes for static contact,” *Journal of Micromechanics and Microengineering*, vol. 21, no. 8, p. 085 003, Jun. 2011.
- [104] K. G. Kalhauge, H. H. Henrichsen, F. Wang, O. Hansen, and D. H. Petersen, “Vibration tolerance of micro-electrodes,” *Journal of Micromechanics and Microengineering*, vol. 28, no. 9, p. 095 010, 2018.
- [105] K. G. Kalhauge, “Design of vibration tolerant microelectrodes and field effect characterization of MoS₂,” Ph.D. dissertation, Technical University of Denmark, 2019.
- [106] T. Ansbæk, D. H. Petersen, O. Hansen, J. B. Larsen, T. M. Hansen, and P. Bøggild, “Fundamental size limitations of micro four-point probes,” *Microelectronic Engineering*, vol. 86, no. 4, pp. 987–990, 2009, MNE '08, ISSN: 0167-9317.
- [107] D. W. Koon, F. Wang, D. Hjorth Petersen, and O. Hansen, “Sensitivity of resistive and hall measurements to local inhomogeneities,” *Journal of Applied Physics*, vol. 114, no. 16, p. 163 710, 2013.
- [108] D. W. Koon, F. Wang, D. H. Petersen, and O. Hansen, “Sensitivity of resistive and hall measurements to local inhomogeneities: Finite-field, intensity, and area corrections,” *Journal of Applied Physics*, vol. 116, no. 13, p. 133 706, 2014.
- [109] P. F. Nielsen, D. H. Petersen, R. Lin, A. Jensen, H. H. Henrichsen, L. Gammelgaard, D. Kjær, and O. Hansen, “Microprobe metrology for direct sheet resistance and mobility characterization,” in *2012 12th International Workshop on Junction Technology*, 2012, pp. 100–105.
- [110] I. Harvey and H. Collins, “Precise resistance ratio measurements using a superconducting dc ratio transformer,” *Review of Scientific Instruments*, vol. 44, no. 12, pp. 1700–1702, 1973.
- [111] J. Bojkovski, V. Zuzek, V. Batagelj, and J. Drnovsek, “The influence of the resistor temperature coefficient to the uncertainty of the temperature measurement,” International Conference on Heat Transfer, Fluid Mechanics and Thermodynamics, 2015.
- [112] G. Fernqvist, P. Dreesen, G. Hudson, and J. Pickering, “Characteristics of burden resistors for high-precision dc current transducers,” in *2007 IEEE Particle Accelerator Conference (PAC)*, IEEE, 2007, pp. 317–319.

- [113] S. Yoneoka, J. Lee, M. Liger, G. Yama, T. Kodama, M. Gunji, J. Provine, R. T. Howe, K. E. Goodson, and T. W. Kenny, “Electrical and thermal conduction in atomic layer deposition nanobridges down to 7 nm thickness,” *Nano letters*, vol. 12, no. 2, pp. 683–686, 2012.
- [114] H. S. Carslaw and J. C. Jaeger, “Conduction of heat in solids,” Clarendon Press, Tech. Rep., 1959, p. 263.
- [115] P. Teunissen, “Nonlinear least squares,” *manuscripta geodaetica*, vol. 15, pp. 137–150, 1990.
- [116] MATLAB, *Version 9.9.0.1467703 (R2020b)*. Natick, Massachusetts: The MathWorks Inc., 2020.
- [117] Z. Instruments. (2016). “Principles of lock-in detection and the state of the art,” [Online]. Available: https://www.zhinst.com/sites/default/files/li_primer/zi_whitepaper_principles_of_lock-in_detection.pdf (visited on 10/29/2021).
- [118] C. Multiphysics, *v.5.5*. Stockholm, Sweden: COMSOL AB, 2020.
- [119] B. Guralnik, O. Hansen, H. H. Henrichsen, J. M. Caridad, W. Wei, M. F. Hansen, P. F. Nielsen, and D. H. Petersen, “Effective electrical resistivity in a square array of oriented square inclusions,” *Nanotechnology*, vol. 32, no. 18, p. 185706, 2021.
- [120] J. Chaston, “The oxidation of the platinum metals,” *Platinum Metals Review*, vol. 19, no. 4, pp. 135–140, 1975.
- [121] T. A. Marangoni, B. Guralnik, K. A. Borup, O. Hansen, and D. H. Petersen, “Determination of the temperature coefficient of resistance from micro four-point probe measurements,” *Journal of Applied Physics*, vol. 129, no. 16, p. 165105, 2021.
- [122] D. Kjaer, O. Hansen, F. W. Østerberg, H. H. Henrichsen, C. Markvardsen, P. F. Nielsen, and D. H. Petersen, “Characterization of positional errors and their influence on micro four-point probe measurements on a 100 nm ru film,” vol. 26, no. 9, p. 095005, Jul. 2015.
- [123] F. Wang, D. H. Petersen, T. M. Hansen, T. R. Henriksen, P. Bøggild, and O. Hansen, “Sensitivity study of micro four-point probe measurements on small samples,” *Journal of Vacuum Science & Technology B, Nanotechnology and Microelectronics: Materials, Processing, Measurement, and Phenomena*, vol. 28, no. 1, pp. C1C34–C1C40, 2010.
- [124] D. Worledge, “Reduction of positional errors in a four-point probe resistance measurement,” *Applied Physics Letters*, vol. 84, no. 10, pp. 1695–1697, 2004.

- [125] R. Rymaszewski, “Relationship between the correction factor of the four-point probe value and the selection of potential and current electrodes,” vol. 2, no. 2, pp. 170–174, Feb. 1969. DOI: 10.1088/0022-3735/2/2/312. [Online]. Available: <https://doi.org/10.1088/0022-3735/2/2/312>.
- [126] D. H. Petersen, O. Hansen, T. M. Hansen, P. R. Petersen, and P. Bøggild, “Static contact micro four-point probes with <11nm positioning repeatability,” *Microelectronic Engineering*, vol. 85, no. 5, pp. 1092–1095, 2008, Proceedings of the Micro- and Nano-Engineering 2007 Conference, ISSN: 0167-9317.
- [127] D. Petersen, O. Hansen, R. Lin, P. Nielsen, T. Clarysse, J. Goossens, E. Rosseel, and W. Vandervorst, “High precision micro-scale hall effect characterization method using in-line micro four-point probes,” in *2008 16th IEEE International Conference on Advanced Thermal Processing of Semiconductors*, 2008, pp. 251–256.
- [128] D. Kjaer, O. Hansen, F. W. Østerberg, H. H. Henrichsen, C. Markvardsen, P. F. Nielsen, and D. H. Petersen, “Characterization of positional errors and their influence on micro four-point probe measurements on a 100 nm ru film,” *Measurement Science and Technology*, vol. 26, no. 9, p. 095005, 2015.
- [129] D. Kjaer, “Advanced metrology for characterization of magnetic tunnel junctions,” Ph.D. dissertation, Technical University of Denmark, 2015.
- [130] J. B. Johnson, “Thermal agitation of electricity in conductors,” *Physical review*, vol. 32, no. 1, p. 97, 1928.
- [131] H. Nyquist, “Thermal agitation of electric charge in conductors,” *Physical review*, vol. 32, no. 1, p. 110, 1928.
- [132] D. H. Petersen, “Micro four-point probe and micro hall effect: Methods for reliable electrical characterization of ultra-shallow junctions,” Ph.D. dissertation, Technical University of Denmark, 2009.
- [133] N. Simões and A. Tadeu, “Transient conduction and convection heat transfer across a multi-layer floor subjected to multiple heat sources,” *Building and Environment*, vol. 41, no. 10, pp. 1299–1310, 2006.
- [134] A. G. Kokkas, “Thermal analysis of multiple-layer structures,” *IEEE Transactions on Electron Devices*, vol. 21, no. 11, pp. 674–681, 1974.
- [135] E. J. Carr and N. G. March, “Semi-analytical solution of multilayer diffusion problems with time-varying boundary conditions and general interface conditions,” *Applied Mathematics and Computation*, vol. 333, pp. 286–303, 2018.

Appendix A

TCR extraction from ruthenium thin films

Initially the M4PP-TCR method was tested on several ruthenium thin film samples. These samples differed from the platinum samples. The ruthenium was deposited on a silicon substrate with a 90 nm barrier layer, as picture in Fig. A.1. When the quasi-static model is applied to the measured increase in resistance, the extracted TCR's are highly configuration dependent and do not match expected results (from thin film TCR models) nor do the different configurations return the same TCR value. Furthermore the method was tested using three different probe sizes which all returned different TCR values.

The ruthenium samples had several issues which prompted the move to the platinum samples. Firstly, the low current measurements are noisy, as can be seen in Fig. A.2. These measurements are not included in the fit and the '3- ω ' correction must be utilised to obtain R_0 . Secondly the signal strength is quite small. Figure A.2 displays the response for a identical 10 μm probe used in the platinum measurements which shows signals ~ 25 times smaller than measured on the platinum samples.

The main issue however is a that the SiO_2 barrier layer likely induces significant lateral heat transport in the metal film so that the thermal model, that assumes that heat conduction is dominated by the substrate (silicon), poorly represents the true heat transport. Evaluation of these ruthenium thin film samples require an extension to the thermal model to include multilayer heat transport.

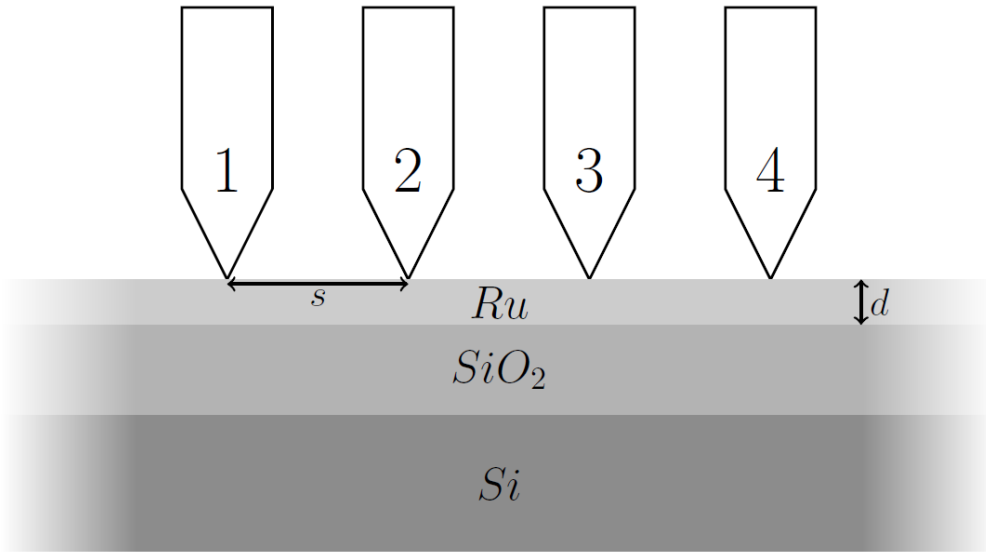


Figure A.1: A schematic overview of the ruthenium film samples. The ruthenium film thickness d was of the order of 3 – 30 nm, while the SiO₂ barrier layer was 90 nm thick.

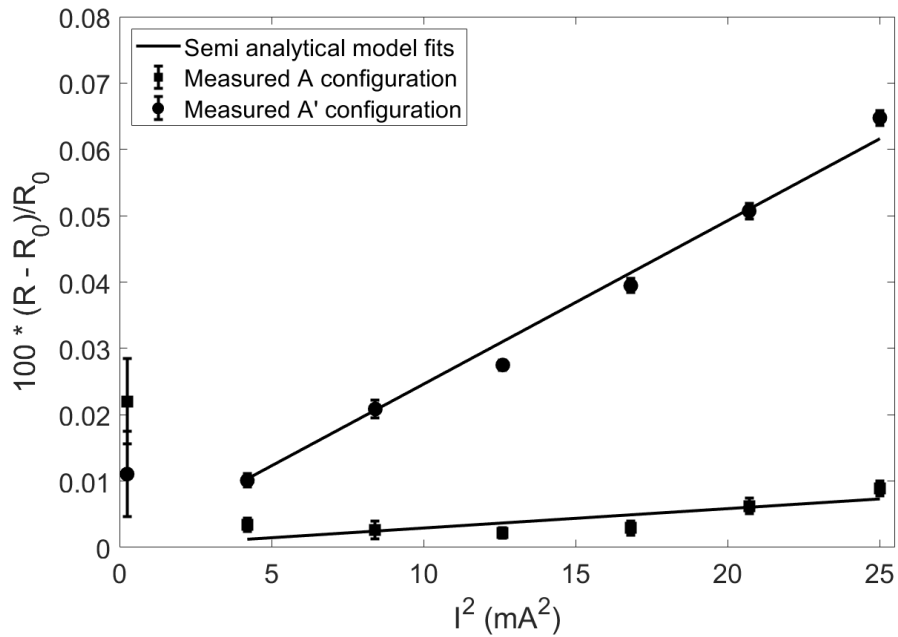


Figure A.2: Quasi-static model fit to the measured resistance increase on a 9 nm ruthenium film sample. The data is taken on the 10A subprobe of a L7PP (equidistance 10 μ m pitch probe).

Appendix B

TCR extracted from remaining configurations and subprobes on platinum thin film samples

Additional results from the remaining configurations and sub-probes measured during the measurements on the platinum thin films in section 3.4.1, obtained from the quasi-static semi-analytical model. The probe used was the L7PP, pictured in Fig. 1.4, which has seven electrodes equidistantly spaced by $10\ \mu\text{m}$. Three subprobes were used in the measurement. The '10A', which utilises the four left-most electrodes (1,2,3,4). '10B' which uses the four right-most electrodes (4,5,6,7) and '20' which is the $20\ \mu\text{m}$ pitch subprobe (1,3,5,7).

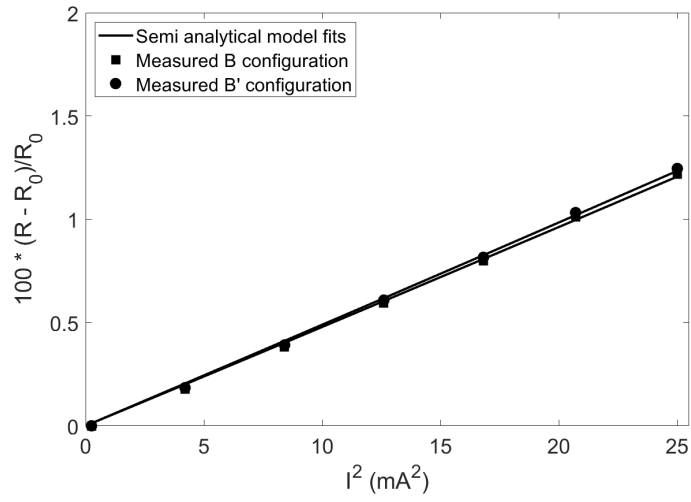
B.1 B and C configurations on the 10A sub-probe

Film thickness (nm)	coupon ID	Sheet resistance (Ω)	M4PP TCR B (10^{-3} K)	M4PP TCR B' (10^{-3} K)	TCR PPMS (10^{-3} K)
7	Pt-7nm-b	50.59	0.73 ± 0.01	0.76 ± 0.01	0.96 ± 0.05
	Pt-7nm-c	50.40	0.75 ± 0.01	0.74 ± 0.01	0.97 ± 0.05
10	Pt-10nm-a	28.05	1.18 ± 0.01	1.13 ± 0.01	1.38 ± 0.07
	Pt-10nm-b	24.05	1.40 ± 0.01	1.37 ± 0.01	1.60 ± 0.08
16	Pt-16nm-a	14.55	1.63 ± 0.01	1.63 ± 0.01	1.71 ± 0.09
	Pt-16nm-c	14.48	1.61 ± 0.01	1.63 ± 0.01	1.77 ± 0.09

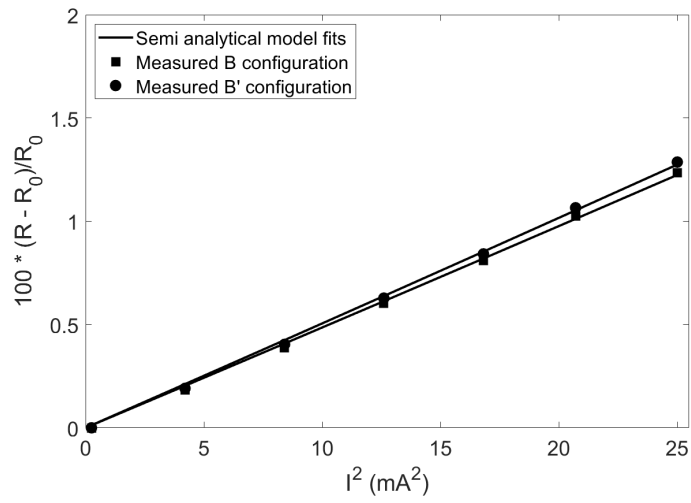
Table B.1: *The results of the B configuration fit on the 10 μm pitch 10A subprobe. The reported errors are the standard error from the fit.*

Film thickness (nm)	coupon ID	Sheet resistance (Ω)	M4PP TCR C (10^{-3} K)	M4PP TCR C' (10^{-3} K)	TCR PPMS (10^{-3} K)
7	Pt-7nm-b	50.59	0.75 ± 0.01	0.74 ± 0.01	0.96 ± 0.05
	Pt-7nm-c	50.40	0.77 ± 0.01	0.73 ± 0.01	0.97 ± 0.05
10	Pt-10nm-a	28.05	1.22 ± 0.01	1.12 ± 0.01	1.38 ± 0.07
	Pt-10nm-b	24.05	1.44 ± 0.01	1.34 ± 0.01	1.60 ± 0.08
16	Pt-16nm-a	14.55	1.75 ± 0.01	1.58 ± 0.01	1.71 ± 0.09
	Pt-16nm-c	14.48	1.75 ± 0.01	1.58 ± 0.01	1.77 ± 0.09

Table B.2: *The results of the C configuration fit on the 10 μm pitch 10A subprobe. The reported errors are the standard error from the fit.*



(a)



(b)

Figure B.1: *The semi-analytical model fits to the measured increase in resistance in the B-configuration on the '10A' subprobe. Symmetry means both the B and B' show the same response. The coupons shown are as follows: (a) Pt-16a, (b) Pt-16c.*

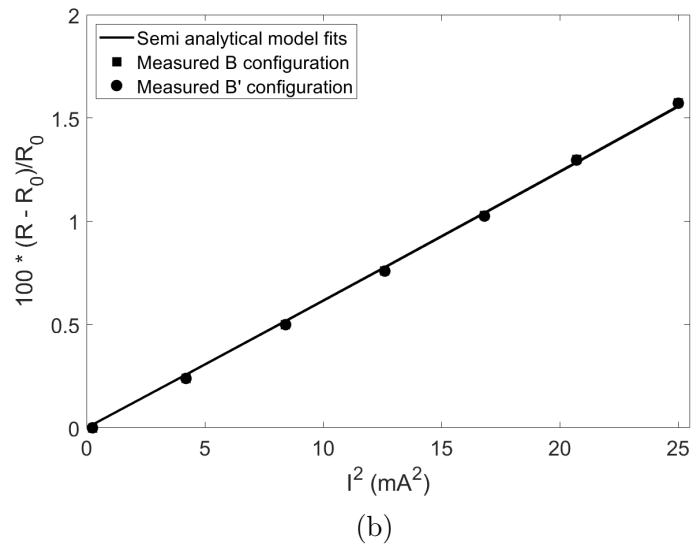
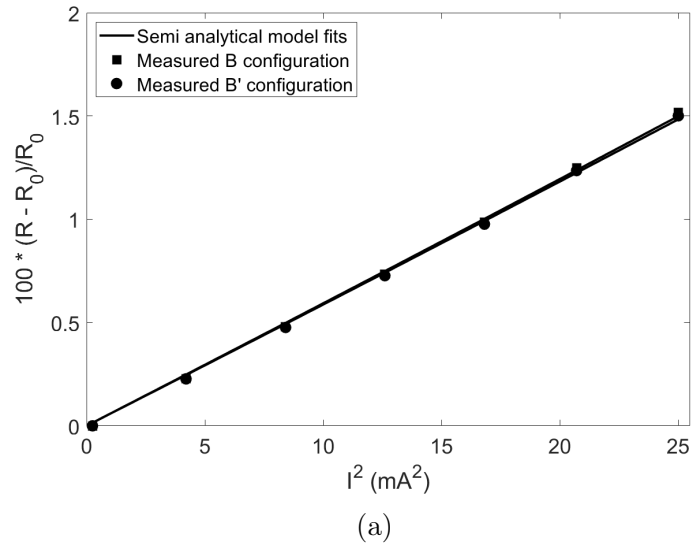


Figure B.2: *The semi-analytical model fits to the measured increase in resistance in the B-configuration on the '10A' subprobe. Symmetry means both the B and B' show the same response. The coupons shown are as follows: (a) Pt-10a, (b) Pt-10b.*

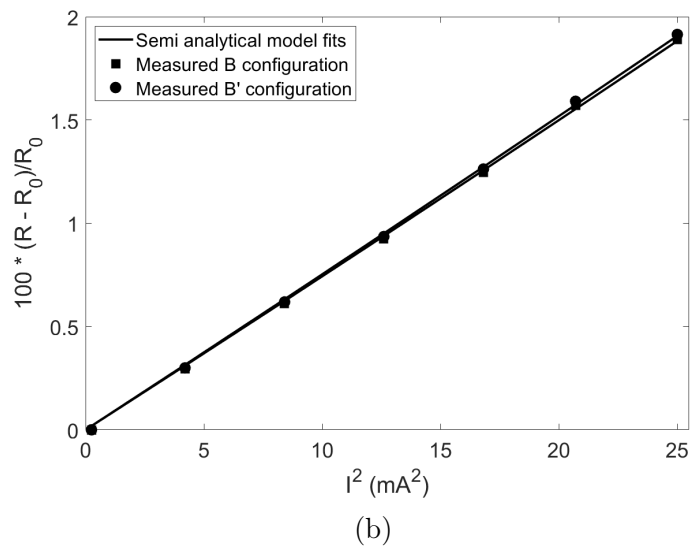
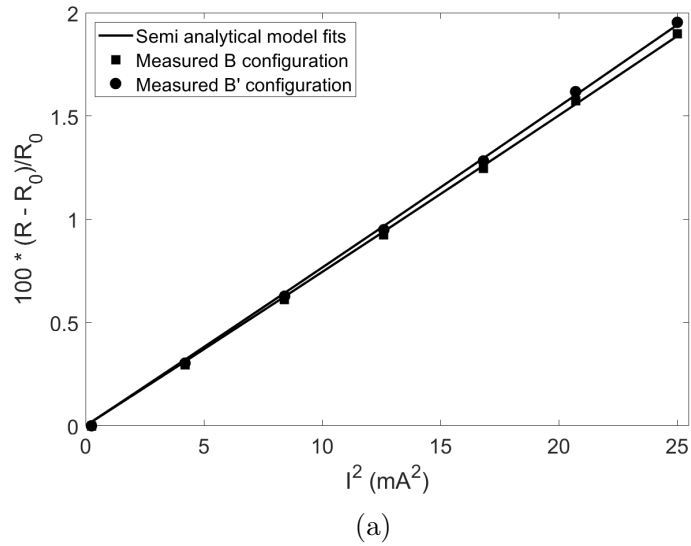
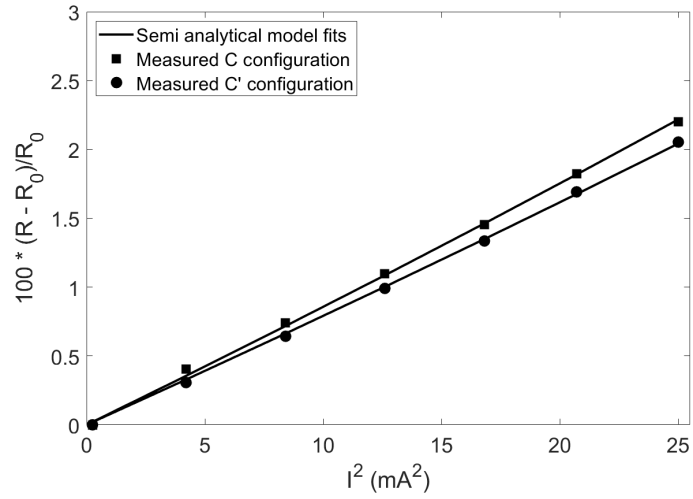
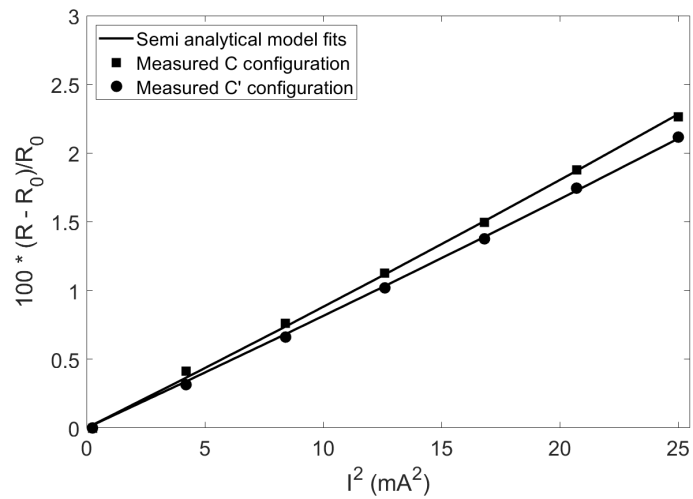


Figure B.3: *The semi-analytical model fits to the measured increase in resistance in the B-configuration on the '10A' subprobe. Symmetry means both the B and B' show the same response. The coupons shown are as follows: (a) Pt-7b, (b) Pt-7c.*

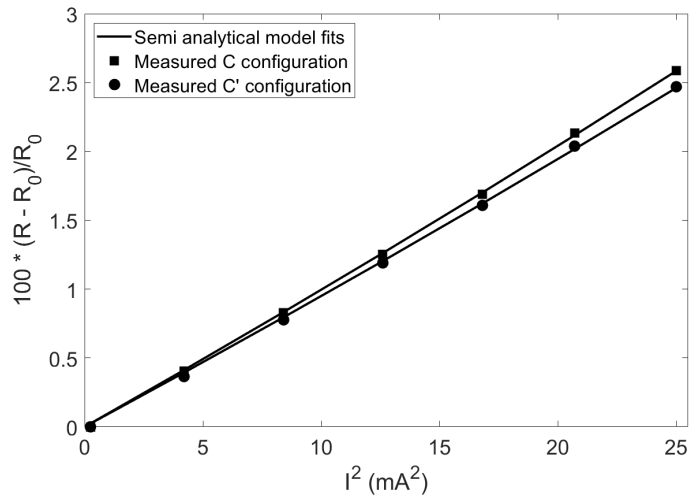


(a)

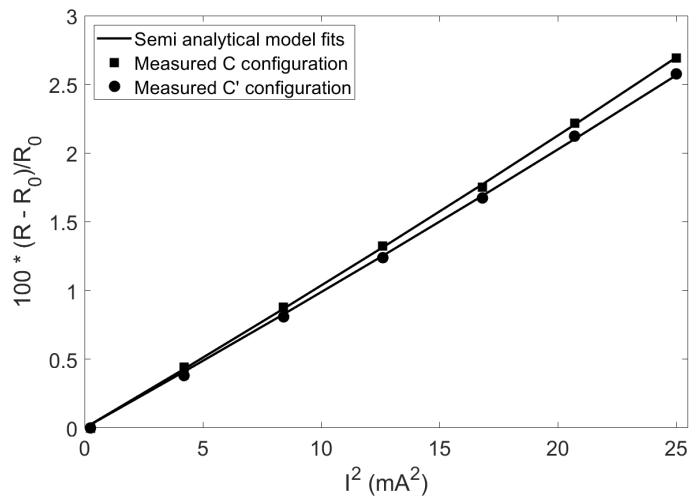


(b)

Figure B.4: The semi-analytical model fits to the measured increase in resistance in the C-configuration on the '10A' subprobe. Symmetry means both the C and C' show the same response. The coupons shown are as follows: (a) Pt-16a, (b) Pt-16c.



(a)



(b)

Figure B.5: The semi-analytical model fits to the measured increase in resistance in the C-configuration on the '10A' subprobe. Symmetry means both the C and C' show the same response. The coupons shown are as follows: (a) Pt-10a, (b) Pt-10b.

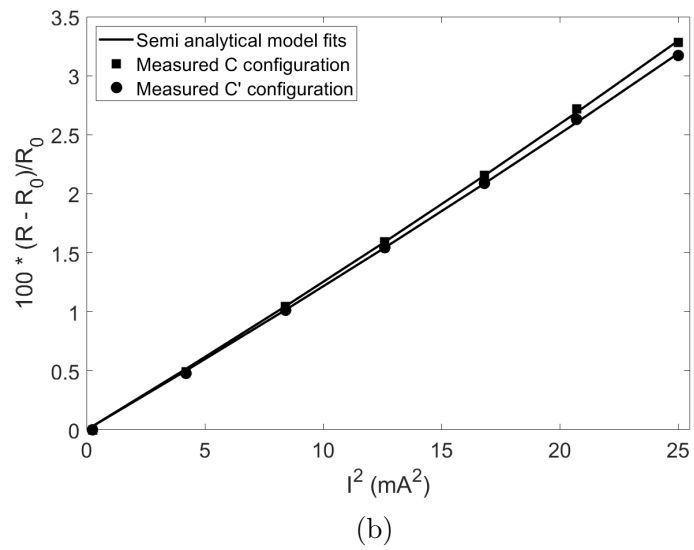
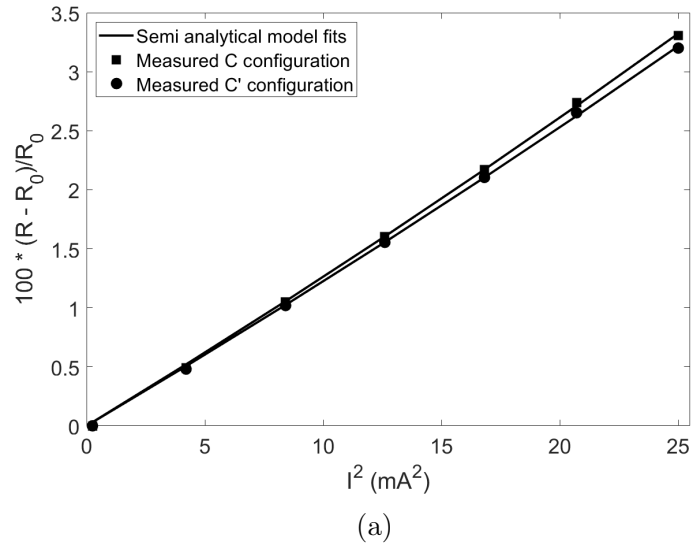


Figure B.6: *The semi-analytical model fits to the measured increase in resistance in the C-configuration on the '10A' subprobe. Symmetry means both the C and C' show the same response. The coupons shown are as follows: (a) Pt-7b, (b) Pt-7c.*

B.2 A, B and C configuration on the 10B subprobe

Film thickness (nm)	coupon ID	Sheet resistance (Ω)	M4PP TCR A (10^{-3} K)	M4PP TCR A' (10^{-3} K)	TCR PPMS (10^{-3} K)
7	Pt-7nm-b	50.59	0.73 ± 0.01	0.74 ± 0.01	0.96 ± 0.05
	Pt-7nm-c	50.40	0.75 ± 0.01	0.76 ± 0.01	0.97 ± 0.05
10	Pt-10nm-a	28.05	1.12 ± 0.01	1.18 ± 0.01	1.38 ± 0.07
	Pt-10nm-b	24.05	1.34 ± 0.01	1.42 ± 0.01	1.60 ± 0.08
16	Pt-16nm-a	14.55	1.54 ± 0.02	1.57 ± 0.01	1.71 ± 0.09
	Pt-16nm-c	14.48	1.56 ± 0.02	1.50 ± 0.01	1.77 ± 0.09

Table B.3: *The results of the A configuration fit on the 10 μm pitch 10B subprobe. The reported errors are the standard error from the fit.*

Film thickness (nm)	coupon ID	Sheet resistance (Ω)	M4PP TCR B (10^{-3} K)	M4PP TCR B' (10^{-3} K)	TCR PPMS (10^{-3} K)
7	Pt-7nm-b	50.59	0.72 ± 0.01	0.75 ± 0.01	0.96 ± 0.05
	Pt-7nm-c	50.40	0.76 ± 0.01	0.74 ± 0.01	0.97 ± 0.05
10	Pt-10nm-a	28.05	1.17 ± 0.01	1.14 ± 0.01	1.38 ± 0.07
	Pt-10nm-b	24.05	1.40 ± 0.01	1.37 ± 0.01	1.60 ± 0.08
16	Pt-16nm-a	14.55	1.46 ± 0.02	1.61 ± 0.02	1.71 ± 0.09
	Pt-16nm-c	14.48	1.49 ± 0.02	1.52 ± 0.02	1.77 ± 0.09

Table B.4: *The results of the B configuration fit on the 10 μm pitch 10B subprobe. The reported errors are the standard error from the fit.*

Film thickness (nm)	coupon ID	Sheet resistance (Ω)	M4PP TCR C (10^{-3} K)	M4PP TCR C' (10^{-3} K)	TCR PPMS (10^{-3} K)
7	Pt-7nm-b	50.59	0.70 ± 0.01	0.76 ± 0.01	0.96 ± 0.05
	Pt-7nm-c	50.40	0.73 ± 0.01	0.77 ± 0.01	0.97 ± 0.05
10	Pt-10nm-a	28.05	1.15 ± 0.01	1.20 ± 0.01	1.38 ± 0.07
	Pt-10nm-b	24.05	1.36 ± 0.01	1.44 ± 0.01	1.60 ± 0.08
16	Pt-16nm-a	14.55	1.51 ± 0.01	1.65 ± 0.01	1.71 ± 0.09
	Pt-16nm-c	14.48	1.55 ± 0.01	1.53 ± 0.01	1.77 ± 0.09

Table B.5: *The results of the C configuration fit on the 10 μm pitch 10B subprobe. The reported errors are the standard error from the fit.*

B.3 A, B and C configurations on the 20 sub-probe

Film thickness (nm)	coupon ID	Sheet resistance (Ω)	M4PP TCR A (10^{-3} K)	M4PP TCR A' (10^{-3} K)	TCR PPMS (10^{-3} K)
7	Pt-7nm-b	50.59	0.65 ± 0.01	0.75 ± 0.01	0.96 ± 0.05
	Pt-7nm-c	50.40	0.67 ± 0.01	0.75 ± 0.01	0.97 ± 0.05
10	Pt-10nm-a	28.05	0.98 ± 0.01	1.14 ± 0.01	1.38 ± 0.07
	Pt-10nm-b	24.05	1.19 ± 0.02	1.35 ± 0.01	1.60 ± 0.08
16	Pt-16nm-a	14.55	1.30 ± 0.03	1.50 ± 0.02	1.71 ± 0.09
	Pt-16nm-c	14.48	1.31 ± 0.03	1.46 ± 0.02	1.77 ± 0.09

Table B.6: *The results of the A configuration fit on the 20 μm pitch 20 subprobe. The reported errors are the standard error from the fit.*

Film thickness (nm)	coupon ID	Sheet resistance (Ω)	M4PP TCR B (10^{-3} K)	M4PP TCR B' (10^{-3} K)	TCR PPMS (10^{-3} K)
7	Pt-7nm-b	50.59	0.67 ± 0.01	0.75 ± 0.01	0.96 ± 0.05
	Pt-7nm-c	50.40	0.70 ± 0.01	0.75 ± 0.01	0.97 ± 0.05
10	Pt-10nm-a	28.05	1.05 ± 0.01	1.10 ± 0.01	1.38 ± 0.07
	Pt-10nm-b	24.05	1.25 ± 0.01	1.31 ± 0.01	1.60 ± 0.08
16	Pt-16nm-a	14.55	1.29 ± 0.02	1.55 ± 0.02	1.71 ± 0.09
	Pt-16nm-c	14.48	1.33 ± 0.02	1.54 ± 0.02	1.77 ± 0.09

Table B.7: *The results of the B configuration fit on the 20 μm pitch 20 subprobe. The reported errors are the standard error from the fit.*

Film thickness (nm)	coupon ID	Sheet resistance (Ω)	M4PP TCR C (10^{-3} K)	M4PP TCR C' (10^{-3} K)	TCR PPMS (10^{-3} K)
7	Pt-7nm-b	50.59	0.72 ± 0.01	0.73 ± 0.01	0.96 ± 0.05
	Pt-7nm-c	50.40	0.74 ± 0.01	0.74 ± 0.01	0.97 ± 0.05
10	Pt-10nm-a	28.05	1.15 ± 0.01	1.09 ± 0.01	1.38 ± 0.07
	Pt-10nm-b	24.05	1.39 ± 0.01	1.30 ± 0.01	1.60 ± 0.08
16	Pt-16nm-a	14.55	1.53 ± 0.02	1.59 ± 0.02	1.71 ± 0.09
	Pt-16nm-c	14.48	1.55 ± 0.02	1.55 ± 0.02	1.77 ± 0.09

Table B.8: *The results of the C configuration fit on the 20 μm pitch 20 subprobe. The reported errors are the standard error from the fit.*

Supplementary material

Attached are three articles (two published, one in preparation) that have been produced in relation to the PhD project.

Paper I

'Determination of the temperature coefficient of resistance from micro four-point probe measurements.'

Thomas A. Marangoni, Benny Guralnik, Kasper A. Borup, Ole Hansen, and
Dirch H. Petersen

*Reproduced from J. Appl. Phys. 129(16), 165105., with the permission of AIP
Publishing.*

Determination of the temperature coefficient of resistance from micro four-point probe measurements **F**

Cite as: J. Appl. Phys. **129**, 165105 (2021); <https://doi.org/10.1063/5.0046591>

Submitted: 04 February 2021 . Accepted: 08 April 2021 . Published Online: 27 April 2021

 Thomas A. Marangoni,  Benny Guralnik,  Kasper A. Borup,  Ole Hansen, and  Dirch H. Petersen

COLLECTIONS

F This paper was selected as Featured



View Online



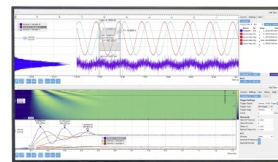
Export Citation



CrossMark

Challenge us.

What are your needs for periodic signal detection?



Zurich Instruments

Determination of the temperature coefficient of resistance from micro four-point probe measurements

Cite as: J. Appl. Phys. **129**, 165105 (2021); doi: [10.1063/5.0046591](https://doi.org/10.1063/5.0046591)

Submitted: 4 February 2021 · Accepted: 8 April 2021 ·

Published Online: 27 April 2021



Thomas A. Marangoni,^{1,2}  Benny Guralnik,^{1,3}  Kasper A. Borup,⁴  Ole Hansen,⁵  and Dirch H. Petersen^{1,a)} 

AFFILIATIONS

¹Department of Energy Conversion and Storage, Technical University of Denmark, Fysikvej, Building 310, DK-2800 Kgs. Lyngby, Denmark

²Department of Physics, Technical University of Denmark, Fysikvej, Building 307, DK-2800 Kgs. Lyngby, Denmark

³CAPRES—a KLA company, Diplomvej 373, 2800 Kgs. Lyngby, Denmark

⁴Department of Chemistry, Aarhus University, Langelandsgade 140, DK-8000 Aarhus C, Denmark

⁵National Centre for Nano Fabrication and Characterization, DTU Nanolab, Technical University of Denmark, DK-2800 Kgs. Lyngby, Denmark

^{a)}Author to whom correspondence should be addressed: dhpe@dtu.dk

ABSTRACT

Current characterization methods of the temperature coefficient of resistance (TCR) of thin films are often limited to slow macroscale measurements, which further require a direct determination of temperature. In this work, we present an innovative application of micro four-point probe (M4PP) sensing, which enables a fast, non-destructive, local measurement of Joule heating effects that can be translated into TCR of the thin film. Analytical expressions for the four-point resistance response to local heating, and ultimately the temperature profile during an M4PP measurement, are derived and validated against finite element models. The method is successfully demonstrated on three metal thin films (7, 10, and 16 nm platinum deposited on fused silica). We evaluate TCR using two different electrode configurations, resulting in unique temperature fields, and observe a measurement repeatability of <2% for each configuration. Furthermore, the M4PP-TCR method shows only a minor (~18%) systematic offset relative to reference TCR measurements obtained via an independent physical property measurement system. Our results demonstrate a new technique for characterizing TCR on the micrometer scale, adequately backed by theory. The measurement time is just a few seconds and could allow for thin film TCR mapping or in-line process monitoring on test structures.

© 2021 Author(s). All article content, except where otherwise noted, is licensed under a Creative Commons Attribution (CC BY) license (<http://creativecommons.org/licenses/by/4.0/>). <https://doi.org/10.1063/5.0046591>

I. INTRODUCTION

The temperature coefficient of resistance (TCR) is a coefficient of a polynomial (typically linear) approximation of the fractional change in the electrical resistivity ρ of a material ($d\rho/\rho$) upon an incremental change in temperature (dT), validated and applicable within a certain thermal range.¹ Considering that the exact functional relationship $\rho = f(T)$ depends on a multitude of material properties (e.g., geometry, grain size, chemical composition, defects and impurities, etc.), it becomes susceptible to mathematical description only for certain isolated effects, such as thin film

thickness² or semiconductor doping level.³ TCR, on the other hand, is a phenomenological and straightforward experimental metric, obtained by fitting the fractional change in resistivity over a certain temperature range using a polynomial of temperature,⁴ most often sufficiently well described by its linear part alone.¹ During the 19th and the early 20th centuries, the TCR of metals (positive, and generally falling within the 2–6‰ K⁻¹ range) received considerable attention from leading experimentalists including Lenz, Becquerel, Siemens, Clausius, Kirchhoff, and Matthiesen.⁵ Following the boom of semiconductors and functional oxides after the Second World

War, materials with negative TCR have been discovered, documented, and heavily utilized in thermometry.⁶ Most recent advances of the past decade include the fabrication of zero-TCR^{7,8} or tunable-TCR materials.^{9,10}

Today, the TCR has a wide range of applications in microelectronics and material and device characterization. Tunable or zero TCR materials such as antiperovskite compounds^{7–10} are desirable in reference resistors and anti-surge resistors in high power applications. In addition, zero- to low-TCR conductors are beneficial in limiting the effects of self-heating of micro- and nanoelectronic devices which, in turn, promotes low energy-consumption electronics.^{11,12} The characterization of the resistance and cross-sectional area^{13,14} as well as the reliability and performance of interconnects^{15,16} can be achieved via measurements of TCR. A precise knowledge of TCR is also essential in the fabrication of, e.g., thermal¹⁷ and flow¹⁸ sensors. In addition, TCR can be applied to determine doping levels in silicon-based resistors.³ Thus, both the engineering and the post-fabrication determination of TCR remain an extremely relevant and active field of research, as thermal effects start bringing Moore's law to a stall.¹⁹

As materials are scaled down to nanometer dimensions, the TCR deviates from its bulk value. This deviation is predicted by an adaptation of the Mayadas–Schatzkes model of thin film resistivity^{2,20} and observed in nanometer thin films.^{21–25} Current techniques for characterizing TCR are limited to measuring patterned thin film resistors^{22,26,27} and additionally require a separate, independent temperature measurement. This could be in the form of a temperature controlled chamber,²² keeping the entire sample at an equilibrium temperature. Alternatively, one can locally measure the temperature during a resistance measurement via a fabricated thermocouple near the points of interest.²⁸ While this does encompass self-heating and local effects, it requires the need for complex sample preparation.

In this work, we present a method capable of locally measuring the TCR of ultrathin conductive films without requiring a separate temperature measurement by utilizing a by-product of four-terminal sensing, namely, Joule heating. The micro four-point probe (M4PP)²⁹ is a widely used metrology for the characterization of metallic and semiconducting thin films, including magnetic

tunnel junctions³⁰ and ultrashallow junctions.³¹ Sheet resistance of thin films^{32,33} can be rapidly measured with high precision,³⁴ and it is possible to measure accurately in small test pads down to $10 \times 10 \mu\text{m}^2$ ^{35,36} or perform entire wafer scans.³⁷ It is even possible to measure the line resistance on fins down to 20 nm width.^{38,39} So far, Joule heating in M4PP has been perceived as a problem and addressed primarily via minimization strategies.^{40,41} Conversely, in this study, we instead amplify Joule heating and utilize it to constrain important material properties previously unaddressed by a M4PP measurement setup.

II. THEORY

A. Transfer resistance of a thin film obeying a linearized resistivity model

During a four-point probe measurement, current I flows through a material with resistivity ρ , from the current source electrode located at \mathbf{r}_+ to the drain electrode at \mathbf{r}_- , while the resulting potential difference is being sensed across two other electrodes located at \mathbf{r}_{V+} and \mathbf{r}_{V-} . In this work, we focus on the current distribution in an “infinitely thin” conductive sheet (e.g., a metallic thin film), whose thickness d is negligible in comparison to all other distances considered [Fig. 1(a)]. For convenience, electric resistivity and film thickness are hereforth combined into the sheet resistance $R_S = \rho/d$.

During the measurement, the electric sheet current density \mathbf{J}_S at an arbitrary location \mathbf{r} on the sheet may be obtained via a superposition of the radial current densities around the source and drain electrodes, respectively,

$$\mathbf{J}_S(\mathbf{r}) = \frac{I(\mathbf{r} - \mathbf{r}_+)}{2\pi|\mathbf{r} - \mathbf{r}_+|^2} + \frac{-I(\mathbf{r} - \mathbf{r}_-)}{2\pi|\mathbf{r} - \mathbf{r}_-|^2}. \quad (1)$$

Consequently, the sheet power density at \mathbf{r} is given by

$$R_S(\mathbf{r})|\mathbf{J}_S(\mathbf{r})|^2 = \frac{R_S(\mathbf{r})I^2}{4\pi^2} \left(\frac{|\mathbf{r}_+ - \mathbf{r}_-|}{|\mathbf{r} - \mathbf{r}_+||\mathbf{r} - \mathbf{r}_-|} \right)^2, \quad (2)$$

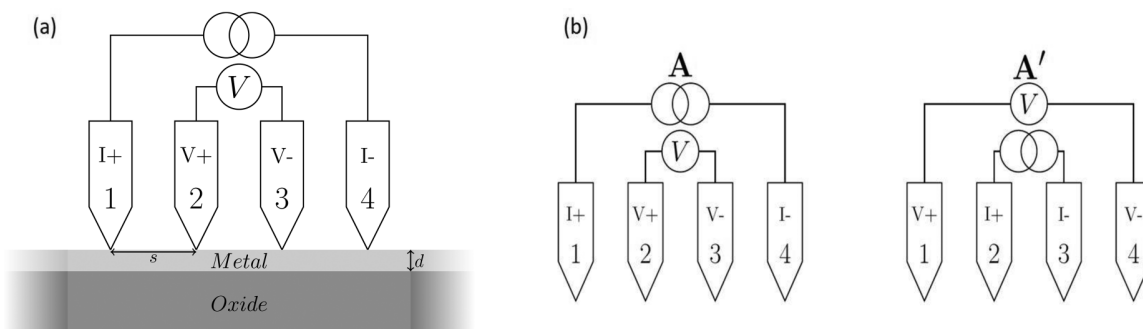


FIG. 1. (a) Schematic of a collinear and equidistant micro four-point probe, in contact with a thin metal film deposited onto a thick oxide. (b) Two specific configurations of current and voltage assignment (A and A') were utilized for numerical simulations and actual measurements. I+ and I- denote the current injection and extraction electrodes, respectively, while V+ and V- indicate the voltage probing electrodes and their polarities. A' is considered as the adjoint configuration of A (and vice versa), since it is obtained by swapping the current and voltage assignments (see text).

where $R_S(\mathbf{r})$ is the local sheet resistance, and the bracketed fraction is the source-to-drain distance further divided by the separation distances of \mathbf{r} from both the source and the drain.

Joule heating, defined to be proportional to the power in Eq. (2), causes a local change in the surface temperature $\Delta T(\mathbf{r})$ and thereby a local change in $R_S(\mathbf{r})$, which under a linear TCR approximation⁴² is given by

$$R_S(\mathbf{r}) = R_{S,0}[1 + \alpha_{\text{TCR}}\Delta T(\mathbf{r})], \quad (3)$$

where α_{TCR} is the temperature coefficient of resistance and $R_{S,0}$ is the sheet resistance at a reference temperature T_0 (relative to which $\Delta T = T - T_0$ is evaluated).

To predict how the behavior of a system obeying Eqs. (1)–(3) is reflected in M4PP measurements, we start by considering the case of $\alpha_{\text{TCR}} = 0$ leading to a spatially uniform $R_S(\mathbf{r}) = R_S$. The potential drop ΔV measured across the voltage pins divided by the current is known as “transfer resistance” $R = \Delta V/I$ and is given by

$$R = \frac{R_S}{F}, \quad F = 2\pi / \ln \left(\frac{|\mathbf{r}_+ - \mathbf{r}_{V-}| |\mathbf{r}_- - \mathbf{r}_{V+}|}{|\mathbf{r}_+ - \mathbf{r}_{V+}| |\mathbf{r}_- - \mathbf{r}_{V-}|} \right), \quad (4)$$

where F is a transfer function, depending on four inter-electrode separation distances.^{32,43} To generalize Eq. (4) for $\alpha_{\text{TCR}} > 0$ where $R_S(\mathbf{r})$ becomes non-uniform, we replace R_S with a spatial integral of $R_S(\mathbf{r})$ according to Koon *et al.*,⁴³

$$R = \frac{\int_{\Omega} R_S(\mathbf{r}) \hat{S}(\mathbf{r}) d\Omega}{F}, \quad \hat{S}(\mathbf{r}) = \frac{\mathbf{J}_S(\mathbf{r}) \cdot \tilde{\mathbf{J}}_S(\mathbf{r})}{\int_{\Omega} [\mathbf{J}_S(\mathbf{r}) \cdot \tilde{\mathbf{J}}_S(\mathbf{r})] d\Omega}, \quad (5)$$

where Ω is the area of the sheet, $d\Omega$ its infinitesimal element, and $\hat{S}(\mathbf{r})$ is the M4PP sensitivity to a local perturbation at \mathbf{r} . From Eq. (5), it is clear that $\hat{S}(\mathbf{r})$ acts as a spatial weighting function with units of (m^{-2}) (cf. Ref. 43, who further nondimensionalized \hat{S} through multiplication by an arbitrary area). The weights in \hat{S} magnify or suppress the effect of local R_S variations on the resultant single value of R according to the dot product between \mathbf{J}_S , the actual current density in the system [Eq. (1)], and $\tilde{\mathbf{J}}_S$, the hypothetical current density in an adjoint system with interchanged current and voltage assignments⁴⁴ [e.g., $\tilde{\mathbf{J}}_{S,A} = \mathbf{J}_{S,A'}$ and $\tilde{\mathbf{J}}_{S,A'} = \mathbf{J}_{S,A}$ in Fig. 1 (b)].

Combining Eqs. (3) and (5), we can express the fractional change in the M4PP transfer resistance as

$$\frac{R - R_0}{R_0} = \alpha_{\text{TCR}} \int_{\Omega} \Delta T(\mathbf{r}) \hat{S}(\mathbf{r}) d\Omega, \quad (6)$$

where R_0 is the “zero-current resistance,”⁴⁵ i.e., its idealized value unaffected by Joule heating.

B. Calculation of the temperature profile in a thin film blanket

To put Eq. (6) into practice, we proceed to consider a thin film “blanket,” e.g., a thin layer of metal deposited onto an “infinitely thick” and electrically inert substrate. We expect the thermal resistance of the system to be dominated by the thermal

conductivity κ of the substrate. Thus, for simplicity, we neglect lateral heat transport through the thin film and the thermal loss to air. We further assume Peltier heat displacement is negligible.

We will divide the sheet into two distinct regions, namely, the contact areas under the current source and drain, and all the remaining areas outside of both contacts. We can approximate the contact geometry under the current electrodes as circular disks of radius r_0 , and define that all the resistance at distances $r < r_0$ (including contribution from contact resistivity and spreading resistance) contributes to the “contact resistance” R_+ and R_- , at the current source and drain respectively (for calculation of R_+ and R_- , from two terminal resistance data, see Appendix A). Consequently, these contact areas will be excluded from Eq. (2). The Joule heat produced by R_+ and R_- at \mathbf{r}_+ and \mathbf{r}_- , respectively, can be modeled as a point heat source. Solving for heat diffusion from a point source into a bulk half-space,⁴⁶ the temperature rise at an arbitrary location \mathbf{r} should obey

$$\Delta T_{\text{contacts}}(\mathbf{r}) = \frac{I^2 R_+}{2\pi\kappa} \frac{1}{|\mathbf{r} - \mathbf{r}_+|} + \frac{I^2 R_-}{2\pi\kappa} \frac{1}{|\mathbf{r} - \mathbf{r}_-|}. \quad (7)$$

Treating the sheet power density [Eq. (2)] as a continuous distribution of point heat sources yields a similar expression,

$$\Delta T_{\text{sheet}}(\mathbf{r}) = \int_{\mathbf{r}' \in \Omega} \frac{R_S(\mathbf{r}') |\mathbf{J}_S(\mathbf{r}')|^2}{2\pi\kappa} \frac{d\Omega}{|\mathbf{r} - \mathbf{r}'|}, \quad (8)$$

where \mathbf{r}' is an arbitrary location where the sheet power density is $R_S(\mathbf{r}') |\mathbf{J}_S(\mathbf{r}')|^2$ according to Eq. (2), and $d\Omega$ is its corresponding infinitesimal area. The total temperature change at an arbitrary location \mathbf{r} is then the sum of Eqs. (7) and (8), with $R_S(\mathbf{r}')$ further substituted from Eq. (3),

$$\Delta T(\mathbf{r}) = \frac{I^2}{2\pi\kappa} \left(\frac{R_+}{|\mathbf{r} - \mathbf{r}_+|} + \frac{R_-}{|\mathbf{r} - \mathbf{r}_-|} + \frac{R_{S,0} |\mathbf{r}_+ - \mathbf{r}_-|^2}{4\pi^2} \int_{\mathbf{r}' \in \Omega} \frac{1 + \alpha_{\text{TCR}} \Delta T(\mathbf{r}')}{|\mathbf{r}' - \mathbf{r}_+|^2 |\mathbf{r}' - \mathbf{r}_-|^2 |\mathbf{r}' - \mathbf{r}|} d\Omega \right). \quad (9)$$

Note that Eq. (9) is implicit with regard to ΔT , arising from the circular dependence of the sheet resistance on temperature in the TCR definition [Eq. (3)], and of temperature on sheet resistance in the Joule heating [Eqs. (2) and (8)]. Despite the recursion, Eq. (9) does rapidly converge for a broad range of realistic values [typically within 3 iterations for an initial guess of $\Delta T = 0$ and $R_S(\mathbf{r}) = R_S$]. Since the contact areas are negligible, the contact resistances R_+ and R_- are assumed to be constant, i.e., independent of current and temperature; relaxing this assumption leads to practically unaltered results, on the expense of another level of implicitness for ΔT , i.e., $R_{\pm} = f(I, \Delta T)$.

C. Practical considerations

The treatment in Secs. II A and II B has been developed and numerically validated for an arbitrary M4PP pin configuration, applicable as long as its relevant current distributions (self \mathbf{J}_S and adjoint $\tilde{\mathbf{J}}_S$) can be calculated. Hereafter, we proceed to focus on

only two collinear and equidistant pin configurations A and A' [Fig. 1(b)], whose induced current flow in the sample, and thus the heat generation and resulting temperature distribution, are markedly different [Figs. 2(a) and 2(b), respectively]. However, since A and A' are mutually adjoint configurations [Fig. 1(b)], they both share the same sensitivity function [\hat{S} in Eq. (5)], depicted in Fig. 2(c). This shared sensitivity allows us to attribute any deviations of the observed resistance R from zero-current resistance R_0 to thermal effects only [cf. Eq. (6)]. Additionally, the symmetry of both configurations about the probe center makes them

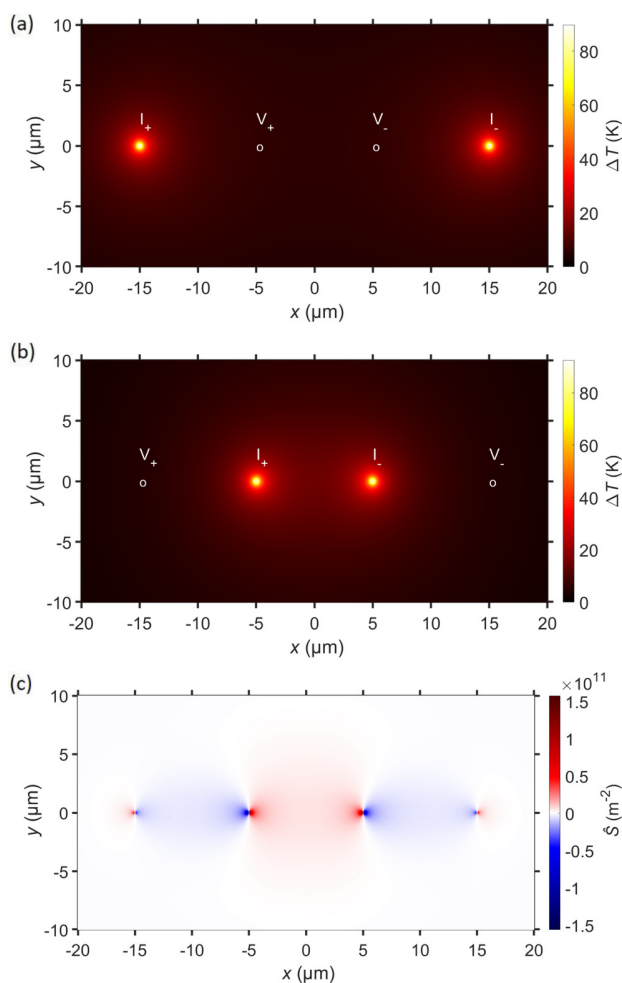


FIG. 2. (a) The surface temperature increase generated during a 5 mA M4PP measurement on a 16 nm platinum film in the A configuration, obtained from a finite element simulation with $R_S = 14.4 \Omega$, $\alpha_{\text{TCR}} = 2 \times 10^{-3} \text{ K}^{-1}$ and no contact resistance. The locations of the voltage electrodes are indicated. (b) The surface temperature increase, obtained from an identical finite element simulation with the probe in the A' configuration, with the locations of the voltage electrodes indicated. (c) The calculated probe sensitivity for this probe, valid for both the A and A' configurations.

significantly less sensitive to variation in contact resistance (R_{\pm}) across the four probe pins [cf. Eq. (9)].

Finite element simulations of the temperature rise $\Delta T(\mathbf{r})$, associated with a M4PP measurement of a $R_S = 14.4 \Omega$ thin film with a DC current of 5 mA under configurations A and A', are shown in Figs. 2(a) and 2(b), respectively (probe pitch $10 \mu\text{m}$, $\alpha_{\text{TCR}} = 2 \times 10^{-3} \text{ K}^{-1}$, $R_{\pm} = 0 \Omega$). Figure 2(c) shows the associated sensitivity function, common to both A and A'. The areas of positive (negative) sensitivity imply an increase (decrease) in the measured transfer resistance R , given a local increase in R_S due to a positive TCR. From a qualitative study of Fig. 2, we may expect a higher increase in R in the A' configuration, since more of the heated area is concentrated within a region of positive sensitivity $\hat{S}(\mathbf{r}) > 0$.

III. METHODS

A. Materials and instrumentation

Three metal-on-insulator thin films were fabricated by e-beam evaporation as follows. The substrate of all samples consisted of a 1 mm thick and double side polished 4-inch wafer of fused silica, chosen to serve two purposes: to restrict Joule heating solely to the thin film, and to magnify the resultant thermal gradients (given its low thermal conductivity, presumed to be $1.4 \text{ W m}^{-1} \text{ K}^{-1}$). An adhesion layer of 1 nm Ti, followed by a platinum thin film of a desired thickness, was deposited on one side of the wafer via e-beam evaporation (Wordentec QCL800). A total of three samples, with nominal Pt film thicknesses of 7, 10, or 16 nm, were fabricated (the observed non-uniformity of the 10 nm thin film may be attributed to a broken vacuum seal during its fabrication). The fabricated wafers were subsequently split into smaller coupons, up to $11 \times 14 \text{ mm}$ in size.

To obtain an independent estimate of the TCR, several coupons of each wafer (Table I) were measured using a physical property measurement system (PPMS from Quantum Design). For those measurements, the surface of the platinum thin film was contacted at four locations at the coupon's edges, allowing for a four-terminal measurement of the film's resistance. The sample was then placed in a temperature controlled chamber, where temperature was ramped from 290 to 310 K in steps of 5 K, while the resistance being continuously measured using an AC current with $I_{\text{RMS}} = 5 \text{ mA}$ at $f = 18.3 \text{ Hz}$. To obtain the TCR at room temperature (293 K), $R = R_0[1 + \alpha_{\text{TCR}}\Delta T]$ [cf. Eq. (3)] was directly fitted to the paired T and R data.

The M4PP measurements were performed on a microRSP A300 system from CAPRES A/S, which measures the resistance using a lock-in amplifier. We used a collinear seven-point probe with equidistant $10 \mu\text{m}$ pitch.⁴⁷ The polysilicon electrodes were coated with a 100 nm Ni layer serving as the current carrier. After the probe is brought into physical contact with the sample surface, electric measurements proceed at user-selected currents and pin configurations. For reproducibility, we performed up to 30 consecutive engages, laterally spaced apart by $20 \mu\text{m}$. At each engagement, an AC current at $f = 12.055 \text{ Hz}$ is forced through the sample while switching through several electrode configurations, including the aforementioned A and A' configurations (Sec. II C). During each engagement, the AC current was ramped from $I_{\text{RMS}} = 5 \text{ mA}$ down to 0.5 mA in seven steps, and ramped up again for three replicate

measurements. The potential drop across the voltage electrodes V is measured with a lock-in amplifier and reported as transfer resistance $R = V/I_{\text{RMS}}$. The corresponding sheet resistance is calculated using the dual configuration method.⁴⁸

To calibrate lead resistances and monitor potential drift in contact resistances, a reference M4PP measurement on a thick nickel slab is performed before and after every group of ten measurements on the samples. The reference measurement frequency, pin configurations and currents are identical to an engage on a real sample; given that the $R_s = 0.48 \Omega$ of the Ni reference is by ~ 2 orders of magnitude lower than that of the studied samples, we evaluate the two-point resistance of the calibration measurements as dominated by the lead resistance, that is, the contribution from all sample-unrelated sources (following all the interconnects from the electrode cantilevers up to the current generator). This lead resistance is then subtracted from measurements made on the Pt thin films⁴⁹ (the calculation of contact resistances is detailed in Appendix A).

B. Numerical approach

To extract the TCR from M4PP resistance measurements on the microRSP A300 as described in Sec. III A, Eq. (6) has to be adapted to AC currents, and solved. The adaptation to AC currents is straightforward (Appendix B), scaling the solution by a constant $c = 3/2$. However, since the integral in Eq. (6) does not appear amenable to a closed-form solution, a semi-analytical approach was adopted, namely, evaluating an adapted Eq. (6) over a mesh of n finite elements,

$$\frac{dR}{R} \cong \frac{R - R_0}{R_0} = c\alpha_{\text{TCR}} \sum_{i=1}^n \Delta T(\mathbf{r}_i) \hat{S}(\mathbf{r}_i) \Omega_i, \quad (10)$$

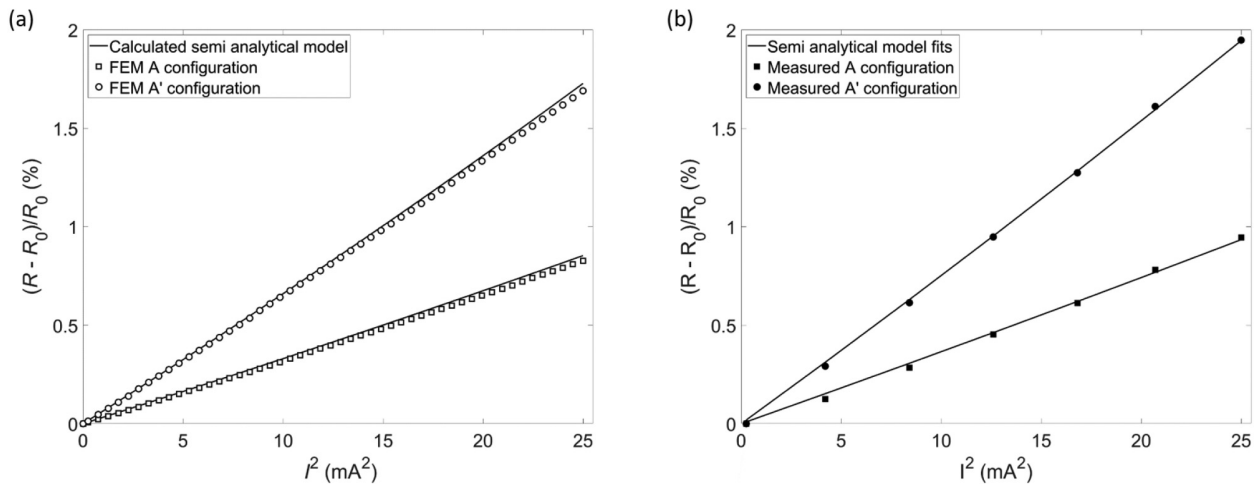


FIG. 3. (a) The increase in resistance given by the DC semi-analytical model [Eq. (10) with $c = 1$] and finite element simulations (FEM) of both the A and A' configurations, on the same simulated 16 nm Pt film with the same arbitrary TCR value. (b) The AC semi-analytical model [Eq. (10) with $c = 3/2$] fit to measured data taken on a 16 nm Pt film for both the A and A' configurations with a probe pitch of $10 \mu\text{m}$. The measured data shown is the mean value over 20 engagements with the error bars inside the symbols. The semi-analytical model is shown as a continuous line corresponding to calculated resistance values using the TCR obtained from the nonlinear least square fit.

where $c = 3/2$ is the AC prefactor (Appendix B), \mathbf{r}_i is the centroid of a mesh element i , and Ω_i the corresponding element's area. After testing several straightforward implementations (including densely meshed regular grids, quad-trees,⁵⁰ and DistMesh,⁵¹ the best tradeoff between computational time and calculation accuracy was achieved by constructing a specialized mesh as follows. For each configuration, each of the theoretically circular electrode contacts at \mathbf{r}_+ , \mathbf{r}_- , \mathbf{r}_{V+} , and \mathbf{r}_{V-} is approximated as an 18-sided hollow regular polygon; the rest of the mesh is constructed by the advancing front technique, i.e., via concentric polygons at geometrically progressing radii (growth rate of 1.08), which are triangulated to existing nodes at each incremental step. The outer extent of the mesh, determined by the condition $\int_{\Omega} [\mathbf{J}_S(\mathbf{r}_i) \cdot \mathbf{J}_S(\mathbf{r}_i)] d\Omega \cong (I/2\pi)^2$, was practically achieved (to within 0.01%) by reaching a perimeter that is three times the probe footprint (maximum inter-electrode distance) away from the probe's center. To further increase the performance by twofold, (anti)symmetric triangles sharing a long side were merged into quadrangles, leaving only $\sim 1\%$ of patching triangles at points of irregularity (convergence of arcs belonging to different centers). The final mesh typically contains a few thousand elements. For each element, the sensitivity $[\hat{S}(\mathbf{r}_i)]$ via Eq. (5) must be pre-calculated only once, while three iterations of temperature $[\Delta T(\mathbf{r}_i)]$ via Eq. (10) per a given current, converge to a stable value on the sub-second timescale.

IV. RESULTS

The results of the semi-analytical model [Eq. (10)] were benchmarked against a matching finite element model (FEM) implemented in COMSOL Multiphysics,⁵² simulating M4PP measurements in the 0.5–5 mA range (DC) on a conductive thin film with a TCR value of $2\% \text{K}^{-1}$ (probe pitch of $10 \mu\text{m}$ and contact radii of $r_0 = 100 \text{nm}$). The COMSOL model takes advantage of the

TABLE I. Overview of all TCR values compared to the reference values measured via PPMS on the same films. The TCR is extracted on each sample separately for the A and A' configurations, all measured on the same probe with a pitch of $10\ \mu\text{m}$. The M4PP values show the standard error, while the PPMS carries a 5% measurement error.

Nominal thin film thickness (nm)	Coupon ID	Sheet resistance (Ω)	Temperature coefficient of resistance ($10^{-3}\ \text{K}^{-1}$)		
			M4PP A	M4PP A'	PPMS (cm-scale)
7	Pt-7nm-b	50.59	0.73 ± 0.01	0.76 ± 0.01	0.96 ± 0.05
	Pt-7nm-c	50.40	0.74 ± 0.01	0.74 ± 0.01	0.97 ± 0.05
10	Pt-10nm-a	28.05	1.13 ± 0.02	1.17 ± 0.01	1.38 ± 0.07
	Pt-10nm-b	24.05	1.34 ± 0.02	1.40 ± 0.01	1.60 ± 0.08
16	Pt-16nm-a	14.55	1.59 ± 0.03	1.63 ± 0.01	1.71 ± 0.09
	Pt-16nm-c	14.48	1.58 ± 0.02	1.63 ± 0.01	1.77 ± 0.09

“heat transfer in solids” module for the substrate, and “electric currents in shells” module for the metallic thin film, linked through the “electromagnetic heating multiphysics.” The sample was represented by an $800 \times 800 \times 400\ \mu\text{m}$ square of fused silica with a thin, electrically conductive shell at its top boundary, the latter further assigned a linearized resistance model [Eq. (3)], with a room temperature sheet resistance $R_{S,0}$ equivalent to a 16 nm Pt film. Centered on the top boundary, the M4PP was modeled as four equidistantly placed circles serving as the electrode contacts, with a DC current injected at the perimeter of the I+ contact, and extracted at the perimeter of the I- contact. The induced voltage was measured at the center of the two voltage electrode contacts, mimicking the M4PP voltage measurement.

The predicted fractional change in the measured transfer resistance $dR/R \cong (R - R_0)/R_0$ for the considered configurations (A/A'), as calculated using the semianalytical [solid lines in Fig. 3(a)] and the FEM approach [“□”/“○” in Fig. 3(a)], shows acceptable agreement (<1%) over a broad range of currents, thus validating the use of Eq. (10) for data reduction of actual measurements [Fig. 3(b)].

The results of all PPMS and M4PP measurements on the three samples (2 coupons per sample) are listed in Table I and summarized in Fig. 4. The derivation of each particular TCR is further exemplified in Fig. 3(b), showing experimental data for the Pt-16nm-c coupon, and the best-fit semianalytical model [Eq. (10)] for configurations A and A'. These fits were obtained via a nonlinear least square optimization of multiple instances of Eq. (10) for different currents, assuming a shared α_{TCR} . To avoid bias (mixing of different thermal fields), configurations A and A' are fitted separately. The observed increase in dR/R with respect to I^2 is overwhelmingly linear, as expected from the linearized resistivity model. Equally linear plots of dR/R vs I^2 were observed also for the two thinner samples. The data are reproducible across dozens of M4PP engages, with a relative standard deviation of 1%–3% for all currents ≥ 2 mA. In terms of signal to noise ratio, the TCR “signal” ($R - R_0$) is up to 2% of R at the highest current; given typical associated electrical noise at the 0.1% level, we conclude that TCR effects are most readily detectable by M4PP.

Estimates of TCR from M4PP data are compared to direct measurements of TCR using PPMS in Table I and Fig. 4. Both methods indicate a decrease in TCR for thinner films, as predicted by the Mayades–Schatzkes theory and previously documented

elsewhere.^{2,22} The TCRs from A configurations are marginally lower than those from the A' configurations (by up to 4%); in turn, both configuration underestimate the independent PPMS measurements by $\sim 18\%$ (discussed in detail in Sec. V). Despite such underestimations, seen at large, the two independent datasets PPMS and M4PP are strikingly correlated (a Pearson's correlation coefficient of 0.99), and pave a promising route for the application of M4PP to TCR monitoring. Initially perceived as an obstacle, the low homogeneity of the 10 nm thin film (“□” symbols in Fig. 4), serves well for methodological intercomparison, as the minor variance in TCR across two coupons of the same sample is perfectly correlated across the two methods, suggesting that the presented

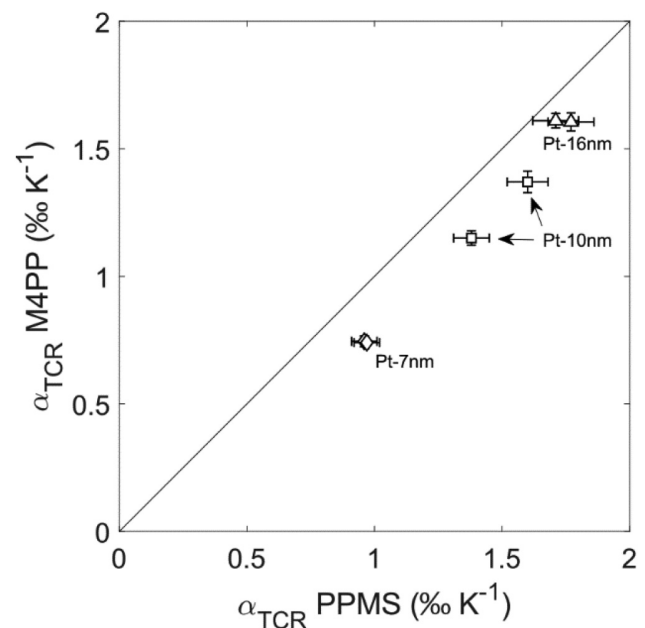


FIG. 4. The TCR obtained via the from the M4PP-TCR method compared to independent reference measurements performed on a PPMS on a total of six coupons taken from the three samples with varying platinum film thickness. During the fabrication of the 10 nm sample, the vacuum seal was broken.

M4PP methodology is at least as sensitive as direct TCR measurements with PPMS.

V. DISCUSSION AND CONCLUSION

To address the M4PP underestimation of $\alpha_{\text{TCR}} = dR/RdT$ relative to PPMS, we stress that since M4PP is extremely precise (<0.1%)³⁴ in measuring resistance and thus resistance differences (dR and R), the most straightforward reason for the underestimation is that our model overestimates the effective dT . To this end, the thermal model in Secs. II A and II B is certainly incomplete, and we can try to evaluate which critical parts are missing. While thermoelectric effects (primarily Peltier heat) have been neglected, their contribution to temperature is expected to be minimal, as the Seebeck coefficient of bulk Pt is only around $-5 \mu\text{V K}^{-1}$.⁵³ Second, a “cold finger” effect, i.e., heat dissipation through the electrodes rather than the substrate, could be in place, for which the theory does not account either. Third, ignoring heat transfer through the thin film builds up local thermal gradients which would otherwise be dissipated away.

While all of the above effects might need closer inspection, it is our impression that the key contributor to temperature overestimation is a time delay between the instantaneous heat generation at a location r' , and its arrival at another arbitrary location r , resulting in a temperature distribution that is slightly out of phase from the one calculated in Eq. (9).

This work has demonstrated that four-terminal sensing at micrometer scale can induce significant and measurable Joule heating effects, which under favorable measurement conditions, reasonable assumptions, and theoretical approximations can be converted into relatively accurate TCR estimates of ultrathin metal films. Both the advantage and the disadvantage of the presented method are that it requires no external temperature measurement, as the temperature is estimated directly from Joule heating, alongside assumptions about the sample's geometry and thermal conductivity. If the latter are reasonably known, M4PP applications require no sample preparation (*in situ* measurements), impose minimal sample damage, are extremely rapid (10 s per measurement), and capable of highly precise resistance measurements (<0.1%). The drawback of the method, as evident from Eq. (9), is that an external assumption must be made about the thermal conductivity (thermal resistance) of the thin film's substrate, which may become progressively difficult when multilayered substrates are considered. One possible solution to bypass the uncertainties that go into the thermal modeling is by scaling the observed dR/R trends by power (instead of temperature), and reporting the best-fit slopes as the “Power Coefficient of Resistance” (PCR), which is a useful metric for the estimation of self-heating of high precision electronics and interconnects.^{54–56} However, given the apparent definition fluidity whether PCR does or does not include the TCR effect, we currently prefer that our method be labeled as “TCR estimation,” rather than “PCR measurement.”

We believe that the presented methodology opens a new portfolio of M4PP applications, enabling the characterization of thin film TCR and their spatial variance at unprecedented spatial scales. Although this study is limited to homogenous platinum thin films, we expect that the method can be extended to semiconductor thin

films by taking into account thermoelectric properties and non-ohmic contacts.

ACKNOWLEDGMENTS

This work has been supported by the Innovation Fund Denmark (Grant Nos. 8054-00020B and 8057-00010B) and the Sapere Aude (Independent Research Fund Denmark) (No. 8048-00088B). We thank Frederik W. Østerberg, Henrik H. Henrichsen, and Peter F. Nielsen of CAPRES A/S and Bo B. Iversen of Aarhus University with their valuable input.

APPENDIX A: CALCULATION OF CONTACT RESISTANCE ON A THIN SHEET

The two-point resistance $R_{\text{load},ij}$ measured during a M4PP measurement between electrode pins i and j corresponds to the in-series (sum) resistance of the sample $R_{\text{samp},ij}$, the contact resistances $R_{c,i}$ and $R_{c,j}$ in the proximity of each electrode-sample interface, and the lead resistances $R_{\text{lead},i}$ and $R_{\text{lead},j}$ within the electrodes themselves and all the interconnects up to the voltmeter,

$$R_{\text{load},ij} = R_{\text{samp},ij} + R_{c,i} + R_{c,j} + R_{\text{lead},i} + R_{\text{lead},j}. \quad (\text{A1})$$

The sample resistance $R_{\text{samp},ij} = \frac{R_{s,0}}{\pi} \text{arccosh}\left(\frac{D_{ij}}{2r_0}\right)$, where D_{ij} is the electrode separation distance.⁴⁹ In Eq. (A1), $R_{\text{load},ij}$ is a measured value, while lead resistances $R_{\text{lead},i}$ and $R_{\text{lead},j}$ are known from the probe design (and can be further validated via measurements on highly conductive substrates). Writing $\tilde{R}_{ij} = R_{\text{load},ij} - R_{\text{lead},i} - R_{\text{lead},j} - R_{\text{samp},ij}$ leaves only $R_{c,i}$ and $R_{c,j}$ as unknowns, which can be determined via three measurements,

$$\begin{aligned} \tilde{R}_{1,2} &= R_{c,1} + R_{c,2}, \\ \tilde{R}_{1,3} &= R_{c,1} + R_{c,3}, \\ \tilde{R}_{2,3} &= R_{c,2} + R_{c,3}, \end{aligned} \quad (\text{A2})$$

which can be linearly combined to yield

$$R_{c,1} = \frac{\tilde{R}_{1,2} + \tilde{R}_{1,3} - \tilde{R}_{2,3}}{2}, \quad (\text{A3})$$

and analogously for $R_{c,2}$ and $R_{c,3}$. This well-known approach⁵⁷ may be generalized for n two-point resistance measurements utilizing a total of m electrodes as follows. Let us write Eq. (A1) in matrix form as

$$R_c = (M^T M)^{-1} M^T (R_{\text{load}} - R_{\text{samp}} - M R_{\text{lead}}), \quad (\text{A4})$$

where R_{load} and R_{samp} are column vectors $n \times 1$, containing the observed load resistance, and the estimated sample resistance, and R_c and R_{lead} are row vectors $1 \times m$, containing the contact resistance of each electrode (to be solved for), and its lead resistance. The sparse matrix M consists of n rows (each representing a certain measurement configuration) and m columns (two of which are flagged as 1, marking the current electrodes, all the rest being 0).

Equation (A4) can be solved if the number of independent observations is equal or higher to the number of unknowns.

APPENDIX B: ADAPTATION OF THE SEMIANALYTICAL MODEL TO ALTERNATING CURRENTS

Let us rewrite Eq. (6) in terms of voltage,

$$V = IR_0(1 + \alpha_{\text{TCR}}\Delta T_{\text{eff}}), \quad (\text{B1})$$

where $\Delta T_{\text{eff}} = \int_{\Omega} \Delta T(\mathbf{r}) \hat{S}(\mathbf{r}) d\Omega$ is an effective temperature change. Despite the implicit form of $\Delta T(\mathbf{r})$ in Eq. (9), its dependence on I^2 is explicit from the definition of Joule heating, thus enabling us to write

$$\Delta T_{\text{eff}} = \theta P = \theta R_{\text{eff}} I^2, \quad (\text{B2})$$

where P is the applied power, θ is the thermal resistance of the system and, R_{eff} is the effective resistance of the system. Let I be a sinusoidal current with amplitude I_0 and angular frequency ω ,

$$I = I_0 \cos(\omega t) = \sqrt{2} I_{\text{RMS}} \cos(\omega t). \quad (\text{B3})$$

Combining Eqs. (B1)–(B3), one has

$$V = R_0 [I_0 \cos(\omega t) + \alpha_{\text{TCR}} \theta R_{\text{eff}} I_0^3 \cos^3(\omega t)]. \quad (\text{B4})$$

Considering the substitution $I_0 = \sqrt{2} I_{\text{RMS}}$, the identity $\cos^3(x) = \left[\frac{3}{4} \cos(x) + \frac{1}{4} \cos(3x)\right]$, and that the lock-in amplifier extracts the voltage only at the measurement frequency ω , the root mean square voltage extracted at ω is

$$V_{\text{RMS},1\omega} = R_0 I_{\text{RMS}} \left(1 + \frac{3}{2} \alpha_{\text{TCR}} \theta R_{\text{eff}} I_{\text{RMS}}^2\right), \quad (\text{B5})$$

which differs by a factor 3/2 from Eq. (9), given the replacement $\theta R_{\text{eff}} I_{\text{RMS}}^2 = \int_{\Omega} \Delta T(\mathbf{r}) \hat{S}(\mathbf{r}) d\Omega$, and that four-point transfer resistances are reported as $R = V_{\text{RMS},1\omega} / I_{\text{RMS}}$ by the CAPRES microRSP A300.

DATA AVAILABILITY

The data that support the findings of this study are available from the corresponding author upon reasonable request.

REFERENCES

- H. A. Schafft and J. S. Suehle, *Solid State Electron.* **35**, 403 (1992).
- C. Tellier, A. Tossier, and C. Boutrif, *Thin Solid Films* **44**, 201 (1977).
- M. Olszacki, C. Maj, M. Al Bahri, J. Marrot, A. Boukabache, P. Pons, and A. Napieralski, *J. Micromech. Microeng.* **20**(6), 064008 (2010).
- F. Kerrou, A. Boukabache, and P. Pons, *J. Sens. Technol.* **2**, 132 (2012).
- S. Reif-Acherman, *Rev. Bras. Ensino Fis.* **33**, 4602 (2011).
- A. Feteira, *J. Am. Ceram. Soc.* **92**, 967 (2009).
- L. Ding, C. Wang, L. Chu, J. Yan, Y. Na, Q. Huang, and X. Chen, *Appl. Phys. Lett.* **99**(25), 251905 (2011).
- E. O. Chi, W. S. Kim, and N. H. Hur, *Solid State Commun.* **120**(7–8), 307 (2001).
- J. Lin, B. Wang, P. Tong, S. Lin, W. Lu, X. Zhu, Z. Yang, W. Song, J. Dai, and Y. Sun, *Scr. Mater.* **65**, 452 (2011).
- S. Lin, B. Wang, J. Lin, Y. Huang, W. Lu, B. Zhao, P. Tong, W. Song, and Y. Sun, *Appl. Phys. Lett.* **101**, 011908 (2012).
- P. Sun, M. Zhu, K. Wang, M. Zhong, J. Wei, D. Wu, and H. Zhu, *ACS Appl. Mater. Interfaces* **5**, 9563 (2013).
- S. Cho, K. Kikuchi, E. Lee, M. Choi, I. Jo, S.-B. Lee, S.-K. Lee, and A. Kawasaki, *Sci. Rep.* **7**(1), 14943 (2017).
- C. Adelmann, *Solid State Electron.* **152**, 72 (2019).
- H. A. Schafft, S. Mayo, S. N. Jones, and J. S. Suehle, in *Proceedings of 1994 IEEE International Integrated Reliability Workshop (IRWS)* (IEEE, 1994), p. 5.
- A. Von Glasow, A. Fischer, and G. Steinlesberger, in *2003 IEEE International Reliability Physics Symposium Proceedings* (IEEE, 2003), p. 126.
- J. D. Meindl, *Comput. Sci. Eng.* **5**, 20 (2003).
- T. Dinh, H.-P. Phan, A. Qamar, P. Woodfield, N.-T. Nguyen, and D. V. Dao, *J. Microelectromech. Syst.* **26**, 966 (2017).
- S. Wu, Q. Lin, Y. Yuen, and Y.-C. Tai, *Sens. Actuators A* **89**, 152 (2001).
- M. M. Waldrop, *Nat. News* **530**(7589), 144 (2016).
- F. Warkusz, *J. Phys. D: Appl. Phys.* **11**, 689 (1978).
- C. Tellier and A. Tossier, *Thin Solid Films* **43**, 261 (1977).
- H. J. K. Kim, K. E. Kaplan, P. Schindler, S. Xu, M. M. Winterkorn, D. B. Heinz, T. S. English, J. Provine, F. B. Prinz, and T. W. Kenny, *ACS Appl. Mater. Interfaces* **11**, 9594 (2019).
- T. Schössler, F. Schön, C. Lemier, and G. Urban, *Thin Solid Films* **698**, 137877 (2020).
- Q. Zhang, X. Zhang, B. Cao, M. Fujii, K. Takahashi, and T. Ikuta, *Appl. Phys. Lett.* **89**, 114102 (2006).
- K. Gregorczyk, P. Banerjee, and G. W. Rubloff, *Mater. Lett.* **73**, 43 (2012).
- A. Maffucci, F. Micciulla, A. E. Cataldo, G. Miano, and S. Bellucci, *IEEE Trans. Compon. Packag. Manuf. Technol.* **7**, 485 (2017).
- S. Dutta, S. Kundu, A. Gupta, G. Jamieson, J. F. G. Granados, J. Bömmels, C. J. Wilson, Z. Tökei, and C. Adelmann, *IEEE Electron. Device Lett.* **38**, 949 (2017).
- G. P. Szakmany, A. O. Orlov, G. H. Bernstein, and W. Porod, *IEEE Trans. Nanotechnol.* **13**(6), 1234 (2014).
- C. L. Petersen, T. M. Hansen, P. Bøggild, A. Boisen, O. Hansen, T. Hassenkamm, and F. Grey, *Sens. Actuators A* **96**, 53 (2002).
- D. Worledge and P. Trouilloud, *Appl. Phys. Lett.* **83**, 84 (2003).
- D. H. Petersen, O. Hansen, T. M. Hansen, P. Bøggild, R. Lin, D. Kjær, P. F. Nielsen, T. Clarysse, W. Vandervorst, E. Rosseel, N. S. Bennett, and N. E. B. Cowern, *J. Vac. Sci. Technol. B* **28**(1), 27 (2010).
- F. Smits, *Bell Syst. Tech. J.* **37**, 711 (1958).
- A. Uhrlir Jr., *Bell Syst. Tech. J.* **34**, 105 (1955).
- D. Kjær, R. Lin, D. H. Petersen, P. M. Kopalidis, R. Eddy, D. A. Walker, W. F. Egelhoff, and L. Pickert, *AIP Conf. Proc.* **1066**, 167 (2008).
- S. Thorsteinsson, F. Wang, D. H. Petersen, T. M. Hansen, D. Kjær, R. Lin, J.-Y. Kim, P. F. Nielsen, and O. Hansen, *Rev. Sci. Instrum.* **80**, 053902 (2009).
- E. Rosseel, D. H. Petersen, F. W. Osterberg, O. Hansen, J. Bogdanowicz, T. Clarysse, W. Vandervorst, C. Orttoland, T. Hoffmann, and P. Chan, in *2009 17th International Conference on Advanced Thermal Processing of Semiconductors* (IEEE, 2009), p. 1.
- D. M. Mackenzie, K. G. Kalhauge, P. R. Whelan, F. W. Ostergaard, I. Pasternak, W. Strupinski, P. Bøggild, P. U. Jepsen, and D. H. Petersen, *Nanotechnology* **31**, 225709 (2020).
- J. Bogdanowicz, S. Folkersma, S. Sergeant, A. Schulze, A. Moussa, D. H. Petersen, O. Hansen, H. H. Henrichsen, P. F. Nielsen, and W. Vandervorst, *Phys. Status Solidi A* **215**, 1700857 (2018).
- S. Folkersma, J. Bogdanowicz, A. Schulze, P. Favia, D. H. Petersen, O. Hansen, H. H. Henrichsen, P. F. Nielsen, L. Shiv, and W. Vandervorst, *Beilstein J. Nanotechnol.* **9**, 1863 (2018).
- K. Serbulova and Y. Vountesmery, in *2019 IEEE 39th International Conference on Electronics and Nanotechnology (ELNANO)* (IEEE, 2019), p. 369.
- D. C. Gupta and J. Y. Chan, *Rev. Sci. Instrum.* **41**(2), 176 (1970).
- S. O. Kasap, *Principles of Electronic Materials and Devices* (Tata McGraw-Hill, 2006).

- ⁴³D. W. Koon, F. Wang, D. H. Petersen, and O. Hansen, *J. Appl. Phys.* **114**(16), 163710 (2013).
- ⁴⁴S. Director and R. Rohrer, *IEEE Trans. Circuit Theory* **16**(3), 318 (1969).
- ⁴⁵J. L. Riddle, G. T. Furukawa, and H. H. Plumb, *Platinum Resistance Thermometry* (National Bureau of Standards, 1973).
- ⁴⁶H. S. Carslaw and J. C. Jaeger, *Conduction of Heat in Solids* (Clarendon Press, 1959).
- ⁴⁷H.H. Henrichsen, O. Hansen, D. Kjær, P.F. Nielsen, F. Wang, and D. H. Petersen, in *2014 International Workshop on Junction Technology* (IEEE, 2014), p. 1.
- ⁴⁸L. J. van der Pauw, *Philips Tech. Rev.* **20**, 220 (1958).
- ⁴⁹T. Ansbæk, D. H. Petersen, O. Hansen, J. B. Larsen, T. M. Hansen, and P. Bøggild, *Microelectron. Eng.* **86**, 987 (2009).
- ⁵⁰M. Yerry and M. Shephard, *IEEE Comput. Graph. Appl.* **1**, 39 (1983).
- ⁵¹P. O. Persson and G. Strang, *SIAM Rev.* **46**(2), 329 (2004).
- ⁵²COMSOL Multiphysics® v.5.5, COMSOL AB, Stockholm, Sweden, see www.comsol.com.
- ⁵³M. Kockert, R. Mitdank, A. Zykov, S. Kowarik, and S. F. Fischer, *J. Appl. Phys.* **126**(10), 105106 (2019).
- ⁵⁴I. K. Harvey and H. Collins, *Rev. Sci. Instrum.* **44**, 1700 (1973).
- ⁵⁵J. Bojkovski, V. Zuzek, V. Batagelj, and J. Drnovsek, in *11th International Conference on Heat Transfer, Fluid Mechanics and Thermodynamics* (International Conference on Heat Transfer, Fluid Mechanics and Thermodynamics, 2015).
- ⁵⁶G. Fernqvist, P. Dreesen, G. Hudson, and J. Pickering, in *2007 IEEE Particle Accelerator Conference (PAC)* (IEEE, 2007), p. 317.
- ⁵⁷T. E. Dinan, U.S. Patent 6,037,790 (International Business Machines Corp., 2000).

Paper II

' 3ω correction method for eliminating resistance measurement error due to Joule heating'

Benny Guralnik, Ole Hansen, Henrik H. Henrichsen, Braulio Beltrán-Pitarch, Frederik W. Østerberg, Lior Shiv, Thomas A. Marangoni, Andreas R. Stilling-Andersen, Alberto Cagliani, Mikkel F. Hansen, Peter F. Nielsen, Herman Oprins, Bjorn Vermeersch, Christoph Adelman, Shibesh Dutta, Kasper A. Borup, Besira M. Mihiretie, and Dirch H. Petersen

Reproduced from Rev. Sci. Instr. 92(9), 094711., with the permission of AIP Publishing.

3 ω correction method for eliminating resistance measurement error due to Joule heating ^{EP}

Cite as: Rev. Sci. Instrum. **92**, 094711 (2021); <https://doi.org/10.1063/5.0063998>

Submitted: 19 July 2021 . Accepted: 06 September 2021 . Published Online: 29 September 2021

 Benny Guralnik,  Ole Hansen, Henrik H. Henriksen, et al.

COLLECTIONS

 This paper was selected as an Editor's Pick



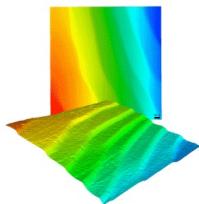
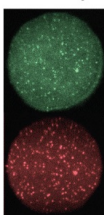
View Online



Export Citation



CrossMark

 <p>MCL MAD CITY LABS INC. www.madcitylabs.com</p>	<p>Nanopositioning Systems</p> 	<p>Modular Motion Control</p> 	<p>AFM and NSOM Instruments</p> 	<p>Single Molecule Microscopes</p> 
---	--	--	---	--

3ω correction method for eliminating resistance measurement error due to Joule heating

Cite as: Rev. Sci. Instrum. **92**, 094711 (2021); doi: 10.1063/5.0063998
Submitted: 19 July 2021 • Accepted: 6 September 2021 •
Published Online: 29 September 2021



Benny Guralnik,^{1,2,a)}  Ole Hansen,²  Henrik H. Henrichsen,¹ Braulio Beltrán-Pitarch,² 
Frederik W. Østerberg,¹  Lior Shiv,¹ Thomas A. Marangoni,²  Andreas R. Stilling-Andersen,² 
Alberto Cagliani,¹  Mikkel F. Hansen,¹  Peter F. Nielsen,¹  Herman Oprins,³  Bjorn Vermeersch,³ 
Christoph Adelman,³  Shibesh Dutta,³  Kasper A. Borup,⁴  Besira M. Mihiretie,⁵ 
and Dirch H. Petersen² 

AFFILIATIONS

¹CAPRES – A KLA Company, Diplomvej 373, 2800 Kgs. Lyngby, Denmark

²Technical University of Denmark, DK-2800 Kgs. Lyngby, Denmark

³Imec, Kapeldreef 75, B-3001 Leuven, Belgium

⁴Department of Chemistry, Aarhus University, Langelandsgade 140, DK-8000 Aarhus C, Denmark

⁵Hot Disk AB, SE-41288 Gothenburg, Sweden

^{a)} Author to whom correspondence should be addressed: benny.guralnik@gmail.com

ABSTRACT

Electrical four-terminal sensing at (sub-)micrometer scales enables the characterization of key electromagnetic properties within the semiconductor industry, including materials' resistivity, Hall mobility/carrier density, and magnetoresistance. However, as devices' critical dimensions continue to shrink, significant over/underestimation of properties due to a by-product Joule heating of the probed volume becomes increasingly common. Here, we demonstrate how self-heating effects can be quantified and compensated for via 3ω signals to yield zero-current transfer resistance. Under further assumptions, these signals can be used to characterize selected thermal properties of the probed volume, such as the temperature coefficient of resistance and/or the Seebeck coefficient.

© 2021 Author(s). All article content, except where otherwise noted, is licensed under a Creative Commons Attribution (CC BY) license (<http://creativecommons.org/licenses/by/4.0/>). <https://doi.org/10.1063/5.0063998>

I. INTRODUCTION

Here, we wish to introduce the 3ω technique^{1,2} into the context of micro-four-point probe (M4PP) electrical metrology,^{3–9} with the aim of improving the measurement *accuracy* of the latter via quantification and compensation for the so-called Self-Heating Effect (SHE).^{10,11} The undesirable heating associated with electrical micro-probing came to attention in the early 1960s, when the contact size between the metallic electrodes and the probed semiconductors dropped below ~ 0.1 μm .^{12–14} Since then, critical dimensions of semiconductor devices have shrunk by multiple orders of magnitude, while self-heating effects are often intentionally amplified.^{15,16} Thus, the elimination of undesirable by-products of heating in electrical microprobing has become increasingly relevant¹⁷ and is the main focus of the present contribution.

Traditionally, the unintentional generation of Joule heat during electrical microprobing has been mitigated via, e.g., measurement at sufficiently low^{14,18} or transient/pulsed currents¹⁷ and/or via optimization of the probing geometry.^{18,19} In a recent paradigm shift, we demonstrated⁹ that the seemingly undesired heating at such scales is highly reproducible and may be intentionally amplified in order to quantify the thermal properties of the material stack under test. [Figure 1](#) summarizes the key highlights from Ref. [9](#), where an equidistant micro-four-point probe with a pitch of 10 μm [[Fig. 1\(a\)](#)] was used to measure the sheet resistance of an ultrathin (16 nm) Pt film deposited on top of a fused silica substrate. The observed increase in the sheet resistance with the sampling current was proportional to the current squared in the 0.5 – 5 mA range [[circles in Fig. 1\(b\)](#), error bars within symbols]. A semianalytical approximation predicting this behavior was validated by finite element method

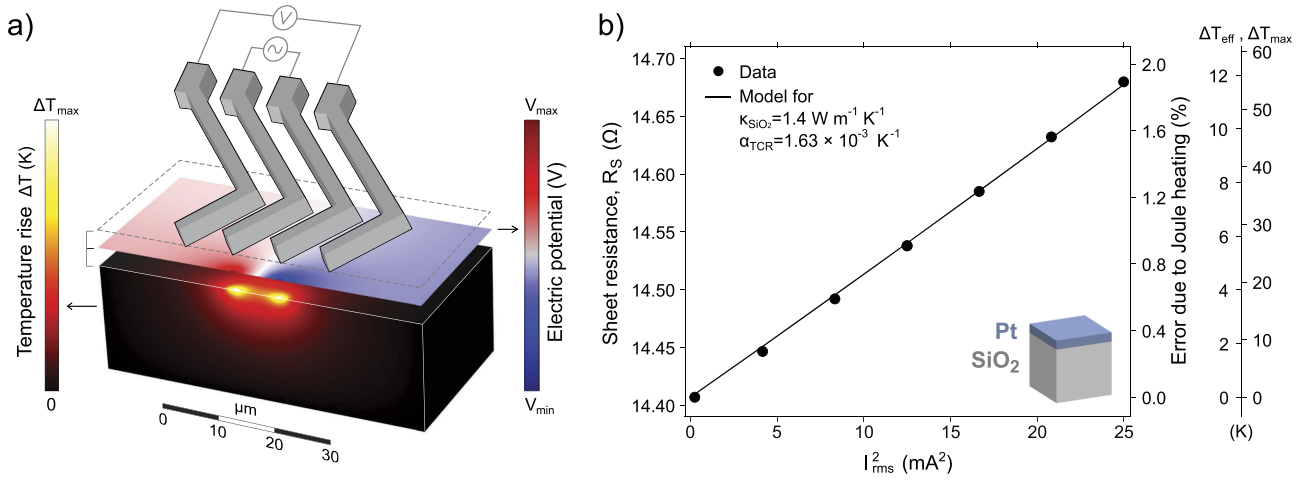


FIG. 1. The principle of TCR determination using the M4PP.⁹ (a) Numerical simulation (to scale) of a micro-four-point probe measurement of a Pt thin film on fused silica. The high current density in the vicinity of the two innermost, current-conducting electrodes results in surficial Joule heat and its conduction into the substrate (left color bar); in turn, locally elevated surface temperatures affect sheet resistivity, the electric field (right color bar), and ultimately, the effective sheet resistance. (b) The measured sheet resistance of Pt on fused silica (inset) increases linearly with squared rms current (\sim power), deviating from its idealized “zero-current” level by 1.9% at 5 mA. This trend can be numerically matched (line) via nonunique combinations of several thermal properties, in this case being the thermal conductivity of the substrate (presumed to be independently known) and the TCR of the thin film (designated as the unknown). Calculated for a presumed electric contact radius of 250 nm, the domain-averaged [Eq. (2)] and the maximum expected temperatures do also scale linearly with the current squared.

(FEM) simulations [continuous line in Fig. 1(b)]. Furthermore, by treating the thermal conductivity of the substrate as a known parameter, the temperature coefficient of resistance (TCR) of the thin film could be estimated with an excellent ($<2\%$) precision across multiple consecutive measurements (Table 1 in Ref. 9).

A classic correction for self-heating effects involves the extrapolation of the linear trend in Fig. 1(b) to zero current^{10,11} to obtain the heat-unaffected, “zero-current” resistance R_0 . However, such a correction requires two or more resistance measurements at well-separated currents. This requirement not only prolongs the measurement time but also exposes the target to potential irreversible changes at higher currents. Noting that mainstream M4PP metrology uses lock-in amplification (LIA) to reduce electrical noise,⁷ here we explore the possibility of estimating zero-current resistance by isolating and quantifying the thermally induced voltage component from higher voltage harmonics. Falling into the broad category of 1ω – 2ω – 3ω methods,² our particular M4PP measurement strategy and 3ω correction scheme are briefly outlined below.

II. THEORY

The following mathematical treatment is a recapitulation of Dames and Chen.² For further simplification, we shall assume a slowly varying measurement current (quasi-DC) such that any electrical and thermal lags (e.g., due to electrical and thermal capacitances) can be ignored. Thus, the location- and time-dependent temperature increment $\Delta T(\mathbf{r}, t)$ of the probed volume instantaneously follows the Joule heat dissipation distribution, which to first order can be expressed in terms of the position-dependent sample resistivity $\rho_0(\mathbf{r})$ and current density $\mathbf{J}(\mathbf{r}, t)$ as $\rho_0(\mathbf{r})|\mathbf{J}(\mathbf{r}, t)|^2$. Furthermore, using $\mathbf{J}(\mathbf{r}, t) = \mathbf{g}_r(\mathbf{r})I(t)$, where $I(t)$ is the instantaneous current and $\mathbf{g}_r(\mathbf{r})$ is the measurement geometry-dependent vector

function,²⁰ the instantaneous temperature increment can be written as $\Delta T(\mathbf{r}, t) = \psi(\mathbf{r})I^2(t)$. Note that $\psi(\mathbf{r})$ is a transfer function from the current squared into temperature, which explicitly depends only on the probing geometry (and implicitly on the material properties of the probed volume).

We shall assume a linearized resistivity model $\rho(\mathbf{r}, t) = \rho_0(\mathbf{r})[1 + \alpha\Delta T(\mathbf{r}, t)]$, where α is the temperature coefficient of resistivity (TCR), such that the instantaneous transfer resistance $R(t)$ becomes:

$$\begin{aligned} R(t) &= \int_{\Omega} \rho(\mathbf{r}, t) \hat{S}(\mathbf{r}) d\Omega \\ &= R_0 \left[1 + \alpha \frac{\int_{\Omega} \rho_0(\mathbf{r}) \Delta T(\mathbf{r}, t) \hat{S}(\mathbf{r}) d\Omega}{\int_{\Omega} \rho_0(\mathbf{r}) \hat{S}(\mathbf{r}) d\Omega} \right] \\ &= R_0 [1 + \alpha \Delta T_{\text{eff}}(t)]. \end{aligned} \quad (1)$$

Here, R_0 is the zero-current transfer resistance, and $\hat{S}(\mathbf{r})$ is the M4PP sensitivity to a local change in resistivity,^{9,20} which in this paper is defined as:

$$\hat{S}(\mathbf{r}) = \frac{\mathbf{J}(\mathbf{r}) \cdot \tilde{\mathbf{J}}(\mathbf{r})}{I\tilde{I}}$$

where $\tilde{\mathbf{J}}$ and \tilde{I} are the hypothetical current density and intensity in an adjacent system with interchanged current and voltage assignments.^{9,20} The function $\Delta T_{\text{eff}}(t)$ is a domain-averaged “effective” temperature increment,^{2,9} which for M4PP may be expressed as

$$\Delta T_{\text{eff}}(t) = \left(\frac{\int_{\Omega} \rho_0(\mathbf{r}) \psi(\mathbf{r}) \hat{S}(\mathbf{r}) d\Omega}{\int_{\Omega} \rho_0(\mathbf{r}) \hat{S}(\mathbf{r}) d\Omega} \right) I^2(t) = \Psi I^2(t). \quad (2)$$

With this definition of Ψ as a domain-scaled and -averaged $\psi(\mathbf{r})$, the instantaneous transfer resistance becomes

$$R(t) = R_0 [1 + \alpha \Psi I^2(t)], \quad (3)$$

and the instantaneous measured voltage becomes

$$V(t) = R(t)I(t) = R_0I(t) + R_0\alpha\Psi I^3(t). \quad (4)$$

If we use a low-frequency sinusoidal measurement current at the angular frequency $\omega = 2\pi f$,

$$I(t) = I_0 \sin(\omega t), \quad (5)$$

the instantaneous measured voltage becomes

$$\begin{aligned} V(t) &= R_0I_0 \sin(\omega t) + R_0\alpha\Psi I_0^3 \sin^3(\omega t) \\ &= \left(R_0 + \frac{3}{4}R_0\alpha\Psi I_0^2\right)I_0 \sin(\omega t) + \left(-\frac{1}{4}R_0\alpha\Psi I_0^2\right)I_0 \sin(3\omega t) \\ &= R_{1\omega}I_0 \sin(\omega t) + R_{3\omega}I_0 \sin(3\omega t), \end{aligned} \quad (6)$$

where we have introduced the first and third harmonic resistances, defined as $R_{1\omega} = R_0 + \frac{3}{4}R_0\alpha\Psi I_0^2$ and $R_{3\omega} = -\frac{1}{4}R_0\alpha\Psi I_0^2$, respectively. Note that for a positive α , the expected third harmonic voltage phase

angle is $\varphi_{3\omega} = \pi$, making $R_{3\omega}$ negative; for a negative α , $\varphi_{3\omega} = 0$ and $R_{3\omega}$ is positive.

Equation (6) also shows that the zero-current transfer resistance R_0 can be recovered from harmonic resistances $R_{1\omega}$ and $R_{3\omega}$ by the simple calculation

$$R_0 = R_{1\omega} + 3R_{3\omega}. \quad (7)$$

The temperature coefficient of resistivity can then be calculated from

$$\alpha = \frac{-4R_{3\omega}}{R_0\Psi I_0^2} = \frac{-4R_{3\omega}}{(R_{1\omega} + 3R_{3\omega})\Psi I_0^2} = \frac{-4}{(R_{1\omega}/R_{3\omega} + 3)\Psi I_0^2}, \quad (8)$$

which is easily derived from Eqs. (6) and (7).

III. MATERIALS AND METHODS

A. Samples

In this study, we focus on four industrially relevant samples, including a metallic nanoscale interconnect [Fig. 2(a)], a metallic

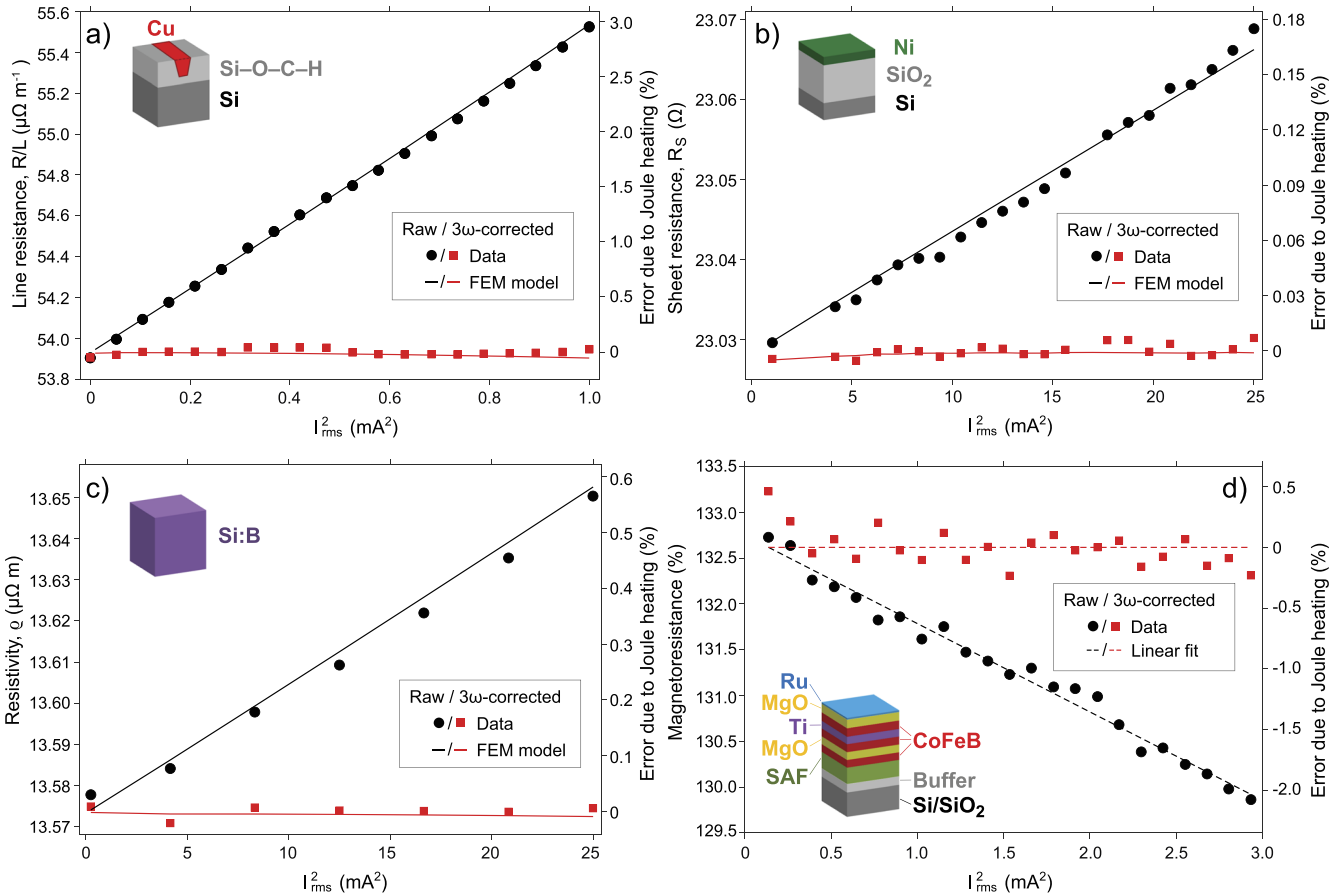


FIG. 2. Raw (circles) and 3ω -corrected [squares, Eq. (7)] line resistance (a), sheet resistance (b), bulk resistivity (c), and magnetoresistance (d) in four industrially relevant devices under test (insets, see Sec. III A for a detailed description of each device). Right y-axes show the measurement error due to Joule heating, which is dominated by the TCR [(a) and (b)] and a combination of the TCR and thermoelectric voltage [(c) and (d)]. Continuous lines in (a)–(c) correspond to FEM best fits to the experimental data; dashed lines in (d) are merely linear fits (as numerical simulation of the MTJ stack was not attempted). Note that the highest currents in each subplot approach the regime for thermal failure of either the probe and/or the device under test.

ultrathin film [Fig. 2(b)], a highly doped semiconductor [Fig. 2(c)], and a magnetic tunneling junction [MTJ], Fig. 2(d)], all of which were characterized by independent techniques as follows:

- Cu nanowires (1D electric domain):** Fabricated via extreme ultraviolet lithography (EUVL), the nanowires are embedded in an 87 nm thick organosilicate glass (OSG) thin film with a dielectric constant of 3.0. The OSG is deposited on top of a structured 775 μm thick Si substrate. The nominal dimensions of the nanowires are 100 μm (L) \times 50 nm (W) \times 77 nm (H), with a sidewall angle of 87° and 450 nm spacing between neighboring wires. The thermal conductivities of both the low-k OSG ($\kappa_{\text{low-k}} = 0.33 \text{ W m}^{-1} \text{ K}^{-1}$) and Si substrate ($\kappa_{\text{Si}} = 150 \text{ W m}^{-1} \text{ K}^{-1}$) were determined using conventional 3ω metrology,² implementing the multilayer matrix formalism.²¹
- Ni thin film (2D electrical domain):** The metallic thin film was fabricated by physical vapor deposition of Ni on 300 mm wafers in a Canon Anelva EC7800 system. The material stack consists of a 10 nm Ni thin film on a 90 nm SiO₂ layer [$\kappa_{\text{SiO}_2} = 0.93 \text{ W m}^{-1} \text{ K}^{-1}$ estimated from Eq. (6) of Ref. 22], deposited on top of a 775 μm thick bulk Si substrate ($\kappa_{\text{Si}} = 150 \text{ W m}^{-1} \text{ K}^{-1}$ as mentioned above).
- Bulk Si:B (3D electrical domain):** The sample is a Czochralski-grown, industrial-grade, boron-doped silicon wafer ($\varnothing = 100 \text{ mm}$ in diameter and 550 μm thick). The carrier concentration is spatially uniform and is estimated at $\sim 1 \times 10^{20} \text{ cm}^{-3}$. The thermal conductivity $\kappa_{\text{Si:B}} = 65.3 \text{ W m}^{-1} \text{ K}^{-1}$, diffusivity $D = 41.2 \text{ mm}^2 \text{ s}^{-1}$, and specific heat $c_p = 1585 \text{ J m}^{-3} \text{ K}^{-1}$ of Si:B were determined at the macroscale using the transient plane source technique,²³ yielding characteristically suppressed values for highly doped Si.²⁴ A Seebeck coefficient of $S = 250 \mu\text{V K}^{-1}$ was measured using a custom-built thin film Seebeck measurement system (adapted from Ref. 25). Additionally, we directly estimated the TCR ($\alpha = 2.05 \pm 0.02 \times 10^{-3} \text{ K}^{-1}$ within the range 296–336 K) via M4PP measurements utilizing a portable hotplate with a proportional–integral–derivative (PID) controller.
- Magnetic Tunnel Junction (multi-layered quasi-2D electrical domain):** The sample is an industrially relevant, single-junction stack (cf., Ref. 26) of a spin-transfer torque magnetoresistive random access memory (STT-MRAM). The synthetic antiferromagnet is placed below the tunnel barrier, with a 3 Å Ta spacer between the two CoFeB films composing the free layer and a thin MgO layer on top of the free layer (further capped with 30 Å of Ru to facilitate contact with CAPRES probes²⁷).

B. Instrumentation

Electric resistance measurements at the microscale were performed using a CAPRES microRSP[®]-A300 tool utilizing digital lock-in amplification (LIA).⁷ Specifically, and in contrast to its default (factory) settings of extracting solely the first harmonic,⁷ the proprietary LIA module of the A300 tool (cf., Ref. 28) was programmatically extended to extract the transfer resistance R_{nw} and its phase φ_{nw} up to the third harmonic ($n = 1, 2, 3$) of the input current frequency. This extended LIA module was thoroughly tested against a

manifold of known waveforms as well as benchmarked against an external best-in-class tool (MFLI from Zürich Instruments).

Samples (a)–(c) were characterized using an equidistant probe with a pitch of 8 μm ;⁷ sample (d) with a specialized current-in-plane tunneling (CIPT) probe with varying distances in the 0.5–10 μm range.²⁷ Measurements were performed at low frequencies of $f = 3.01$ [(a) and (b)], 12.06 (c), and 48.22 Hz (d). Lead resistances of all electrodes were monitored, subtracted, and regressed into individual contact resistances, as detailed in Ref. 9.

C. Numerical simulations

While the complexity of simulating an MTJ stack [Fig. 2(d)] goes beyond the scope of this work,^{29,30} all other experimental data [circles and squares in Figs. 2(a)–2(c)] were numerically reproduced [lines in Figs. 2(a)–2(c)] using COMSOL Multiphysics[®].³¹ All models included coupled *electric currents* and *heat transfer in solids* modules; the simulation of sample (c) included *thermoelectric effects* as well. All nominal device dimensions/geometries were accurately reproduced (with domain reduction due to symmetry wherever possible), and all the experimentally obtained physical constants (Sec. III A) were assigned. Model element sizes were on average a factor of 5–10 smaller than the critical dimensions in their vicinity. The initial conditions of potential (0 V) and temperature (300 K) were supplemented by a thermal insulation on the probing surface (the upper plane of each device) and a constant temperature of 300 K on all other external surfaces. In all models, two terminals of opposite polarity were located 8 μm apart, delivering a sinusoidal current through corresponding trapezoidal (a), semicircular (b), and hemispherical (c) contact geometries (with effective contact radii further denoted as r_0). For the metal–semiconductor contacts in (c), an additional thermal flux at each contact (arising from a contact resistance of 50 Ω , obtained experimentally) was added, following the procedure described in Ref. 9. A time-dependent solver was used to simulate the underlying waveforms (64 time points per period) for each of the observation points in Figs. 2(a)–2(c), with numerical tolerance $< 10^{-5}$. Boundary probes (a) or point probes [(b) and (c)] were used to obtain the voltage at the approximated (a) or precise [(b) and (c)] locations of the two sensing electrodes. The voltage harmonics were then extracted using a numerical lock-in amplifier (thoroughly validated against synthetic waveforms). Convergence tests were conducted to verify that the domain size, meshing, and tolerance were adequately selected.

IV. RESULTS AND DISCUSSION

A. De-trending resistivity measurements from self-heating effects

The linear response of line resistance [Fig. 2(a)], sheet resistance [Fig. 2(b)], bulk resistivity [Fig. 2(c)], and magnetoresistance [Fig. 2(d)] as a function of the square of the probing current is ubiquitous in all studied materials, leading to fractional errors of up to a few percent.³² Given that the M4PP method is generally associated with a precision and reproducibility of $< 0.1\%$,³³ self-heating errors of up to a few percent cannot be regarded as negligible and necessitate an adept correction scheme. In contrast, the proposed 3ω correction method, involving a linear combination of the first and third harmonics [Eq. (7)], yields current-insensitive “flat” trends [squares

in Figs. 2(a)–2(d)], whose slopes are statistically indistinguishable from 0 and whose means overlap with the zero-current intercept that may be regressed from the uncorrected measurements.^{10,11}

B. Determination of thermal properties

The trends of the uncorrected measurements [intentionally removed by Eq. (7)] bear valuable information regarding the thermal properties of the sample [which can be utilized by Eq. (8)]. Since the domain-averaged transfer coefficient Ψ [Eq. (2)] may be difficult to evaluate even in the simplest of geometries⁹ and the potential contribution of thermoelectric voltage is not included in Eq. (3), we resort to a fully numerical approach, where we simulate the observed data via the FEM (Sec. III C). The continuous lines in Figs. 2(a)–2(c) are the numerical best fits to the experimental data, yielding the following regressed parameters:

- Cu nanowire*: $R_0/L = 53.93 \mu\Omega \text{ m}^{-1}$, $\alpha = 1.13 \times 10^{-3} \text{ K}^{-1}$, and $r_0 \sim 50 \text{ nm}$.
- Ni thin film*: $R_{S,0} = 22.8494 \Omega$, $\alpha = 3.34 \times 10^{-3} \text{ K}^{-1}$, and $r_0 = 250 \text{ nm}$.
- Bulk Si:B*: $\rho_0 = 13.295 \mu\Omega \text{ m}$, $\alpha = 1.93 \times 10^{-3} \text{ K}^{-1}$, and $r_0 = 125 \text{ nm}$.

The obtained TCR estimates quoted above are in remarkable agreement with the literature. Specifically, the best fit $\alpha = 1.13 \times 10^{-3} \text{ K}^{-1}$ for the 50 nm wide Cu nanowire promptly extends the trend emerging from wider lines (80–330 nm)³⁴ and is also in line with more recent findings.³⁵ The $\alpha = 3.34 \times 10^{-3} \text{ K}^{-1}$ of the Ni thin film is well bracketed by the broad range reported in Ref. 36 and specifically matches the estimate for a 12.3 nm thick Ni film in Ref. 37 (estimated $3.2 \pm 0.4 \times 10^{-3} \text{ K}^{-1}$ from their Fig. 2). Finally, the best-fit $\alpha = 1.93 \times 10^{-3} \text{ K}^{-1}$ of Si:B not only matches its theoretically expected values,^{38,39} but is also within ~6% of its direct and independent M4PP measurement on a hotplate. Our best fit contact radii (r_0), while technically representing a method-specific parameter rather than any useful sample–probe interaction, are nevertheless consistent with scanning electron microscopy estimates (e.g., Ref. 19).

V. CONCLUSION

The gradual miniaturization of microelectronic devices results in the increase of undesirable self-heating effects when these devices are subjected to electrical/electromagnetic probing using the M4PP. Key fingerprints of heating in response to an applied alternating current can be detected in higher harmonics of the measured voltage,^{2,12,13} which are easy to isolate by means of lock-in amplification.⁷ Here, we have presented the theory (Sec. II), experimental proof (symbols in Fig. 2), and numerical verification (lines in Fig. 2) for the use of 3ω voltage signals for de-trending M4PP resistance measurements from self-heating effects. The presented 3ω correction [Eq. (7)] was demonstrated on samples of broadly varying structures and dimensionalities (Fig. 2). In all studied materials, a definitive (percent-level) improvement in accuracy of M4PP measurements was demonstrated. This marks the 3ω correction as yet another qualitative breakthrough in the evolving accuracy of M4PP resistance metrology (cf., Ref. 27).

The success in reproducing both raw and de-trended M4PP observations via FEM simulations supports the applicability of our quasi-DC assumption to the low-frequency range (<50 Hz), within which routine M4PP measurements are typically performed.^{8,9} While an extension of the theory for true AC is highly desirable,² the electrical and thermal fields arising from even the simplest four-point probing geometries are complex⁹ and render such a mathematical treatment significantly beyond the scope of this work. It should be noted that the presented DC-limit correction has been observed to perform well even at higher frequencies of ~400 Hz. Nevertheless, since the cut-off frequency for the proposed 3ω correction depends on a multiplicity of parameters (including, among others, the desired tolerance, probe geometry, material properties, etc.), we are currently hesitant to report a guiding cut-off frequency. Instead, we encourage to explore and set such thresholds for particular case scenarios via sensitivity analysis based on numerical modeling [cf., Figs. 2(a)–2(c)].

We believe that this study solidifies the recently demonstrated capability of the M4PP for TCR metrology,⁹ extending it to a much broader range of materials, device geometries, and electrical dimensionalities (Fig. 2). At the same time, we emphasize that in our current state-of-the-art, the thermal properties obtained from such M4PP measurements are highly model-driven and are not to be mistaken for a straightforward measurand (as transfer resistance is). Nevertheless, we believe that the prospects of the higher harmonic M4PP measurements to complement, overlap, and perhaps even crossover with scanning thermal microscopy techniques^{40,41} are rather self-evident and highly promising.

ACKNOWLEDGMENTS

This work was supported by Innovation Fund Denmark (Grant Nos. 8054-00020B and 8057-00010B) and Independent Research Fund Denmark (Grant No. 8048-00088B). Roel Gronheid and Andrew Cross (KLA) are thanked for coordinating the fabrication of the nanowire sample and Nini Pryds (DTU) for the portable hotplate equipment.

DATA AVAILABILITY

The data and models that comprise Figs. 1 and 2 are available from the corresponding author upon reasonable request.

REFERENCES

- D. G. Cahill, *Rev. Sci. Instrum.* **61**, 802 (1990).
- C. Dames and G. Chen, *Rev. Sci. Instrum.* **76**, 124902 (2005).
- C. L. Petersen, F. Grey, I. Shiraki, and S. Hasegawa, *Appl. Phys. Lett.* **77**, 3782 (2000).
- D. C. Worledge, *Appl. Phys. Lett.* **84**, 1695 (2004).
- R. Lin, P. Bøggild, and O. Hansen, *J. Appl. Phys.* **96**, 2895 (2004).
- D. H. Petersen, O. Hansen, T. M. Hansen, P. Bøggild, R. Lin, D. Kjær, P. F. Nielsen, T. Clarysse, W. Vandervorst, E. Rosseel, N. S. Bennett, and N. E. B. Cowern, *J. Vac. Sci. Technol., B* **28**, C1C27 (2010).
- P. F. Nielsen, D. H. Petersen, R. Lin, A. Jensen, H. H. Henrichsen, L. Gammelgaard, D. Kjær, and O. Hansen, in *Proceedings of the 12th International Workshop on Junction Technology* (IEEE, 2012), p. 1; available at <https://ieeexplore.ieee.org/abstract/document/6212819>.
- J. Bogdanowicz, S. Folkersma, S. Sergeant, A. Schulze, A. Moussa, D. H. Petersen, O. Hansen, H. H. Henrichsen, P. F. Nielsen, and W. Vandervorst, *Phys. Status Solidi A* **215**, 1700857 (2018).

- ⁹T. A. Marangoni, B. Guralnik, K. A. Borup, O. Hansen, and D. H. Petersen, *J. Appl. Phys.* **129**, 165105 (2021).
- ¹⁰J. L. Riddle, G. T. Furukawa, and H. H. Plumb, *Nat. Bureau Stand.* **126**, 1 (1973); available at <https://searchworks.stanford.edu/view/10766229>.
- ¹¹V. Batagelj, J. Bojkovski, and J. Drnovšek, *Meas. Sci. Technol.* **14**, 2151 (2003).
- ¹²M. Cutler, *J. Appl. Phys.* **32**, 1075 (1961).
- ¹³M. Cutler, *Adv. Energy Convers.* **2**, 29 (1962).
- ¹⁴R. G. Mazur and D. H. Dickey, *J. Electrochem. Soc.* **113**, 255 (1966).
- ¹⁵M. M. Waldrop, *Nature* **530**, 144 (2016).
- ¹⁶J. He and T. M. Tritt, *Science* **357**, 6358 (2017).
- ¹⁷K. Serbulova and Y. Vountesmery, in *IEEE 39th International Conference on Electronics and Nanotechnology* (IEEE, 2019), p. 369.
- ¹⁸D. C. Gupta and J. Y. Chan, *Rev. Sci. Instrum.* **41**, 176 (1970).
- ¹⁹T. Ansbaek, D. H. Petersen, O. Hansen, J. B. Larsen, T. M. Hansen, and P. Bøggild, *Microelectron. Eng.* **86**, 987 (2009).
- ²⁰D. W. Koon, F. Wang, D. H. Petersen, and O. Hansen, *J. Appl. Phys.* **114**, 163710 (2013).
- ²¹B. W. Olson, S. Graham, and K. Chen, *Rev. Sci. Instrum.* **76**, 053901 (2005).
- ²²T. Yamane, N. Nagai, S.-i. Katayama, and M. Todoki, *J. Appl. Phys.* **91**, 9772 (2002).
- ²³M. Gustavsson, E. Karawacki, and S. E. Gustafsson, *Rev. Sci. Instrum.* **65**, 3856 (1994).
- ²⁴Y. Lee and G. S. Hwang, *Phys. Rev. B* **86**, 075202 (2012).
- ²⁵S. Iwanaga, E. S. Toberer, A. LaLonde, and G. J. Snyder, *Rev. Sci. Instrum.* **82**, 063905 (2011).
- ²⁶H. Sato, M. Yamanouchi, S. Ikeda, S. Fukami, F. Matsukura, and H. Ohno, *Appl. Phys. Lett.* **101**, 022414 (2012).
- ²⁷A. Cagliani, F. W. Østerberg, O. Hansen, L. Shiv, P. F. Nielsen, and D. H. Petersen, *Rev. Sci. Instrum.* **88**, 095005 (2017).
- ²⁸Stanford Research Systems Manual, “Model SR830 DSP Lock-In Amplifier,” 2005, www.thinksrs.com.
- ²⁹D. H. Lee and S. H. Lim, *Appl. Phys. Lett.* **92**, 233502 (2008).
- ³⁰X. Zhang, G. Zhang, L. Shen, P. Yu, and Y. Jiang, *Solid-State Electron.* **173**, 107878 (2020).
- ³¹COMSOL Multiphysics®, v. 5.6., www.comsol.com, COMSOL AB, Stockholm, Sweden.
- ³²Massive errors of up to ~20%, observed in bulk Bi₂Te₃, will be reported elsewhere.
- ³³D. Kjaer, R. Lin, D. H. Petersen, P. M. Kopalidis, R. Eddy, D. A. Walker, W. F. Egelhoff, and L. Pickert, *AIP Conf. Proc.* **1066**, 167 (2008).
- ³⁴Q. Huang, C. M. Lilley, M. Bode, and R. Divan, *J. Appl. Phys.* **104**, 023709 (2008).
- ³⁵R. S. Smith, E. T. Ryan, C.-K. Hu, K. Motoyama, N. Lanzillo, D. Metzler, L. Jiang, J. Demarest, R. Quon, L. Gignac, C. Breslin, A. Giannetta, and S. Wright, *AIP Adv.* **9**, 025015 (2019).
- ³⁶R. B. Belser and W. H. Hicklin, *J. Appl. Phys.* **30**, 313 (1959).
- ³⁷J. W. C. De Vries, *Thin Solid Films* **150**, 209 (1987).
- ³⁸P. W. Chapman, O. N. Tufte, J. D. Zook, and D. Long, *J. Appl. Phys.* **34**, 3291 (1963).
- ³⁹W. M. Bullis, F. H. Brewer, C. D. Kolstad, and L. J. Swartzendruber, *Solid-State Electron.* **11**, 639 (1968).
- ⁴⁰T. Borca-Tasciuc, *Annu. Rev. Heat Transfer* **16**, 211 (2013).
- ⁴¹Y. Zhang, W. Zhu, F. Hui, M. Lanza, T. Borca-Tasciuc, and M. Muñoz Rojo, *Adv. Funct. Matter* **30**, 1900892 (2020).

Paper III (in preperation)

'Removing the dependence on measurement parameters in M4PP-TCR
measurements'

Thomas A. Marangoni, Benny Guralnik, Ole Hansen, Braulio Beltrán-Pitarch,
Andreas R. Stilling-Andersen, Søren E. Hansen, and Dirch H. Petersen

Removing the dependence on measurement parameters in M4PP-TCR measurements

Thomas A. Marangoni^{1,2}, Benny Guralnik^{1,3}, Ole Hansen⁴, Braulio Beltrán-Pitarch¹, Andreas R. Stilling-Andersen¹, Søren E. Hansen⁵, Dirch H. Petersen¹

¹Department of Energy Conversion and Storage, Technical University of Denmark, Fysikvej, Building 310, DK-2800 Kgs. Lyngby, Denmark

²Department of Physics, Technical University of Denmark, Fysikvej, Building 307, DK-2800 Kgs. Lyngby, Denmark

³CAPRES – a KLA company, Diplomvej 373, 2800 Kgs. Lyngby, Denmark

⁴National Centre for Nano Fabrication and Characterization, DTU Nanolab, Technical University of Denmark, DK-2800 Kgs. Lyngby, Denmark

⁵Department of Photonics Engineering, Technical University of Denmark, Ørstedes Plds, Building 343, DK-2800 Kgs. Lyngby, Denmark

Corresponding author e-mail: dhpe@dtu.dk

Abstract

Accurate knowledge of a materials' temperature coefficient of resistance (TCR) is essential in both the fabrication and operation of micro- and nano-electronics and sensors. Previously, we have demonstrated a precise (<2%) measurement of the TCR of nanometer thin films using the widely used and versatile micro four-point probe (M4PP) tool, which enabled fast TCR characterization without the need of an independent temperature measurement. However, while the high precision allowed the method to be especially suited for relative comparisons, the accuracy of the method suffered from the assumed static temperature model, which did not fully account for the application of AC currents. In this work, we extend the temperature model, by expressing the temperature in complex exponentials, to account for the time dependent power deposited in the sample during a measurement. The resulting trends predicted by the extended model match those observed in finite element simulations and measured data. The result is that the extracted TCR from M4PP measurements is no longer dependent on the chosen measurement frequency and probe size, which allows the M4PP-TCR method to be employed in high accuracy environments such as in-line process monitoring.

Keywords: Micro four-point probe, Temperature coefficient of resistance, Joule heating

1. Introduction

The temperature coefficient of resistance (TCR) characterizes the relationship between a material's electrical resistance and its temperature. [2] The TCR is an important material parameter in the fabrication and operation of micro- and nano-electronics and sensors. An accurate knowledge of TCR is required in the design of micro- and nano-electronic devices to limit the self-heating effect, which hinders device efficiency [3] and reliability. In addition, the operation of sensors, e.g. thermal sensors [7] or flow sensors [8], demand accurate and precise characterization of TCR. Furthermore, the TCR can be used to characterize several material and device properties such as interconnect cross-sectional area [4] and reliability [5] as well as the doping level in silicon resistors [6].

Due to the complex relationship between electrical resistance and temperature (dependent on e.g. defects, grain size and device geometry [20]), the TCR is generally an

empirical metric, obtained by simply measuring the resistance change over a known temperature gradient. [2] Recently we have demonstrated a novel method to characterize the TCR of nanometer thin metal films [1] using the micro four-point probe tool (M4PP) [9] [14], a commonly used four-terminal sensing technique to characterize conductive thin films [10] [11], magnetic tunnel junctions [12] and ultra-shallow junctions [13]. By utilizing the Joule heating effect, a precise (<2%) measurement of thin film TCR was obtained without requiring an independent measurement of temperature. [1] The M4PP-TCR method excels in relative comparisons between different films due to its high precision and fully exploits the benefits of the M4PP, such as requiring minimal sample preparation and an extremely rapid measurement time (relative to present methods). However the method suffers in accuracy, namely due to the obtained TCR being dependent on two experimental parameters: the chosen frequency of the applied current and the size of the measuring probe.

This work aims to address these shortcomings by extending the temperature models used in the M4PP-TCR method [1]. The temperature fields are derived from the time dependent Joule heating power, instead of assuming static conditions. This correction enables the determination of thin film TCR from M4PP measurements to be independent of the chosen measurement frequency and probe size.

2. Theory

The M4PP-TCR system is as follows: four electrodes are brought into contact with the surface of a thin metal film deposited on an isolating substrate. An AC current is sourced between two electrodes (positioned at \mathbf{r}_+ and \mathbf{r}_- representing the current inlet and current outlet respectively), during which the induced voltage is measured by the two remaining electrodes (positioned at \mathbf{r}_{V+} and \mathbf{r}_{V-}), as depicted in Fig. 1. The electrode roles can be freely interchanged to obtain several probe configurations. In this work we consider the so called A and A' (A prime) configurations. The electrodes are separated by a distance s (probe pitch). When the thickness of the metal thin film (d) is much smaller than the probe pitch ($d \ll s$), the film can be treated as an infinitely thin conducting sheet and 2D current transport can be assumed. In addition, heat transport through the film is assumed to be negligible and any heat dissipation is governed solely by heat conduction through the substrate below. Joule heating in the film raises the local temperature and modifies the local sheet resistance according to the linearized resistivity model. We have previously shown that the TCR can be extracted from the fractional increase in

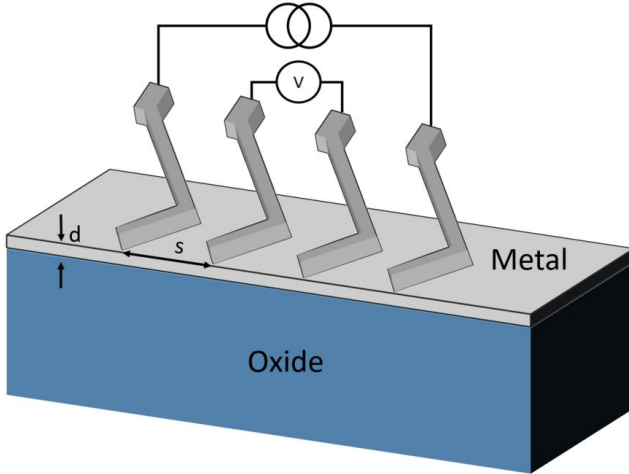


Figure 1. A schematic overview of a M4PP-TCR measurement. The electrodes contact the surface of a metal film of thickness d . The L-shape of the electrodes is more vibration tolerant and prevents movement during the measurement. Two electrode source the current while the remaining two measure the induced voltage. Shown is the A configuration. Its reciprocal counterpart is the A' (A prime) configuration, where the current and voltage electrodes are interchanged.

measured M4PP resistance from the ideal ‘zero current’ resistance R_0 via [1]:

$$\frac{R - R_0}{R_0} = c\alpha_{\text{TCR}} \int_{\Omega} \Delta T(\mathbf{r}) \hat{S}(\mathbf{r}) d\Omega \quad (1)$$

where $\Delta T(\mathbf{r})$ is the increase in surface temperature induced by Joule heating, $\hat{S}(\mathbf{r})$ is the M4PP sensitivity weighing function [17], relating variations in local sheet resistance to the final measured resistance R and Ω is the measured area. The constant c takes either the value 1 or $3/2$ for DC or AC measurements respectively. The integral in Eq. 1 can be evaluated using the so-called semi-analytical model after which the TCR is obtained by fitting the right hand side to the measured data using the TCR (α_{TCR}) as the fitting parameter. In the case of AC M4PP measurements, $c = 3/2$ does not fully capture the thermal delays and the resultant effect on the magnitude of the local temperature and use of Eq. 1 requires a full time dependent analysis of $\Delta T(\mathbf{r})$.

2.1 Time dependent temperature fields

The Joule heating power of a point source at a location \mathbf{r} on a conductive sheet driven by an AC current ($I(t) = \text{Re}(I_0 \exp i\omega t)$) with frequency $\omega = 2\pi f$ can be described by:

$$P(t) = \text{Re} \left(\frac{I_0^2 R}{2} (1 + \exp(i2\omega t)) \right) \quad (2)$$

where $\omega = 2\pi f$ and R is the resistance at location \mathbf{r} . It can be shown [15] that the time dependent complex temperature $\Delta \tilde{T}$ resulting from this point heat source (placed on the surface of a semi-infinite sample with thermal conductivity κ , density ρ and specific heat capacity c_p) driven by a sinusoidal current (since $\Delta T(r, 0) = 0$ K) is:

$$\Delta \tilde{T}(r, t) = \frac{P_0}{2\pi\kappa r} \times \left[\frac{1}{2} (1 - \exp(i2\omega t) \exp(-(1+i)k_n r)) \right] \quad (3)$$

where $k_n = \sqrt{\frac{n\omega}{2D}}$, $P_0 = I_0^2 R_S$, and $D = \frac{\rho c_p}{\kappa}$. The temperature rise due to the power deposited in the entire conductive sheet can be modeled as a superposition of point heat sources whose power is determined by the sheet power density at each location. The M4PP sheet power density in the 2D conducting sheet is obtained from the sheet current density $\mathbf{J}_S(\mathbf{r})$ and can be shown to be [1]:

$$R_S(\mathbf{r}) |\mathbf{J}_S(\mathbf{r})|^2 = \frac{R_S(\mathbf{r}) I^2}{4\pi^2} \left(\frac{|\mathbf{r}_+ - \mathbf{r}_-|}{|\mathbf{r} - \mathbf{r}_+| |\mathbf{r} - \mathbf{r}_-|} \right)^2 \quad (4)$$

Substituting the sheet power density into Eq. 3 and summing over all point sources within the measured area Ω gives, while considering that the sheet resistance is modified by the TCR via the linear approximation ($R_S = R_{S,0}[1 + \alpha_{TCR}\Delta T]$):

$$\Delta\tilde{T}_{sheet}(\mathbf{r}, t) = \frac{I_0^2 R_{S,0} |\mathbf{r}_+ - \mathbf{r}_-|^2}{2\pi\kappa \frac{4\pi^2}{1 + \alpha_{TCR}\Delta T(\mathbf{r}')}} \times \int_{\mathbf{r}' \in \Omega} \frac{1 + \alpha_{TCR}\Delta T(\mathbf{r}')}{|\mathbf{r}' - \mathbf{r}_+|^2 |\mathbf{r}' - \mathbf{r}_-|^2 |\mathbf{r}' - \mathbf{r}|} \times \left[\frac{1}{2} (1 - \exp(i2\omega_0 t) \exp(-(1+i)k_2 |\mathbf{r}' - \mathbf{r}|)) \right] d\Omega \quad (5)$$

Note that Eq. 5 is implicit regarding ΔT . However, Eq. 4 (and subsequently Eq. 5) has two singularities at the current electrode contacts (\mathbf{r}_+ and \mathbf{r}_-). Therefore, the surface is divided into three regions: two contact regions determined by a chosen contact radius r_0 and the remaining sheet region. All resistance inside the contact regions (e.g. any sheet heating or spreading resistance) is attributed to a contact resistance, R_+ or R_- (for the current inlet or outlet contact respectively). The contacts are modelled as a singular point heat source placed at the contact center (\mathbf{r}_+ or \mathbf{r}_-). The complex temperature field resulting from the power deposited at the contacts then follows from Eq. 3:

$$\Delta\tilde{T}_{contact}(\mathbf{r}, t) = \frac{I_0^2 R_{\pm}}{2\pi\kappa |\mathbf{r} - \mathbf{r}_{\pm}|} \times \left[\frac{1}{2} (1 - \exp(i2\omega_0 t) \exp(-(1+i)k_2 |\mathbf{r} - \mathbf{r}_{\pm}|)) \right] \quad (6)$$

Combining Eq. 5 and 6 gives the time dependent temperature at a location \mathbf{r} and time t :

$$\Delta T(\mathbf{r}, t) = \text{Re} \left(\Delta\tilde{T}_{contact}(\mathbf{r}, t) + \Delta\tilde{T}_{sheet}(\mathbf{r}, t) \right) \quad (7)$$

Equations 5-7 can be used, together with the already known sensitivity function [17] to evaluate the integral in Eq. 1 and determine the TCR for a given $(R(t) - R_0)/R_0$.

Recently, it has been shown [21] that the TCR signal can be successfully extracted from AC M4PP measurements using the 3rd harmonic. Since the third harmonic signal solely contains the TCR response (i.e. $R_{3\omega,0} = 0 \Omega$), the third harmonic is the preferable signal. In our AC M4PP measurements, the obtained signal (left hand side of Eq. 1) is reported as a resistance value obtained from the RMS voltage. Therefore, in order to extract the TCR, the M4PP voltage needs to be calculated based on the four-point resistance expressed in [17]:

$$V(t) = I(t)R(t) = \frac{I(t)}{F} \int R_S(\mathbf{r}, t) \hat{S}(\mathbf{r}) d\Omega \quad (8)$$

$$= \frac{I(t)}{F} \int R_{S,0}(\mathbf{r}) (1 + \alpha_{TCR}\Delta T(\mathbf{r}, t)) \hat{S}(\mathbf{r}) d\Omega$$

Where F is the M4PP geometric correction factor and $\hat{S}(\mathbf{r})$ is the sensitivity as defined in [1]:

$$F = 2\pi / \ln \left(\frac{|\mathbf{r}_+ - \mathbf{r}_{V-}| |\mathbf{r}_- - \mathbf{r}_{V+}|}{|\mathbf{r}_+ - \mathbf{r}_{V+}| |\mathbf{r}_- - \mathbf{r}_{V-}|} \right)$$

$$\hat{S}(\mathbf{r}) = \frac{\mathbf{J}_S(\mathbf{r}) \cdot \tilde{\mathbf{J}}_S(\mathbf{r})}{\int_{\Omega} [\mathbf{J}_S(\mathbf{r}) \cdot \tilde{\mathbf{J}}_S(\mathbf{r})] d\Omega}$$

The third harmonic voltage is then obtained by inserting $V(t)$ into a digital lock-in amplifier from which the measured resistance value can be calculated.

3. Methods

3.1 Materials and instrumentation

M4PP-TCR measurements are taken on an ultra-thin platinum film with a nominal thickness of 16 nm deposited by e-beam evaporation (Wordentec QCL800) on a thick (1 mm), double side polished 4 inch wafer of fused silica acting as the substrate. A 1 nm Ti layer was deposited first to aid the adhesion of the platinum thin film to the substrate.

The M4PP measurements were performed on the MicroRSP A300 tool from Capres A/S, which is capable of fully automated M4PP resistance measurements with 0.1% precision. The tool delivers AC currents up to $I_{RMS} = 5$ mA and frequencies $f = 3.0137 \times 2^n$ Hz with $n \in [0, 1, 2, \dots]$. In this work however we restrict ourselves to frequencies for which the Joule heating response in the third harmonic has been demonstrated [21] (up to $f = 3.0137 \times 2^7 \approx 385.75$ Hz). The highest current of $I_{RMS} = 5$ mA is chosen as it will induce the largest TCR response. A ten point probe (L10PP) was selected, capable of creating 3 equidistant M4PP sub-probes with pitches of 10, 20, and 30 μm . The probe consists of polysilicon cantilever bases on top of which a 100 nm Ni layer is deposited serving as the current carrier. At each engage, the tool cycles through several configurations, including the A and A' configurations. The induced voltage is analyzed using a lock-in amplifier and harmonics are reported as a resistance, e.g.: $R_{1\omega} = V_{1\omega}^{RMS} / I^{RMS}$. The sheet resistance is obtained from the dual configuration method. [18, 19] Lead resistances, and subsequently the contact resistances are obtained using the same techniques as described in [1].

3.2 Extended semi-analytical model

A semi-analytical approach is taken to evaluate Eq. 8. The surface is meshed using a custom developed mesh, which starts at the four electrode contacts positioned at \mathbf{r}_+ , \mathbf{r}_- , \mathbf{r}_{V+} and \mathbf{r}_{V-} . The circular contacts are approximated by an 18-sided polygon. The mesh then expands radially outwards from the contacts by constructing concentric polygons with increasing radii with a

growth rate of 1.08. The maximum extent of the mesh is three times the probe footprint. Any remaining irregularities (e.g. at the convergence of two concentric polygons belonging to different contacts) are patched with triangular elements. The generated mesh provides a good compromise between high fidelity near the contacts and computational speed. At the center of each mesh element the sensitivity and temperature are calculated for a given time. To obtain the time dependent voltage, a period is divided into 64 time steps, where at each time step:

$$V(t) = \frac{I(t)}{F} \sum_{n=1}^N R_{S,0}(\mathbf{r}_n) [1 + \alpha_{TCR} \Delta T(\mathbf{r}_n, t)] \hat{S}(\mathbf{r}_n) dA_n \quad (9)$$

Where \mathbf{r}_n is the location of mesh element n , N is the total number of mesh elements and dA_n is the area of mesh element n . The temperature is obtained from two iterations of Eq. 7. The obtained voltage is then fed into a digital lock-in amplifier which returns the third harmonic voltage ($V_{3\omega}$), from which the third harmonic resistance as expressed by the A300 tool can easily be calculated: $R_{3\omega} = V_{3\omega} / (\sqrt{2} I^{RMS})$. To obtain the TCR from a measured third harmonic resistance value, the above technique is applied as a non-linear fit to the measured $R_{3\omega}$ with the TCR as the fitting parameter.

4. Results and discussion

The extended semi-analytical model is tested against a finite element model (FEM) developed in COMSOL multiphysics [16]. The model consists of hemispherical domain to which the module ‘heat transfer in solids’ is applied. The module ‘electric currents in shells’ is applied to the top boundary to represent the metallic thin film. The two modules are linked via the ‘electromagnetic heating multiphysics’ tool. On the outer boundary the reference temperature is maintained. A radius of fifty times the probe footprint (150 s) was found to be sufficient for the solution to converge at the lowest tested frequency (10^{-5} Hz). The contacts with radius r_0 are represented by four circles equidistantly placed on the top boundary, so that the probe center is positioned at the hemispherical origin. The area inside the contacts is excluded from the electrical domain and the current is injected and extracted from the contact boundaries so that the current flow is modelled as a flow between two cylinders with equipotential boundaries, as is assumed in the system and the semi-analytical model. The metal film is represented by designating the linearized resistivity model with a room temperature sheet resistance $R_{S,0}$ of a typical 16 nm thin platinum film with $\alpha_{TCR} = 1.75 \times 10^{-3} \text{ K}^{-1}$. The hemispherical domain was assigned the parameters $\rho = 2200 \text{ Kg m}^{-3}$, $C_p = 730 \text{ J Kg}^{-1} \text{ K}^{-1}$ and $\kappa = 1.4 \text{ W m}^{-1} \text{ K}^{-1}$ to represent the fused silica substrate. These parameters were subsequently used in the semi-analytical model, where the contact resistances were set to zero

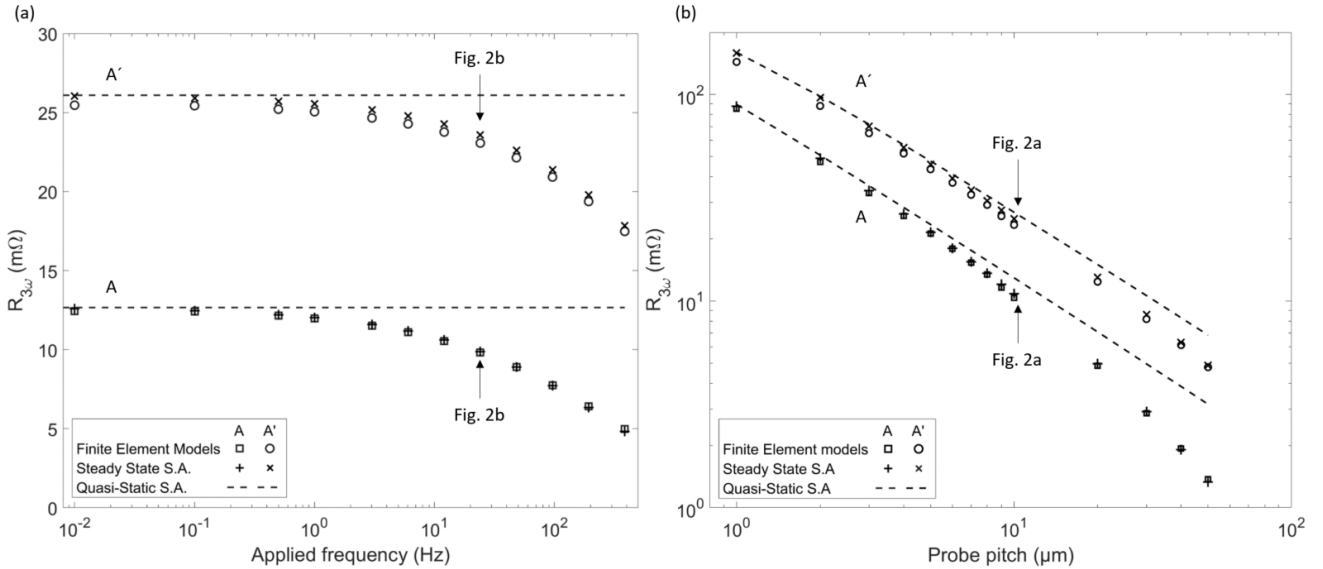


Figure 2. (a) The obtained third harmonic resistance ($R_{3\omega} = V_{RMS}^{3rd} / I_{RMS}$) from a simulation of an AC M4PP measurement on a 16 nm platinum thin film on a fused silica substrate using the extended model (steady state S.A.), the previous (quasi-static S.A.) model and finite element modelling. The frequency of the applied current is varied from the DC-limit to the highest measured frequency. The probe pitch was set to $10 \mu\text{m}$ in both the A and A' configurations (b) An identical simulation of the third harmonic resistance using the three models with varying probe at a fixed current frequency of $f = 12.055 \text{ Hz}$. The points that overlap in the two figures are indicated.

to mimic the FEM setup and two iterations were used in the calculation of the temperature fields.

The probe pitch and measurement frequency were varied across typical measurement values. Both the semi-analytical model and the FEM simulated the induced voltage as measured by the M4PP during the measurement. The FEM was taken over multiple current periods where the first period was omitted in the for analysis to minimize any transient effects, as they are not included in the semi-analytical model and can easily be eliminated in the measurements by introducing a settle time. The obtained voltage traces were inserted in a digital lock-in amplifier from which the third harmonic resistance is obtained as explained.

The results of the comparison are shown in Fig. 2, where Fig. 2a shows the obtained third harmonic resistances with varying frequency for a probe pitch of $s = 10 \mu\text{m}$, and Fig. 2b shows the obtained third harmonic resistances with varying probe pitch at a frequency of $f = 3.0137 \times 2^2 \approx 12.055 \text{ Hz}$. In addition, the third harmonic resistances obtained using the quasi-static model from [1] are plotted in both figures as a dashed line. Both the semi-analytical model (SA) and the FEM show a decrease in the third harmonic resistance with increasing frequency in both the A and A' configurations. The two models agree strongly on this trend and only differ up to 3% in absolute values. The majority of this offset likely arises from the temperature dependence of the current density, currently not accounted for in the semi-analytical model, which

will impact the sensitivity. Figure 2 clearly shows that the use of the quasi-static model will lead to large overestimations of $R_{3\omega}$, and subsequently an underestimation in TCR. The difference of ~18% observed in [1] could be explained by the observed deviations in $R_{3\omega}$ shown in Fig. 2. The measured resistance decreases more strongly with increased pitch than the quasi-static model. These large differences highlight the importance of the model extension in obtaining accurate thin film TCR values. It is valuable to note that the frequency dependent effects are much less severe at smaller probe pitches. The use of the quasi-static model may be warranted (as the data analysis process is significantly faster) in measurements with small ($< 3 \mu\text{m}$) probe pitches and low (3.0137 Hz) frequencies, as this only gives a relative difference of $< 2 \%$ in $R_{3\omega}$.

Figure 3a shows the third harmonic resistance measured on the 16 nm platinum thin film deposited on fused silica taken at the three different probe sizes with varying frequency. The predicted decrease in $R_{3\omega}$ amplitude from the measured $R_{3\omega}$ at the lowest applied frequency ($f \approx 3.01 \text{ Hz}$) by the steady state semi-analytical model is in excellent agreement with the measured values. A similar match is seen when comparing the measured and predicted values across the three different pitches, shown in Fig. 3b for several selected frequencies. The results shown in Figs. 2 and 3 solidify the extended semi-analytical model as the appropriate theory to describe the TCR responses in AC M4PP measurements.

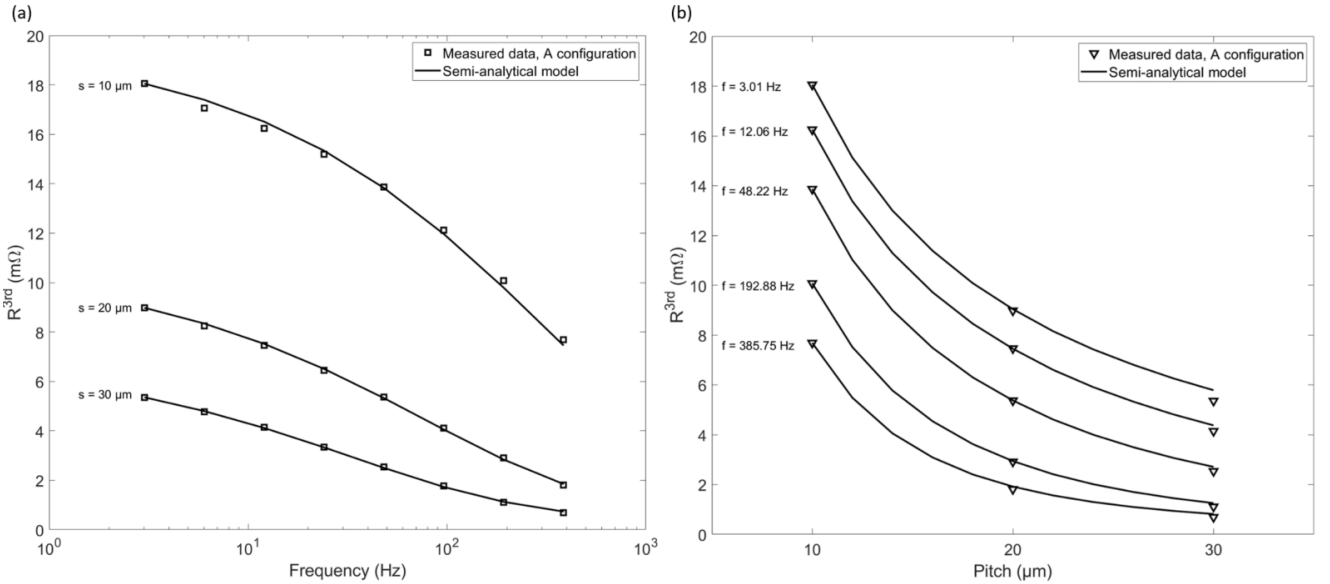


Figure 3. (a) Measured M4PP third harmonic resistance data (R^{3rd}) taken on a thin platinum film with a nominal thickness of 16 nm, using the L10PP probe in the A configuration, allowing for measurements on three sub probes of probe pitch of 10, 20 and 30 μm . The measurement is performed at 8 different frequencies. The expected decline of the magnitude of R^{3rd} from the 3 Hz measurement is obtained from the extended semi-analytical (S.A.) model calculations across all three measured probe sizes and is plotted as the solid lines. (b) The measured M4PP third harmonic resistance data from the same measurement across the three sub probe pitches compared to the expected decline in R^{3rd} magnitude given by the semi-analytical model. The data is shown for 5 selected frequencies.

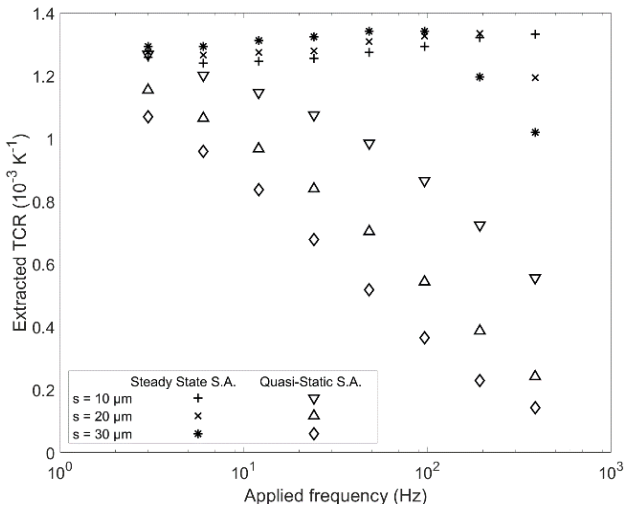


Figure 4. The extracted TCR from an A configuration M4PP measurement on a 16 nm platinum film using the extended model (Steady state. S.A.) and the previous model (quasi-static S.A.). The measurement is taken at various frequency steps using a L10PP probe allowing for measurements at three different equidistance probe pitches.

Figure 4 shows the TCR extracted from M4PP measurements on the 16 nm platinum thin film samples after the full data analysis procedure for both the quasi-static and extended steady state model across all measured frequencies and pitch sizes. As expected, the TCR obtained from the quasi-static model is both dependent on frequency and pitch, with TCR values 2-5 times lower at 385 Hz compared to 3 Hz. The extended model however obtains a steady TCR value across all varied parameters. Figure 4 highlights the improvement of the extended model, allowing ultra-thin film M4PP-TCR measurements to be taken at any frequency and with any probe size. In particular the independence of frequency is of interest, as it allows for a much faster measurement time. One must be mindful however of transient effects. FEM simulations at the highest frequency have demonstrated that from the second current period onwards transient effects had become negligible. Instituting a waiting period (settle time) before the voltage measurement can eliminate transient effects.

While the extended semi-analytical model has shown to allow for accurate TCR measurements, it does significantly increase the data analysis time, as an entire voltage period must be calculated (Eq. 8). In addition, while temperature iteration has been relatively straightforward to implement, the results in Fig. 2 suggest additional iteration of the current density is required. For the case of ultra-thin film measurements the semi-analytical model agrees with simulations to an acceptable level (<2%), however if one wants to apply the M4PP-TCR method to more complex structures, the semi-analytical model might start to become cumbersome. Data analysis using finite element modelling, rather than the semi-analytical approach taken so far, might prove to be the way forward in more complex

devices or materials such as multilayer structures or materials with a significant Seebeck coefficient. Finite element modeling also allows for easy inclusion of transient effects, reducing the measurement time as a waiting period is no longer necessary.

5. Conclusion

In this work we have demonstrated an extension to the semi-analytical data analysis method to account for the time dependent power deposited in sample during M4PP measurements. The measured resistance increase due to TCR predicted by extended model show excellent agreement with finite element modelling and measured data on a 16 nm platinum film across a range of measurement frequencies and probe sizes. We believe that with the extended model the M4PP-TCR method has become a powerful approach to metal thin film TCR characterization. The high precision (<2%) demonstrated previously [1] is now paired with excellent accuracy across the full range of possible measurement parameters. With the flexibility of the M4PP tool, this allows for TCR characterization at high spatial resolution, minimal sample damage and at unprecedented measurement speed. In addition, the time dependent temperature fields calculated by the extended semi-analytical model can be applied in other M4PP measurements that require knowledge of the thermal system.

Acknowledgements

This work has been supported by the Innovation Fund Denmark (Grant Nos. 8054-00020B and 8057-00010B) and the Sapere Aude (Independent Research Fund Denmark) (No. 8048-00088B).

Data availability statement

The data that support the findings of this study are available from the corresponding author upon reasonable request.

References

- [1] Marangoni, T. A., Guralnik, B., Borup, K. A., Hansen, O., & Petersen, D. H. (2021). Determination of the temperature coefficient of resistance from micro four-point probe measurements. *Journal of Applied Physics*, 129(16), 165105.
- [2] H. A. Schafft and J. S. Suehle, *Solid State Electron.* 35, 403 (1992).
- [3] M. M. Waldrop, *Nat. News* 530(7589), 144 (2016).
- [4] H. A. Schafft, S. Mayo, S. N. Jones, and J. S. Suehle, in *Proceedings of 1994 IEEE International Integrated Reliability Workshop (IRWS)* (IEEE, 1994), p. 5.

- [5] A. Von Glasow, A. Fischer, and G. Steinlesberger, in 2003 IEEE International Reliability Physics Symposium Proceedings (IEEE, 2003), p. 126.
- [6] M. Olszacki, C. Maj, M. Al Bahri, J. Marrot, A. Boukabache, P. Pons, and A. Napieralski, *J. Micromech. Microeng.* 20(6), 064008 (2010).
- [7] T. Dinh, H.-P. Phan, A. Qamar, P. Woodfield, N.-T. Nguyen, and D. V. Dao, *J. Microelectromech. Syst.* 26, 966 (2017).
- [8] S. Wu, Q. Lin, Y. Yuen, and Y.-C. Tai, *Sens. Actuators A* 89, 152 (2001).
- [9] Petersen, C. L., Grey, F., Shiraki, I., & Hasegawa, S. (2000). Microfour-point probe for studying electronic transport through surface states. *Applied Physics Letters*, 77(23), 3782-3784.
- [10] F. Smits, *Bell Syst. Tech. J.* 37, 711 (1958).
- [11] A. Uhlir Jr., *Bell Syst. Tech. J.* 34, 105 (1955).
- [12] D. Worledge and P. Trouilloud, *Appl. Phys. Lett.* 83, 84 (2003).
- [13] D. H. Petersen, O. Hansen, T. M. Hansen, P. Bøggild, R. Lin, D. Kjær, P. F. Nielsen, T. Clarysse, W. Vandervorst, E. Rosseel, N. S. Bennett, and N. E. B. Cowern, *J. Vac. Sci. Technol. B* 28(1), 27 (2010).
- [14] Nielsen, P. F., Petersen, D. H., Lin, R., Jensen, A., Henrichsen, H. H., Gammelgaard, L., ... & Hansen, O. (2012, May). Microprobe metrology for direct sheet resistance and mobility characterization. In 2012 12th International Workshop on Junction Technology (pp. 100-105). IEEE.
- [15] H. S. Carslaw and J. C. Jaeger, *Conduction of Heat in Solids* (Clarendon Press, 1959), p. 263
- [16] COMSOL Multiphysics®, v. 5.6., www.comsol.com, COMSOL AB, Stockholm, Sweden.
- [17] D. W. Koon, F. Wang, D. H. Petersen, and O. Hansen, *J. Appl. Phys.* 114(16), 163710 (2013).
- [18] L. J. van der Pauw, *Philips Tech. Rev.* 20, 220 (1958).
- [19] S. Thorsteinsson, F. Wang, D. H. Petersen, T. M. Hansen, D. Kjær, R. Lin, J.-Y. Kim, P. F. Nielsen, and O. Hansen, *Rev. Sci. Instrum.* 80, 053902 (2009).
- [20] Kasap S., Koughia C., Singh J., Ruda H., O'Leary S. (2006) *Optical Properties of Electronic Materials: Fundamentals and Characterization*. In: Kasap S., Capper P. (eds) *Springer Handbook of Electronic and Photonic Materials*. Springer Handbooks. Springer, Boston, MA. https://doi.org/10.1007/978-0-387-29185-7_3
- [21] Guralnik, B., Hansen, O., Henrichsen, H. H., Beltrán-Pitarch, B., Østerberg, F. W., Shiv, L., ... & Petersen, D. H. (2021). 3ω correction method for eliminating resistance measurement error due to Joule heating. *Review of Scientific Instruments*, 92(9), 094711.

